Universidad de La Laguna
Oficina de Sede Electrónica
Entrada
Nº registro: 2021/71850
Nº reg. oficina: OF002/2021/71029
Fecha: 13/07/2021 14:47:32

DEPARTAMENTO DE ASTROFISICA

Universidad de La Laguna

The QUIJOTE-MFI northern sky survey at 10–20 GHz: construction and study of the maps, and characterization of the microwave Haze

Memoria que presenta
D. Federica Guidi
para optar al grado de
Doctor en Ciencias Físicas.

INSTITUTO Ð ASTROFISICA Ð CANARIAS
julio de 2021

Examination date: September, 2021
Thesis supervisor: José Alberto Rubiño-Martín and Ricardo Génova-Santos

ISBN: xx-xxx-xxxx-x
Depósito legal: TF-xxxx/2002
published

To three shining stars,
nonno Gigio, nonno Cicci,
and Cristina.

Acknowledgments

As a fair beginning of this long manuscript, I would like to express my greatest acknowledgments to the people that contributed, together with my full dedication to this thesis project, to the achievement of this new accomplishment.

My supervisors, Alberto and Ricardo, deserve my first acknowledgements. Thank you for making this thesis possible, from the beginning to the end. All what I learned and achieved in these last years is thanks to you. Thanks also to Carlos and Mike, for dedicating their time reading thorough this thesis, contributing with comments and suggestions that helped me to improve it. I sincerely acknowledge also all the members of the QUIJOTE group. To the scientific team (including collaborators in IFCA, Manchester and Cambridge): thank you all for the continuous exchange of ideas that doubtless contributed to my formation. To the QUIJOTE engineering team: thank you for building up and taking care our *"microwave eyes"*, without which the results presented in this thesis and in the forthcoming papers would have never been possible.

Thanks to all the new friends that came across my path in Tenerife, and in particular to those that are walking with me right now. To Jaume, Nuria, Nuria, Paula and Vir, thank you for the smiles, reflections, experiences, games, pizzas, and cats that we've shared during this time. Thanks also to Rosa for bringing her light every day in the office, and for her precious advices on how to grow up orchids, as well as happiness. People like you all make the world a better place.
Graicas a todos los amigos que han cruzado mi camino en Tenerife, y especialmente a aquellos que están caminando conmigo ahora. A Jaume, Nuria, Nuria, Paula y Vir, por las sonrisas, reflexiones, experiencias, juegos, pizzas y gatos que compartimos durante este tiempo. Gracias también a Rosa por llevar su luz todos los días en el corralón, y por los preciosos consejos sobre como crecer

orquídeas, así como la felicidad. Personas como vosotros hacen del mundo un lugar mejor.

Thanks Eve, Armando, Estrella, Sara, and Víctor, my Canarian family, for welcoming me in the island and in their lives even before knowing who I was. Ours is the prettiest story ever, and I will always carry it with me to face the new changes in my life.
Gracias a Eve, Armando, Estrella, Sara, y Víctor, mi familia Canaria, por acogerme en la isla y en vuestras vidas sin saber ní quién era. La nuestra es la historia más bonita del mundo, y siempre la llevaré conmigo para enfrentar los nuevos cambios en mi vida.

Thanks to my family. Mom, Dad, Fra, my grandmas Oliva, Anna and Giuliana, aunt Mizzi, Alessandro and Giulia, thank you for being always with me, besides the distance. In particular thanks to Mom and Dad for setting solid foundations to the life that I am building up now.
Grazie alla mia famiglia. Mamma, Papà, Fra, nonna Oliva, nonna Anna e nonna Giuliana, zia Mizzi, Alessandro e Giulia, grazie per esserci sempre nonostante la lontananza. In particolare grazie a Mamma e Papà per aver gettato le solide fondamenta della vita che sto costruendo.

Thanks to my little Linda for giving me back all the love with kisses and bites in equal measure.
Miao.

Finally, thanks to Andrea for being always and forever on my side, respecting, accepting and supporting my dream of becoming a great scientist.
Infine, grazie Andrea per essere sempre e per sempre al mio fianco, rispettando, accettando e supportando il mio sogno di diventare una grande scienziata.

Resumen

Las ondas gravitacionales primordiales generadas durante la inflación deberían observarse como un huella característica en la polarización a gran escala angular del Fondo de Microondas Cósmico (CMB). Esta huella se conoce como modos B del CMB, y aún no ha sido observada. Con el fin de poder obtener una detección limpia de los modos B primigenios, es extremadamente importante caracterizar la emisión Galáctica polarizada de polvo y sincrotrón, y controlar con alta precisión los efectos sistemáticos de la instrumentación de microondas.

Esta tesis se desarrolla en este contexto, presentando un análisis de los datos del instrumento MFI del experimento QUIJOTE, que, desde 2012, mide la intensidad y la polarización lineal del cielo de microondas desde el Observatorio del Teide, en el rango de frequencias 10–20 GHz. El objetivo de QUIJOTE-MFI es caracterizar con alta precisión la emision Galáctica de baja frecuencia, en particular la emisión anómala de microondas (AME) y el sincrotrón polarizado, para complementar el estudio de las anisotropías de polarización del CMB.

Con ese fin, en esta tesis se ha desarrollado el código de elaboración de mapas PICASSO, basado en la técnica de *destriping* (Keihänen et al., 2010), el cual se utiliza para construir los mapas de intensidad y de polarización lineal (parametros de Stokes Q y U) del experimento QUIJOTE. PICASSO permite una reconstrucción muy precisa de las grandes escala angulares de la señal de cielo, siendo fundamental para estudios relacionados con los modos B. La implementación del código se inició en un proyecto de tesis anterior (Pelaez Santos, 2019), y su desarrollo continuó durante esta tesis con la inclusión del uso de priors para el ruido $1/f$ y una técnica para el ajuste de patrones en el dominio temporal durante la construcción del mapa. PICASSO ha sido validado con simulaciones realistas de datos de QUIJOTE-MFI, mostrando que la reconstrucción de la señal del cielo es precisa en un 0.001% en multipolos en el rango $20 \lesssim \ell \lesssim 200$. Además, el estudio de la función de transferencia del código ha demostrado que el 100% de la señal del cielo se recupera en escalas $\ell \gtrsim 10$, con

solo un $\sim 2\%$ de pérdida de potencia en $2 \lesssim \ell \lesssim 8$ para los modos E y B de la señal polarizada. Estos análisis han sido presentados en un artículo que ya fue enviado a publicar (Guidi et al., enviado).

Este código ha sido aplicado para construir los mapas finales en intensidad y polarización de todo el hemisferio norte Galáctico (*wide-survey*), en cuatro frecuencias en el rango 10–20 GHz, y utilizando datos obtenidos durante un tiempo efectivo de observación de un año. Esta tesis presenta una caracterización detallada de estos mapas, basada principalmente en el cálculo de sus espectros de potencias. Los espectros de potencias de estos mapas en polarización (que están claramente dominados por emisión sincrotrón) fueron modelados utilizando una ley de potencias $C_\ell \propto \ell^\alpha$, con $\alpha = -3.00 \pm 0.16$ para el modo E y $\alpha = -3.09 \pm 0.41$ para el B, en latitudes galácticas $|b| > 5°$ y declinaciones $6° < \delta < 70°$, en el rango de multipolos $30 < \ell < 300$. Asimismo, se ha medido el cociente entre la amplitud de la potencia de los modos E y B en $\ell = 80$, obteniendo $A_{\rm BB}/A_{\rm EE} = 0.34 \pm 0.10$, dentro del área del cielo antes mencionada. Este valor es menor que el cociente para la emisión de polvo térmico derivado de los datos de Planck ($A_{\rm BB}/A_{\rm EE} = 0.5$; Planck Collaboration et al., 2018c). También se han medidos los espectros TB y EB de los mapas, siendo éstos compatibles con cero dentro de las incertidumbres, y se ha detectado marginalmente el espectro TE en multipolos bajos. Además, se han presentado los resultados de diferentes pruebas de validación de los datos, que incluyen el análisis de test nulos para la caracterización del ruido en los mapas, y unos análisis de correlación cruzada destinados a la validación de la calibración de los datos. Estos resultados se publicarán en Rubiño-Martín et al. (en preparación), que irá acompañado por un conjunto de artículos centrados en la explotación científica de los datos del wide-survey de QUIJOTE-MFI. Los mapas se harán públicos a partir de estas publicaciones.

Por último se analizaron nuevos datos de QUIJOTE-MFI, en combinación con los del wide-survey, en el Haze, una región que se extiende alrededor del centro Galáctico hasta altas latitudes ($|b| < 35°$) y que presenta una fuerte emisión en microondas, con contrapartidas en otras longitudes de onda: las burbujas de Fermi en rayos gamma, y las plumas polarizadas observadas en radio (a 2.3 GHz). El Haze es una emisión difusa de origen incierto e interesante, posiblemente asociada con el decaimiento de partículas de materia oscura, o con actividad nuclear del centro Galáctico. Utilizando datos de QUIJOTE-MFI, detectamos, con un nivel de confianza de $\sim 9\sigma$, un exceso de señal difusa en intensidad, el cual podría atribuirse a la emisión del Haze, y cuyo espectro presenta una ley de potencias correspondiente a un sincrotrón con índice espectral $\beta^H = -2.79 \pm 0.08$, en el rango de frequencias 11–60 GHz. Este índice espectral es ligeramente distinto de los publicados anteriormente (por ejemplo, Planck Collaboration et al., 2013) que estimaron $\beta^H = -2.56 \pm 0.05$. Sin embargo, y de acuerdo con trabajos anteriores, observamos que el espectro del Haze es más plano que el del sincrotrón total en la misma área y rango de frecuencias, el cual presenta un índice espectral $\beta^s = -3.00 \pm 0.03$. Además, se observó una diferencia entre el índice espectral de intensidad de las burbujas Norte y Sur del Haze, con un nivel de confianza de $\sim 6\sigma$. Finalmente, se realizó un estudio de las estructuras y filamentos polarizados posiblemente asociados con el Haze, observando un cambio del índice espectral hacia valores con una pendiente mayor en bajas frecuencias, en consistencia con los resultados de trabajos anteriores (Carretti et al., 2013). Estos resultados se publicarán en Guidi et al. (en preparación).

x

Abstract

Primordial gravitational waves generated during inflation are expected to imprint a peculiar footprint in the large angular scale polarization of the Cosmic Microwave Background (CMB), the so-called B-modes, which however are still undetected. Characterizing Galactic foregrounds such as polarized dust and synchrotron emission, as well as having very precise control of instrumental effects, is extremely important to target a clean detection of the CMB B-modes.

This thesis is set in this context, and presents an analysis of the data of the MFI instrument of the QUIJOTE experiment. QUIJOTE-MFI has been installed at the Teide Observatory since 2012, with the aim to observe the intensity and linear polarization of the microwave sky at four frequencies in the range 10–20 GHz. The purpose of QUIJOTE-MFI is to measure the low frequency Galactic foregrounds such as anomalous microwave emission (AME) and polarized synchrotron, which need to be precisely characterized to complement the study of the CMB polarization anisotropies.

An important part of this thesis is dedicated to the development of the PICASSO map-making code, which is based on the destriping technique (e.g., Keihänen et al., 2010), and which is used to construct the intensity and linear polarization (Stokes Q and U) maps for the QUIJOTE experiment. PICASSO allows a precise reconstruction of the signal at large angular scales, which is key for B-modes searches. A first version of the code was initially implemented in a previous thesis by Pelaez Santos (2019), and it was further developed during this thesis by including the use of priors for the $1/f$ noise, and a technique for the fitting of templates in the time domain to the data, during the map-making step. PICASSO was validated with realistic simulations of QUIJOTE-MFI data, showing that the reconstruction of the sky signal is precise at the 0.001% level and for multipoles $20 \lesssim \ell \lesssim 200$. In addition, the study of the transfer function of the code showed that 100% of the sky signal is recovered at scales $\ell \gtrsim 10$, with only $\sim 2\%$ power loss at $2 \lesssim \ell \lesssim 8$ for EE and BB. This work will soon be

published in Guidi et al., (submitted).

Afterwards, this thesis describes the application of this code for the construction, validation, and study of the QUIJOTE-MFI wide-survey maps, which are obtained from approximately one year of effective observations of the full northern sky, at 10–20 GHz, taken in the period 2012–2018. The wide-survey maps are presented, analyzed and characterized, in conjunction with their angular power spectra. The angular power spectra of the polarization maps (which are synchrotron dominated) can be modeled, at 11 GHz, with a power law $C_\ell \propto \ell^\alpha$, with $\alpha = -3.00 \pm 0.16$ for EE and $\alpha = -3.09 \pm 0.41$ for BB, at Galactic latitudes $|b| > 5^\circ$ and declinations $6^\circ < \delta < 70^\circ$, in the multipole range $30 < \ell < 300$. The relative amplitude of the power of the E and B-modes at $\ell = 80$ is measured to be $A_{\rm BB}/A_{\rm EE} = 0.34 \pm 0.10$ within the aforementioned sky area, it being lower than the BB/EE ratio measured for dust emission by Planck ($A_{\rm BB}/A_{\rm EE} = 0.5$; Planck Collaboration et al., 2018c). The TB and EB spectra of the maps are measured to be compatible with zero within the uncertainties, and the TE spectrum is marginally detected at low multipoles. In addition, a complete set of validation tests, including the analyses of null-tests for the characterization of the noise in the maps, and cross-correlation analysis for the validation of the calibration of the data are presented. These results will be published in Rubiño-Martín et al. (in prep.), which will also be accompanied by a set of papers focused on the scientific exploitation of the QUIJOTE-MFI wide-survey data. The maps will be made publicly available.

Finally, new data taken in the region surrounding the Galactic center were analyzed in combination with the wide-survey data, with the aim of studying the so-called microwave Haze. The Haze is a diffuse emission with uncertain and interesting origin, since it could be attributed to dark matter annihilation in the Galactic bulge, or to nuclear activity in the Galactic center. It extends from the Galactic center up to high Galactic latitudes ($|b| < 35^\circ$), with spatial correspondence to the Fermi bubbles observed in γ-rays, and to the polarized radio plumes observed by the S-PASS survey at 2.3 GHz. The Haze area is studied in intensity and in polarization, using the new data provided by the QUIJOTE experiment. An excess of diffuse signal that could be attributed to the Haze is detected in intensity with $\sim 9\sigma$ confidence level. The intensity spectrum of this emission was modeled using a power-law spectrum, leading to a spectral index $\beta^H = -2.79 \pm 0.08$, in the range 11–60 GHz. This result is in slight tension with previous measurements (e.g., Planck Collaboration et al., 2013) that estimated $\beta^H = -2.56 \pm 0.05$. However, in agreement with previous works, it can be observed that the spectrum of the the Haze is flatter than that of the total synchrotron in the same area and frequency range, which has a spectral index $\beta^s = -3.00 \pm 0.03$. In addition, we observed a difference between the intensity spectral index of the North and South Haze bubbles, at $\sim 6\sigma$ confidence level. Finally, a study of the polarized spurs and plumes that are possibly associated with the Haze is presented, where a clear steepening of the spectrum between 11 GHz and 23 GHz can be observed, in agreement with previous works (Carretti et al., 2013). These results will be published in Guidi et al. (in prep.).

Contents

Acknowledgments **v**

Resumen **vii**

Abstract **xi**

1 Introduction **1**
- 1.1 Historical perspective 1
- 1.2 The Standard Cosmological model 4
  - 1.2.1 The homogeneous and isotropic expanding Universe . . . 4
  - 1.2.2 Thermal history of the Universe 7
  - 1.2.3 Inflation and the perturbed Universe 8
- 1.3 Cosmic Microwave Background (CMB) anisotropies 10
  - 1.3.1 Physics of the CMB anisotropies 10
  - 1.3.2 CMB polarization 12
  - 1.3.3 Scalar, vector and tensor perturbations: why we want to detect the B-modes 13
- 1.4 Harmonic space formalism for CMB anisotropies 15
  - 1.4.1 CMB dipole 16
  - 1.4.2 Temperature anisotropies 17
    - 1.4.2.1 Spherical harmonics formalism 17
    - 1.4.2.2 Cosmological estimator and cosmic variance . . 20
    - 1.4.2.3 Convolution with instrumental beam 21
  - 1.4.3 Polarization anisotropies 22
    - 1.4.3.1 Spherical harmonic formalism 24
    - 1.4.3.2 Cosmological estimators 26
- 1.5 Galactic foregrounds 26
  - 1.5.1 Synchrotron 29

1.5.2 Free-free 30
1.5.3 Thermal dust 31
1.5.4 Anomalous Microwave Emission (AME) 32
1.5.5 CO transition line emission 32
1.5.6 Extragalactic point sources 33
1.6 Current status of the field 33
1.6.1 Space missions 33
1.6.2 Ground-based experiments 35
1.7 Motivation of the thesis 39
1.8 Scientific goals of the thesis 40

2 The QUIJOTE experiment 41
2.1 Overview of the QUIJOTE experiment 41
2.2 The Multi Frequency Instrument (MFI) 43
2.2.1 Objectives 43
2.2.2 Observing strategies 44
2.2.3 Results obtained with the MFI 46
2.3 MFI Instrument model 47
2.3.1 Instrumental response 47
2.3.1.1 Response to the IQU Stokes parameters 49
2.3.2 Noise 51
2.3.2.1 Noise generalities 51
2.3.2.2 Noise of the MFI 52
2.4 MFI pipeline 53
2.4.1 Overview of the MFI pipeline 54
2.4.2 TOD Calibration 54
2.4.2.1 Calibrators 55
2.4.2.2 Gain amplitude calibration 56
2.4.2.3 Relative amplitude calibration: r-factor 56
2.4.2.4 Polarization angle 57
2.4.2.5 Polarization efficiency 58
2.4.3 Beams 58
2.4.4 Bandpass and colour corrections 60
2.4.5 Radio Frequency Interference (RFI) 62
2.4.6 Map-making 63
2.4.7 Power spectrum estimation 64
2.5 Atmosphere 64

3 Map-making for QUIJOTE-MFI 67
3.1 Introduction 67
3.2 Map-making problem 69
3.2.1 Destriper algorithm 70
3.2.2 Noise covariance matrix 72
3.3 QUIJOTE-MFI map-making 74
3.3.1 QUIJOTE-MFI instrumental response 75
3.3.2 QUIJOTE pointing matrix 76
3.3.3 IQU analytical solution 77
3.3.4 Estimating the baselines with noise priors 79
3.3.5 Destriping QUIJOTE-MFI data with priors 80
3.3.6 Fitting a template function 80
3.4 The PICASSO code 82
3.4.1 Data 82
3.4.2 Noise simulations 83
3.4.3 Gaps in the data 83
3.4.4 Template functions 83
3.4.4.1 Atmosphere 84
3.4.4.2 CMB dipole 85
3.4.5 Destriping 85
3.4.6 Projecting into the I, Q, and U maps 87
3.5 Simulations 87
3.5.1 Wide survey scanning strategy 88
3.5.2 Simulated sky signal 88
3.5.3 Noise 89
3.6 Results 90
3.6.1 Reconstructed maps and real space statistics 90
3.6.2 Validation with angular power spectra 96
3.6.2.1 Fit of the noise angular power spectrum 100
3.6.3 Transfer function 101
3.6.4 Fit of a template function 102
3.7 Conclusions 105

4 The QUIJOTE-MFI wide survey 107
4.1 Data 107
4.1.1 Scanning strategy 107
4.1.2 Periods 108
4.1.3 Noise statistics 109
4.1.4 Atmosphere 113

4.1.5 Interference . . . 115
4.1.6 Flagging . . . 116
4.2 Pipeline . . . 116
4.2.1 Map-making . . . 116
4.2.2 Re-calibration and post-processing . . . 117
4.3 Maps . . . 117
4.3.1 Sky maps . . . 118
4.3.2 $n_{\rm hit}$ maps . . . 118
4.3.3 Weights maps . . . 119
4.4 Angular power spectra . . . 127
4.4.1 Fit of EE and BB auto-power spectra . . . 129
4.4.2 TE, TB and EB cross-power spectra at 11 GHz . . . 130
4.5 Noise characterization . . . 131
4.5.1 Null-tests formalism . . . 131
4.5.2 Null-tests of the wide-survey maps . . . 132
4.5.2.1 Construction of the null-test maps . . . 134
4.5.2.2 Angular power spectra of the null-tests . . . 134
4.5.3 Noise angular power spectra from the *half*-difference . . . 136
4.5.4 Inter-frequency correlation . . . 139
4.5.5 Inter-channel correlation . . . 141
4.6 Internal calibration tests with cross-correlations . . . 143
4.6.1 Inter-horn . . . 143
4.6.2 Inter-period . . . 147
4.6.3 Intra-nulltest . . . 150
4.6.4 Detection of the CMB anisotropies . . . 153
4.7 Conclusions . . . 157

5 Study of the microwave Haze as observed by QUIJOTE 159
5.1 Introduction . . . 160
5.1.1 Discovery of the microwave Haze . . . 160
5.1.2 γ-ray and X-ray counterparts . . . 160
5.1.3 Polarization at radio and microwave frequencies . . . 161
5.1.4 Haze models . . . 162
5.2 Data . . . 163
5.2.1 QUIJOTE-MFI data . . . 164
5.2.2 Ancillary data . . . 168
5.2.3 Faraday rotation correction to S-PASS . . . 173
5.2.4 Selection of the regions . . . 175
5.3 Methodology . . . 177

5.3.1 Template fitting 177
  5.3.1.1 Templates 178
  5.3.1.2 Priors 183
5.3.2 Polarization T-T plots 185
  5.3.2.1 T-T plots of P_{MAS} 185
  5.3.2.2 T-T plots of Q and U combined projection . . . 186
  5.3.2.3 T-T plots posterior distribution 187

5.4 Results 188
  5.4.1 Intensity template fitting 188
    5.4.1.1 Intensity Haze maps 190
    5.4.1.2 Intensity Haze spectrum 193
  5.4.2 Polarization template fitting 198
    5.4.2.1 Polarization residual maps 198
    5.4.2.2 Polarization residual spectrum 200
  5.4.3 T-T plots of Haze polarized plumes and spurs 203
5.5 Discussion 206
  5.5.1 South Haze area 206
  5.5.2 North Haze bubble 208
  5.5.3 Comparison between South and North Haze bubbles . . . 209
  5.5.4 North Haze filament 210
5.6 Conclusions 211

6 Conclusions and future prospects 215
6.1 Implementation and validation of the PICASSO map-making and code 216
6.2 Characterization and validation of the QUIJOTE-MFI wide-survey maps 217
6.3 Analysis of the microwave Haze using new QUIJOTE-MFI data 219
6.4 Publications 220
6.5 Future prospects 220

A Appendix 223
A.1 PICASSO input commands 223
A.2 Posterior analysis of the T-T plots 227

Bibliography 233

1

Introduction

"When we started to bet there was still nothing that could make us predict anything, except a few particles that were spinning, electrons thrown here and there as they come, and protons up and down each on its own."
Italo Calvino, Le Cosmicomiche

1.1 Historical perspective

Considerations on the formation of the first elements in the early Universe, formulated by Gamow and collaborators (Gamow, 1946; Alpher et al., 1948), predicted in 1946 that the Universe is populated by a background of primordial photons, the so-called Cosmic Microwave Background (CMB). This cosmological radiation was thought to have a black body spectrum, and that it was released during the early stage of the Universe. Alpher and Herman, a few years later (Alpher & Herman, 1950), computed the expected temperature of this black body, obtaining $T_{\rm CMB} \approx 5\,{\rm K}$ at present time, while independent later studies by Peebles (Peebles, 1965), estimated $T_{\rm CMB} \approx 10\,{\rm K}$. These are the first theoretical predictions of the existence and of the properties of the CMB radiation.

Around the same years, Penzias and Wilson were undertaking microwave observations with a huge horn antenna sensitive to wavelengths of 7.5 cm ($\approx 4\,{\rm GHz}$), with which they detected an unexpected isotropic emission with $T \approx 3.5 \pm 1.0\,{\rm K}$ (Penzias & Wilson, 1965). This excess of signal could not be explained by any source of noise or interference, it was concluded that they were observing the CMB for the first time, in agreement with the cosmological predictions. For the serendipitous detection of the CMB, Penzias and Wilson were awarded with the Physics Nobel Prize in 1978. The discovery of the CMB still represents today one of the greatest achievements in the history of modern cosmology.

Many more observations were performed in the following years, trying to constrain the CMB black body spectrum at low frequencies (long wavelengths $\lambda > 0.3\,\mathrm{cm}$) in the Rayleigh-Jeans regime (e.g., Roll & Wilkinson, 1966). However, in order to confirm the black body origin of the observed radiation, it was necessary to test the high frequencies of the spectrum (short wavelengths) and observe the exponential cut-off on the other side of the black body peak. This was achieved with astonishing precision with the CMB space mission launched in November 1989: the Cosmic Background Explorer Satellite (COBE) and the Far InfraRed Absolute Spectrophotometer (FIRAS) instrument on board. In Mather et al. (1990), after just one year of operations of COBE-FIRAS, they presented the first measurement of the CMB spectrum taken from a region in the vicinity of the north Galactic pole, at frequencies $30\,\mathrm{GHz} < \nu < 600\,\mathrm{GHz}$ ($1.0\,\mathrm{cm} > \lambda > 0.5\,\mathrm{mm}$). Fig. 1.1 shows the COBE-FIRAS CMB spectrum measurement, which is also the most precise black body ever measured in nature, with deviations of less than 1%.

Although the black body spectrum measured by COBE-FIRAS is doubtless a milestone in the context of CMB science, another instrument on board COBE, the Differential Microwave Radiometer (DMR),[1] made possible another important discovery. COBE-DMR observed for the first time[2] the CMB temperature *anisotropies*, which are tiny spatial fluctuations of the CMB temperature. As shown in Fig. 1.1, besides the isotropic monopole with $T \approx 3\,\mathrm{K}$ radiation (top image), the CMB shows a dipole component with an amplitude of $\approx 3\,\mathrm{mK}$ (central image), and, at smaller angular scales, fluctuations at the level of 1 part over 100,000, with an r.m.s. of $\approx 18\mu\mathrm{K}$ (bottom image). The CMB anisotropies are clearly observed at high Galactic latitudes, while they are obscured at low latitudes by the emission of dust and gas in our Galaxy, which constitute a foreground contamination to the CMB background light (bright horizontal feature in the bottom image of Fig. 1.1; see Sec 1.5). John C. Mather and George F. Smoot were awarded the Nobel Prize in Physics in 2006, for their contributions in the field of cosmology with COBE.

The most recent space missions WMAP and Planck, as well as other experiments from the ground, followed COBE, measuring with increasing precision

---

[1] COBE-DMR operated in three frequency bands: at 31.5, 53, and 90 GHz (see Sec. 1.6.1).

[2] The Russian space mission RELIKT-1, which operated until February 1984 at 37 GHz (8 mm) with an angular resolution of 5.8 deg, measured first, and prior to COBE, the CMB dipole and the Galactic plane emission, and constrained the quadrupole moment (Klypin et al., 1992).

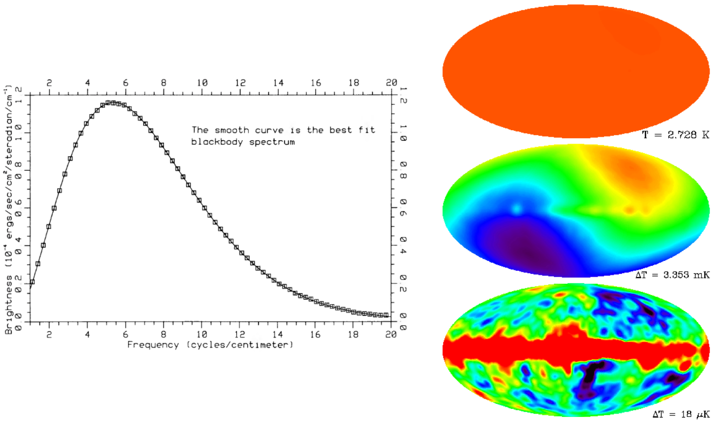

FIGURE 1.1— Left: first measurement of the CMB black body spectrum, by COBE-FIRAS (Mather et al., 1990). Note that the error bars are smaller than the data points. Right: four-year full sky map obtained by COBE-DMR at 53 GHz, in Galactic coordinates, smoothed at an effective angular resolution of 10 deg to increase the signal to noise (Image from the LAMBDA webpage: `https://lambda.gsfc.nasa.gov/product/cobe/dmr_image.cfm`). In the top panel, the data of DMR in a scale from 0 - 4 K, showing the uniformity of the CMB radiation at ∼3 K. In the middle, the same data in a scale intended to display the dipole anisotropy. In the bottom, the data after subtraction of the CMB dipole, where we can appreciate the emission of the Galaxy (horizontal band in the map) and the CMB temperature anisotropies at higher latitudes.

and angular resolution the CMB temperature anisotropies. We refer to Sec. 1.6 for a more detailed description of these experiments. Currently, the best full-sky map of the CMB intensity anisotropies is that obtained from the Planck satellite (Planck Collaboration et al., 2018a), as shown in Fig. 1.2.

The CMB anisotropies are also polarized at 10% level, and they are usually decomposed into two components: the so-called E and B-modes (see Sec. 1.3.2). The E-modes of the CMB have been observed for the first time by the DASI experiment (Kovac et al., 2002), and have been later characterized in detail by several other space (WMAP and Planck; see Sec. 1.6.1), balloon-borne (e.g., SPIDER Collaboration et al., 2021) and ground-based (see Sec. 1.6.2) experiments. Also B-modes produced by lensing effects have been observed (e.g., Polarbear Collaboration et al., 2014; Omori et al., 2017; see Sec. 1.3.3), however, one of the main challenges of modern CMB experiments is the detection of the primordial B-modes, which are expected to be imprinted in the polarization

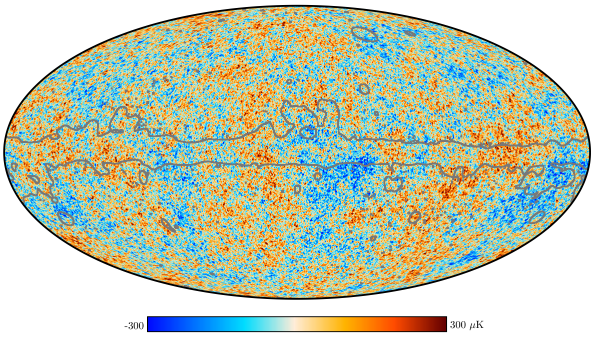

FIGURE 1.2— Planck 2018 CMB temperature anisotropies map, extracted with the SMICA method. The grey lines show the contour of the confidence mask for CMB reconstruction, corresponding to complex Galactic emission regions. (Image taken from `https://www.cosmos.esa.int/web/planck/picture-gallery`).

of the CMB by gravitational waves generated during inflation (see Sec. 1.2.3). The primordial B-modes have not been detected yet, and upper limits have been set (see e.g. Tristram et al., 2020). Nevertheless, current measurements of the intensity and polarization CMB anisotropies provided a incredibly powerful data set to constrain the cosmological properties of the Universe, starting the era of precision cosmology (see e.g. Planck Collaboration et al., 2020a).

1.2 The Standard Cosmological model

In this section we present the Standard Cosmological Model that is currently used to describe the Universe. We provide a qualitative description of the Big Bang ΛCDM model, which constitutes the theoretical background for cosmological studies, and which is nowadays tested with various cosmological probes, such as, for example, the CMB. We refer to a variety of cosmology textbooks[3] for rigorous and detailed derivation of the equations below.

1.2.1 The homogeneous and isotropic expanding Universe

The first principle in which we base the modern cosmological model is the *Cosmological Principle*, according to which the Universe, on large scales ($\gtrsim$100 Mpc), is homogeneous and isotropic. This principle is supported by an observational evidence: we measure the same smooth and global cosmological properties in

---

[3] See for example Padmanabhan (1993); Coles & Lucchin (2002); Dodelson (2003)

any direction of observation. The level of anisotropy of the primordial Universe, as observed in the CMB, is very low, being at the order of $\sim 10^{-5}$ at large scales. The tiny primordial anisotropies constitute the seeds at the origin of the structures that populate the Universe today, which grew up under the effect of gravity.

One more fundamental property, also supported by observational evidence, is that the Universe is an *expanding* system: the galaxies around us are moving away with a greater speed the more distant they are, as Edwin Hubble observed early in 1929 (Hubble, 1929), and as we are confirming with increasing precision to date (Riess et al., 2016; Planck Collaboration et al., 2020a) by measuring the Hubble constant H_0. Given that the Universe is expanding, there must exist an initial time in which distances were infinitesimally small, in a singularity of the space-time. This consideration implies the formulation of the *Big Bang* model, which assumes that the observable Universe was initially infinitely small, hot and dense, and that it expanded to a macroscopic size, driven by inflation first (see Sec. 1.2.3), and by the energy-density of its components later.

The main tool employed for the mathematical modeling of the Universe is *General Relativity*, which relates the geometry (given by the metric $g_{\mu\nu}$) with the pressure and energy density[4] of the system through the Einstein equations. The metric, in cosmology, is usually given by the Friedmann-Lemaître-Robertson-Walker (FLRW) tensor:

$$g_{\mu\nu} = \begin{pmatrix} -1 & 0 & 0 & 0 \\ 0 & a^2(t) & 0 & 0 \\ 0 & 0 & a^2(t) & 0 \\ 0 & 0 & 0 & a^2(t) \end{pmatrix} \tag{1.1}$$

where $a(t)$ is the so-called *scale factor* (a function of the proper time[5] t, related also with redshift as $a = (1+z)^{-1}$) that is used to model the evolution of the space coordinates with time, obeying the Cosmological Principle. The speed at which the scale factor changes is usually given as the *Hubble rate*:

$$H(t) = \dot{a}/a \tag{1.2}$$

that, if computed today ($t = t_0$, $a = 1$), corresponds to the aforementioned Hubble constant H_0. One more useful quantity to define is the *comoving horizon*,

---

[4] This is given by the energy-momentum diagonal tensor $T_{\mu\nu}$, where $T_{00} = -\rho$ is the energy density of the fluid and $T_{ii} = P$ $(i = 1, ..., 3)$ is its pressure.

[5] t is the time measured by a clock that is moving with the element of the fluid with comoving coordinates $x = (ct, x^1, x^2, x^3)$, there c is the speed of light. In this section we will use natural units with $c = 1$.

which is the comoving distance traveled by a photon, in absence of interaction, from the beginning of time ($t = 0$) to a certain time t:

$$R_h(t) = \int_0^t \frac{dt'}{a(t')} \tag{1.3}$$

The horizon corresponds to the radius of a sphere within which different points are in causal contact, and therefore could have interacted at some point in their evolution.

The connection between the geometry and the energy density of the Universe is elegantly developed in the first Friedmann equation, which, when combined with the equation of state of different fluids composing the Universe[6], can be expressed as:

$$H(t) = H_0\sqrt{(\Omega_{\rm c} + \Omega_{\rm b})a^{-3} + (\Omega_{\rm rad})a^{-4} + \Omega_{\rm k}a^{-2} + \Omega_{\rm DE}a^{-3(1+\omega)}} \tag{1.4}$$

where $\Omega_{\rm x} = \rho_{\rm x}(t = t_0)/\rho_{\rm cr}$ are the density parameters at the present time, and where "x" indicates the various components of the universe, which are: cold dark matter (c), baryonic matter (b), radiation (rad), space-time curvature (k), and dark energy[7] (DE) with equation of state parameter ω, and where $\rho_{\rm cr} = 3H_0^2/(8\pi G)$ is the critical energy density. The benchmark model today is the so-called Λ*CDM model*, which assumes (supported by observational evidence) a flat universe ($\Omega_{\rm k} = 0$), populated today by ordinary baryonic matter at $\sim 5\%$, cold dark matter (CDM) at $\sim$26 %, and dark energy with $\omega = -1$, modeled therefore as cosmological constant ($\Omega_{\rm DE} = \Omega_\Lambda$), at $\sim$69 %.

We can see from Eq. 1.4 that the different energetic components of the Universe evolve differently with the scale factor, meaning that the Universe passed through different epochs during which one component dominates over the other: radiation dominates first, then matter (baryonic plus dark), and finally dark energy. The second Friedman equation relates the acceleration of the Universe with the energy-density and pressure of the fluid, as:

$$\frac{\ddot{a}}{a} = -\frac{4\pi}{3}G(\rho + 3P) \tag{1.5}$$

The joint solution of the first and second Friedman equations, given the equation of state of the fluids, allows us to model the evolution of the homogeneous and isotropic Universe with time.

---

[6] The equation of state of a fluid is given as $P = \omega\rho$ with $\omega = 0$, $1/3$, -1 for respectively non relativistic matter, radiation, and dark energy.

[7] The dark energy part can also be given in term of cosmological constant as $\Omega_\Lambda = \Omega_{\rm DE}a^{-3(1+\omega)}$, with $w = -1$.

1.2.2 Thermal history of the Universe

Within the framework of the Big Bang model, at early times of the Universe evolution, all types of elementary particles had very high energies, and were compressed into a small volume. During the first three minutes after the Big Bang, nuclear reactions were possible, and the lightest nuclei (hydrogen, deuterium, helium and lithium) formed, in a process called *nucleosynthesis* (Boesgaard & Steigman, 1985; Steigman, 2004). However, electrons were still too hot to be bound with protons into atoms, and continuous scattering of photons with electrons (and protons) was keeping matter and radiation in thermal equilibrium. The spectral radiance[8] of photons in thermal equilibrium is modeled by the Planck law of a black body at temperature T:

$$B_\nu(T) = \frac{2h\nu^3}{c^2}\frac{1}{e^{\frac{h\nu}{k_\mathrm{B}T}} - 1} \tag{1.6}$$

where h is the Planck's constant, k_B is the Boltzmann's constant and c is the speed of light. In this primordial plasma, due to Thomson scattering, the mean free path of photons was so short that they could not propagate: the Universe was opaque.

As the Universe evolved its volume increased, and the temperature gradually decreased. Approximately 370,000 years after the Big Bang, when the temperature approached $T\ \sim$3000 K$\sim$ 0.26 eV, free protons and electrons started to combine into neutral atoms, in a process called *recombination*. This in turn caused an increase of the mean free path of the photons, which almost instantaneously led to the *decoupling* of radiation and matter, allowing light to propagate almost freely for the first time. The photons released after decoupling constitute the CMB radiation, which is therefore the most ancient and primordial light that we can ever observe. The recombination epoch, although it was not an instantaneous process, is usually associated with an ideal time surface with certain width, the *last scattering surface*, from which the CMB photons started to propagate across the Universe, without (ideally) any other interaction before they reach the observer in the current day.

The CMB radiation keeps the original thermal black body spectrum distribution also at later times, but its temperature gets red-shifted, scaling in time with the expansion of the Universe, as:

$$T(t) = T(t_\mathrm{ls})\frac{a(t_\mathrm{ls})}{a(t)} \tag{1.7}$$

---

[8] Power (Watt) per unit solid angle (steradian), frequency (Hertz) and area (m^2) projected in the direction of observation. $[B_\nu] = \mathrm{W}/(\mathrm{m}^2 \cdot \mathrm{sr} \cdot \mathrm{Hz})$.

being $a(t_{\mathrm{ls}})$ and $a(t)$ the scale factor at the time of last scattering t_{ls}, and at an arbitrary time t (see Weinberg (2008) for derivation). Following Eq. 1.7, the CMB temperature today ($z = 0$) can be simply expressed as:

$$T_{\mathrm{CMB}} = \frac{T_{\mathrm{ls}}}{1 + z_{\mathrm{ls}}}. \tag{1.8}$$

The current best measurement of the CMB monopole temperature to date is $T_{\mathrm{CMB}} = 2.72548 \pm 0.00057\,\mathrm{K}$ (Fixsen, 2009), based on COBE/FIRAS data. Considering this observational result and the physical prediction for the temperature of the Universe at last scattering ($T_{\mathrm{ls}} \approx 3000\,\mathrm{K}$, as mentioned above), we can obtain an estimate of the redshift of the last scattering surface, which is $z_{\mathrm{ls}} \approx 1100$.

1.2.3 Inflation and the perturbed Universe

The CMB monopole is a piece of evidence for the Big Bang theory, and it is one of the main representations of a uniform and isotropic Universe. However, as anticipated (see Fig. 1.2), the CMB radiation shows some small anisotropies in its temperature (and polarization) distribution across the sky. In addition, the Universe observed today shows evident structures (galaxies, cluster of galaxies, the cosmic web), that cannot arise from perfect homogeneity. The presence of fluctuations (deviations from homogeneity) is explained by the theory of inflation,[9] a quick ($t \sim 10^{-36}\,\mathrm{s}$) and exponential (factor $\sim 10^{26}$) expansion of the infant Universe (at energies $\sim 10^{16}\,\mathrm{GeV}$), which freezes primordial quantum fluctuation into macroscopic over-densities, which later grew up under the effect of gravity to from the structures that we observe today.

Cosmology aims to predict and observe the properties of these fluctuations, which are imprinted in the anisotropies of the CMB, and in the large scale distribution of galaxies across the Universe (the so-called large scales structure, LSS). It is usual to defined the *contrast density field* that traces the matter overdensities in space:

$$\delta(\mathbf{x}) = \frac{\rho(\mathbf{x}) - \bar{\rho}}{\bar{\rho}} \tag{1.9}$$

---

[9] Inflation was first theorized by Guth (1981) to explain the missing a magnetic monopole problem, the observed level of isotropy (the cosmological horizon problem) and the measured flatness of the Universe (flatness problem). Indeed, the same ∼3 K temperature of the CMB is observed at all scales in the sky, also from regions that entered in causal contact later than last scattering. If we account for the fact that they were in causal contact before inflation, when space abruptly expanded disconnecting points that were previously causally connected, the problem is solved. In addition, the curvature of the Universe should have been fine-tuned with incredible precision in order to fit with the measured Hubble rate, unless we consider the space stretching caused by inflation.

where $\bar{\rho}$ is the average matter density. This can be studied from a statistical point of view, defining the auto-correlation function[10] $\xi(|\mathbf{x}-\mathbf{x}'|)$ and its Fourier transform, the matter power spectrum $P(k)$:

$$\xi(|\mathbf{x}-\mathbf{x}'|) = \left\langle \delta(\mathbf{x})\delta(\mathbf{x}') \right\rangle \; ; \; \left\langle \tilde{\delta}(\mathbf{k})\tilde{\delta}^*(\mathbf{k}') \right\rangle = (2\pi)^3 P(k)\delta^3(\mathbf{k}-\mathbf{k}') \tag{1.10}$$

where the $\tilde{}$ indicates the Fourier transform operation, δ^3 is the Dirac delta function, and $< \cdot >$ is an average over ensembles of the Universe (by applying the ergodic theorem; see Sec. 1.4.2). When studying the CMB, we normally define the photon temperature fluctuation on the sphere (analogous to the contrast density field), and we study the angular power spectrum C_ℓ (analogous to the matter power spectrum), as explained in detail in Sec. 1.4.2.

Under the hypothesis of Gaussianity of the density perturbations, the auto-correlation function can be used to compute the variance of the density contrast, as $\xi(|\mathbf{x}-\mathbf{x}'| = 0) = \left\langle |\delta(\mathbf{x})|^2 \right\rangle = \sigma^2$. The power spectrum $P(k)$ has units of (lenght)^3, therefore it is common to use the dimensionless quantity (Dodelson, 2003):

$$\Delta^2(k) \equiv k^3 P(k)/2\pi^2, \tag{1.11}$$

which satisfies the relation:

$$\sigma^2 = \int \frac{d^3\mathbf{k}P(k)}{(2\pi)^3} = \int \Delta^2 \, d\ln k \tag{1.12}$$

where in the first equality we applied the Fourier transformation, and in the second one we use the definition of Δ. We can see that $\Delta^2(k)$ corresponds to the variance of the density perturbations in a logarithmic interval.

The initial conditions of the fluctuations are set by inflation, and can be of scalar or tensor origin (respectively labelled as "s" or "t" below, see Sec. 1.3.3 for more details). Due to the quantum origin of the primordial perturbations, they are expected to be Gaussian distributed, and they can be statistically described by the dimensionless power spectra (Eq. 1.11):[11]

$$\Delta_s(k) = \frac{A_s}{2\pi^2}\left(\frac{k}{k_*}\right)^{n_\mathrm{s}-1} \; ; \; \Delta_t(k) = \frac{A_t}{2\pi^2}\left(\frac{k}{k_*}\right)^{n_\mathrm{t}} \tag{1.13}$$

where k_* is a typical (arbitrary) scale, and n_s, n_t are the so-called *scalar* and *tensor spectral indices.* A power spectrum of scalar perturbations with $n_\mathrm{s} = 1$

---

[10] The auto-correlation function is the excess probability, as compared to a random distribution, of finding two galaxies at relative distance $r = |\mathbf{x}-\mathbf{x}'|$.

[11] See Eq. 6.100 in Dodelson (2003) for the complete formula and derivation.

is called Harrison-Zel'dovich spectrum (Harrison, 1970; Zeldovich, 1972), which is scale invariant, meaning that Δ_s is constant at all scales k. Inflation theory predicts n_s to be slightly smaller than one, and indeed this is what we observe, being the current most precise measurement $n_\mathrm{s} = 0.9626 \pm 0.0057$ (Planck Collaboration et al., 2018b). Analogously, a spectrum of tensor perturbations is scale invariant if $n_\mathrm{t} = 0$. According to the theory of inflation, n_t is expected to be slightly different from zero, but tensor perturbations have not been detected, so n_t has not been measured yet.

The time evolution of the matter and photon density fields, which are those of main interest for cosmology, can be derived by solving the Boltzmann equations for each species populating the Universe, in order to take into account every possible interaction between different species, other that gravity, starting from the initial conditions given by inflation. The solution of Boltzmann equations (see e.g., Dodelson, 2003) provides a statistical prediction, depending on the cosmological model, for the matter and photon density fields observed today, which can be used to ultimately predict the matter power spectrum $P(k)$ and photon angular power spectrum C_ℓ, which when fitted to observations, allows us to constrain the cosmological model. This is implemented in cosmological Boltzmann codes like (e.g.,) ed LINGER/PLINGER (Bode & Bertschinger, 1995), CMBFAST (Seljak & Zaldarriaga, 1996; Zaldarriaga et al., 1998), CAMB (Lewis & Challinor, 2011), CMBEASY (Doran, 2005), CLASS (Blas et al., 2011; Lesgourgues, 2011).

1.3 Cosmic Microwave Background (CMB) anisotropies

The density fluctuations of the photon fluid can be observed as spatial anisotropies in the temperature and linear polarization of the CMB. We provide here a brief overview of the main physical mechanisms that are at the origin of the CMB fluctuations.

1.3.1 Physics of the CMB anisotropies

We can distinguish between primary and secondary CMB intensity anisotropies, depending on when they were generated. Primary anisotropies are generated at (or before) last scattering, and are due to:

- *Intrinsic anisotropies of the photon fluid* injected by inflation as previously described. This has an effect at the intermediate-small angular scales of the temperature fluctuations ($\theta \lesssim 1\,\mathrm{deg}$). Moreover, the coupled growth of photons and baryons perturbations in dark-matter over-densities, before decoupling, is characterized by a continuous compression (driven by the dark matter gravitational potential), and expansion (due to the action of the radiation pressure). This results in the so-called *acoustic oscillations* of the photon-baryon fluid, which show up as a sequence of *acoustic peaks* (and dips; see Fig. 1.3) in the CMB angular power spectrum, at $\ell \gtrsim 100$ (as well as in the matter power spectrum).

- *Doppler effect.* At recombination the photons are released with a certain velocity, which also depends on the phase of the oscillation in which they were trapped. This results in a Doppler shift, relative to the frame where they are observed.
- The *Sachs-Wolfe effect* (SW) (Sachs & Wolfe, 1967). The temperature anisotropies are coupled, before last scattering, with the primordial density fluctuations (δ), which correspond, in the framework of General Relativity, to fluctuation of the gravitational potential (ϕ). At last scattering, photons located in over-dense regions escape the gravitational potential well where they were bounded, loosing part of their energy due to a gravitational redshift effect, and appearing as a cold spots in the CMB as observed at later times. This gravitational phenomena, which simply depends on the difference of the gravitational potential at emission and at arrival of the CMB photons ($\Delta T/T = \Delta\phi/(3c^2)$), takes the name of SW effect. It is a super-horizon[12] source of temperature fluctuations, constituting the main source of anisotropies at large angular scales ($\ell \lesssim 50$; corresponding to the low-multipoles "T" plateau in Fig. 1.3).

Secondary anisotropies are generated at later stages, during the travel of CMB photons towards the observer. They are:

- The *Sunyaev–Zeldovich effect* (SZ) (Sunyaev & Zeldovich, 1980). This is a distortion of the CMB spectrum due to Compton scattering of CMB photons with electrons of hot ionized plasma contained in galaxy clusters. The CMB photons gain a net quantity of energy from the scatters with the electrons in the cluster medium, resulting in cold spots if observed in the Rayleigh-Jeans regime (low frequencies), a null around 217 GHz, and a hot spot at high frequencies. This is the so-called "thermal" SZ effect. In addition, if there is a bulk motion of the gas, then there is a "kinetic" SZ component.
- The *Integrated Sachs-Wolfe effect* (ISW) (Sachs & Wolfe, 1967). This is similar to the SW effect described above, but it is due to the interaction

---

[12] Meaning that this is an effect at angular scales larger than the dimension of the horizon at decoupling.

with the gravitational potential at all stages of the evolution of the Universe, integrated along the path of the CMB photons from last scattering to the observer. ISW is particularly sensitive to dark energy. However, it is a large angular scales (low multipoles) effect, therefore its detection suffers from cosmic variance (see Sec. 1.4.2).

- *Gravitational lensing*. The CMB photons are deflected by gravitational lensing effect due to the interaction with massive structures that populate the Universe at different stages of its evolution, from last scattering to the observer (Planck Collaboration et al., 2020b). Large scale potentials are the dominant responsible of the deflections. The effect is a smoothing of the acoustic peaks in intensity and polarization, and, as we will see later (Sec. 1.3.3), it generates B-modes polarization.

- *Reionization*. During the late time reionization of the Universe ($6 \lesssim z \lesssim 20$; e.g., Becker et al., 2001; Fan et al., 2002), new free electrons interact with the CMB photons through Thomson scattering, with an efficiency given by the optical depth τ. The effect of reionization is an exponential ($e^{-\tau}$) cut-off of the CMB anisotropies at angular scales smaller than the horizon at the time of reionization. In addition, as we will see later (Sec. 1.3.3), reionization also generates large angular scale polarization anisotropies, observed in the so-called reionization bump, which emerges at low multipoles.

Finally, a dumping or smearing of the CMB anisotropies also occurs. This is caused by the suppression of structures due to weakly interacting particles like massive neutrinos (*free streaming*), and by the randomized photon-electron scattering in a thick last scattering surface (*Silk damping* from Silk, 1968) that washes out the small scales anisotropies.

This summary is not exhaustive. For other effects that are not mentioned here, we refer to the review by Hu & Dodelson (2002); Chluba (2018).

1.3.2 CMB polarization

The elastic scattering of a photon with a free charged particle like an electron, in the low energy limit,[13] takes the name of Thomson scattering, an interaction that preserves the kinetic energy of the particle and the frequency of the photon, imprinting on it linear polarization. CMB photons and electrons interact at

---

[13] The low energy condition is valid if the energy of the photon is much lower than the rest mass of the particle, therefore if $\nu \ll mc^2/h$, where ν is the frequency of the photon, m is the mass of the particle, and c is the speed of light and h is the Planck constant.

the last scattering surface through Thomson scattering. It follows that the CMB anisotropies are linearly polarized (Hu & White, 1997; Dodelson, 2003), and in particular with an E-mode pattern, which is a direct consequence of the distribution of the perturbations at last scattering, as we will see in the next section. The amplitude of CMB polarization anisotropies is typically one order of magnitude lower than that of the intensity ones, with the exact value depending on the angular scale ($\sim \mu$K). Being so faint, the CMB polarization anisotropies are particularly challenging from the observational point of view.

There are several reasons why the CMB polarization is extremely interesting. First of all, some degree of polarization is expected only if a quadrupole temperature anisotropy is present at last scattering, therefore, if observed, the CMB is definitely of cosmological origin. Second, the fact that we observe the polarization of the CMB is a direct proof that the temperature really had a quadrupole anisotropy at last scattering. Third, Thomson scattering must be rapid in order not to wash out the input temperature quadrupole by random scatter, and the fact that we observe 10% polarized CMB emission tells us about the thickness of the last scattering surface, or equivalently about the duration of the photon-matter primordial decoupling. Finally, as we will see in Sec. 1.3.3, primordial gravitational waves that were generated and amplified during inflation, are predicted to imprint a particular polarized pattern to the CMB, the so called B-modes (e.g., Kamionkowski & Kovetz, 2016). The detection of the CMB B-modes would provide a laboratory for the study of inflation.

However, various phenomena can modify the polarization of the CMB photons, such as lensing, birefringence (Minami et al., 2019), Faraday rotation (Pogosian & Zucca, 2018) and primordial magnetic fields (Renzi et al., 2018), and they must be carefully characterized in order to isolate the CMB signal.

1.3.3 Scalar, vector and tensor perturbations: why we want to detect the B-modes

The polarization of the CMB anisotropies can be of scalar, vector or tensor origin (e.g., Hu & White, 1997). Scalar perturbations are the only ones that are related with matter density fluctuations, and constitute the seeds of structure formation at later times of the Universe. Vector perturbations are generated by vortical motions of the matter. They are not associated with density perturbations, and the expansion of the Universe is expected to suppress them. Because of that, vector perturbations of the CMB are usually neglected. Finally, tensor perturbations are generated by the stretch of the space-time by gravitational waves.

The expected CMB angular power spectra are represented in Fig. 1.3, which

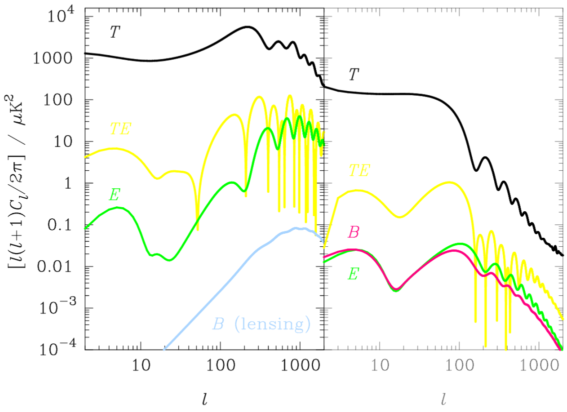

FIGURE 1.3— Predicted CMB angular power spectra from scalar (left) and tensor (right) perturbations, with $r = 0.38$ (image taken from Challinor, 2006).

shows, in the left panel, the power spectra originated by scalar perturbations, and, on the right, that from tensor perturbations (Challinor, 2006). We can see that both scalar and tensor perturbations contribute to the temperature angular power spectrum C_ℓ^{TT} (black lines), to the cross spectrum of temperature and E-modes C_ℓ^{TE} (yellow lines) and imprint different polarization patterns to the CMB. Scalar perturbations can generate only the E-modes polarization pattern (green line, left panel). However, some E-modes are converted into small scales (large ℓ, light blue curve, left panel) B-modes by gravitational lensing effects during the CMB photon's propagation from last scattering to the observer. Finally, large angular scales E-modes are also produced in the reionization epoch, when the CMB photons are re-scattered from the electrons of the reionized Universe, resulting in a bump of the E-modes angular power spectrum at scales of the horizon at reionization time.

Vector perturbations originate mainly B-modes but are expected to be totally negligible, and are not shown in Fig. 1.3. Finally, tensor perturbations generate both E and B-modes at comparable level (green and red line, right panel). As already mentioned, gravitational waves during the inflation are predicted to be the only source of tensor perturbations to the CMB. Therefore, if we observed a B-modes signal of the CMB at large angular scales, the only possible origin would be from gravitational waves during inflation.

A detection of the B-modes at large angular scales would be the first direct proof of inflation. There is a wide range of inflationary models, which are characterised by different inflationary potentials, and which predict totally different values of the *tensor-to-scalar ratio* r (different by orders of magnitude). The tensor-to-scalar ratio is a quantity that is commonly used to quantify the level of the power spectrum of tensor perturbation $P_{\mathrm{t}}(k)$ with respect to the scalar ones $P_s(k)$ (given in Eq. 1.13; e.g., Tristram et al. 2020), as:

$$r = \frac{P_{\mathrm{t}}(k_*)}{P_{\mathrm{s}}(k_*)} \tag{1.14}$$

with k_* as the pivot scale. Upper limits on the tensor to scalar ratio are related to the upper bounds on the energy scale of inflation (at 95% C.L.) through the relation (Planck Collaboration et al., 2018b):

$$r = 0.0085 \frac{V_*}{(10^{16}\,\mathrm{GeV})^4}. \tag{1.15}$$

where V is the inflation's potential, which is proportional to E^4, where E is the energy scale of inflation, which imply r to be proportional to the fourth power of the energy of inflation. However, no lower limits can be set for the amplitude of the B-mode signal, it can be infinitely small, even at a level of being undetectable. For these reasons, the exceptional control of systematics and of the contamination from Galactic foregrounds (see Sec. 1.5) is needed in order to attempt the detection of primordial B-modes.

While B-modes from lensing of the CMB have been observed (Polarbear Collaboration et al., 2014), the gravitational wave B-modes have not been detected yet, and upper limits have been set for r. The joint analysis of Planck 2020 data (Planck hlpTT+lowT+lowlEB) combined with BICEP/*Keck* 2015 data (BICEP2 Collaboration et al., 2018) were recently presented in Tristram et al. (2020). They reported the most stringent constraints on r to date, being $r_{k_*=0.05} < 0.044$, which imply $V_* < (1.5 \times 10^{16}\,\mathrm{GeV})^4$ at 95% C.L.

1.4 Harmonic space formalism for CMB anisotropies

In this section we provide an analytical characterization of the intensity and polarization CMB anisotropies. In particular we derive the properties of the CMB dipole, and we set up the commonly used spherical harmonics framework, which is broadly used to analyze the CMB anisotropies at a statistical level, as projected on the celestial sphere.

1.4.1 CMB dipole

The first and simplest departure from isotropy of the CMB is a dipole with amplitude $\Delta T \approx 3\,\mathrm{mK}$, as shown in the middle/right panel of Fig. 1.1. The CMB dipole, contrary to the small scale anisotropies, is not generated at the last scattering surface, but it has a local origin related to the peculiar motion of the observer with respect to the CMB rest frame. The homogeneity of the CMB radiation, indeed, provides the definition of a reference frame from which we can observe the cosmological radiation with the same temperature from any direction on the sky (except for small fluctuations). This frame provides a reference from which we can define the relative velocities of galaxies, including the Milky Way, with respect to the CMB rest frame.

The reference frame of an observer located in a moving galaxy is not at rest with respect to the CMB. The CMB radiation observed from a moving frame maintains the spectral shape of a black body, but its temperature varies across the sky with a dipole pattern, which is induced by the Doppler shift of CMB photons in the frame of the observer. This is the case for an observer located in the solar system, which has a peculiar motion induced by the drift of the Milky Way Galaxy in the local group, and by the Sun's motion in the Galaxy. In the reference frame of the Sun, the CMB is observed with a *solar dipole* component of $\sim 3\,\mathrm{mK}$, plus an extra annual modulation introduced by the Earth's spin around the Sun, the so-called *orbital dipole*, with an amplitude of $\sim 200\,\mu\mathrm{K}$.

The temperature T' of the CMB measured by an observer which is in motion at velocity $\vec{v}$ with respect to the CMB rest frame, is given by (Peebles & Wilkinson, 1968):

$$T'\left(\theta'\right) = \frac{T}{\gamma\left(1 - \beta\cos\theta'\right)} \tag{1.16}$$

where T is the CMB temperature at rest, and θ' is the angle between the velocity vector of the observer and the direction of observation (which is parallel and opposite to the direction of the incoming photon), in the observer's frame. The quantities $\gamma = 1/\sqrt{1-\beta^2}$ and $\beta = v/c$ are the usual factors defined in special relativity, with c being the speed of light. The velocity of the Sun with respect to the CMB rest frame is of the order of few hundreds kilometers per second, which imply $\gamma \approx 1$ and $\beta \approx 10^{-3} \ll 1$. We can expand therefore the dipole temperature fluctuation in 1.16 in powers of β as:

$$\Delta T\left(\theta'\right) = T'\left(\theta'\right) - T = T\left(\beta\cos\theta' + \mathcal{O}\left(\beta^2\right)\right) \tag{1.17}$$

According to this last equation, the leading term of the temperature fluctuation is projected in the sky as a dipole with amplitude $T\beta$, excluding effects at

$\mathcal{O}(\beta^2)$. The CMB temperature is larger (blue-shifted) if we observe in the same direction towards which the Earth is moving, where $\cos(\theta' = 0) = 1$, and is lower (red-shifted) in the opposite direction, where $\cos(\theta' = \pi) = -1$.

Conklin (1969) reported the first measurement of the CMB dipole effect from the ground, and measured the Earth's velocity in the Earth's equatorial plane to be $v = 350\,\mathrm{km/s}$, in the direction of right ascension $RA \approx 11^h 20^m$, observing at declination $\delta = 32°$. Today, the Planck satellite provides the most accurate measurement of the CMB solar dipole, with an amplitude of $T\beta = 3364.4 \pm 3.1\,\mu\mathrm{K}$, in the direction, in Galactic coordinates, $(l, b) = (263°.998 \pm 0°.051, 48°.265 \pm 0°.015)$ (Table 3 in Planck Collaboration et al. (2020f)), which corresponds to the proximity of the Hydra and Centaurus galaxy clusters.

In term of multipoles (see Sec. 1.4.2), the CMB dipole corresponds to the multipole $\ell = 1$. The angular power spectrum at $\ell = 1$, C_1, can be computed using Eq. 1.27 and 1.35. It is:

$$C_1 = \frac{4}{9}\pi(T\beta)^2 \tag{1.18}$$

For a typical value of the dipole amplitude $T\beta \approx 3.36\,\mathrm{mK}$, we get $C_1 \approx 15.76\,\mathrm{mK}^2$.

1.4.2 Temperature anisotropies

1.4.2.1 Spherical harmonics formalism

The anisotropies constitute the main observable for cosmological studies with the CMB. They are observed as Gaussian distributed tiny fluctuations (1 part in 10^5) of the $\sim$3 K microwave radiation released after the last scattering of photons with matter, as shown in Fig. 1.2. The CMB anisotropies are commonly studied from a statistical point of view, to characterize their size, amplitude and distribution on the sphere.

Let us introduce the definition and main properties of the *spherical harmonics*, $Y_{\ell m}(\hat{\mathbf{n}})$, which are at the foundation of CMB formalism. The spherical harmonics constitute a complete imaginary basis on the sphere, where a point is identified by the angles (θ, ϕ), or equivalently by the pointing vector[14] $\hat{\mathbf{n}}$. The spherical harmonics in the direction $\hat{\mathbf{n}}$ are defined as:

$$Y_{\ell m}(\hat{\mathbf{n}}) = \sqrt{\frac{2\ell+1}{4\pi}\frac{(\ell-m)!}{(\ell+m)!}} P_{\ell m}(\cos(\theta)) e^{im\phi} \tag{1.19}$$

---

[14] The unit vector in spherical coordinates is given by $\hat{\mathbf{n}} = (\sin\theta\cos\phi, \sin\theta\sin\phi, \cos\theta)$, with $\theta \in [0, \pi)$ and $\phi \in [0, 2\pi)$.

where $\ell \in \mathbf{N} : \ell = \{0, ..., \infty\}$ and $m \in \mathbf{Z} : |m| \leq \ell$, and $P_{\ell m}(\cos(\theta))$ are the associated Legendre polynomials as a function of $\cos(\theta)$. The $Y_{\ell m}$'s satisfy the basic properties of:

- Completeness: any function[15] $\Theta(\hat{\mathbf{n}})$ can be expressed as a linear combination of spherical harmonics, as:

  $$\Theta(\hat{\mathbf{n}}) = \sum_{\ell=0}^{\infty} \sum_{m=-\ell}^{m=+\ell} a_{\ell m} Y_{\ell m}(\hat{\mathbf{n}}), \tag{1.20}$$

  where the *harmonic coefficients* $a_{\ell m}$ are complex numbers.

- Orthonormality:

  $$\int_{\theta=0}^{\pi} \int_{\phi=0}^{2\pi} Y_{\ell m} Y^{*}_{\ell' m'} d\Omega = \delta_{\ell \ell'} \delta_{m m'}. \tag{1.21}$$

- Symmetry:

  $$Y^{*}_{\ell m}(\hat{\mathbf{n}}) = Y_{\ell -m}(\hat{\mathbf{n}}), \tag{1.22}$$

  which, if the function $\Theta(\hat{\mathbf{n}})$ is real, is translated into the *reality condition* of the harmonic coefficients

  $$a^{*}_{\ell m} = a_{\ell -m} \tag{1.23}$$

  with * representing the complex conjugation.

- Addition theorem:

  $$\sum_{m=-\ell}^{\ell} Y_{\ell m}(\hat{\mathbf{n}}) Y^{*}_{\ell m}(\hat{\mathbf{n}}') = \frac{2\ell + 1}{4\pi} P_{\ell}(\hat{\mathbf{n}} \cdot \hat{\mathbf{n}}'), \tag{1.24}$$

  where we use the notation $P_{\ell} = P_{\ell 0}$.

We can use the spherical harmonics formalism to study the temperature anisotropies on the sky, which are usually defined as the relative fluctuation of the temperature at direction $\hat{\mathbf{n}}$, with respect to the mean sky temperature T_0, with the observer located in $\mathbf{x}$:

$$\frac{\Delta T}{T_0}(\hat{\mathbf{n}}, \mathbf{x}) \equiv \frac{T(\hat{\mathbf{n}}, \mathbf{x}) - T_0}{T_0}, \;\; T_0 = \int_{\theta=0}^{\pi} \int_{\phi=0}^{2\pi} T(\hat{\mathbf{n}}, \mathbf{x}) d\Omega \tag{1.25}$$

---

[15] This is valid for L^2 function: $\int |\Theta(x)|^2 dx < \infty$

For brevity, we drop the specification of $\mathbf{x}$ hereafter. We can expand this quantity in the space of multipoles ℓ using the spherical harmonics $Y_{\ell m}(\hat{\mathbf{n}})$ (as in Eq. 1.20):

$$\frac{\Delta T}{T_0}(\hat{\mathbf{n}}) = \sum_{\ell=1}^{\infty} \sum_{m=-\ell}^{m=+\ell} a_{\ell m} Y_{\ell m}(\hat{\mathbf{n}}) \tag{1.26}$$

which is equivalent to its inverse version:[16]

$$a_{\ell m} = \int_{\theta=0}^{\pi} \int_{\phi=0}^{2\pi} \frac{\Delta T}{T_0}(\hat{\mathbf{n}}) Y^*_{\ell m}(\hat{\mathbf{n}}) d\Omega \tag{1.27}$$

The term $\ell = 0$ corresponds to a monopole contribution which is zero for $\frac{\Delta T}{T_0}$, by definition. $\ell = 1$ is a dipole, and $\ell \geq 2$ correspond to fluctuations at smaller angular scales. The conversion from multipole space (ℓ) to the angular size on the sky (θ) is usually given by the approximate relation (White et al., 1994) $\theta \approx \frac{180°}{\ell}$. Low multipoles correspond to large angular scales, while high multipoles correspond to small scales.

It is interesting to consider that the $\ell = 1$ term, which is dominated by the CMB dipole (as seen in Sec. 1.4.1), does not depend only on the condition at last scattering, but also on the peculiar Earth's position and velocity in the Universe. On the other hand, the smaller scales (larger multipoles) have cosmological origin, and must be studied in terms of averages over an ensemble of possible configurations of the Universe. The first mean quantity that we can define is the average of the temperature fluctuations, which, under the assumptions of homogeneity and isotropy of the Universe, is simply:

$$\left\langle \frac{\Delta T}{T_0}(\hat{\mathbf{n}}) \right\rangle = 0, \quad \langle a_{\ell m} \rangle = 0 \tag{1.28}$$

where $< \cdot >$ indicates an ensemble average. Let us define then second order statistic quantity, also called *auto-correlation function* of the temperature fluctuations:

$$C(\theta) = \left\langle \frac{\Delta T}{T_0}(\hat{\mathbf{n}}) \frac{\Delta T}{T_0}^*(\hat{\mathbf{n}}') \right\rangle \tag{1.29}$$

where θ is the angle between two directions of observation: $\cos(\theta) = \hat{\mathbf{n}} \cdot \hat{\mathbf{n}}'$. By definition, $C(\theta = 0)$ is the variance of the temperature fluctuations. We can expand this relation with spherical harmonics, to get:

$$C(\theta) = \sum_{\ell,m} \sum_{\ell',m'} \langle a_{\ell m} a^*_{\ell' m'} \rangle \, Y_{\ell m}(\hat{\mathbf{n}}) Y^*_{\ell' m'}(\hat{\mathbf{n}}') \tag{1.30}$$

---

[16] Eq. 1.27 can be easily obtained from Eq. 1.26, by applying the orthonormality condition of the spherical harmonics, expressed in Eq. 1.21.

If the temperature fluctuations are Gaussian (as ensured by the initial conditions in inflationary models where anisotropies are seeded by quantum fluctuations), they are fully characterized by their variance, which is encoded in the *angular power spectrum* C_ℓ, defined as:

$$\langle a_{\ell m} a^*_{\ell' m'} \rangle = \left\langle |a_{\ell m}|^2 \right\rangle = \delta_{mm'} \delta_{\ell\ell'} C_\ell \tag{1.31}$$

where δ_{ij} is the Kroneker function and C_ℓ is a real and positive function of the only multipoles ℓ, which is independent on m thanks to isotropy. We can finally write the correlation function (Eq. 1.30), after applying the property in Eq. 1.24 and 1.31, as:

$$C(\theta) = \frac{1}{4\pi} \sum_{\ell=1}^{\infty} (2\ell+1) C_\ell P_\ell(\cos(\theta)) \tag{1.32}$$

and the variance of the temperature fluctuations can be expressed as:

$$C(\theta=0) = \frac{1}{4\pi} \sum_{\ell=1}^{\infty} (2\ell+1) C_\ell . \tag{1.33}$$

1.4.2.2 Cosmological estimator and cosmic variance

Note however that only one realization of the Universe is available to us as observers, and that therefore we can not recur to ensemble averages. In principle, under the assumptions of the ergodic theorem (see Appendix D in Weinberg, 2008), ensemble averages can be replaced by space averages ($< \cdot > \rightarrow < \cdot >_{\mathbf{x}}$), by locating the observer at different positions $\mathbf{x}$ to observe the sky, and averaging among them. In addition, under the hypothesis of statistical isotropy, for each location $\mathbf{x}$, we can average the sky properties observed at different directions, by computing the mean over the $2\ell+1$ possible m for any multipole ℓ. We can write therefore:

$$C_\ell = \left\langle |a_{\ell m}|^2 \right\rangle = \left\langle |a_{\ell m}|^2 \right\rangle_{\mathbf{x}} = \frac{1}{2\ell+1} \sum_{m=-\ell}^{m=\ell} \left\langle |a_{\ell m}|^2 \right\rangle_{\mathbf{x}} , \tag{1.34}$$

where the first equality defines the angular power spectrum (Eq. 1.31), the second applies ergodicity, the third one uses isotropy. However, we can only observe the Universe from one single position $\mathbf{x} = \mathbf{x}_0$, where the observer is located. We define therefore an *experimental estimator*, C_ℓ^{obs}, which is is obtained from the $a_{\ell m}$ computed for a unique CMB realization observed from one single location of the observer:

$$C_\ell^{\mathrm{obs}} = \frac{1}{2\ell+1} \sum_{m=-\ell}^{m=\ell} |a_{\ell m}|^2_{\mathbf{x}=\mathbf{x}_0} . \tag{1.35}$$

$C_\ell^{\rm obs}$ is an unbiased estimator of the true C_ℓ ($\langle C_\ell^{\rm obs}\rangle = C_\ell$), however there is one important point to stress with this approach: at high multipoles, a large number independent modes m are available to average, and the estimator in Eq. 1.35 provides a precise measurement of the true angular power spectrum. However, at low multipoles, we have very few independent modes, and the determination of C_ℓ through the estimator is subjected to large uncertainty. The fractional variance of the angular power spectrum estimator with respect to the true one is commonly called *cosmic variance*, and it is given by:

$$\left\langle \left(\frac{C_\ell - C_\ell^{\rm obs}}{C_\ell} \right)^2 \right\rangle = \frac{2}{2\ell+1} \tag{1.36}$$

Finally, it can be shown that the fluctuations of the estimator $C_\ell^{\rm obs}$ as compared with the true C_ℓ are uncorrelated for different multiples ($\ell' \neq \ell$):

$$\left\langle \left(\frac{C_\ell - C_\ell^{\rm obs}}{C_\ell} \right) \left(\frac{C_{\ell'} - C_{\ell'}^{\rm obs}}{C_{\ell'}} \right) \right\rangle = 0, \tag{1.37}$$

(see Weinberg (2008) section 2.6 for a complete derivation).

1.4.2.3 Convolution with instrumental beam

Any radio telescope, including CMB dedicated experiments, observes the sky temperature convolved with a beam with finite angular resolution. The beam profile is given by a function $B(\hat{\mathbf{n}}, \hat{\mathbf{m}})$, which indicates the instrument response to a signal coming from a direction $\hat{\mathbf{m}}$, while pointing towards $\hat{\mathbf{n}}$. The beam profile can be applied to the ideal measured temperature T to provide the experimental temperature $\tilde{T}$ (e.g., White & Srednicki 1995) as:

$$\tilde{T} = \int d\Omega_{\hat{\mathbf{m}}} B(\hat{\mathbf{n}}, \hat{\mathbf{m}}) T(\hat{\mathbf{m}}). \tag{1.38}$$

It follows that the auto-correlation function (Eq. 1.29) of the experimental temperature is give by:

$$\begin{aligned} \tilde{C}(\hat{\mathbf{n}}, \hat{\mathbf{n}}') &= \int d\Omega_{\hat{\mathbf{m}}} \int d\Omega_{\hat{\mathbf{m}}'} B(\hat{\mathbf{n}}, \hat{\mathbf{m}}) B(\hat{\mathbf{n}}', \hat{\mathbf{m}}') \times \left\langle \frac{\Delta T}{T_0}(\hat{\mathbf{m}}) \frac{\Delta T}{T_0}^*(\hat{\mathbf{m}}') \right\rangle \\ &= \frac{1}{4\pi} \sum_{\ell=1}^{\infty} (2\ell+1) W_\ell(\hat{\mathbf{n}}, \hat{\mathbf{n}}') C_\ell, \end{aligned} \tag{1.39}$$

in which, after applying the relation in Eq. 1.32, we defined the *beam window function* $W_\ell(\hat{\mathbf{n}}, \hat{\mathbf{n}}')$ as:

$$W_\ell(\hat{\mathbf{n}}, \hat{\mathbf{n}}') \equiv \int d\Omega_{\hat{\mathbf{m}}} \int d\Omega_{\hat{\mathbf{m}}'} B(\hat{\mathbf{n}}, \hat{\mathbf{m}}) B(\hat{\mathbf{n}}', \hat{\mathbf{m}}') P_\ell(\hat{\mathbf{m}} \cdot \hat{\mathbf{m}}') \tag{1.40}$$

It shall be noted that the beam profile usually is (in good approximation) independent from the direction of observation, which means $B(\hat{\mathbf{n}}, \hat{\mathbf{m}}) = B(\hat{\mathbf{n}} \cdot \hat{\mathbf{m}})$. In addition, the window function is usually defined at zero lag ($\hat{\mathbf{n}} = \hat{\mathbf{n}}'$, $\theta = 0$), therefore its notation can be simplified as $W_\ell(\hat{\mathbf{n}}, \hat{\mathbf{n}}') = W_\ell$. It is then useful to expand the beam profile in Legendre polynomials as:

$$B(\hat{\mathbf{n}}, \hat{\mathbf{m}}) = \frac{1}{4\pi} \sum_{\ell=1}^{\infty} (2\ell + 1) B_\ell P_\ell(\hat{\mathbf{n}} \cdot \hat{\mathbf{m}}) \tag{1.41}$$

where B_ℓ is commonly called *beam transfer function.* It can be shown (White & Srednicki, 1995) that the relation between W_ℓ and B_ℓ is simply given by:

$$W_\ell = B_\ell^2 P_\ell(\cos(\theta = 0)) = B_\ell^2. \tag{1.42}$$

If we compare now Eq. 1.33 with Eq. 1.39, we can notice that the beam window function changes the angular power spectrum as a multiplicative function of ℓ:

$$\tilde{C}_\ell = B_\ell^2 \cdot C_\ell. \tag{1.43}$$

The same relation is valid for the angular power spectrum estimator C_ℓ^{obs}.

In an experiment, in the simplest case, the beam profile function is Gaussian, and is defined as a function of the angle θ, as:

$$B(\theta) = B \exp\left(-\frac{\theta^2}{2\sigma_{\mathrm{b}}^2}\right) \tag{1.44}$$

where B is a normalization factor, σ_{b} is the width of the Gaussian beam in radians, and it is related with the full width half maximum (FWHM) of the beam with FWHM $= \sqrt{8\ln(2)}\sigma_{\mathrm{b}}$. For a Gaussian beam with a profile given as in Eq. 1.44, W_ℓ is given (see e.g., Challinor et al., 2000) by:

$$W_\ell = B_\ell^2 \approx 2\pi B \sigma_{\mathrm{b}}^2 \exp\left(-\ell(\ell+1)\sigma_{\mathrm{b}}^2\right). \tag{1.45}$$

To conclude, the effect of the window function in the multipole space is an exponential cut-off of the power at large multipoles, depending on the width σ_{b} of the beam profile.

1.4.3 Polarization anisotropies

Let us briefly introduce the main concepts and the formalism that is commonly applied to treat the polarization of light, and of the CMB in particular. In general, the electric field of an electromagnetic monochromatic wave that propagates with frequency ω_0 in the direction of the z axis, is described by its x and y components:

$$E_x = a_x(t)\cos(\omega_0 t - \theta_x(t)), \;\; E_y = a_y(t)\cos(\omega_0 t - \theta_y(t)) \tag{1.46}$$

where t is the time dependence, and θ_x and θ_y are the phases in the two components (Kamionkowski et al., 1997b). If the E_x and E_y have some relative correlation, the light is polarized. The polarization of the photon is usually characterized by the Stokes parameters, which are defined as the following time averages:[17]

$$\begin{aligned} I &=< a_x^2 > + < a_y^2 > \\ Q &=< a_x^2 > - < a_y^2 > \\ U &=< 2a_x a_y \cos(\theta_x - \theta_y) > \\ V &=< 2a_x a_y \sin(\theta_x - \theta_y) > \end{aligned} \tag{1.47}$$

The parameter I is the intensity of the radiation, Q and U quantify the linear polarization (at 0° and 45°, $\theta_x - \theta_y = 0$ or π), and V the circular polarization (right or left, $\theta_x - \theta_y = \pm\pi/2$) (Fowles, 1968).

Thomson scattering is not expected to produce circular polarization, therefore the parameters of interest are I, Q and U.[18] Under the assumption of linear polarization only, we can define the polarized intensity as:

$$P = \sqrt{Q^2 + U^2} \tag{1.48}$$

and the polarization angle as:

$$\phi = \frac{1}{2}\arctan\left(-\frac{U}{Q}\right) \tag{1.49}$$

---

[17] There are two different conventions for the definition of the reference frame where the Stokes parameters are computed, the so-called IAU and CMB (or COSMO, or HEALpix) conventions (see https://healpix.jpl.nasa.gov/pdf/intro.pdf and references therein). The difference between the two consists of the orientation of the y axis (towards the North for the IAU, or the South for the CMB), which imply a change of the sign in the Stokes parameter U: $U_{\rm CMB} = -U_{\rm IAU}$. In this thesis we use the CMB convention.

[18] The usual convention for CMB studies, is to work in terms of the difference in brightness temperature with respect to the mean brightness temperature of the CMB. This is because the CMB has a well known black body spectrum, which can be described by a single parameter: the temperature, independently on the frequency. Both intensity and polarization of the CMB follow the same black body spectrum, so all the Stokes parameters I, Q and U are usually expressed in units of temperature.

The intensity parameter is invariant under rotations. This property allowed us to develop the statistic formalism presented in Sec. 1.4.2. Contrarily, the Q and U Stokes parameters transform under rotation by an angle ψ around the direction of propagation $\hat{\mathbf{n}}$ as:

$$\begin{aligned} Q' &= Q\cos(2\psi) + U\sin(2\psi) \\ U' &= -Q\sin(2\psi) + U\cos(2\psi) \end{aligned} \tag{1.50}$$

1.4.3.1 Spherical harmonic formalism

We may want, also in this case, to define an angular power spectrum for the polarization of the CMB. However, the transformation under rotation of Q and U complicates the problem: we cannot construct a C_ℓ^{QQ} or C_ℓ^{UU} directly from the Q and U maps as we did for the intensity in Sec. 1.4.2. The problem was solved independently by Zaldarriaga & Seljak (1997) and Kamionkowski et al. (1997a,b), who formulated the methodology that is currently used in the field,[19] which is summarized as follows. Let us construct the two combinations $Q \pm iU$ that transform as a spin±2 quantity:

$$(Q \pm iU)'(\hat{\mathbf{n}}) = e^{\mp 2i\psi}(Q \pm iU)(\hat{\mathbf{n}}) \tag{1.51}$$

Similarly to what we have done in intensity (Eq. 1.26), we can expand it in the spin±2 spherical harmonics basis $Y_{\pm 2,\ell m}(\hat{\mathbf{n}})$ (Zaldarriaga & Seljak, 1997) as:

$$\begin{aligned} (Q + iU)(\hat{\mathbf{n}}) &= \sum_{\ell=2}^{\infty} \sum_{m=-\ell}^{m=\ell} a_{2,\ell m} Y_{2,\ell m}(\hat{\mathbf{n}}) \\ (Q - iU)(\hat{\mathbf{n}}) &= \sum_{\ell=2}^{\infty} \sum_{m=-\ell}^{m=\ell} a_{-2,\ell m} Y_{-2,\ell m}(\hat{\mathbf{n}}) \end{aligned} \tag{1.52}$$

The spin±2 spherical harmonics $Y_{\pm 2,\ell m}(\hat{\mathbf{n}})$ constitute an orthonormal basis, and it can be shown that the polarization harmonic coefficients satisfy a relation similar to Eq. 1.23:

$$a^*_{-2,\ell m} = a_{2,\ell -m} \tag{1.53}$$

It is convenient to define a special linear combination of the polarization harmonic coefficients:

$$\begin{aligned} a_{E,\ell m} &= -\frac{1}{2}(a_{2,\ell m} + a_{-2,\ell m}) \\ a_{B,\ell m} &= \frac{i}{2}(a_{2,\ell m} - a_{-2,\ell m}) \end{aligned} \tag{1.54}$$

---

[19] M. Kamionkowski, U. Seljak, and M. Zaldarriaga were awarded with the Gruber Prizer of Cosmology in 2021 for their important contribution to the study of the CMB (`https://www.iau.org/news/pressreleases/detail/iau2103/`).

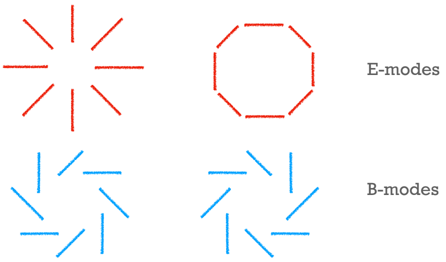

FIGURE 1.4— Sketch of the polarization directions for E and B fields.

Under parity transformation,[20] a_E and a_B behave differently: a_E is unchanged, while a_B changes sign. We can notice an analogy between the a_E parity behaviour with that of an electric field, or of the gradient of a scalar field, and between a_B and a magnetic field, or the curl of a vector field (see Fig. 1.4).

Finally, the set of harmonic coefficients $(a_{T,\ell m}, a_{E,\ell m}, a_{B,\ell m})$[21] provides a full description of the intensity and polarization of the sky, in the harmonic space. As we have already seen in Sec. 1.4.2, under the hypothesis of statistical isotropy and Gaussianity we can define the complete set of angular power spectra and cross-spectra of the sky signal on the sphere, as:

$$\begin{aligned}
\langle a_{T,\ell m} a^*_{T,\ell' m'} \rangle &= \delta_{\ell\ell'}\delta_{mm'} C_\ell^{TT} \\
\langle a_{E,\ell m} a^*_{E,\ell' m'} \rangle &= \delta_{\ell\ell'}\delta_{mm'} C_\ell^{EE} \\
\langle a_{B,\ell m} a^*_{B,\ell' m'} \rangle &= \delta_{\ell\ell'}\delta_{mm'} C_\ell^{BB} \\
\langle a_{T,\ell m} a^*_{E,\ell' m'} \rangle &= \delta_{\ell\ell'}\delta_{mm'} C_\ell^{TE} \\
\langle a_{T,\ell m} a^*_{B,\ell' m'} \rangle &= \delta_{\ell\ell'}\delta_{mm'} C_\ell^{TB} \\
\langle a_{E,\ell m} a^*_{B,\ell' m'} \rangle &= \delta_{\ell\ell'}\delta_{mm'} C_\ell^{EB}
\end{aligned} \tag{1.55}$$

Considerations of transformations under parity of T, E and B, specifically for the CMB radiation (Kamionkowski et al., 1997b), require:

$$\begin{aligned}
C_\ell^{TB} &= 0 \\
C_\ell^{EB} &= 0
\end{aligned} \tag{1.56}$$

---

[20] A parity transformation consists of inverting the sign of the three spatial coordinates: $(x, y, z) \to (-x, -y, -z)$.

[21] Hereafter, for clarity, we change the notation of the intensity harmonic coefficients defined in Sec. 1.4.2: $a_{\ell m} \to a_{T,\ell m}$.

However, the power spectra of Galactic foreground emission do not necessary follow this condition (Clark et al., 2021). In addition, the birefringence effect mentioned earlier can lead to $C_\ell^{EB} \neq 0$ (Minami et al., 2019).

1.4.3.2 Cosmological estimators

As we did for the intensity, we now have to substitute averages over realizations of the sky with averages over uncorrelated patches of one single sky realization (or m), in order to define the estimators of the angular power spectra. For the CMB polarization, they are:

$$\begin{aligned}
C_\ell^{TT,\mathrm{obs}} &= \frac{1}{2\ell+1}\sum_{m=-\ell}^{m=\ell} |a_{T,\ell m}|^2 \\
C_\ell^{EE,\mathrm{obs}} &= \frac{1}{2\ell+1}\sum_{m=-\ell}^{m=\ell} |a_{E,\ell m}|^2 \\
C_\ell^{BB,\mathrm{obs}} &= \frac{1}{2\ell+1}\sum_{m=-\ell}^{m=\ell} |a_{B,\ell m}|^2 \\
C_\ell^{TE,\mathrm{obs}} &= \frac{1}{2\ell+1}\sum_{m=-\ell}^{m=\ell} a_{T,\ell m} a^*_{E,\ell m}
\end{aligned} \tag{1.57}$$

The most recent collection of CMB angular power spectrum measurements is shown in Fig. 1.5 (Choi et al., 2020). In the top panel we can see the TT, EE and BB angular power spectra as measured by Planck, ACT, SPTpol, POLARBEAR and BICEP2/*Keck*. These experiments are briefly presented in Sec. 1.6. In the bottom panel the cross TE spectrum is shown.

1.5 Galactic foregrounds

We understood in the previous sections that the first light that propagated in the Universe is the CMB radiation, which started to propagate from the last scattering surface at $z \approx 1100$. However, the evolved Universe is also populated by baryonic matter lying between the last scattering surface and the observer, which absorbs and emits radiation constituting a foreground for the CMB radiation. Even the non-baryonic matter produces a foreground effect, as the potential wells of dark matter structures deflect the CMB photons with gravitational lensing. In this context, also the ISW effect due to dark matter potential wells (see Sec. 1.3.1) can be regarded as a foreground component.

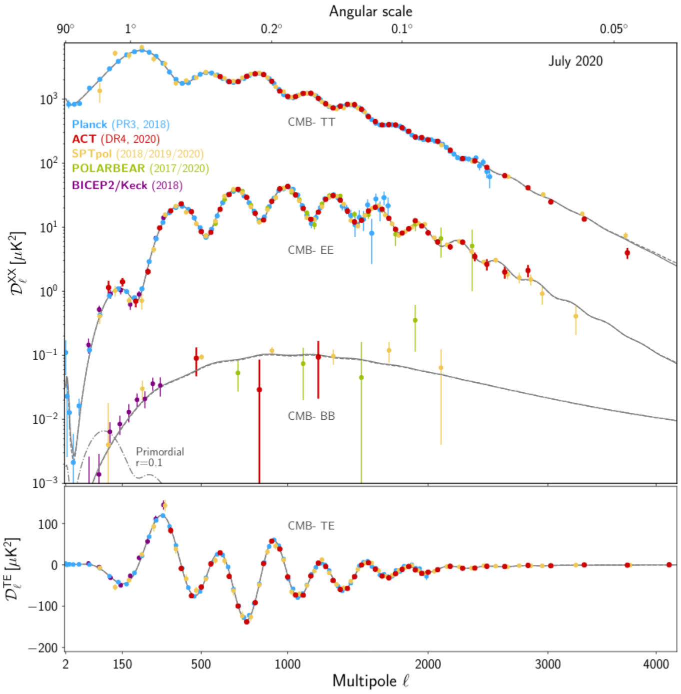

FIGURE 1.5— State of the art of CMB angular power spectra measurements for TT, EE, BB (top) and TE (bottom), where $D_\ell = \ell(\ell+1)C_\ell/(2\pi)$. The primordial B-mode signal for $r = 0.1$ is also shown. The D_ℓ shown in this figure were obtained by the following experiments: Planck (blue), ACT (red), SPTpol (yellow), POLARBEAR (green) and BICEP2/*Keck* (purple) (see Sec. 1.6 for a description of the experiments; image taken from Choi et al., 2020).

The foregrounds of main interest for this thesis work are those produced by our own host Galaxy, the Milky Way. Indeed, the dust and gas embedded in the magnetic field of the Galaxy emit radiation which is, in most of the cases, much brighter than the CMB, both in intensity and polarization. Therefore, if we want to unveil the radiation of cosmological origin, we need to characterize and separate the Galactic foreground components from the CMB light.

Fig. 1.6 shows the landscape of Galactic foregrounds contamination as a function of frequency, in intensity and polarization, as compared with the CMB.

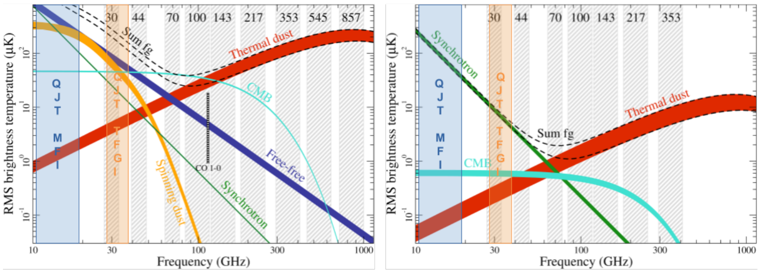

FIGURE 1.6— Spectrum of the brightness temperature r.m.s. of Galactic foregrounds, in intensity (left) with resolution of 1° FWHM, and polarization (right) with 40′ FWHM resolution. The upper and lower bounds of the foregrounds rms spectra are given by two different sky fractions (81-93% in intensity and 73-93% in polarization). The grey shaded areas represent the Planck frequency bands, which have been used to obtain these constraints. The blue and orange shaded areas represent the range of frequencies observed with the QUIJOTE experiment, respectively, with the instruments MFI (10-20 GHz) and TFGI (30 and 40 GHz). (Image taken from `https://www.cosmos.esa.int/web/planck/picture-gallery` (Planck Collaboration et al., 2016a), and adapted to highlight the frequency bands covered by the QUIJOTE experiment).

The foregrounds in intensity are produced by synchrotron, free-free, CO rotational transition lines, thermal dust and anomalous microwave emission (AME), which is likely due to spinning dust (although it is not clear yet, see Sec. 1.5.4). In addition, synchrotron and thermal dust are also known to be polarized, while AME and free-free might be polarised at very low levels (see Ichiki, 2014; Dickinson, 2016 for brief review on Galactic foregrounds fro CMB studies).

We can observe from Fig. 1.6 that there are multiple components that produce foreground emission in intensity. However, it is clear that at frequencies $\nu \approx 70 - 90\,\mathrm{GHz}$ there is a window where the CMB is dominant over the other components. On the other hand, in polarization, even if there are only two foreground mechanisms, they dominate over the CMB at all frequencies. This is the reason why Galactic foreground separation in polarization is a very important step in the process of doing cosmology with the CMB.

In order to perform an accurate separation of the Galactic foregrounds, a wide frequency coverage over large sky fractions is required. High frequency observations ($\nu > 100\,\mathrm{GHz}$) can trace the thermal dust emission, while the low frequencies ($\nu < 40\,\mathrm{GHz}$) are sensitive to synchrotron, and also to free-free and AME in intensity. The next paragraphs of this section present a quick review of the emission mechanisms that generate the aforementioned Galactic foregrounds, in intensity and polarization.

1.5.1 Synchrotron

The spiral motion of relativistic cosmic ray electrons interacting with the Galactic magnetic field produces synchrotron radiation. The emitted brightness temperature from synchrotron depends on the energy spectrum of the cosmic ray electrons $N(E)$, and on the strength of the magnetic field $\mathbf{B}$. The energy distribution of cosmic rays in the Galaxy is usually described by the power law $N(E) \propto E^{-p}$, and produces a synchrotron spectral flux density:[22]

$$S(\nu) \propto \nu^{-(p-1)/2} = \nu^{\alpha} \tag{1.58}$$

where $\alpha = -(p-1)/2$ is the flux density synchrotron spectral index. However, it is more common in the CMB community to work in units of temperature. The brightness temperature of the synchrotron emission is given by:

$$T_{\mathrm{b}}^{\mathrm{s}}(\nu) \propto \frac{S(\nu)}{\nu^2} = \nu^{\alpha-2} = \nu^{\beta} \tag{1.59}$$

where $\beta = \alpha - 2 = -(p+3)/2$ is the temperature synchrotron spectral index.[23]

The spiral motion of cosmic ray electrons along the magnetic field lines means that synchrotron photons are linearly polarized along the orthogonal direction to the magnetic field. The spectrum of the polarized synchrotron radiation follows the same power law as in Eq. 1.59. The predicted degree of polarization for an homogeneous magnetic field is $\Pi = (p+1)/(p+7/3)$ (Rybicki & Lightman, 1986), which could reach levels of 75% for typical values of the synchrotron spectral index ($\beta = -3$, $p = 3$). However, incoherence of the magnetic field, superposition of multiple synchrotron components along the line of sight, and other depolarization effects such as beam and Faraday depolarization, significantly reduce the effective polarization fraction. It has been measured that the level of synchrotron polarization at CMB frequencies is typically of the order of 10–40% at high Galactic latitudes (Vidal et al., 2015; Planck Collaboration et al., 2016a,c).

Typical values for the synchrotron spectral index at frequencies $\geq 2\,\mathrm{GHz}$ are $\beta \approx -3$ ($\alpha \approx -1$, $p = 3$), with flattening at lower frequencies, towards $\beta \approx -2.5$ (e.g., Planck Collaboration et al., 2018c; Carretti et al., 2013). Recent works also showed hints of spatial variations of the synchrotron spectral index in polarization (Fuskeland et al., 2014; Krachmalnicoff et al., 2018; Fuskeland et al., 2019; Jew & Grumitt, 2020), which is mainly due to the ageing of cosmic

---

[22] Spectral flux density is power per unit volume and frequency. $[S_\nu] = \mathrm{W/m^3/Hz} = 10^{26}$ Jy.

[23] Except otherwise stated, any mention on this thesis to spectral index will refer to the temperature spectral index β.

ray electrons located at high Galactic latitudes, which induce a steepening of the spectrum.

The data that are currently used for the study of synchrotron radiation are: the Planck full-sky maps from the low frequency channels at 28.4 and 44.1 GHz (Planck Collaboration et al., 2018a), the WMAP full-sky maps from the low frequency channels at 23 and 33 and 41 GHz (Bennett et al., 2013), the C-BASS North and South ground-based surveys at 5 GHz (not publicly available yet Jones et al., 2018), the S-PASS survey of the southern sky at 2.3 GHz (Carretti et al., 2019), the southern sky 2.3 GHz map by Jonas et al. (1985) (intensity only), the combined Stockert and Villa-Elisa 1.4 GHz map (only in intensity, full-sky, Reich & Reich, 1986; Reich et al., 2001), the DRAO 1.4 GHz northern sky map (in polarization Wolleben et al., 2006), the Haslam survey at 408 MHz (only in intensity, Haslam et al., 1982). The QUIJOTE experiment, whose data are central for this thesis, is placed in this context, providing maps at complementary frequencies of 11, 13, 17 and 19 GHz, in intensity and polarization.

1.5.2 Free-free

The scattering of free electron with ions (typically protons) of the interstellar medium (ISM) produces bremsstrahlung or free-free emission (Rybicki & Lightman, 1986). The electron-ion Coulomb interaction is intrinsically polarized, but given that it occurs in randomly orientated directions, the free-free radiation is not globally polarized, except for in sharp HII cloud borders. Indeed, at the edge of dense clouds, self Thomson scattering interaction can induce polarization at the level $\Pi < 10\%$, in the direction tangential to the cloud border. The current upper limits for free-free polarization are $\Pi < 1\,\%, 3\%$, respectively in compact HII regions and from diffuse emission at high Galactic latitudes (Macellari et al., 2011). Free-free contamination is not expected to be critical for CMB studies in polarization.

The free-free spectrum is well known. In the optically thin approximation, which is generally valid for CMB relevant frequencies, it can be approximated as a power law in brightness temperature[24] (Dickinson et al., 2003):

$$T_{\rm b}^{\rm ff}(\nu) = 8.235 \cdot 10^{-2} \cdot a T_{\rm e}^{-0.35}(1+0.08)\mathrm{EM}_{\rm cm^{-6}pc}\nu^{-2.1} \propto \nu^{-2.1} \qquad (1.60)$$

where a is a function of the free-free optical depth, $T_{\rm e}$ is the electron temperature in Kelvin, EM is the emission measure[25] in units of $\mathrm{cm}^{-6}\mathrm{pc}$, and ν is the

---

[24] More recent and sophisticated models are also available, as presented in Draine (2011).

[25] The emission measure is the integrated squared electron density $n_{\rm e}$ along the line of sight: $\mathrm{EM} = \int n_{\rm e}^2 dl$

frequency in GHz. The electron temperature has typical values of $T_\mathrm{e} \approx 7000\,\mathrm{K}$, but it could change across the sky. The spectrum of free-free radiation is a well defined power law with spectral index $\beta^\mathrm{ff} \approx -2.14$, with small variations with frequency.

The spatial distribution of free-free radiation is usually highly correlated with Hα line emission. Therefore, Hα surveys (e.g., Finkbeiner, 2003), after a correction for dust absorption, can be used to trace the free-free emission. Thanks to this correlation, but particularly to the different spectral behaviour of other foregrounds, we can disentangle the free-free from other low frequency components, such as synchrotron and AME.

1.5.3 Thermal dust

Interstellar dust grains[26] absorb radiation from the ISM and re-emit thermally, in the far-infrared, being dominant at frequencies $\nu > 70\,\mathrm{GHz}$. The flux density spectrum of thermal dust radiation is given by a modified black body:

$$S_\nu \approx \nu^{\beta_\mathrm{d}} B_\nu(x_\mathrm{d}), \tag{1.61}$$

which is modeled as a power law with spectral index β_d, multiplied by a black body spectrum $B_\nu(T_\mathrm{d})$ (Eq. 1.6) at temperature T_d. To first order, the thermal dust temperature is $T_\mathrm{d} \approx 20\,\mathrm{K}$ and the spectral index is $\beta_\mathrm{d} \approx 1.5$ (Planck Collaboration et al., 2016a, 2020h).

Aspherical dust grains tend to align their longer axis perpendicular to the Galactic magnetic field, and to absorb more efficiently the background radiation along the same axis. Due to these effects, thermal dust emission is polarized in the direction of the longer axis of the grains, which is perpendicular to the Galactic magnetic field. On the other hand, the background light that undergoes dust absorption, gets polarized in the direction parallel to the magnetic field (Hildebrand et al., 2000; Lazarian & Finkbeiner, 2003; Lazarian, 2007). The polarization fraction of thermal dust can reach the $\sim 20\%$ level, while at high Galactic latitudes the average polarized fraction is $\sim 10\%$, making thermal dust an important source of contamination of CMB in polarization (Planck Collaboration et al., 2015, 2016f).

At the angular power spectrum level, Planck Collaboration et al. (2016b, 2020h) showed that thermal dust radiation follows a power law in multipoles given by $C_\ell \propto \ell^\alpha$, with the slope $-2.4 \lesssim \alpha \lesssim -2.5$. This means that thermal dust has high power at low multipoles, or equivalently, at large angular scales.

---

[26] Insterstellar dust is made mostly by of graphites, silicates, Polycyclic Aromatic Hydrocarbons (PAHs).

The best full-sky data to date of thermal dust radiation are provided by the HFI instrument of Planck, from 100 to 857 GHz (Planck Collaboration et al., 2020c), and the IRAS maps (at 12, 25, 60 and 100 microns Neugebauer et al., 1984).

1.5.4 Anomalous Microwave Emission (AME)

Anomalous Microwave Emission (AME) is an extra foreground component that was unexpectedly observed at intermediate frequencies in the data of COBE-DMR (Kogut et al., 1996), and then confirmed by WMAP (Miville-Deschênes et al., 2008), Planck (Planck Collaboration et al., 2011, 2014b), and several other experiments, among them COSMOSOMAS (Watson et al., 2005) and QUIJOTE (Génova-Santos et al., 2015, 2017; Poidevin et al., 2019, Poidevin et al., in prep). AME consists of an excess of intensity emission at frequencies $10\,\mathrm{GHz} < \nu < 60\,\mathrm{GHz}$, which spatially correlates with thermal dust radiation. The origin of AME is usually attributed to electric dipole radiation emitted by spinning small dust grains ($\approx$ nm size) with an electric dipole moment: the so-called *spinning dust* grains. Other models have been proposed to explain the origin of AME, such as the emission by magnetic dust (Draine & Lazarian, 1999; Draine & Hensley, 2013), or by amorphous dust (Jones, 2009; Nashimoto et al., 2020). While models based on electric dipole emission predict very low levels of polarization, under certain geometrical and physical assumptions, the magnetic dust models predict polarization fractions of up to $\sim$15%.

However, several recent observations in compact regions indicate that AME should have very low (or zero) polarization. The most stringent constraints to date for the AME polarization fraction are $\Pi_{\mathrm{AME}} < 0.22\%$ (95% C.L. at 41 GHz, Génova-Santos et al., 2017), making magnetic dust models less likely. Anyhow, the origin and characterization of AME is still controversial, because the separation of this component from free-free and synchrotron is not a trivial task, especially at high Galactic latitudes. In addition, even a low fraction of polarization of AME could affect CMB studies, therefore, in the CMB community, there is particular interest on this topic. A comprehensive and recent review on AME can be found in Dickinson et al. (2018a).

1.5.5 CO transition line emission

The rotational transition of carbon monoxide molecules (CO) emit at 115 GHz (J=(1-0)), 230 GHz (J=(2-1)), and 345 GHz (J=(3-2)).These emission lines are observed in the 100, 217 and 353 GHz bands of Planck-HFI, constituting a foreground component in intensity. CO emission is correlated with thermal dust, since the presence of CO molecules is more concentrated in dense dust clouds.

In particular, at 100 GHz, it is shown that CO contributes to the angular power spectrum at small angular scales ($\ell \gtrsim 1000$ Ichiki et al., 2014), constituting source of contamination at a frequency where the cosmological emission is close to its maximum.

1.5.6 Extragalactic point sources

One more source of foreground at small angular scales is produced by extragalactic point sources that emit at radio wavelengths, such as distant radio galaxies, active galactic nuclei (AGNs), quasars, etc. This kind of sources emit synchrotron radiation, and are therefore polarized. If we assume a random distribution and orientation of radio sources, the average polarization should cancel. However, it is possible that some residual correlation could introduce spurious modes in the polarization angular power spectra, as well as in the intensity one, and contaminate the detection of the CMB (Tucci et al., 2004; Battye et al., 2011; Perrott et al., 2021). For this reason, an accurate removal of the sources is needed both in intensity an polarization, in particular in order to achieve the goal of B-modes detection. This is effect especially important for the small angular sales.

1.6 Current status of the field

In this section we present the current status of the field, starting with a description of the CMB space missions (Sec. 1.6.1), and providing an overview of the main currently ongoing ground-based CMB experiments.

1.6.1 Space missions

- **COBE** (COsmic Background Explorer), was launched by NASA in 1989, carrying three instruments: DMR[27] (Differential Microwave Radiometer; Smoot et al., 1990; Bennett et al., 1992), made by six differential horn antennas measuring the sky at positions separated by 60 deg to make absolute maps of the CMB, at 31.5, 53 and 90 GHz, with a 7 deg FWHM beam. One full-sky map was obtained every six months, over a period of observation of four years (until December 1993); FIRAS[28] (Far Infrared Radiometer Spectrometer; Mather et al., 1990), a polarizing Michelson interferometer aimed to measure the spectrum of the CMB at wavelengths 0.1–10 mm with 5% spectral resolution, and with a field of view of 7 deg. FIRAS surveyed the sky 1.6 times (until 21 September 1990);

---

[27] `https://lambda.gsfc.nasa.gov/product/cobe/about_dmr.cfm`
[28] `https://lambda.gsfc.nasa.gov/product/cobe/about_firas.cfm`

and DIRBE[29] (Diffuse Infrared Background Explorer) for the search of the Cosmic Infrared Background (CIB) at wavelenghts 1.25–240 microns.

- **WMAP** (Wilkinson Microwave Anisotropy Probe), was proposed to NASA in 1995, launched in 2001 to the Sun-Earth L2 Lagrange point, and it operated until 2010 observing the full sky every 6 months (`https://map.gsfc.nasa.gov/mission/`). WMAP measured the three Stokes parameters of the light: I (intensity), Q and U (polarization). In order to separate the emission of Galactic foregrounds from the CMB radiation, WMAP used five frequency bands between 22 and 90 GHz (bands: K, Ka, Q, V, W, with FWHM resolution of, respectively, 0.93°, 0.68°, 0.53°, 0.35°, 0.23°), and achieved an average sensitivity of of $20\,\mu$K per 0.3° square pixel, with control of systematic artifacts down to $5\,\mu$K per pixel.
- **Planck** was an ESA[30] mission with significant NASA[31] contribution, selected in 1995 to be an Medium-Sized (M3) mission in the Horizon 2000 Scientific Program. Planck was equipped with two instruments: the LFI and HFI (respectively, Low and High Frequency Intrument) both sensitive to intensity and polarization of light, measuring the I, Q and U Stokes parameters. Planck was launched in 2009, and located in the Sun/Earth L2 Lagrangian point, and completed two surveys of the full sky, with both instruments, in 30 months (2011). The LFI lasted even longer, and continued taking data until 2013. The LFI (Zacchei et al., 2011) covers three frequency bands between 30 and 70 GHz, centered at about 30, 44 and 70 GHz, with approximate angular resolution (FWHM) of, respectively, of 33, 24 and 14 arcmin. The HFI (Planck HFI Core Team et al., 2011) covers 6 frequency bands between 100 and 857 GHz, centered at 100, 143, 217, 353, 545, 857 GHz, (the last two frequency for intensity only) with angular resolution (FWHM) ranging from 9.9 to 4.4 arcmin. Planck data provided the current most accurate full-sky images of the CMB intensity and polarization anisotropies (Planck Collaboration et al., 2018c), which have been used as one of the most powerful cosmological probes to date (e.g., Planck Collaboration et al., 2020a). A map of the CMB temperature anisotropies measured by Planck is shown in Fig. 1.2.

A comparison of the intensity maps of the CMB anisotropies as obtained by the three space missions COBE, WMAP and Planck, is shown in Fig. 1.7.

---

[29] `https://lambda.gsfc.nasa.gov/product/cobe/about_dirbe.cfm`
[30] `https://www.cosmos.esa.int/web/planck`
[31] `https://lambda.gsfc.nasa.gov/product/planck/curr/`

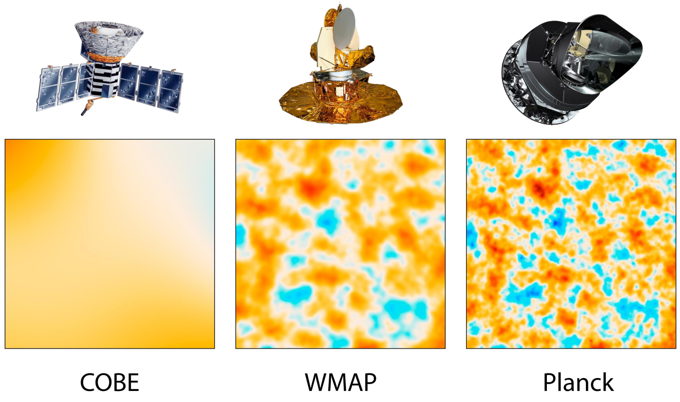

FIGURE 1.7— Comparison of the CMB anisotropies in intensity in a 10 $\deg^2$ sky patch, as observed by COBE (left), WMAP (middle) and Planck (center) (Image taken from: `https://photojournal.jpl.nasa.gov/catalog/PIA16874`).

1.6.2 Ground-based experiments

Several ground-based experiments are currently observing the microwave sky from all across the globe, with the common goal of measuring the CMB, particularly in polarization, to derive cosmological information about the initial state and the evolution of the Universe. An historical and complete list of CMB experiments can be found in `https://lambda.gsfc.nasa.gov/product/expt/`, while the state of the art of CMB angular power spectrum measurements is shown in Fig. 1.5 (Choi et al., 2020).

We report here a review of the main present and future CMB experiments, subdivided by the observing sites, which are Antarctica (BICEP2/Keck, SPT), Atacama (ABS, POLARBEAR, ACT, CLASS), and Tenerife (QUIJOTE, GroundBIRD, STRIP).

1. Antarctica

- The **BICEP2/*Keck*** CMB polarization experiment[32] is located in Antarctica and observes the sky at frequencies 95, 150, 220 GHz. The last constrain on the tensor-to-scalar ratio obtained from BICEP/*Keck* are $r < 0.07$ (BICEP2 Collaboration et al., 2018), and $r < 0.04$ in combination with Planck (Tristram et al., 2020). The project is currently evolving

---

[32] `http://bicepkeck.org/`

into the BICEP Array, at 30/40, 95, 150 and 220/270 GHz, adding more frequency channels for the control of the foregrounds, and targeting a sensitivity of $\sigma(r)$ between 0.002 and 0.004 (Soliman et al., 2020).

- The **South Pole Telescope** (SPT)[33] is located in Antarctica, close to the BICEP site. It observed for three seasons with different cameras. First, SPT-SZ observed a 2500 $\deg^2$ sky area with arcminutes resolution, at 95, 150 and 220 GHz, searching for galaxy clusters through the Sunyaev–Zel'dovich (SZ) effect. Second, SPTpol observed 100 $\deg^2$ (enlarged later to 500 $\deg^2$), at 95 and 150 GHz providing the first indirect detection of lensing B-modes, through cross-correlations with an estimate of the lensing potential map from the Herschel-SPIRE map of the cosmic infrared background (Hanson et al., 2013). In 2018 a third survey began with the SPS-3G camera, at 90, 150, and 220 GHz. It will cover 1500 $\deg^2$ which completely overlap with the BICEP Array field, joining the efforts for B-modes detection in the South Pole Observatory (SPO).

2. Atacama

- **ABS** (Atacama B-Mode Search) is located in the Atacama desert, and it observed 2400 $\deg^2$ of the sky with a resolution of 32 arcmin (FWHM), at 145 GHz. The observations took place from 2012 to 2014. The results from ABS are in agreement with those obtained by the Planck mission (Kusaka et al., 2018).

- **POLARBEAR**[34] observed from the Atacama desert a 30 $\deg^2$ sky area with 3.5 arcmin resolution, at 150 GHz. They detected the direct B-mode signal from lensing for the first time (Polarbear Collaboration et al., 2014). The last results by the Polarbear collaboration can be found in Polarbear Collaboration et al. (2020).

- **ACT** (Atacama Cosmology Telescope)[35] observed 15000 $\deg^2$ at 95 and 150 GHz, with a resolution of 1.35 and 1.49 arcmin (FWHM), respectively. Regions with smaller areas are observed deeper. The most recent ACT maps are presented in Choi et al. (2020). Based on these maps they carried out a detailed cosmological analysis and produced angular power spectra up to very high multipoles $\ell \approx 4000$.

---

[33] `https://pole.uchicago.edu/`

[34] `http://bolo.berkeley.edu/polarbear/`

[35] `https://act.princeton.edu/`

- **CLASS** (Cosmology Large Angular Scale Surveyor)[36] is a telescope array located in the Atacama desert, which observes the large angular scales fluctuation on the sky with a resolution of $\sim 1^\circ$ (FWHM), at frequencies 40, 90, 150, and 220 GHz. CLASS is planned to perform a wide survey, covering 75% of the southern sky. At the present time, CLASS is accumulating data, targeting a tensor-to-scalar ration $r = 0.01$.

3. Tenerife.

The Teide observatory in Tenerife (Spain), 2400 m a.s.l., has a long tradition with CMB experiments. To date, it is the only European site suitable for CMB observations, which require a very stable and dry atmosphere. In the past, the Teide observatory hosted the CMB anisotropies experiments Tenerife (10, 15, 33 GHz), IAC-Bartol (91, 142, 230, 272 GHz), JBO-IAC (33 GHz), Cosmosomas (10, 13, 15, 17 GHz) and VSA (33 GHz). Today, there are three ongoing projects:

- **QUIJOTE** is a pair of telescopes and two instruments experiment, led by Spain. It covers the frequencies 11, 13, 17 and 19 GHz with the first instrument, the Multi Frequency Instrument (MFI). The second instrument, the Thirty and Forty GHz Instrument (TFGI) is sensitive to 30 and 40 GHz. QUIJOTE is providing maps of the full northern sky at low frequencies, covering 78% of the sky, with an angular resolution better than 1° (FWHM). The MFI data provide an accurate characterization of the low frequency foregrounds, especially of AME and of polarized synchrotron. The final goal of QUIJOTE is to achieve a detection the primordial B-modes if $r < 0.05$. This thesis is devoted to the analysis of QUIJOTE data, therefore a much more detailed description of the QUIJOTE experiment can be found in Chapter 2, Sec. 2.1.

- **GroundBIRD** is a Japanese/Korean led experiment installed at the Teide observatory. It is planned to observe the large angular scales of the CMB at frequencies 145 and 220 GHz, with a resolution of 0.6° (FWHM) at 145 GHz. GroundBIRD is installed and under commissioning. It will soon start to carry out a wide-survey of the norther sky, covering approximately the same area observed by QUIJOTE (Nagasaki et al., 2018).

- **STRIP** is the low frequency instrument of the Large-Scale Polarization Explorer (LSPE)[37], an Italian led project. STRIP will be installed at the Teide observatory in 2022, and will carry out a wide-survey at 43 and 90 GHz. Together with SWIPE (a complementary balloon at 150 GHz)

---

[36] `https://sites.krieger.jhu.edu/class`

[37] `http://lspe.roma1.infn.it/`

they are planned to detect the B-modes with a tensor-to-scalar ratio down to $r = 0.01$ (Lamagna et al., 2020).

- **TMS** (Tenerife Microwave Spectrometer) is a spectrometer at 10–20 GHz that will operate from the Teide observatory, complementary to QUIJOTE (more details in Alonso-Arias et al., 2020; Rubiño Martín et al., 2020 and Sec. 2.1). The TMS aims to be a prototype experiment for CMB spectral distortions (Chluba et al., 2019).

There are two other experiments that is worth mentioning at this stage. These projects are devoted to produce sky surveys (full sky or half sky generally) at lower frequencies, aimed at providing a precise characterization of the low frequency foregrounds for the detection of CMB B-modes. This kind of surveys are not devoted only to CMB studies, but also provide data for the study of Galactic emission mechanisms, magnetic fields, etc. They are:

- **S-PASS** (S-Band Polarization All-Sky Survey), a southern sky survey at 2.3 GHz. The data were taken with the Parkes radio telescope, with a FWHM resolution of 8.9 arcmin (Carretti et al., 2019). The S-PASS maps have been used to constrain the level of contamination of the CMB polarization from polarized synchrotron, showing that, even in the cleanest sky regions, the tensor-to-scalar ratio generated by foregrounds is $r_{\rm FG} = 0.001$ at any frequency (Krachmalnicoff et al., 2018).
- **C-BASS** (C-Band All Sky Survey)[38] is aimed to image the full sky at 5 GHz from the ground, with an angular resolution of 1°. The northern sky was observed with a telescope installed in the Owens Valley Observatory (OVRO) in California. This survey is concluded and the maps will be publicly delivered. The southern survey is carried out from the second telescope located in the SKA basecamp in the Karoo desert (South Africa). C-BASS data will help to characterize and remove the low frequency Galactic emission for current and future CMB experiments (Jones et al., 2018).

For the future, several large ground-based projects are planned: the Simons Observatory,[39] CMB-S4[40] and ELFS (European Low Frequency Survey), this last one from Europe, probably from the Teide observatory site. Finally, a new space mission, LiteBIRD,[41] has been approved by the Japanese space agency

---

[38] `https://cbass.web.ox.ac.uk/`
[39] `https://simonsobservatory.org/`
[40] `https://cmb-s4.org/`
[41] `http://litebird.jp/eng/`

JAXA. LiteBIRD will be launched in 2029, aiming to measure the B-modes tensor-to-scalar ratio r with a precision of $\sigma(r) < 0.001$.

1.7 Motivation of the thesis

As reviewed in Sec. 1.2, the intensity and polarization of the CMB constitutes a window towards the initial conditions of the Universe. CMB intensity measurements have been extensively exploited with the Planck space mission, providing constraints on the cosmological model with a precision at percent level (Planck Collaboration et al., 2020a). In the last years, the interest is moving towards the study of the polarization anisotropies of the CMB, as indeed they may eventually unveil primordial perturbations of tensor origin, the CMB B-modes, which would be an extremely powerful proof of inflation.

However, the sensitivity of past experiments was not sufficient to detect the primordial B-modes, and there is no theoretical lower limit for their expected power. For this reason, measurements of the CMB polarization anisotropies are going deeper day by day, while meeting new observational challenges. Indeed, it is now fundamental to characterize instrumental systematic effects that were previously negligible. Similarly, a very precise characterization of the Galactic foregrounds emission is needed, in order to unequivocally detect the CMB B-modes.

The QUIJOTE experiment operates in this context, observing the northern sky in the frequency range 10–40 GHz, and providing an important contribution to the measurement and characterization of the low frequency Galactic foregrounds. The MFI instrument of QUIJOTE has been observing the full northern sky for 6 years, allowing the construction of maps at 11, 13, 17 and 19 GHz in intensity and polarization. These data will be made publicly available, and can be used by the scientific community to characterize synchrotron emission across the northern sky, determining the effect of spectral index curvature, spatial variations, as well as to provide strong upper limits on the polarization of AME, and to study the diffuse AME component across the sky.

Moreover, future 30 and 40 GHz data from the TFGI instrument of QUIJOTE, in combination with the 10–20 GHz MFI data, can be used for CMB polarization science, with a target tensor-to scalar ratio $r \gtrsim 0.05$. As reported above, the current best upper limit on r is more stringent than what QUIJOTE alone will be able to achieve. However, QUIJOTE data will be extremely useful for other more sensitive CMB experiments that observe at frequencies closer to the CMB frequency window ($\sim$100 GHz), joining the effort towards the final common goal of a positive detection of r.

Finally, QUIJOTE data provide a picture of the Galactic emission in intensity and polarization, which is, by itself, extremely interesting to study. One example is the study the excess of emission associated with the Galactic center, the so-called the microwave Haze (counterpart of the γ-ray Fermi Bubbles), whose origin is still unclear, and on which we try to shed light using QUIJOTE data.

1.8 Scientific goals of the thesis

The MFI instrument of QUIJOTE (10–20 GHz, see Sec. 2.3) has been operative from 2012 to 2018. This thesis has been dedicated to the analysis of these data, starting from the implementation of the map-making step, moving to the validation of the constructed maps, and ending with the scientific exploitation of data in the Haze region. The objectives that were initially proposed for this thesis are:

1. To implement of the map-making code for QUIJOTE-MFI. The code presented in Pelaez Santos (2019) will be further developed, by including $1/f$ noise priors, a template fitting procedure at the map-making level, and accounting for the modifications of instrumental response equations with time. The map-making code will be validated with end-to-end simulations, at the pixel and angular power spectrum level. This will be presented in chapter 3 and in Guidi et al. (submitted).
2. To construct, study and validate the QUIJOTE-MFI wide survey maps. The map-making code mentioned in the previous point will be applied to construct the QUIJOTE-MFI wide survey maps. The angular power spectra of the maps will be computed and analyzed, and null-tests based on different data-splits will be studied. Various consistency checks based on cross-correlation analysis will be carried out, to contribute to the validation of the calibration of the maps. This work will presented in chapter 4, and in the paper presenting the wide-survey maps (Rubiño-Martín et al., in prep).
3. To study the microwave Haze, an excess of emission associated with the Galactic center, and which extends up to high Galactic latitudes, in correspondence of the γ-ray emission from the Fermi Bubbles, and with the polarized radio plumes observed at 2.3 GHz by the S-PASS survey. For this analysis, additional QUIJOTE-MFI data, from raster scan observations dedicated to the Haze region, will be analyzed and combined with the wide-survey data. This work will be presented in chapter 5, and in the paper Guidi et al., (in prep).

2

The QUIJOTE experiment

"We continue our run with the system that is used in these cases, which is to create the space in front of us as we advance."
Italo Calvino, Le Cosmicomiche

This chapter describes the experiment on which this thesis is based on: the QUIJOTE (QUI-Joint TEnerife) experiment for CMB polarization observations at low frequencies (10–40 GHz). In the following sections, we give an overview of the experiment, describing the different instruments that are developed for the project, and presenting the objectives that drive our research. We describe in more detail the Multi Frequency Instrument (MFI), which provided the data that are analyzed in this thesis.

2.1 Overview of the QUIJOTE experiment

QUIJOTE is an experiment aimed to observe the polarized sky at microwave frequencies. It is located at the Teide Observatory (OT), Tenerife, Spain, at 2400 m above the sea level, with geographical latitude +28 deg. Due to special meteorological conditions,[1] the atmosphere in this site is very stable, and the precipitable water vapour (PWV) is remarkably low. With an average PWV of

---

[1] The combination of the large-scale atmospheric wind circulation, the geographical location of Tenerife, and the configuration of winds around this position, which is dominated by the trade winds originated in the Azores low pressure system, leads to a very dry and stable atmosphere at high altitudes (>1500 m) characterised by laminar winds. The Teide Observatory benefits from these conditions.

FIGURE 2.1— Picture of the QUIJOTE experiment. QT-1 with MFI on the left and QT-2 with TFGI on the right.

~ 3.5 mm (Castro-Almazán et al., 2016), the OT is currently one of the best sites for CMB observations in the northern hemisphere. The scientific context in which QUIJOTE operates is described in the introduction of this thesis. The final goal of QUIJOTE is to characterize the low frequency polarized Galactic foregrounds, and to detect the B-modes of the CMB, if $r \geq 0.05$.

The QUIJOTE project is a collaboration of Spanish and British institutions: Instituto de Astrofísica de Canarias (IAC), Instituto de Fisíca de Cantabria (IFCA), University of Manchester, University of Cambridge, Departamento Ingeniería de Comunicaciones (DICOM) and the IDOM company.

QUIJOTE consists of two Cross-Dragone telescopes (QT-1 and QT-2) with effective 2.25 m primary and 1.9 m secondary, as shown in Fig. 2.1. The telescopes are fitted with two different instruments: The Multi Frequency Instrument (**MFI**; see Sec. 2.2 and 2.3) and the Thirty and Forty GHz Instruments (TGI and FGI).

TGI and **FGI** are developed to operate from the second QUIJOTE telescope (QT-2), enclosed in the same cryostat. All pixels have a bandwidth of ~ 8 and ~ 10 GHz, and the angular resolution is 0.32 and 0.26 deg (FWHM), at 30 and 40 GHz respectively. The TGI and FGI had first light in 2016 and started the commissioning observations in 2018-2019, during which they observed calibrators (Tau A, Cas A, M42, Moon) and fields of scientific interest (Perseus, Galactic Center, Cygnus). They are currently stopped due to cryogenic problems, but they are planned to be operative again in summer 2021. The target sensitivity of the full TGI and FGI array is $\sim 100\,\mu\mathrm{K}\cdot\mathrm{s}^{1/2}$. In combination with MFI data that characterize the synchrotron emission, the TGI and FGI aim to map the CMB anisotropies in intensity and polarization, for B-modes searches.

Currently, the QUIJOTE project is evolving towards new and more sensitive instrumentation at 10–20 GHz: the MFI will be soon replaced by the MFI-2, and the development of new spectroscopic experiment, the TMS, is in progress. The **MFI-2** is an upgraded version of the MFI. It will have 5 horns: three covering the 10–14 GHz band, and two covering 16–20 GHz. The MFI-2 is under construction, and it is expected to be mounted on QT-1 in 2021. The aim of the MFI-2 is to increase the mapping speed of the MFI by a factor 3. In addition, the MFI-2 will have a digital backend based on Field Programmable Gate Arrays (FPGA) that would allow the sampling of the band in frequency, and thence allowing for an efficient radio frequency interference (RFI) removal.

The **TMS** is a new IAC project, to be installed at the OT next to QUIJOTE (Rubiño Martín et al., 2020; Alonso-Arias et al., 2020). The TMS will provide ground-based low resolution spectroscopic observations, in the $10-20$ GHz range, with 0.25 GHz spectral resolution (40 bands), and a ~ 2 deg beam. The TMS is aimed to characterize the foreground monopole signal, its spectral dependence, and CMB spectral distortions. In addition, TMS data will provide frequency inter-calibration for QUIJOTE-MFI.

2.2 The Multi Frequency Instrument (MFI)

The MFI is the first instrument of the QUIJOTE experiment, mounted on the telescope QT-1. It has four horns: two of them are sensitive at $10-14$ GHz, and the other two at $16-20$ GHz. The frequency band of each horn is splitted in two sub-bands with $\sim$2 GHz bandwidth, providing finally four frequency channels, centered at 11, 13, 17, 19 GHz. The angular resolution of the MFI is $\sim$ 0.63–0.92 deg (FWHM; depending on the frequency) and the typical sensitivity is $\sim$ 500–600 $\mu\mathrm{K}\cdot\mathrm{s}^{1/2}$ per channel, per horn. The MFI started operations in November 2012 and concluded the observing campaign in November 2018. In the following, we describe the objectives, observations, and results of the MFI, while a technical description of the instrument is presented in Sec. 2.3.

2.2.1 Objectives

The MFI has two principal objectives: the detailed study of selected Galactic regions (e.g., sources with a strong AME component), and the characterization of low frequency Galactic foregrounds, in the northern sky and in three cosmological fields, in intensity and polarization. Indeed, as we introduced in chapter 1, the MFI data can provide new information about the AME and the polarized synchrotron emission, allowing to achieve a more accurate component separation for present and future CMB experiments, and to detect, if existing, some polarized AME.

In order to achieve these goals, the MFI program has three main objectives:

1. The observation of **selected Galactic regions**. The selected regions are shown in Fig. 2.2 and are:
    - the Perseus molecular complex (Génova-Santos et al., 2015);
    - the W44 supernova remnant, W43 and W47 molecular complexes (Génova-Santos et al., 2017);
    - the Taurus molecular cloud and L1527 (Poidevin et al., 2019);
    - the W49, W51 and IC443 supernova remnants (Tramonte et al., in prep);
    - the Fan diffuse emission region (Ruiz-Granados et al., in prep);
    - the Cygnus region, including the radio galaxy Cygnus A (or (3C405)) and the W63 supernova remnant;
    - the nearby galaxy of Andromeda (M31);
    - rho-OphW cloud complex;
    - the Haze diffuse emission region, in correspondence of the Galactic center (Guidi et al., in prep and chapter 5 of this thesis).
2. The production of a **wide-survey** of the full northern sky (Rubiño-Martín et al., in prep; chapter 4 of this thesis), for the characterization of large scales diffuse foregrounds emission. The wide-survey covers $\sim 20,000\,\mathrm{deg}^2$ with a sensitivity of $40 - 55\,\mu\mathrm{K}/1°$beam.
3. The observation of three **cosmological fields**, specifically for CMB science. The cosmological fields are marked in Fig. 2.2, and cover in total $\sim 3,000\,\mathrm{deg}^2$ with a sensitivity of $\sim 10\,\mu\mathrm{K}/\mathrm{deg}$.

2.2.2 Observing strategies

The observations of the fields described in items 1 and 3 in the above section were performed using “raster scans”, consisting of constant elevation back and forth scans of the telescope in a fixed azimuth interval. This scanning strategy allows us to map a specific sky patch that transits across the azimuth segment pointed by the telescope, while ensuring the best possible stability in term of atmospheric contamination. Indeed, constant elevation scans observe at constant air mass, and the atmospheric contribution from it can be (ideally) easily modeled with time varying constant baselines.

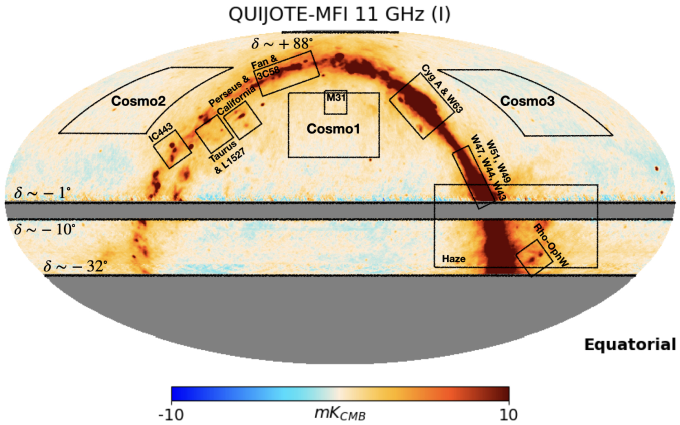

FIGURE 2.2— Sky fields observed with the MFI, overlaid on the QUIJOTE-MFI 11 GHz wide-survey intensity map, in equatorial coordinates. The declination lines ($\delta \sim -32^\circ$ and $\delta \sim +88^\circ$) represent the region of the sky accessible from the Teide observatory, which is observed in the wide-survey program. The central missing band $-10^\circ \lesssim \delta \lesssim -1^\circ$ is flagged due to interference from geostationary satellites.

For the wide-survey (item number 2 section above), the scanning strategy is the so-called "nominal" mode, which consists of continuous 360° scans at constant elevation during the whole day. In this way the full sky accessible from the telescope site is covered once a day, corresponding to a declination (horizontal) band in a map in equatorial coordinates, as shown in Fig. 2.2. Depending on the observed elevation we can observe a different declination range: lower elevations allow to observe larger sky regions, while higher elevations have access to a more restricted sky area. The wide-survey observations were performed at elevations $el = [30, 35, 40, 50, 60, 65, 70, 75, 80]$ deg. At elevation $el = 30$ deg we can observe the declination band $\delta \in [-32, 88]$ deg. However, as well as low elevation observations opening up a larger sky window, they also observe through a larger air mass, resulting in an atmospheric noise level that is larger than that at higher elevations. In addition, the combination of observations at different elevations provides a sky coverage that is more uniform than observing at one single elevation. These are the reasons why the QUIJOTE-MFI wide survey is a combination of observations at several different elevations.

Another routine observation is the "sky-dips", in which the telescope is moved up and down in elevation to observe a varying air mass, at a fixed azimuth position. Sky-dips are typically used for atmospheric monitoring and for calibration purposes.

More observing modes (transit mode, sky raster mode, local maps) are presented in Vignaga (2018).

2.2.3 Results obtained with the MFI

All the observations listed in Sec. 2.2.1 are concluded. The analysis of some of the raster scan observations dedicated to specific Galactic regions have already been published (Perseus molecular complex Génova-Santos et al., 2015, W44 supernova remnant, W43 and W47 molecular complexes (Génova-Santos et al., 2017), Taurus molecular complex (Poidevin et al., 2019), and some are in preparation (Fan region (Ruiz-Granados et al., in prep), W49, W51 and IC443 supernova remnants (Tramonte et al., in prep.), Haze region[2] (Guidi et al., in prep)). An important result achieved with these observations is the significant detection of AME in several sources (W44, W43, W47, Taurus, L1527, W49 and W51). In addition, the study of W43 (Génova-Santos et al., 2017) remarkably provided the most stringent AME polarization constraint up to date, being $\Pi_{\rm AME} < 0.39\%$ from QUIJOTE-MFI at 17 GHz and $\Pi_{\rm AME} < 0.22\%$ at 41 GHz from WMAP, at 95% C.L.

On the other hand, the wide-survey data have been analyzed, and the maps will be made publicly available by the end of 2021. The scientific results achieved with the MFI wide-survey are numerous. They consist of:

- the production of new foregrounds maps in polarization, providing a particularly accurate separation of polarized synchrotron (De la Hoz et al. in prep.);
- the characterization of the polarized diffuse synchrotron with cross-correlations (Vansyngel et al., in prep.);
- the detection of AME in various compact sources, allowing to perform a statistical study over the AME parameters and the correlation with other foregrounds (Poidevin et al., in prep.);
- the study of the brightest polarized loop in the sky, the North Polar Spur (Watson et al., in prep.), and of other polarized spurs (Peel et al., in prep);
- the production of a catalog of radio-sources at the MFI frequencies (Herranz et al., in prep.);

---

[2] The maps of the W49, W51, IC443, Fan, and Haze fields have been obtained with the joint raster scans and wide-survey data, as described in chapter 5.

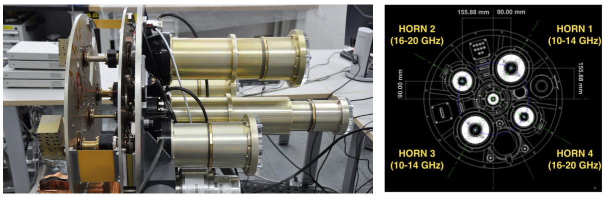

FIGURE 2.3— Left: picture of the MFI. The tubes on the right hand side are the feedhorns, while the components on the left hand side compose the FEM (polar modulators and OMT from right to left) and are then enclosed in the cryostat at 20 K. Right: design of the MFI focal plane as seen by the secondary mirror (credit Tramonte, 2017).

- the characterization of spatial variation of the AME parameters in the Lambda-Orionis region (Cepeda-Arroita et al., 2021) and in the Galactic plane (Fernández Torreiro et al., in prep);
- the systematic study of supernova remnants including data at MFI frequencies (López-Caraballo et al., in prep).

Finally, the maps of cosmological fields have not been produced yet. This constitutes future work.

2.3 MFI Instrument model

It is presented in this section a schematic description of the MFI instrument model, and of its noise properties.

2.3.1 Instrumental response

As shown in the picture in Fig. 2.3, the MFI is composed by four feed-horn pixels, two of them for the low frequencies (10–14 GHz), and other two for the high frequencies (16–20 GHz). The four pixels were built with an initial common configuration (top panel in Fig. 2.4), which was improved at a later stage (bottom panel in Fig. 2.4), as the following describes.

In the *first configuration* of the MFI horns (top image in Fig. 2.4), the radiation is collected by a corrugated feedhorn, and enters in a 20 K front-end cryogenic module (FEM). In the FEM, there is a polar modulator that rotates the incoming polarized radiation by four times the encoder angle[3] (4θ), followed

---

[3] The MFI polar modulator is usually oriented in four positions, stepping the angle by 22.5 deg.

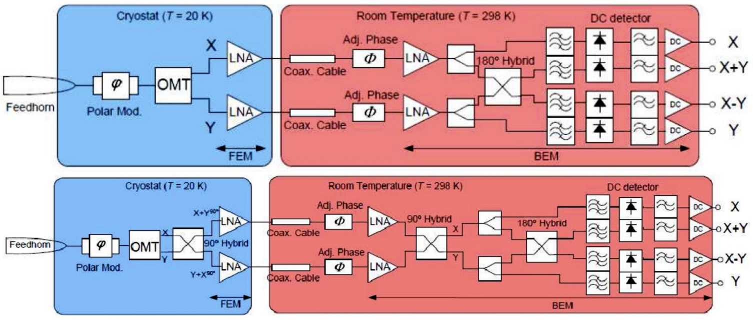

FIGURE 2.4— Scheme of one pixel of the MFI. First configuration in the top figure, where only the (X+Y) and (X-Y) channels are correlated. Second configuration in the bottom figure, where both the (X),(Y) and (X+Y),(X-Y) channels are correlated. More details in the text (Sec. 2.3.1).

by an orthomode transducer (OMT) that produces two channels with orthogonal polarization, and two independent low noise amplifiers (LNAs). The LNAs amplify the signal of the two branches, but they also introduce in the data time-correlated gain drifts that are commonly known as $1/f$ noise (see Sec. 2.3.2), which has to be carefully treated in order to minimize its effect on the processed data.

The outputs of the FEM are then processed by the back-end module (BEM) at room temperature. Here, two power splitters divide each orthogonal polarization branch (X and Y) into two, producing four output channels, that are conventionally called (X), (Y), (X+Y) and (X-Y). In the final part of the BEM, the channels (X+Y) and (X-Y) enter in a 180° hybrid that introduces a correlation between the two, with the result that the (X+Y) and (X-Y) channels are affected by the same $1/f$ noise. For this reason, we adopt the convention of calling the ((X+Y),(X-Y)) channel pair as the "correlated" channels, while ((X),(Y)) are the "uncorrelated" channels. As presented in the following sections, the correlation of the noise between different channels is a useful property that allows the suppression of the final noise in the polarization measurements.

The *second configuration* (bottom image in Fig. 2.4) is an improvement of the initial MFI design, mainly motivated to reduce the $1/f$ noise of polarization data. With this aim, it was introduced a correlation also among the noise of the (X) and (Y) channels (though we will keep calling them the "uncorrelated" channels). The difference between this configuration and the previous one consists of inserting a 90° hybrid in the FEM before the LNAs, and a second 90° hybrid in the BEM before the power splitters. It was tested in horn number 1 starting from April 2014 and then applied to the other three horns from December 2015.

In both configurations, the four output channels, are finally split in two sub-bands: the low frequency and high frequency of the full initial bandwidth, therefore each horn produces in total eight output channels. Horns number 1 and 3 cover the frequency range $10-14\,\mathrm{GHz}$, so the two frequency channels are centered at 11 and 13 GHz. Horns number 2 and 4 cover the frequency range $16-20\,\mathrm{GHz}$, so the two frequency channels are centered at 17 and 19 GHz. In total there are 32 output channels from the MFI, four sets of correlated and uncorrelated channel pairs, for every horn and frequency combination.

2.3.1.1 Response to the IQU Stokes parameters

Each channel measures a linear combination of the intensity I and of the linear polarization Q and U of the observed sky, as:

$$\begin{aligned}\mathbf{V}_j^i = \frac{1}{2}(I-(-1)^i(&\mathbf{A}_j\sin(2\boldsymbol{\phi})Q+\mathbf{B}_j\cos(2\boldsymbol{\phi})U+ \\ &\mathbf{C}_j\cos(2\boldsymbol{\phi})Q+\mathbf{D}_j\sin(2\boldsymbol{\phi})U))+\mathbf{n}_j^i\end{aligned} \tag{2.1}$$

where j=1,2 indicates respectively the correlated or uncorrelated pairs, i=1,2 indicates the channel[4] of the pair selected by j, and $\mathbf{n}_j^i$ is the noise of the corresponding channel. $\boldsymbol{\phi}$ is related to observed polarization direction, being $\boldsymbol{\phi}=2(\boldsymbol{\theta}-\boldsymbol{\theta}_0)+\boldsymbol{\phi}_\mathrm{p}$, where $\boldsymbol{\theta}$, $\boldsymbol{\theta}_0$ and $\boldsymbol{\phi}_\mathrm{p}$ are, respectively, the polar modulator encoder, polar modulator reference[5] and parallactic angle.[6].

As we can see from Eq. 2.1, the output voltage in each channel is composed by the intensity I plus the polarization signal Q and U, modulated by sinusoidal functions. **A**, **B**, **C** and **D** are the parameters that define the equation of the detector response to Q and U as a function of time, depending on the instrument configuration, and they can take the values $(0,\pm1)$, as listed in Tab. 2.1. Eq. 2.1

---

[4] The uncorrelated channels ($j=1$, $i=1,2$) are $(\mathbf{V}_1^1,\mathbf{V}_1^2)=(\mathbf{V}_\mathrm{X},\mathbf{V}_\mathrm{Y})$, while the correlated channels ($j=2$, $i=1,2$) are $(\mathbf{V}_2^1,\mathbf{V}_2^2)=(\mathbf{V}_\mathrm{X+Y},\mathbf{V}_\mathrm{X-Y})$.

[5] The polar modulator angle $\boldsymbol{\theta}$ is the recorded orientation of the polar modulator with respect to a reference angle $\boldsymbol{\theta}_0$, which has to be calibrated.

[6] The parallactic angle is defined as the relative orientation between the alt-azimuthal frame of telescope focal plane and the equatorial coordinates system of a source in the sky.

	Uncorrelated				Correlated			
Horn	A	B	C	D	A	B	C	D
12-Nov-2012 – 30-Nov-2015 (periods 1, 2)								
1	0	0	-1	1	1	1	0	0
2	0	0	-1	1	1	1	0	0
3	0	0	1	-1	1	1	0	0
4	0	0	1	-1	1	1	0	0
01-Dec-2015 – 14-Oct-2016 (periods 3, 4, 5)								
1	0	0	-1	1	1	1	0	0
2	0	0	1	-1	1	1	0	0
3	0	0	1	-1	1	1	0	0
4	0	0	-1	1	1	1	0	0
15-Oct-2016 – 01-Nov-2018 (period 6)								
1	0	0	-1	1	1	1	0	0
2	0	0	-1	1	1	1	0	0
3	0	0	1	-1	1	1	0	0
4	0	0	-1	1	1	1	0	0

TABLE 2.1— A, B, C and D parameters for Eq. 2.1 and 2.3, in different periods of the MFI campaign. See chapter 4, Sec. 4.1.2, for a more detailed definition of periods.

is a general expression of the detector response: it is valid for both the MFI configurations described in Sec. 2.3.1, by only changing the combinations of the **A**, **B**, **C** and **D** parameters. Usually, if Q is modulated by $\cos(2\phi)$, then U is modulated by $\sin(2\phi)$, or the other way around. Therefore, we have non-zero values for only one of the parameter pairs: either (**A**, **B**) or (**C**, **D**) are not null.

The sum and difference of the output voltage in Eq. 2.1 provide the definition of the intensity y^I and polarization y^{P} Time Ordered Data (TOD) vectors, as:

$$\mathbf{y}^{\mathrm{I}}_j = \mathbf{V}^1_j + \mathbf{V}^2_j = I + \mathbf{n}^{\mathrm{I}}_j \tag{2.2}$$

$$\begin{aligned}\mathbf{y}^{\mathrm{P}}_j = \mathbf{V}^1_j - \mathbf{V}^2_j &= \mathbf{A}_j \sin(2\phi)Q + \mathbf{B}_j \cos(2\phi)U + \\ &+ \mathbf{C}_j \cos(2\phi)Q + \mathbf{D}_j \sin(2\phi)U + \mathbf{n}^{\mathrm{P}}_j\end{aligned} \tag{2.3}$$

where $\mathbf{n}^{\mathrm{I}}_j$ and $\mathbf{n}^{\mathrm{P}}_j$ indicate the noise component in the two TODs, obtained from the correlated ($j = 1$) and uncorrelated ($j = 2$) channels.

To summarize, for each horn and frequency split there are two independent TODs that can be used to construct the sky signal maps of intensity (I) and polarization (Stokes Q and U). The 32 MFI channels can be combined to obtain 16 TODs for the intensity and 16 TODs for the polarization.

2.3.2 Noise

2.3.2.1 Noise generalities

The noise in microwave and radio observations is usually comprised of two parts: the white and $1/f$ noise components:

$$\mathbf{n} = \mathbf{w} + \mathbf{n}_{1/\mathrm{f}} \tag{2.4}$$

where the two terms represent, respectively, the white and $1/f$ noise. The white noise $\mathbf{w}$ is the Gaussian, zero averaged, uncorrelated noise component generated by random thermal fluctuation of the detector. The white noise is fully characterized by the standard deviation of the noise distribution σ, which is given by the real radiometer equation:

$$\sigma = \frac{T_{\mathrm{sys}}}{\sqrt{\Delta\nu \cdot \tau}} \tag{2.5}$$

where T_{sys} is system temperature, $\Delta\nu$ is the bandwidth of the experiment and τ is the sampling interval. The covariance matrix of the white noise is diagonal and is defined as:

$$C_{\mathrm{w,nm}} = \langle w_n \cdot w_m \rangle = \delta_{nm}\sigma^2 \tag{2.6}$$

where δ_{nm} is the Kronecker symbol, and $n, m = 1, ..., n_{\mathrm{t}}$, being n_{t} the number of data samples composing the TOD.

The second term in Eq. 2.4, $\mathbf{n}_{1/\mathrm{f}}$, is the $1/f$ noise generated by long term instrumental gain fluctuations that introduce time-correlated baseline drifts.[7] The $1/f$ noise is commonly modeled in the Fourier space by the power spectral density as a function of the frequency f, which is usually driven by a function of the inverse of the frequency. The power spectral density of the total noise in a TOD is usually described as:

$$P(f) = \frac{\sigma^2}{f_{\mathrm{s}}}\left(1 + \left(\frac{f_{\mathrm{k}}}{f}\right)^{\gamma}\right) \tag{2.7}$$

where σ is the white noise level, f_{s} is the sampling frequency of the data,[8] f_{k} and γ are, respectively, the knee frequency and the power of the $1/f$ slope. In particular, the knee frequency traces the transition between a regime of $1/f$ or

---

[7] These drifts are mainly originated by gain fluctuations in the LNAs.

[8] $f_{\mathrm{s}} = \tau^{-1}$

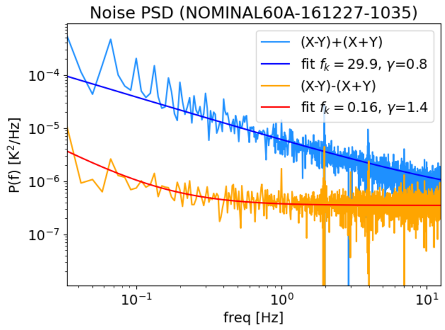

FIGURE 2.5— Noise power spectral density (PSD) of the sum and the difference of correlated channels, from an observation (NOMINAL60A-161227-1035) taken in nominal mode (Sec. 2.2.2), at $el = 60°$, with the instrument in the second configuration. We show the noise PSD of the intensity and polarization data (sum and difference of channels), respectively in in blue and orange color. The dark-blue and red lines are the fits to the measured PSDs, whose parameters are shown in the legend.

white noise. High values of $f_{\rm k}$ and $|\gamma|$ correspond to quick and large fluctuations of the correlated noise.

Large $1/f$ noise drifts project into the maps as stripes along the scanning direction, and introduce spurious signals at large angular scales. The $1/f$ noise stripes must be minimized at the map-making level by using tailored techniques, such as those described in chapter 3.

2.3.2.2 Noise of the MFI

The MFI data-processing relies on the difference between channel pairs, (X+Y)-(X-Y) and (X)-(Y) as in Eq. 2.3, in order to obtain a measurement of the polarization of the sky signal. In the initial configuration of the MFI, the $1/f$ noise of the (X+Y) and (X-Y) channels is respectively correlated, resulting in a partial cancellation of the $1/f$ noise drifts when computing the channel's difference (though the cancellation is not perfect, and some residual $1/f$ affects the subtraction as well). In this configuration, however, the difference of uncorrelated channels, (X)-(Y), does not have the same advantage of $1/f$ noise cancellation, because there is not relative noise correlation between (X) and (Y). For this reason, in this configuration, the polarization measurements obtained from the correlated channels are significantly less noisy than those obtained from the

	$\sqrt{\sigma^2/f_\mathrm{s}}\,[\mathrm{mK}\cdot\mathrm{s}^{1/2}]$	f_k [Hz]	γ
I	0.66-0.90(11–19 GHz)	20.0	1.5
QU	0.66-0.90(11–19 GHz)	0.3	1.8

TABLE 2.2— Typical $1/f$ noise parameters of the MFI, for a noise power spectral density as in Eq. 2.7.

uncorrelated ones.

In the second configuration of the MFI, the noise correlation is introduced also in the uncorrelated channels, therefore, the polarization measurements from both correlated and uncorrelated channel pairs have a reduced $1/f$ noise. We show in Fig. 2.5 the noise power spectral density of the sum and the difference of correlated channels, from an observation in nominal mode (Sec. 2.2.2), at $el = 60°$, taken with the instrument in the second configuration. The fits to the measured power spectra (obtained as described in chapter 4, Sec. 4.1.3) are also shown in the figure, where we can clearly observe that the noise in polarization is significantly suppressed with respect to that in intensity. As a general selection rule for MFI data, we use polarization data only if the pairs of channels are effectively correlated: we obtain polarization maps from the correlated channels in the initial configuration of the MFI, and from uncorrelated and correlated channels in the second one.

However, in order to obtain the intensity of the measured signal, both configurations use the sum of channel pairs (X)+(Y) and (X+Y)+(X-Y) (Eq. 2.2), where there is no suppression of the $1/f$ noise drifts, leading to a noisy measurement of the intensity sky signal from both channel pairs. The high $1/f$ noise in intensity results in a final noise at the map level that is higher by a factor $\sim$3 than in the polarization maps, but the sky signal in intensity is sufficiently bright so that we can detect the emission with sufficiently good signal to noise. Typical values of the MFI intensity and polarization noise are shown in Tab. 2.2, while a more detailed analysis can be found in the thesis by Pelaez Santos (2019), and in chapter 4 (Sec. 4.1.3).

2.4 MFI pipeline

The aim of this section is to introduce the fundamental concepts related to the MFI scientific data processing, besides the MFI characterization and calibration was carried out earlier than the starting of this thesis project. We provide therefore a quick but technical description of the data processing pipeline, which constitutes a necessary background information for the content of the next chapters. We refer to the thesis works by Tramonte (2017), Vignaga (2018), Pelaez Santos (2019), and to Génova-Santos et al. (in prep.) for more details.

2.4.1 Overview of the MFI pipeline

The QUIJOTE-MFI pipeline has been developed in order to convert the raw data into the final scientific data product, which are, for our purposes, maps and angular power spectra. We summarize as follows the main pipeline steps.

The raw data and the basic information regarding the observation are stored in a scientific data file called **TOD** (Time Ordered Data), which contains, with the original sampling rate of 1 kHz: the voltage response of the 32 MFI channels; the azimuth and elevation of the encoder; the Julian date of each time sample (referred to the date of beginning of the commissioning, $jd = 2456244.5$); the position of the polar modulator; and the flags that identify the activation of the calibration diode (see Sec. 2.4.2).

A **BTOD** (Binned TOD) is then constructed from the TOD, by: binning the data into (typically) 60 or 40 ms time bins (depending on the scanning speed of the observation); applying the pointing model of the telescope to project the telescope encoder coordinates into the sky pointing coordinates (see the thesis work by Tramonte, 2017); flagging bright sources (Sun, Moon, geostationary satellites), outliers, and bad data identified by House Keeping files, which keep track of the temperature and pressure of the instrument. The data stored in the BTOD are not calibrated yet, but the amplitude and angle calibration factors (see Sec. 2.4.2) are included in these files.

The data are finally stored in a **CTOD** (Calibrated TOD) after being: calibrated as described in Sec. 2.4.2 and a baseline level subtracted, which is computed as the median value in each scan. If additional flagging or filtering operations are needed, they are applied at the CTOD level.

The CTODs are the final time ordered data products, and are typically used to construct the QUIJOTE-MFI maps. Chapter 3 is dedicated to the description of the map-making step of the pipeline. Additional post processing operations like filtering and re-calibration could be needed at the map level, and are described in chapter 4 and in Rubiño-Martín et al. (in prep), for the case of the wide-survey maps. The final steps consists of the computation of the angular power spectrum of the map. This is described in the thesis work by Pelaez Santos (2019), and summarized in Sec. 2.4.7. In the following, we present some details concerning the pipeline steps that are more relevant for the topics discussed in this thesis.

2.4.2 TOD Calibration

The calibration of the data is a crucial step needed to obtain scientifically relevant measurements. In the case of the MFI, we have to calibrate:

1. the **gain amplitude** of each of the 32 channels;
2. the **polarization reference angle** θ_0 for each of the 4 polar modulators. θ_0 might depend on the bandpass of the channels, therefore we calibrate the angle for each horn and frequency;
3. the **polarization efficiency**.

In this section we provide some general description of the QUIJOTE-MFI calibration steps.

2.4.2.1 Calibrators

The MFI primary calibrators are Cas A and Tau A. Cas A is the MFI default amplitude calibrator because it is bright and lowly polarized ($\Pi_{\rm Cas\,A} = 0.35\%$, from WMAP 7 yr at 22.8 GHz, Weiland et al., 2011). The polarization of Tau A is larger ($\Pi_{\rm Tau\,A} = 7.08\%$, Weiland et al., 2011), so it is not optimal for the amplitude calibration, but it can be used as a cross-check of the calibration obtained with Cas A. Thanks to the large polarization fraction, Tau A is used as default calibrator of the polarization angle.

Improved models of Tau A and Cas A have been produced for the calibration of MFI data, and will be presented in Génova-Santos et al. (in prep.). These models are based in the same data used by Weiland et al. (2011) but include: an improved treatment of the WMAP colour correction and beams; an improved models for Tau A and Cas A secular decreases; and add the Planck-derived values for Tau A and Cas A. We summarized as follows the employed models. The flux density of Cas A is given by:

$$\begin{aligned}\log(S^{2000}_{\rm Cas\,A}({\rm Jy})) =& (2.204 \pm 0.002) - (0.682 \pm 0.011)\log(\nu/40\,{\rm GHz}) + \\ &+ (0.038 \pm 0.008)\log^2(\nu/40\,{\rm GHz})\end{aligned} \tag{2.8}$$

It decreases in time (secular decrease), depending on the frequency[9] as (Hafez et al., 2008):

$$\left(\frac{dS}{Sdt}\right)_{\rm Cas\,A} = (0.68 \pm 0.04) - (0.15 \pm 0.04)\log(\nu/{\rm GHz})\%\,{\rm year}^{-1} \tag{2.9}$$

We assume the polarization fraction and the polarization angle of Cas A to be constant with frequency: $\Pi_{\rm Cas\,A}$=0.35% and $\gamma_{\rm Cas\,A} = 82.7^\circ$ at 22.8 GHz from

---

[9] This is the reason why we referred to epoch 2000 when defining the model in Eq. 2.8.

Weiland et al. (2011).
The flux density model of Tau A (Génova-Santos et al., in prep.) is:

$$S^{2005}_{\mathrm{Tau\,A}}(\mathrm{Jy}) = 358.3(\nu/22.8\,\mathrm{GHz})^{-0.297} \tag{2.10}$$

It is referenced to epoch 2005, and the secular decrease is given by

$$\left(\frac{dS}{Sdt}\right)_{\mathrm{Tau\,A}} = -0.218\%\,\mathrm{year}^{-1} \tag{2.11}$$

with $\Pi_{\mathrm{Tau\,A}}$=7.08% and $\gamma_{\mathrm{Tau\,A}} = -88.5^\circ$ at 22.8 GHz assumed to be constant in frequency (Weiland et al., 2011).

2.4.2.2 Gain amplitude calibration

The amplitude calibration consists in determining the gain factors G that are used to convert the 32 MFI channels from the measured $\boldsymbol{\mathcal{V}}$ in units of voltage (V) to $\mathbf{V} = G\boldsymbol{\mathcal{V}}$ in units of thermodynamic temperature on the sky ($\mathrm{K_{CMB}}$). The gains are computed for each single observation, in the TOD, as:

$$G = \frac{V_{\mathrm{cal}}}{\mathcal{V}_{\mathrm{cal}}} \tag{2.12}$$

where V_{cal} is the expected temperature of the calibrator given the model, and $\mathcal{V}_{\mathrm{cal}}$ is the measured voltage (Génova-Santos et al., in prep.).

A gain calibration system is also applied, which is aimed at mitigating the effect of long gain fluctuations in the data with temporal gain models (e.g., day-night variations). For this purpose, a small antenna (a diode) is used, which is located in front of the focal plane of QT-1 at the centre of the secondary mirror, and activates during 1 s every 30 s injecting a calibration signal in the data. The time variations of the diode signal are used to trace the gain fluctuations (Génova-Santos et al., in prep., Vignaga, 2018).

The calibration is performed at the TOD level using Cas A as a primary calibrator. However, at this stage the $1/f$ noise may affect the determination of the gain factors, which then propagates through the full pipeline, up to the maps. At the map level the $1/f$ noise is suppressed, and a more precise determination of the gain factors can be done, and used to re-calibrate the maps (Rubiño-Martín et al., in prep).

2.4.2.3 Relative amplitude calibration: r-factor

As presented in Sec. 2.3.1, the sum and subtraction of channels pairs provide the TODs of intensity and polarization. However, errors in the determination of the gain factors (Sec. 2.4.2.2) would result in an imperfect balance between the two channel pairs, mixing intensity and polarization in the TODs.

Recalling Eq. 2.3, simplified by using $\mathbf{A} = \mathbf{B} = 1$ and $\mathbf{C} = \mathbf{D} = 0$, and after applying the amplitude calibration, we can write:

$$\mathbf{y}_j^I = \left(\mathbf{V}_j^1 + (r+\epsilon)\mathbf{V}_j^2\right) = (1+\frac{\epsilon}{2r})I - \frac{\epsilon}{2r}\left(\sin(2\phi)Q + \cos(2\phi)U\right) \tag{2.13}$$

$$\mathbf{y}_j^{\mathrm{P}} = \left(\mathbf{V}_j^1 - (r+\epsilon)\mathbf{V}_j^2\right) = (1+\frac{\epsilon}{2r})\left(\sin(2\phi)Q + \cos(2\phi)U\right) - \frac{\epsilon}{2r}I \tag{2.14}$$

where the factor $r = G_j^2/G_j^1$ is the relative gain between pair of channels, and ϵ is a possible mismatch deriving from an incorrect determination of the gains. Note that a possible error in the determination of r ($\epsilon \neq 0$) introduces a fraction of the polarization in the intensity TOD, and of the intensity in the polarization one, plus a change of the polarization efficiency (see next subsection). This produces a polarization to intensity and an intensity to polarization leakage. A leakage of the polarization to the intensity is negligible, but a leakage of intensity to polarization is not, so it must be taken with special caution.

The r-factors of the MFI are computed at the TOD level using Cas A as a primary calibrator, as a median of the ratio of the not calibrated channel pairs, $r = \left\langle \mathbf{V}_j^1/\mathbf{V}_j^2 \right\rangle$ (Génova-Santos et al., in prep.). The r-factor can be also re-calibrated at a later stage, in order to mitigate the possible uncertainty in its determination deriving from $1/f$ contamination, which is large even at small time scales given the high knee frequency ($f_\mathrm{k} \gtrsim 20\,\mathrm{Hz}$) of single channel's noise. In the specific case of the wide-survey maps (Rubiño-Martín et al., in prep), we re-calibrate the r-factor at the map-making level, by fitting a map of the intensity in the polarization TODs with a template fitting technique that is implemented in the map-making (see chapter 3).

2.4.2.4 Polarization angle

The last quantity that needs to be calibrated is the polarization angle θ_0, which is the orientation of the polar modulator with respect to the reference frame of the system. In practice, θ_0 depends on the frequency so one angle per horn and frequency has to be determined.

The angle calibration of MFI data is initially performed at the TOD level. Our default calibrator for the polarization angle is Tau A, which is the brightest polarized source at MFI frequencies. Typical errors on the calibration angles are 1.5°–4°, depending on the horn (Génova-Santos et al., in prep.).

The polarization angle, as well as previous calibration factors defined above, can be re-calibrated at the map level, by rotating the Q and U maps.

Horn	Freq [GHz]	$\rho_{\rm corr}$	$\rho_{\rm uncorr}$
2	17	0.84	0.98
2	19	0.86	0.96
3	11	0.89	0.98
3	13	0.83	0.97
4	17	1.00	0.93
4	19	0.99	0.91

Table 2.3— MFI polarization efficiency measurements. The error is $\sim 1\%$ (~ 0.01).

2.4.2.5 Polarization efficiency

For each channel of the MFI we measured the polarization efficiency, which is defined as the ρ factor in the channel response equation:

$$\mathbf{V} = \frac{1}{2}\left(I - \rho\left(Q\cos(2\phi) + U\sin(2\phi)\right)\right) \tag{2.15}$$

which is obtained from Eq. 2.1, simplified by using $\mathbf{A} = \mathbf{B} = 0$ and $\mathbf{C} = \mathbf{D} = 1$, and where polarization term is modulated by the efficiency parameter ρ (Génova-Santos et al., in prep.).

The polarization efficiency measurements were obtained in August 2020, by injecting a noise diode linearly polarized signal (see Sec. 2.4.2.2) with a horn coupled to the MFI horn, for different position of the modulator angle, also rotating the polarisation direction of the input signal. It is clear from Eq. 2.15 that, from the difference of channel pairs with varying ϕ, we can estimate ρ as the amplitude of the sinusoidal function $Q\cos(2\phi) + U\sin(2\phi)$. The retrieved polarization efficiency values are shown in Tab. 2.3, with an uncertainty of $\sim$1%. In the specific case of the wide-survey maps (Rubiño-Martín et al., in prep), the polarization efficiency was included during the map-making step.

2.4.3 Beams

The definition of the beams consists of the characterization of the optical response of the QUIJOTE-MFI instrument when mounted on QT-1. It is necessary in a CMB experiment to have an accurate determination of beams in order to:

- measure the antenna solid angle $\Omega_{\rm A}$, which is needed to determine the conversion factor between flux density and antenna temperature;
- characterize the near and far sidelobes, which could introduce spurious signal in the maps;

Horn	Freq [GHz]	$\theta_{\rm FWHM}$ [deg]	e	$\Omega_{\rm MB}$ [msr]
1	11	0.934	1.02	0.281
1	13	0.949	1.02	0.287
2	17	0.651	1.03	0.137
2	19	0.674	1.03	0.143
3	11	0.923	1.04	0.274
3	13	0.931	1.04	0.278
4	17	0.645	1.04	0.134
4	19	0.668	1.04	0.141

TABLE 2.4— MFI beam parameters from radial profiles of CST simulations (FWHM of the main beam $\theta_{\rm FWHM}$, ellipticity e and main beam solid angle $\Omega_{\rm MB}$ obtained from the location of the first minima).

- determine the window function of the experiment, necessary for the analysis of the angular power spectrum of the maps (see Sec. 1.4.2.3).

The MFI beams have been characterized with simulations (using the Computer Simulation Technology (CST) asymptotic solver), and with observations of geostationary satellites, and of Tau A and Cas A at 17 GHz, where there are no satellites visible. The satellites,[10] indeed, represent the brightest emission observable at MFI frequencies. On one hand this constitutes a problem because the satellites contaminate the sky observations, but, on the other hand, they provide bright point-like source in the far field limit, that can be used for the characterization of the beam pattern (Vignaga, 2018).

From the study of the maps of satellites and calibrators, the MFI beam shapes were found to be very close to Gaussian, with a circular symmetry. For this reason, we can use symmetrized radially-averaged profiles of the beams given by:

$$B(\theta) = \frac{\int B(\theta,\phi)d\phi}{A\int d\phi} \tag{2.16}$$

with $B(\theta,\phi)$ being the beam shape as a function of the radial and angular coordinates (θ,ϕ) on a map centred on the source. The factor A normalizes the amplitude of the beam shape to unity. The beam profiles of the MFI are obtained by applying Eq. 2.16 to maps of simulated CST beams, as presented in Vignaga (2018), and in Génova-Santos et al. (in prep.). The main parameters of the MFI beams are summarized in Tab. 2.4.

---

[10] The geostationary satellites are distributed along the equatorial plane, with declinations between −4° and 0°. See Sec. 2.4.5.

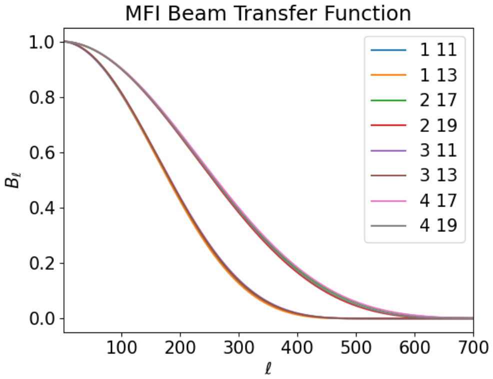

FIGURE 2.6— Beam transfer functions for each frequency channel of the MFI.

For the analysis of the angular power spectrum of a map we need to use the beam function in the harmonic space: the *beam transfer function* defined as (White & Srednicki, 1995):

$$B_\ell = \frac{2\pi}{\Omega_\mathrm{A}} \int B(\theta) P_\ell(\cos(\theta)) d(\cos(\theta)) \tag{2.17}$$

where P_ℓ is the Legendre polynomial of order ℓ. The beam transfer functions of the MFI frequency channels are shown in Fig. 2.6.

2.4.4 Bandpass and colour corrections

A receiver is sensitive to a given range of frequencies with an efficiency that is ideally constant across the band, but which in reality can have a peculiar shape as function of the frequency, the so called *bandpass*, here indicated as $g(\nu)$. The signal measured from the instrument, therefore, is the integration, weighted by the bandpass, of the sky antenna temperature spectrum[11] $T_A(\nu)$, which can be expressed in CMB temperature units by applying a correction (following Planck Collaboration et al. (2014c) and Génova-Santos et al., in prep.) given by the

---

[11] The antenna temperature is the convolution of the brightness temperature with the antenna beam pattern. The antenna temperature spectrum has units of Rayleigh-Jeans brightness temperature ($\mathrm{K_{RJ}}$).

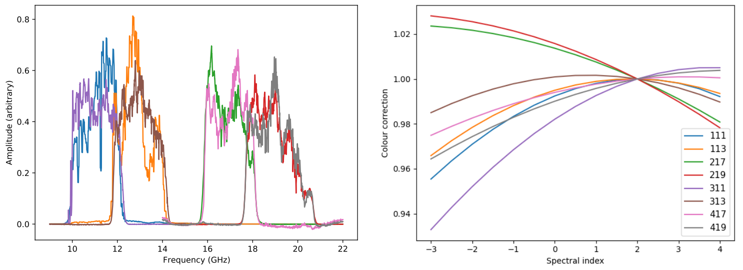

FIGURE 2.7— MFI bandpasses (left) and colour corrections (right). Images produced by Mike Peel (IAC).

following equation:

$$\tilde{T} = \frac{\int g(\nu) T_A(\nu)\ d\nu}{\int \eta_{\Delta T}(\nu) g(\nu)\ d\nu} \tag{2.18}$$

where $\eta_{\Delta T}(\nu) = x^2 e^x/(e^x - 1)^2$ is the conversion factor between CMB-differential thermodynamic temperature ($\mathrm{K_{CMB}}$) and Rayleigh-Jeans brightness temperature ($\mathrm{K_{RJ}}$), with $x = h\nu/k_{\mathrm{B}}T_{\mathrm{CMB}}$, and h and k_{B} the Planck and Boltzmann constants, ν the frequency in Hertz, and T_{CMB} the temperature of the CMB. This is the correction to go from the calibration source (Cas A / Tau A) to CMB calibrated maps.

A precise characterization of the bandpass response is very important for calibration purposes. The bandpasses of the MFI have been measured in the laboratory in 2013, during the commissioning of the experiment, for horn numbers 1, 2 and 3, but not for horn number 4 because of the poor conditions of the LNAs (see the thesis work by Harper, 2016). The measurements were repeated in August 2020 for horn numbers 2, 3 and 4, not for horn number 1 which was not functional by that time. The latest bandpass measurements are shown in Fig. 2.7 (except for Horn 1 that is from 2013 measurements), and the estimated effective frequencies are listed in Tab. 2.5.

QUIJOTE-MFI data have been calibrated by integrating the expected temperature of the primary calibrator Cas A, across the instrument bandpasses, using the spectrum indicated in Eq. 2.8. With this methodology, effectively the data are calibrated to a CMB spectrum. Consequently, when the observed sky has a spectrum different from that of the CMB (e.g., a power law in $\mathrm{K_{CMB}}$ with spectral index $\alpha \neq 2$), we have to apply a correction accounting for the different spectral shape of the emission. This procedure is called *colour correction*.

Horn	Freq [GHz]	c_0	c_1	c_2	ν_0 [GHz]
1	11	0.9926	0.0072	−0.0018	11.2
1	13	0.9950	0.0054	−0.0014	12.8
2	17	1.0136	−0.0054	−0.0007	16.7
2	19	1.0156	−0.0063	−0.0008	18.7
3	11	0.9821	0.0119	−0.0015	11.1
3	13	1.0009	0.0019	−0.0012	12.9
4	17	0.9940	0.0043	−0.0007	17.0
4	19	0.9901	0.0064	−0.0007	19.0

Table 2.5— MFI colour correction parameters (see Eq. 2.21) and central frequencies, obtained from the bandpasses shown in Fig. 2.7.

The colour correction factor is defined, following Planck Collaboration et al. (2014c), as:

$$C(\alpha,\nu_0) = \frac{\int g(\nu)\eta_{\Delta T}(\nu)\ d\nu}{\eta^0_{\Delta T}\int g(\nu)(\nu/\nu_0)^{\alpha-2}\ d\nu} \tag{2.19}$$

where we assumed a power-law spectrum with spectral index α for the sky emission, and where *0* indicates that the quantity is computed at the effective frequency of the band. The color-corrected temperature T_0 is given by:

$$T_0(\alpha) = C(\alpha)\tilde{T} \tag{2.20}$$

Given the instrument bansdpass, it is possible to compute numerically the colour correction factor for different values of α. The colour corrections of the MFI are modeled with polynomial functions for different values of α, as (Peel et al., in prep):

$$C(\alpha) = c_0 + c_1\alpha + c_2\alpha^2 \tag{2.21}$$

that are shown in Fig. 2.7, for the parameters listed in Tab. 2.5 (Génova-Santos et al., in prep.). The colour correction is typically applied when performing the analysis of specific regions, for which we know the expected spectral index. If the spectral index is not known a priori and it has to be determined, the colour correction is applied iteratively until the model converges.

2.4.5 Radio Frequency Interference (RFI)

The main source of RFI at the MFI frequencies is the emission from geostationary satellites.[12] These satellites, indeed, populate the geostationary orbit,

---

[12] http://research.iac.es/proyecto/cmb/pages/posts/impact-of-satellite-ldquomega-constellationsrdquo-on-cmb-experiments-at-the-teide-observatory2.php. A discussion on

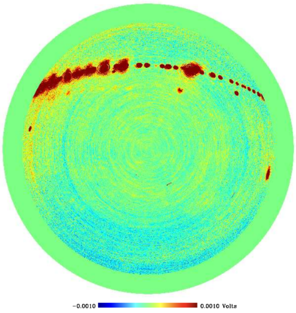

Figure 2.8— Local map from QUIJOTE-MFI, obtained with continuous rotation scans, stepping the elevation to cover the complete elevation range of the telescope. The satellite band is evident in the upper part of the figure, showing a very dense population of bright geostationary satellites. Image taken from Vignaga (2018).

as shown in Fig. 2.8 (declinations $-4^\circ < \delta < 0^\circ$ from the TO) and emit with narrow bandwidths in the X band (8-12 GHz) and Ku band (12-18 GHz), that overlap with the MFI bandwidths. The emission from satellites is very strong as compared with the sky signal, therefore careful identification and flagging must be carried out. The brightest satellites and their positions in local coordinates are catalogued. Data taken at pointing directions in the proximity of the satellites locations are therefore flagged.

Residual interference at large scales, coming for example from the far sidelobes of the experiment, can be removed by filtering the CTODs, and/or the maps at the post-processing level. This is the case of the wide-survey maps, as presented in Rubiño-Martín et al., (in prep), and in chapter 4.

2.4.6 Map-making

For the map-making step, we implemented an internal and independent map-making code, PICASSO, that projects a set of CTODs into an image of the observed sky using the destriping algorithm for the suppression of the $1/f$ noise (e.g., Keihänen et al., 2010). The map-making is one of the main goals of this thesis work, during which we applied further implementations to the code previously presented in the thesis by Pelaez Santos (2019). We provide more

---

the impact of satellite constellations on astronomy is also give in Rawls et al. (2020) and references therein.

detailed information in chapter 3, and in Guidi et al. (submitted).

2.4.7 Power spectrum estimation

Angular power spectra (Eq. 1.57) constitute useful tools for the analysis of the maps, allowing us to study the angular distribution of the signal across the observed sky. However, their computation from an incomplete sky coverage map (like the QUIJOTE maps) is affected by mode coupling due to the applied mask (e.g., Hivon et al., 2002), and by a mixing of the E and B-modes (e.g., Alonso et al., 2019).

In the thesis work by Pelaez Santos (2019) a detailed analysis can be found of different estimators of angular power spectra, with the aim of identifying the optimal one to be used for the QUIJOTE maps. Pseudo-C_ℓ estimators like XPOL[13] (Tristram et al., 2005) and NAMASTER[14] (Alonso et al., 2019), which are based on principles of the MASTER approach (Hivon et al., 2002), or POLSPICE,[15] which is based on the two-point correlation function (Chon et al., 2004), have shown to have optimal performance for sufficiently large sky coverage ($f_{sky} > 0.3$), like that of the QUIJOTE wide-survey. The angular power spectra of small sky patches (e.g., the QUIJOTE cosmological fields, or raster scans in general), instead, are better computed with maximum likelihood estimators, like the quadratic maximum likelihood (QML) method presented in (e.g.,) Tegmark & de Oliveira-Costa (2001); Efstathiou (2006); Bilbao-Ahedo et al. (2021). The QML estimator is also recommended for the computation of the spectrum of the large angular scales (low multipoles), due to possible residual mode coupling of the pseudo-C_ℓ estimators, particularly if there is a dipole pattern in the maps (more details in Sec. 3.6.2).

In this thesis, we use the codes XPOL and NAMASTER to compute the power spectra (and cross-correlations) of the QUIJOTE wide-survey maps, and the QML code ECLIPSE implementated by Bilbao-Ahedo et al. (2021) for the study of the low multipoles.

2.5 Atmosphere

The atmosphere is a source of disturbance for MFI data. Indeed, at microwave frequencies, the atmosphere appears as a black body emission with a brightness temperature of few Kelvins, produced by the emission of oxygen and water vapour, which is usually quantified by the level of Precipitable Water Vapour (PWV). Fig. 2.9 shows the opacity of the atmosphere in the frequency range

---

[13] https://gitlab.in2p3.fr/tristram/Xpol

[14] https://github.com/LSSTDESC/NaMaster

[15] http://www2.iap.fr/users/hivon/software/PolSpice/

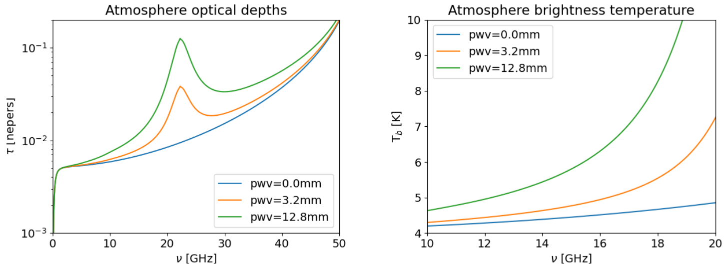

FIGURE 2.9— Left: optical depth of the atmosphere as a function of frequency, at $\nu \leq 50$ GHz. Right: brightness temperature of the atmosphere as a function of frequency, in the range 10–20 GHz. Figures obtained from the models by Otarola (2018), computed for the typical conditions at the OT, in the QUIJOTE frequency range. The profiles for three representative values of PWV values are shown: PWV=0.0 mm (dry atmosphere), PWV=3.2 mm (close to the average at the OT), PWV=12.8 mm (typical high values at the OT).

of interest for QUIJOTE ($\nu \leq 50$ GHz; left), and the atmospheric brightness temperature in the MFI frequency range (10–20 GHz; right). The optical depth has a peak corresponding to the water vapour line ($\nu \sim 22$ GHz), and a high frequency drift driven by the oxygen line ($\nu \sim 60$ GHz).

The water vapour line, in particular, affects the QUIJOTE-MFI data depending on the frequency and on the amount of PWV, at a level that can be characterized by the factors reported in Tab. 2.6. It follows that temporal and spatial fluctuation of the atmospheric emission introduce correlated noise drifts in the MFI data, with a behaviour that is similar to a $1/f$ noise component, which is stronger at 17 and 19 GHz. The atmosphere is practically unpolarized, although several studies have shown that there is some small level of polarization[16] (at μK level), so the $1/f$ atmospheric contribution affects almost only the intensity. However, if there is some residual intensity to polarization leakage, the atmospheric intensity drifts could also affect the polarization data. These considerations qualitatively explain why microwave observations, especially at frequencies larger than that of the MFI, are preferably made from space, or from sites with an extremely dry and stable atmosphere (Antarctica, Atacama, Tenerife).

---

[16] Pietranera et al. (2007) predicted a non-negligible polarization fraction produced by ice crystals in clouds, and Takakura et al. (2019) reported measurements of that linear polarization. In addition, Padilla et al. (2020) and Petroff et al. (2020) measured circular polarization produced by the atmosphere.

PWV [mm]	$T_{b,13/11}$	$T_{b,17/11}$	$T_{b,19/11}$
0.0	1.02	1.08	1.12
3.2	1.04	1.19	1.43
12.8	1.08	1.49	2.24

TABLE 2.6— Average ratios of the atmospheric brightness temperature at MFI frequencies: 13, 17, and 19 GHz relative to the 11 GHz. The values are computed across a top-hat 2 GHz bandwidth centered at the four MFI frequencies.

In order to measure the atmospheric contribution in the MFI data, we perform daily sky-dips observations (see Sec. 2.2.2), scanning the sky in elevation, at a fixed azimuth position, to measure different air masses. With these observations we can derive the temperature of the atmosphere, and obtain a daily estimate of the PWV (see Otarola et al., 2018). In addition, a GPS antenna belonging to the meteorological station AEMET (Agencia Estatal de Meteorología[17]), which is located near to the QUIJOTE site, provides continuous measurements of the PWV, allowing us to control the quality of the data depending on the atmospheric conditions. The typical values of PWV at the Teide observatory are $2 - 10$ mm, with significant seasonal variation, with an average of ~ 3.5 mm (Castro-Almazán et al., 2016).

In the specific case of wide-survey data (Rubiño-Martín et al., in prep.) the $1/f$ atmospheric noise is treated with a tailored technique that applies a Principal Component Analysis (PCA) to the CTODs, which looks for common large angular scale modes characterized by the typical ratios of an atmospheric component across frequencies (Tab. 2.6).

---

[17] `http://www.aemet.es/`

3

Map-making for QUIJOTE-MFI

"The important thing was to build visual images,
and then the eyes would have come consequently."
Italo Calvino, Le Cosmicomiche

Map-making is an important step for the data analysis of Cosmic Microwave Background experiments. It consists in converting the data, which are typically a long, complex and noisy collection of measurements, into a map, which is an image of the observed sky. The implementation of the map-making code for the QUIJOTE experiment is one on the main goals of this thesis. We implemented the PICASSO **(Polarization and Intensity CArtographer for Scanned Sky Observations) code to construct intensity and polarization maps from the MFI instrument of the QUIJOTE.** PICASSO **is based on a destriping algorithm, and is suited to address specific issues of ground-based microwave observations, with a technique that allows the fitting of a template function in the time domain, during the map-making step. In addition, even though the implementation of PICASSO is specific for QUIJOTE-MFI data, it could be adapted to other experiments. The content of this chapter will soon be published in Guidi et al. (submitted), in which we describe the** PICASSO **code, validating it with simulations and assessing its performance.**

3.1 Introduction

The first product of scanned observations at radio and microwave frequencies is not an image of the observed sky, but a Time Ordered Data stream (TOD) (e.g., Tegmark, 1997). The TOD is a long collection of sky signal measurements, recorded by the instrument as a function of time and pointing coordinates, in combination with a component of instrumental and atmospheric noise. The role of map-making is to project and integrate this set of measurements from the time domain to their original sky positions, and to construct a map, which is an image of the observed sky. The map is a compressed version of the data, and can be analyzed in the harmonic space by computing its angular power spectrum, which is also one of the main observables for CMB experiments.

In this chapter, we present the PICASSO map-making code, whose implementation was started during the thesis work of Pelaez Santos (2019) and continued in the context of this thesis, with the aim to optimize the construction of the QUIJOTE-MFI intensity and polarization maps. In particular, PICASSO has been already used to produce maps from raster scans observations in some Galactic regions (Génova-Santos et al., 2017; Poidevin et al., 2019), and is now also applied for the production of the QUIJOTE-MFI wide-survey maps presented in chapter 4 and in Rubiño-Martín et al. (in prep.).

The PICASSO code is based on the destriping algorithm implemented in the MADAM code, which was used for the construction of the Planck-LFI maps (Keihänen et al. 2005, Keihänen et al. 2010, Planck Collaboration et al. 2016g), and which is commonly applied to other CMB experiments (Sutton et al. 2010, Kurki-Suonio et al. 2009, Ashdown et al. 2007). Our code is an independent implementation, and is suited to address specific issues related with QUIJOTE, or, in general, with ground-based microwave experiments.

Furthermore, PICASSO has been implemented with a technique that is useful for ground-based experiments, with the aim of fitting and subtracting a general template at the TOD level from the data during, during the map-making step. We applied this technique for the subtraction of two particular templates that are important at microwave wavelengths: the CMB dipole, and a stable, plane-parallel[1] atmospheric component, but it can also be particularly useful for ground-based experiments, for example for the correction of radio frequency interference (RFI).

In the following sections we present the validation of PICASSO, showing its performance with realistic end-to-end simulations of the QUIJOTE-MFI wide-survey data. We employed TOD simulations containing the foreground sky signal, point sources, CMB anisotropies, CMB dipole, and three different scenarios for the noise: no-noise, only white noise, and correlated noise (including realistic $1/f$ plus a white noise component). We reconstructed maps of the simulated data-set with PICASSO, and we studied their angular power spectra,

---

[1] The atmosphere in the plane-parallel approximation is assumed to be composed by consecutive two-dimensional parallel planes. In this approximation, the angle between the direction of propagation of light across the atmosphere and the normal to the planes is constant.

in order to quantify the ability of the code to reconstruct the injected sky signal. Particular attention was placed on the characterization of the large angular scales signal.

The chapter is organized as follows: in Section 3.2 we describe the generalities of the destriper map-making algorithm, in Section 3.3 we present the specifics of PICASSO suited for QUIJOTE-MFI data, and in Section 3.3.6 the implementation of the template function fitting at the map-making level. Then, in Section 3.4 we briefly describe the structure of the code, and in Section 3.5 we present the realistic end-to-end simulations of the QUIJOTE-MFI wide-survey, that were used to validate the map-making procedure. Finally, the results are reported in Section 3.6, where we show the maps of the simulations, the analysis at the power spectrum level, the transfer function, and two examples of the fitting of a template function, using a static atmosphere and the CMB dipole. We report our conclusions in Section 3.7. The contents of this chapter have also been presented in Guidi et al. (submitted).

3.2 Map-making problem

The map-making problem consists in finding an efficient and optimal way to project the TOD into a map of the observed sky, by accounting simultaneously for the suppression of the correlated noise. Different techniques have been presented in the literature, and they are mainly based on the maximum-likelihood (e.g., Tegmark, 1997) and destriping (Keihänen et al., 2010; Sutton et al., 2010) techniques. In addition, different filtering operations at the map-making level have been proposed (e.g., Poletti et al., 2017), with the aim of reducing unwanted noise modes from the data.

PICASSO is based on the destriping technique, which is widely used in the context of CMB experiments (Kurki-Suonio et al. 2009; Planck Collaboration et al. 2016g; Keihänen et al. 2010; Sutton et al. 2010). All microwave experiments, indeed, have the common goal of obtaining the cleanest possible intensity and polarization maps from data that are affected by correlated $1/f$ noise, but without suppressing the large angular scale modes coming from sky signal. Usually, the TOD of a CMB experiment is contaminated by two noise components: the white noise, which is uncorrelated, and the $1/f$ noise that is correlated in time. As introduced in Sec. 2.3.2, the white noise is produced by random thermal fluctuations of the electrons in the low noise amplifiers, it is Gaussian distributed with zero mean and variance σ^2. On the other hand, the $1/f$ noise is correlated in time, and it consists of long-time drifts which are mainly produced by instrumental gain variation and atmospheric emission. The destriping technique aims to correct for the correlated noise component by

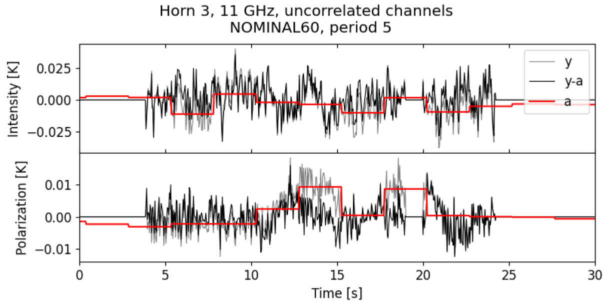

FIGURE 3.1— Data stream of an observation before (grey) and after (black) subtracting the $1/f$ noise with baselines (red). The top and bottom panels are, respectively, for the intensity and polarization TODs, obtained as the sum and difference of uncorrelated channels from a subset of wide-survey observations ($el = 60°$ data from period 5). We show the data in a interval of 30 s, corresponding to one 360 ° scan of the telescope (see Sec. 3.5.1). The baselines length is $t_\mathrm{b} = 2.5$ s. Flagged data are set to zero.

modeling the $1/f$ drifts with a set of consecutive offsets with a given time length t_b, the so called baselines, as shown in Fig. 3.1.

Our reference implementation of the destriping problem is the MADAM code (Keihänen et al., 2005, 2010), which is implemented with priors on the baselines, taking the advantage of the a priori statistical knowledge of the noise of the experiment. Here we describe the mathematics that is at the basis of the destriping algorithm, which is then adapted and expanded for the production of the maps of QUIJOTE-MFI, in the PICASSO map-making code.

3.2.1 Destriper algorithm

The map-making problem requires a solution for the sky map, $\mathbf{m}_\mathrm{sky}$, given the detector TOD, $\mathbf{y}$, which contains n_t data samples. For a experiment measuring intensity and linear polarization like QUIJOTE, the sky map $\mathbf{m}_\mathrm{sky}$ is represented as a set of three HEALPix[2] (Górski et al. 2005) vectors of n_p pixels: the I, Q and U Stokes maps. In general, the TOD vector can be written as a combination of sky signal $\mathbf{s}$, and noise $\mathbf{n}$, as:

$$\mathbf{y} = \mathbf{s} + \mathbf{n} = \mathbf{P} \cdot \mathbf{m}_\mathrm{sky} + \mathbf{n} \tag{3.1}$$

with $\mathbf{s}$ being the sky signal map $\mathbf{m}_\mathrm{sky}$ projected into the time ordered domain by the pointing matrix $\mathbf{P}$ (see Sec. 3.3.2 for the definition of QUIJOTE-MFI

---

[2] https://sourceforge.net/projects/healpix/

pointing matrix).

The destriping algorithm describes the noise vector **n** in the TOD as the sum of two components: a white noise (uncorrelated) part **w**, plus a correlated component (see Sec. 2.3.2), usually ascribed to the $1/f$ noise, modelled as a series of some base functions. For this correlated part, it is commonly used a set of discrete offsets, called baselines. Thus, the noise vector is written as:

$$\mathbf{n} = \mathbf{w} + \mathbf{F} \cdot \mathbf{a}, \tag{3.2}$$

where the term $\mathbf{F} \cdot \mathbf{a}$ is an approximation to model the correlated $1/f$ noise as a sequence of n_{b} baselines **a**, which are projected in a TOD format with the baseline pointing matrix **F**. We call $\mathbf{C}_{\mathrm{n}}$, $\mathbf{C}_{\mathrm{w}}$, and $\mathbf{C}_{\mathrm{a}}$ the covariance matrices of the total, white, and $1/f$ noise components, respectively (see Sec. 3.2.2 for extended description). Combining Eq. 3.1 and 3.2, the data vector can be re-written as:

$$\mathbf{y} = \mathbf{P} \cdot \mathbf{m}_{\mathrm{sky}} + \mathbf{F} \cdot \mathbf{a} + \mathbf{w} \tag{3.3}$$

and can be treated with a Bayesian statistical approach, where the parameters are the baselines vector **a** and sky map $\mathbf{m}_{\mathrm{sky}}$.
The posterior of the map-making problem is given by:

$$P(\mathbf{m}_{\mathrm{sky}}, \mathbf{a}|\mathbf{y}) \propto P(\mathbf{m}_{\mathrm{sky}}, \mathbf{a}) \cdot L(\mathbf{y}), \tag{3.4}$$

where $P(\mathbf{m}_{\mathrm{sky}}, \mathbf{a})$ is the prior of the parameters, $L(\mathbf{y}) = P(\mathbf{y}|\mathbf{m}_{\mathrm{sky}}, \mathbf{a})$ is the likelihood function, and the probability distribution of the data $P(\mathbf{y})$ is assumed to be constant. If we apply the probability product rule to Eq. 3.4, we get:

$$\begin{aligned} P(\mathbf{m}_{\mathrm{sky}}, \mathbf{a}|\mathbf{y}) \propto & P(\mathbf{a}|\mathbf{m}_{\mathrm{sky}}) P(\mathbf{m}_{\mathrm{sky}}) \cdot L(\mathbf{y}) = \\ = & P(\mathbf{a}) P(\mathbf{m}_{\mathrm{sky}}) \cdot L(\mathbf{y}) \end{aligned} \tag{3.5}$$

where $P(\mathbf{m}_{\mathrm{sky}})$ is the prior on the map, and $P(\mathbf{a}|\mathbf{m}_{\mathrm{sky}}) = P(\mathbf{a})$ is the prior on the baselines, where we assume that the baselines values are independent from the sky signal. To avoid imposing any prior on the map, we use a flat prior for $\mathbf{m}_{\mathrm{sky}}$:

$$P(\mathbf{m}_{\mathrm{sky}}) = 1 \tag{3.6}$$

For the baselines, instead, we assign a Gaussian prior given by:

$$P(\mathbf{a}) = \frac{1}{((2\pi)^{n_{\mathrm{b}}} \det(\mathbf{C}_{\mathrm{a}}))^{1/2}} \exp\left(-\frac{1}{2}\mathbf{a}^T \cdot \mathbf{C}_{\mathrm{a}}^{-1} \cdot \mathbf{a}\right) \tag{3.7}$$

where we assume that the baselines have a random and Gaussian (zero centered) distribution.

The likelihood of the data $\mathbf{y}$, using Eq. 3.3, is given by:

$$L(\mathbf{y}) = P(\mathbf{y}|\mathbf{m}_{\rm sky}, \mathbf{a}) = \frac{1}{((2\pi)^{n_{\rm t}} \det(\mathbf{C}_{\rm w}))^{1/2}} \exp\left(-\frac{1}{2}\mathbf{w}^T \cdot \mathbf{C}_{\rm w}^{-1} \cdot \mathbf{w}\right) \quad (3.8)$$

where $\mathbf{C}_{\rm w}$ is the covariance matrix of the white noise defined in Eq. 2.6. Let us now maximize the posterior in Eq. 3.5, or equivalently, a function of its logarithm X:

$$X = -2 \ln \left[P(\mathbf{m}_{\rm sky}, \mathbf{a}|\mathbf{y})\right] \quad (3.9)$$

that, using Eq. 3.3 and the probability density functions in Eq. 3.6, 3.7 and 3.8, can be written as:

$$X = (\mathbf{y} - \mathbf{P} \cdot \mathbf{m}_{\rm sky} - \mathbf{F} \cdot \mathbf{a})^T \mathbf{C}_{\rm w}^{-1} (\mathbf{y} - \mathbf{P} \cdot \mathbf{m}_{\rm sky} - \mathbf{F} \cdot \mathbf{a}) + \mathbf{a}^T \mathbf{C}_{\rm a}^{-1} \mathbf{a} + \text{const} \quad (3.10)$$

The minimization of X with respect to $\mathbf{m}_{\rm out}$ provides the destriper solution for the map:

$$\mathbf{m}_{\rm out} = \mathbf{M}^{-1} \mathbf{P}^T \mathbf{C}_{\rm w}^{-1} (\mathbf{y} - \mathbf{F} \cdot \mathbf{a}) \quad (3.11)$$

with $\mathbf{M} = \mathbf{P}^T \mathbf{C}_{\rm w}^{-1} \mathbf{P}$. We can use now Eq. 3.11 to maximize $X(\mathbf{m} = \mathbf{m}_{\rm out})$ with respect to $\mathbf{a}$, and obtain the equation to determine the baselines $\mathbf{a}_{\rm out}$, which is:

$$\left(\mathbf{D} + \mathbf{C}_{\rm a}^{-1}\right) \cdot \mathbf{a}_{\rm out} = \mathbf{F}^T \mathbf{C}_{\rm w}^{-1} \mathbf{Z} \mathbf{y} \quad (3.12)$$

where we defined the $(n_{\rm t}, n_{\rm t})$ matrix:

$$\mathbf{Z} = \mathbf{1} - \mathbf{P}(\mathbf{M}^{-1} \mathbf{P}^T \mathbf{C}_{\rm w}^{-1}) \quad (3.13)$$

and the $(n_{\rm b}, n_{\rm b})$ matrix:

$$\mathbf{D} = \mathbf{F}^T \mathbf{C}_{\rm w}^{-1} \mathbf{Z} \mathbf{F}. \quad (3.14)$$

Equations 3.11 and 3.12 constitute the solution the map-making problem: with Eq. 3.12 we can estimate the baselines, and with Eq. 3.11 we project the destriped data $(\mathbf{y} - \mathbf{F} \cdot \mathbf{a}_{\rm out})$ into the the I, Q, and U maps.

3.2.2 Noise covariance matrix

We define here the covariance matrix of the noise, distinguishing two different components: the white noise and the correlated $1/f$ noise, modelled with the baselines. The $(n_{\rm t} \times n_{\rm t})$ covariance matrix of the total noise is defined as:

$$\mathbf{C}_{\rm n} = \left\langle \mathbf{n} \cdot \mathbf{n}^T \right\rangle \quad (3.15)$$

	$\sqrt{\sigma^2/f_\mathrm{s}}$ [$mK \cdot s^{-1/2}$]	f_k [Hz]	f_k (prior) [Hz]	γ	f_cut [Hz]
I	0.66-0.90(11-19 GHz)	20.0	40.0	1.5	0.033
QU	0.66-0.90(11-19 GHz)	0.3	0.3	1.8	0.033

TABLE 3.1— Reference values for the $1/f$ noise parameters adopted in this chapter, for a noise power spectral density of the type of Eq. 2.7, with a low frequency cut-off at f_cut (see Fig. 3.2). These values are used both for the noise simulations, and for the noise prior (see Eq. 3.18). The noise prior uses the same parameters of the injected noise simulation, except for the knee frequency in intensity, which takes a relaxed value of 40 Hz instead of 20 Hz (see text for details).

where $<>$ indicates the ensemble average from Eq. 3.2. $\mathbf{C}_\mathrm{n}$ can be expressed as a combination of the covariance of the white noise ($\mathbf{C}_\mathrm{w}$, see Eq. 2.6) and of the $1/f$ component:

$$\mathbf{C}_\mathrm{n} = \mathbf{C}_\mathrm{w} + \mathbf{F}\mathbf{C}_\mathrm{a}\mathbf{F}^T. \tag{3.16}$$

The covariance matrix of the $1/f$ noise can be written in terms of the covariance matrix of the baselines $\mathbf{C}_\mathrm{a}$, which is a projection in the $(n_\mathrm{b} \times n_\mathrm{b})$ space through the matrix $\mathbf{F}$ of the total noise covariance $\mathbf{C}_\mathrm{n}$ (Sutton et al. 2010):

$$\mathbf{C}_\mathrm{a} = \left\langle \mathbf{a}^T\mathbf{a} \right\rangle = \left(\mathbf{F}^T\mathbf{F}\right)^{-1}\mathbf{F}^T\mathbf{C}_\mathrm{n}\mathbf{F}\left(\mathbf{F}^T\mathbf{F}\right)^{-1} = \frac{1}{n_{\mathrm{b}'}^2}\mathbf{F}^T\mathbf{C}_\mathrm{n}\mathbf{F} \tag{3.17}$$

where $n_{\mathrm{b}'}$ is the number of data samples within one baseline. Due to the correlation of the noise, $\mathbf{C}_\mathrm{a}$ is not diagonal in the time domain. However, within a good approximation, $\mathbf{C}_\mathrm{a}$ is a circulant matrix, and the corresponding matrix in Fourier space, $\hat{\mathbf{C}}_\mathrm{a}$, is diagonal. The diagonal of $\hat{\mathbf{C}}_\mathrm{a}$ can be estimated from the power spectral density of the $1/f$ correlated noise, that can be written, similarly to the $1/f$-only term of Eq. 2.7, as:

$$P(f) = \begin{cases} \frac{\sigma^2}{f_\mathrm{s}}\left(\frac{f_\mathrm{k}}{f}\right)^\gamma, & \text{if } f > f_\mathrm{cut} \\ \frac{\sigma^2}{f_\mathrm{s}}\left(\frac{f_\mathrm{k}}{f_\mathrm{cut}}\right)^\gamma, & \text{if } f < f_\mathrm{cut} \end{cases} \tag{3.18}$$

where f_cut is a parameter that marks the transition between the $1/f$ and a flat regime at low frequencies (e.g. in Fig. 3.2), and where we remind that σ is the white noise level, f_s is the data sampling frequency, and f_k and γ are the knee frequency and the slope that define the $1/f$ power spectral density. The sampling rate of QUIJOTE-MFI data is $t_\mathrm{s} = 40\,\mathrm{ms}$, and f_cut is given by the inverse of $t_\mathrm{cut} = 30\,\mathrm{s}$, which is the typical timescale of one scan (see Sec. 3.5.1), within which we remove a median value suppressing the growth of the $1/f$ noise at $f < f_\mathrm{cut}$.

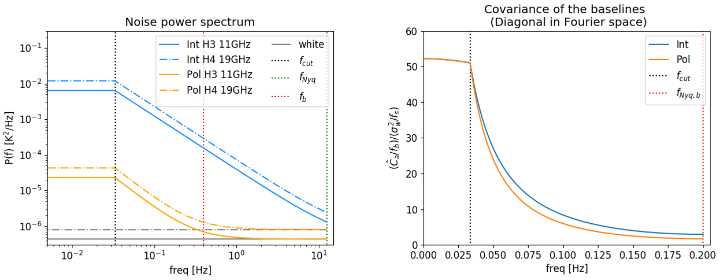

FIGURE 3.2— Left: theoretical power spectral density of the QUIJOTE-MFI noise modelled by Eq. 2.7, for intensity (in blue) and polarization (in orange), using the typical values that are listed in Table 3.1, and applying a low frequency cut-off as describen in to Eq. 3.18. We show the cases of two channels of the MFI: horn number 3 at 11 GHz (thick lines), and horn number 4 at 19 GHz (dot-dashed lines). We represent with vertical dotted lines the typical frequency thresholds: the low frequency threshold $f_{\rm cut}$ in black (see Eq. 3.18), the frequency of the baselines in red, and the Nyquist frequency of the data $f_{\rm Nyq} = 1/(2 \cdot t_{\rm s})$ in green. Right: the diagonal of the covariance matrix of the baselines in Fourier space (Eq. 3.19) as function of frequency, for the QUIJOTE $1/f$ prior parameters in intensity (blue) and polarization (orange), normalized to a baseline frequency of $f_{\rm b} = 1\,$Hz, and to a white noise level of 1 (see Table 3.1). For display purposes, the amplitude of $\hat{C}_{\rm a}({\rm freq} = 0)$ in intensity is normalized to the level of the polarization. The black dotted line shows the low frequency threshold $f_{\rm cut}$ of the power spectrum of the noise, and the red dotted line marks the Nyquist frequency of the baselines $f_{\rm Nyq,\,b} = 1/(2 \cdot t_{\rm b})$, with $t_{\rm b} = 2.5\,$s.

The diagonal of the covariance matrix of the baselines in the Fourier space is given by (Keihänen et al. 2010):

$$\hat{C}_{{\rm a},ii} = P_{\rm a}(f_i) = \frac{1}{t_{\rm b}} \sum_{m=-\infty}^{+\infty} P\left(f_i + \frac{m}{t_{\rm b}}\right) \frac{\sin^2(\pi(f_i t_{\rm b} + m))}{(\pi(f_i t_{\rm b} + m))^2} \tag{3.19}$$

where $P_{\rm a}$ is the spectrum of the baselines, $P(f_j)$ is the power spectral density of the correlated noise (Eq. 3.18) estimated at the discrete frequencies $f_j = j/(n_{\rm b} \cdot t_{\rm b})$, with $j = (0, ..., n_{\rm b}/2)$, where we remind that $t_{\rm b}$ is the time length of the baselines, $n_{\rm b}$ is the number of baselines in the TOD, and that the highest frequency in which we compute the power spectral density is the Nyquist frequency in the baselines space. We represent an example of the diagonal of $\hat{\mathbf{C}}_{\rm a}$ in Fig. 3.2.

3.3 QUIJOTE-MFI map-making

The PICASSO map-making code has been implemented to construct the maps of the MFI instrument of the QUIJOTE experiment. In this section, first we briefly summarize the MFI instrumental response, we describe the QUIJOTE-MFI pointing matrix (Sec. 3.3.2), we derive the analytical equations for the I, Q and U map (Sec. 3.3.3), and we set the noise priors (Sec. 3.2.2 and 3.3.4). Finally, in Sec. 3.3.6 we describe the template function fitting at the map-making level.

3.3.1 QUIJOTE-MFI instrumental response

The instrumental response of QUIJOTE-MFI is presented in Sec. 2.3.1. We briefly remind here the main equations and concepts, for which we adopt here a generalized notation: $\mathbf{V}_1$, $\mathbf{V}_2$, $\mathbf{V}_3$, $\mathbf{V}_4$ correspond, in order, to $\mathbf{V}_{\mathrm{X+Y}}$, $\mathbf{V}_{\mathrm{X-Y}}$, $\mathbf{V}_{\mathrm{X}}$, $\mathbf{V}_{\mathrm{Y}}$. The pair ($\mathbf{V}_1$, $\mathbf{V}_2$) corresponds to the "correlated" channels pair, while $(\mathbf{V}_3, \mathbf{V}_4)$ is the "uncorrelated" channels pair (see Sec. 2.3.1).

For a given horn and frequency band, each one of the four MFI channel provides a combination of intensity I and linear polarization, the Stokes parameters Q and U, as:

$$\mathbf{V}_i = \frac{1}{2}(I - (-1)^i(\mathbf{A}\sin(2\phi)Q + \mathbf{B}\cos(2\phi)U + \tag{3.20}$$

$$+ \mathbf{C}\cos(2\phi)Q + \mathbf{D}\sin(2\phi)U)) + \mathbf{n}_i \tag{3.21}$$

with $i = 1, 2, 3, 4$. A linear combination of these channels ($\mathbf{V}_1$ with $\mathbf{V}_2$ and $\mathbf{V}_3$ with $\mathbf{V}_4$) provides a measurement of the intensity and of the polarization of the sky signal. We can measure the intensity from the sum of pairs of channels, and the polarization from the difference. The polarization has the advantage that, when we make the difference of two pair channels (for example $\mathbf{V}_1 - \mathbf{V}_2$ or $\mathbf{V}_3 - \mathbf{V}_4$), we partially cancel the correlated component of the noise. This can be written as:

$$\mathbf{y}^{\mathrm{I}} = \mathbf{V}_j + \mathbf{V}_{j+1} = I + \mathbf{n}^{\mathrm{I}} \tag{3.22}$$

$$\mathbf{y}^{\mathrm{P}} = \mathbf{V}_j - \mathbf{V}_{j+1} = \mathbf{A}\sin(2\phi)Q + \mathbf{B}\cos(2\phi)U + \tag{3.23}$$

$$+ \mathbf{C}\cos(2\phi)Q + \mathbf{D}\sin(2\phi)U + \mathbf{n}^{\mathrm{P}}$$

with $j = 1, 3$, where $\mathbf{y}^{\mathrm{I}}$ and $\mathbf{y}^{\mathrm{P}}$ are the TODs of the MFI, respectively for intensity and polarization, and $\mathbf{n}^{\mathrm{I}}$ and $\mathbf{n}^{\mathrm{P}}$ represent the noise component in the TOD, for intensity and polarization (see Sec. 2.3.1 for full description of the parameters in the above equations).

In total, the MFI produces two sets of $\mathbf{y}^{\mathrm{I}}$ and $\mathbf{y}^{\mathrm{P}}$ TODs for each horn and frequency, respectively from ($\mathbf{V}_1$, $\mathbf{V}_2$) and $(\mathbf{V}_3, \mathbf{V}_4)$, allowing us to construct four independent maps of I, Q and U, at each frequency.

The data sampling rate of the MFI is 1 ms, but the raw data are subsequently binned with a sampling rate of $t_\mathrm{s} = 40$ ms. The variance of the data in one 40 ms bin, named σ_t^2 $(t = 1, ..., n_\mathrm{t})$, is representative of the white noise level of the binned samples, if we assume that at the scale of one time bin the $1/f$ drifts do not contribute to the noise variance. We define the weights of the binned TOD elements as:

$$w_t = \frac{1}{\sigma_t^2}. \tag{3.24}$$

More details can be found chapter 2 and in Génova-Santos et al. (in prep.), describing the pipeline of the QUIJOTE-MFI data.

3.3.2 QUIJOTE pointing matrix

Starting with the QUIJOTE-MFI instrumental response (Sec. 3.3.1), we can represent a QUIJOTE-MFI TOD with an intensity and polarization part, using the notation:

$$\mathbf{y} = \begin{pmatrix} \mathbf{y}^\mathrm{I} \\ \mathbf{y}^\mathrm{P} \end{pmatrix} \tag{3.25}$$

where the vectors $\mathbf{y}^\mathrm{I}$ and $\mathbf{y}^\mathrm{P}$ of size n_t are defined in Eq. 3.22 and 3.23. Similarly, the noise TOD can be written as:

$$\mathbf{n} = \begin{pmatrix} \mathbf{n}^\mathrm{I} \\ \mathbf{n}^\mathrm{P} \end{pmatrix} \tag{3.26}$$

where $\mathbf{n}^\mathrm{I}$ is the noise vector in the intensity TOD and $\mathbf{n}^\mathrm{P}$ is the noise vector in the polarization one, both with size n_t. The sky map, in this notation, can be written as:

$$\mathbf{m}_\mathrm{sky} = \begin{pmatrix} \mathbf{m}^\mathrm{I} \\ \mathbf{m}^\mathrm{P} \end{pmatrix} = \begin{pmatrix} I \\ \begin{pmatrix} Q \\ U \end{pmatrix} \end{pmatrix} \tag{3.27}$$

where we split again the intensity and polarization part. Let us define now the pointing matrix $\mathbf{P}$ for QUIJOTE-MFI, which is a $(2n_\mathrm{t} \times 3n_\mathrm{p})$ elements matrix:

$$\mathbf{P} = \begin{pmatrix} \mathbf{P}^\mathrm{I} & 0 \\ 0 & \mathbf{P}^\mathrm{P} \end{pmatrix} \tag{3.28}$$

with $\mathbf{P}^\mathrm{I}$ being a block matrix active on the intensity and $\mathbf{P}^\mathrm{P}$ the block matrix of polarization. Given the QUIJOTE-MFI instrumental response (Sec. 3.3.1), if pixel j was observed at time i, the $_{ij}$ block of the pointing matrix $\mathbf{P}$ is:

$$\mathbf{P}_{ij} = \begin{pmatrix} P^{\mathrm{I}}_{ij} & 0 \\ 0 & \mathbf{P}^{\mathrm{P}}_{ij} \end{pmatrix} = \tag{3.29}$$
$$= \begin{pmatrix} 1 & 0 & 0 \\ 0 & \Big(A_i \sin(2\phi_i) + C_j \cos(2\phi_i) & B_i \cos(2\phi_i) + D_i \sin(2\phi_i)\Big) \end{pmatrix}$$

and it vanishes otherwise. The P_{00} element interacts with the I map to project the intensity in the TOD, while the elements P_{11} and P_{12} combine the Q and U maps into the polarization TOD, according to the instrumental response equations. If we develop now the TOD equation starting from Eq. 3.1, and using the definitions in Eq. 3.25-3.29, we obtain the instrumental response of Eq. 3.22 and 3.23, showing the logic in the definition of the pointing matrix $\mathbf{P}$.

3.3.3 IQU analytical solution

The I, Q and U maps can be obtained by solving the map binning equation (Eq. 3.11), which applies the matrix $\mathbf{M}^{-1}\mathbf{P}^{T}\mathbf{C}_{\mathrm{w}}^{-1}$ to the data subtracted by the baselines $(\mathbf{y} - \mathbf{F} \cdot \mathbf{a}_{\mathrm{out}})$. Direct matrix multiplications are computationally expensive for any realistic datasets, which involve a massive number of data points. In order to avoid this problem, we derive an analytical solution for the maps of the three Stokes parameters, taking into account how the pointing matrix of QUIJOTE-MFI (Eq. 3.29) projects them into the TOD.

To get the intensity map we have to solve:

$$\frac{\partial X}{\partial I} = 0 \tag{3.30}$$

where X is given by Eq. 3.10, which gives:

$$I_i = \frac{\sum_{j\in i} \frac{1}{\sigma_j^2}\big(y_j - \sum_{k=1}^{n_{\mathrm{b}}} F_{jk} a_k\big)}{\sum_{j\in i} \frac{1}{\sigma_j^2}} \quad (i = 1, ..., n_{\mathrm{p}};\ j = 1, ..., n_{\mathrm{t}}) \tag{3.31}$$

with an associated variance:

$$\sigma_{I_i}^2 = \frac{1}{\sum_{j\in i} \frac{1}{\sigma_j^2}} \quad (i = 1, ..., n_{\mathrm{p}};\ j = 1, ..., n_{\mathrm{t}}) \tag{3.32}$$

In these expressions, i runs over the pixels and j runs over the data samples with coordinates lying within that pixel. This tells us that the intensity in pixel i is a weighted average of the baseline subtracted data from TODs that cross the pixel, where the weights are $1/\sigma_j^2$, as defined in Eq. 3.24.

Similarly, for the polarization, we have to solve:

$$\begin{cases} \frac{\partial X}{\partial Q} = 0 \\ \frac{\partial X}{\partial U} = 0 \end{cases} \tag{3.33}$$

that leads to the solutions:

$$Q_i = \frac{a_i f_i - d_i c_i}{g_i} \tag{3.34}$$

and

$$U_i = \frac{b_i d_i - c_i f_i}{g_i} \tag{3.35}$$

with:

$$a_i = \sum_{j\in i} \frac{\left(B_j \cos(2\phi_j) + D_j \sin(2\phi_j)\right)^2}{\sigma_j^2} \tag{3.36}$$

$$b_i = \sum_{j\in i} \frac{\left(C_j \cos(2\phi_j) + A_j \sin(2\phi_j)\right)^2}{\sigma_j^2} \tag{3.37}$$

$$c_i = \sum_{j\in i} \frac{\left(B_j \cos(2\phi_j) + D_j \sin(2\phi_j)\right)\left(C_j \cos(2\phi_j) + A_j \sin(2\phi_j)\right)}{\sigma_j^2} \tag{3.38}$$

$$d_i = \sum_{j\in i} \frac{\left(B_j \cos(2\phi_j) + D_j \sin(2\phi_j)\right)\left(y_j - \sum_{k=1}^{n_\mathrm{b}} F_{jk} a_k\right)}{\sigma_j^2} \tag{3.39}$$

$$f_i = \sum_{j\in i} \frac{\left(C_j \cos(2\phi_j) + A_j \sin(2\phi_j)\right)\left(y_j - \sum_{k=1}^{n_\mathrm{b}} F_{jk} a_k\right)}{\sigma_j^2} \tag{3.40}$$

$$g_i = a_i b_i - c_i^2 \tag{3.41}$$

where i runs over the pixels, and j over the data. The coefficients $\mathbf{A}$, $\mathbf{B}$, $\mathbf{C}$ and $\mathbf{D}$ drive the combination of Q and U with $\sin(2\boldsymbol{\phi})$ and $\cos(2\boldsymbol{\phi})$, as explained in Sec. 2.3.1. Finally, the variance maps of Q and U, and their covariance, can be computed as:

$$\left(\sigma_Q^2, \sigma_U^2, cov_{QU}\right)_i = \left(\frac{a_i}{g_i}, \frac{b_i}{g_i}, -\frac{c_i}{g_i}\right) \tag{3.42}$$

For each polarization TOD (Eq. 3.23), two observations of the same pixel with different values of parallactic angles are required to analytically solve for Q and U, hence to invert the polarization block of the $\mathbf{M}$ matrix. We compute a condition number (r_cond) map, which is defined as the ratio of the largest to smallest eigenvalue of the polarization block of the matrix $\mathbf{M}$ (Kurki-Suonio et al., 2009; Sutton et al., 2010), and quantifies the goodness of the inversion of **M**. It reads:

$$r_{\mathrm{cond},i} = \frac{(a_i+b_i)+\sqrt{(a_i-b_i)^2+4c_i^2}}{(a_i+b_i)-\sqrt{(a_i-b_i)^2+4c_i^2}}. \tag{3.43}$$

Small values of r_{cond} ($r_{\mathrm{cond}} \leq 3$) indicate a good reconstruction of the Stokes Q and U maps.

It is worth noticing that the expressions in Eq. 3.34 and 3.35 provide totally general solutions for the polarization maps, in the sense that they can be applied to any instrument that measures a combination of Q and U, modulated by sinusoidal functions. In the case of QUIJOTE-MFI, the detector response changed several times during the multiple observing campaigns, due to upgrades and modifications of the instrument. This changed the way of combining Q and U into the TOD during different periods of observation. However, with the methodology that we described in this section, we can use a time varying combination of **A**, **B**, **C** and **D** to account for modifications of the instrumental configuration, and integrate all the data in one single Q and U map.

Finally, we have to specify that, in this implementation, we do not account for the beam and pixel window function. Therefore, the result is a map of the sky convolved with the beam window function of the experiment, and the pixel window function.

3.3.4 Estimating the baselines with noise priors

In Sections 3.2.1 and 3.2.2 we derived the equations to estimate the baselines $\mathbf{a}_{\mathrm{out}}$, which imply the solution of Eq. 3.12 with a prior on the $1/f$ noise that is given by the covariance matrix of the baselines $\mathbf{C}_{\mathrm{a}}$ defined in Eq. 3.19. However, direct multiplication and inversion of matrices is too expensive computationally, and some approximations must be done here.

Equation 3.12 can be looked as the combination of three terms, which are:

i) $\mathbf{D} \cdot \mathbf{a}_{\mathrm{out}}$

ii) $\mathbf{C}_{\mathrm{a}}^{-1} \cdot \mathbf{a}_{\mathrm{out}}$

iii) $\mathbf{F}^T \mathbf{C}_{\mathrm{w}}^{-1} \mathbf{Z} \mathbf{y}$

The problem consists in finding the vector $\mathbf{a}_{\mathrm{out}}$ that satisfies (i)+(ii)=(iii). To determine the solution for $\mathbf{a}_{\mathrm{out}}$, we adopt the conjugate gradient method (CG), which allows us to move numerically in the baselines parameters space, towards the best $\mathbf{a}_{\mathrm{out}}$ that satisfies Eq. 3.12. With this aim, we have to compute (i) and

(ii) for the set of numerically proposed solutions for $\mathbf{a}_\mathrm{out}$, in order to find the best match with (iii) within a given relative accuracy (which is set to 10^{-5} in PICASSO).

Terms (i) and (iii) can be determined analytically once the map binning equations are fixed (with Eq. 3.31, 3.34, 3.35). However, for (ii) we have to make one additional approximation. It consists in computing the noise prior term $\mathbf{C}_\mathrm{a}^{-1}\cdot\mathbf{a}$ in the Fourier space, where $\hat{\boldsymbol{C}}_\mathrm{a}$ is diagonal (see Sec. 3.2.2). Thanks to that, the inverse $\hat{\boldsymbol{C}}_\mathrm{a}^{-1}$ is the straight scalar inversion of the diagonal elements of $\hat{\boldsymbol{C}}_\mathrm{a}$, and we can compute the product $\hat{C}_\mathbf{a}^{-1}\cdot\hat{\mathbf{a}}$ as the element by element multiplication of the diagonal of $\hat{\mathbf{C}}_\mathrm{a}^{-1}$ (Eq. 3.19) with the Fourier transform of the baseline vector $\hat{\mathbf{a}}$. Afterwards, we can project the result back to the real space, and obtain the multiplication $\mathbf{C}_\mathrm{a}^{-1}\cdot\mathbf{a}$, which gives (ii).

3.3.5 Destriping QUIJOTE-MFI data with priors

In the specific case of QUIJOTE-MFI, the TOD of intensity and polarization pass through the destriping step separately. In fact, as explained in Chapter 2 and in Section 3.3.1, the noise in the intensity and in the polarization TOD are different. An example of the result of destriping is shown in Fig. 3.1.

For the estimation of the baseline prior, we inject a theoretical power spectral density of the type of Eq. 3.18, whose parameters are representative of the average noise properties of QUIJOTE-MFI. The parameters that we use are listed in Table 3.1, and they are obtained as a result of the study of the typical noise properties of the MFI. The f_k and the γ are input parameters of the map-making code, while the white noise level σ is estimated from the data. $f_\mathrm{cut} = 1/30\,\mathrm{s}^{-1}$ is a fixed quantity specific for QUIJOTE, which corresponds to the frequency of one azimuth scan of 360 deg. The median of the data is subtracted in each scan.

In Fig. 3.2 (right panel) we show the diagonal of the baselines covariance matrix in Fourier space, as a function of the frequency, and for the aforementioned noise parameters. This plot represents the prior of the QUIJOTE-MFI noise, for intensity (orange line) and polarization (blue line).

3.3.6 Fitting a template function

We describe now the additional feature that we implemented in PICASSO: the fitting of a template function at the TOD level during the map-making step. With the same logic of cleaning the noise with baselines, we extend the destriper algorithm in order to fit the data with a specific template $\mathbf{f}$ in the time domain.

We can write the TOD as:

$$\mathbf{y}' = \mathbf{y} + A \cdot \mathbf{f} \tag{3.44}$$

where we added to the data $\mathbf{y}$ (Eq. 3.3) a template function $\mathbf{f}$ with amplitude A. The technique to determine the amplitude A can be seen as an extension of the usual destriping presented in Sec. 3.2.1, where we added the $A \cdot \mathbf{f}$ component in the model of the TOD, and where we apply the simplification of neglecting the noise priors term ($\mathbf{C}_\mathrm{a}^{-1} = 0$). We construct the chi-square of the problem, similarly to Eq. 3.10, as:

$$X = (\mathbf{y}' - \mathbf{P} \cdot \mathbf{m}_\mathrm{sky} - \mathbf{F} \cdot \mathbf{a} - A \cdot \mathbf{f})^T \mathbf{C}_\mathrm{w}^{-1} (\mathbf{y}' - \mathbf{P} \cdot \mathbf{m}_\mathrm{sky} - \mathbf{F} \cdot \mathbf{a} - A \cdot \mathbf{f}) + \mathrm{const} \tag{3.45}$$

The minimization with respect to A of $X(\mathbf{m} = \mathbf{m}_\mathrm{out}, \mathbf{a} = \mathbf{a}_\mathrm{out})$, with $\mathbf{m}_\mathrm{out}$ and $\mathbf{a}_\mathrm{out}$ given by Eq. 3.11 and 3.12 (with $\mathbf{C}_\mathrm{a}^{-1} = 0$), provides the equation for the fitted template amplitude:

$$A_\mathrm{out} = C^{-1} \mathbf{f}^T \mathbf{C}_\mathrm{w}^{-1} \mathbf{Q} \cdot \mathbf{y} \tag{3.46}$$

being C a scalar number, and $\mathbf{Q}$ a $(n_\mathrm{t} \times n_\mathrm{t})$ matrix defined as:

$$C = \mathbf{f}^T \mathbf{C}_\mathrm{w}^{-1} \mathbf{Q} \mathbf{f} \tag{3.47}$$

$$\mathbf{Q} = \mathbf{Z}(\mathbf{1} - \mathbf{F} \mathbf{D}^{-1} \mathbf{F}^T \mathbf{C}_\mathrm{w}^{-1} \mathbf{Z}) \tag{3.48}$$

Once A_out is determined, we construct the template subtracted TOD $\mathbf{y} = \mathbf{y}' - A_\mathrm{out} \cdot \mathbf{f}$, and proceed with the usual destriping presented in Sec. 3.2.1.

We can derive analytically the uncertainty on A_out with a Fisher-matrix approach, assuming Gaussianity of the posterior distribution and that the noise is uncorrelated. It is given by:

$$\sigma_{A_\mathrm{out}} = \frac{1}{\sqrt{C}} \tag{3.49}$$

However, with real data, the assumptions that we made to draw Eq. 3.49 are not necessarily valid, leading to an underestimated uncertainty on A_out. A more realistic estimate for σ_{A_out} can be obtained with Monte Carlo simulations, as we will show in Sec. 3.6.4.

The template fitting method presented in this section can be used for multiple purposes, and with any kind of templates. We show in Section 3.6.4 two different applications of particular interest for microwave wavelength data: we fit the CMB dipole and an atmospheric component to the intensity. In addition, this fitting procedure could be easily generalized to fit the templates in selected chunks of data instead of in the full data-set, or to fit several template functions simultaneously. For a number of n_A templates, $\mathbf{A}$ is a vector of n_A elements, $\mathbf{f}$ an $(n_\mathrm{t}, n_\mathrm{A})$ template matrix, and $\mathbf{C}$ an $(n_\mathrm{A}, n_\mathrm{A})$ matrix.

3.4 The PICASSO code

PICASSO is a code of 6519 lines, developed for the map-making of the QUIJOTE experiment. It is a Fortran-90 implementation, with parallelization based on OpenMP (Open Multiprocessing). PICASSO is built in two main blocks: the first for the data reading (see Sec. 3.4.1-3.4.4), and the second for the construction of the baseline-subtracted intensity and polarization maps (see Sec. 3.4.5, 3.4.6). While the data reading is specific for the MFI, the block of map-making is totally general, and is organized in three steps: (i) the TOD template fitting, if required by the user (Sec. 3.4.4), (ii) the destriping (Sec. 3.4.5), and (iii) the projection of the cleaned data into the map (Sec. 3.4.6). In step (iii) we also build a map of the number of hits in each pixel ($n_{\rm hits}$), the error map, and the $r_{\rm cond}$ map (as described in Sec. 3.3.3).

In order to characterize the effect of the noise in the maps with simulations, the code is implemented with a noise generator (see Sec. 3.4.2). This allows us to dynamically add a noise realisation to a simulated sky signal TOD, with a power spectral density of the type of Eq. 2.7. An example of the input interface of PICASSO is given in the appendix (Sec. A.1).

3.4.1 Data

The PICASSO map-making code is currently implemented for the QUIJOTE-MFI data, whose instrumental response is described in Sec. 2.3.1 and 3.3.1. In order to construct the TOD of a selected MFI detector and frequency, we import the data of the MFI channel pairs (e.g., Horn 3, 11 GHz, $\mathbf{V}_1$ and $\mathbf{V}_2$), and we combine them to construct the intensity or polarization TOD, as in the Eq. 3.22 and 3.23. The TODs of the full set of observations that we want to process are then stored in memory, together with their weights and pointing coordinates, in order to proceed with the construction of the map.

It should be noticed that the simultaneous combination of a large amount of observations in one single map is very important. Indeed, it is recommended to have a large number of crossings of the same pixel with different scan orientations on the sky, in order to perform a precise determination of the baselines, and also of the Q and U Stokes parameters which need to be sampled with different orientations of the angle $\boldsymbol{\phi}$. With this aim, the map-making code must be able to handle a large amount of data.

PICASSO has been used to construct the QUIJOTE-MFI wide-survey maps. The full data-set of the QUIJOTE wide-survey consist of $\sim 11,042\,$h of observation, amounting to $\sim 340\,$Gb. For the construction of one single map, we need to store in memory the data of one selected pair of channels, which corresponds to $\sim 340\,{\rm Gb}/16 \approx 21\,$Gb. One single core of a machine that is capable to store this amount of data in memory takes about 15-20 hours to produce a map.

3.4.2 Noise simulations

In PICASSO, we implemented the option to generate and add noise simulations to the TOD, simultaneously with the data reading. With this utility, from one single end-to-end simulation of the sky signal, we can produce a number of realizations of noisy maps, by adding the noise on-the-fly. To simulate the noise, we use a Fourier inversion technique of an input noise power spectral density of the type as in Eq. 2.7. The noise generator has been used to produce the simulations with which we tested the template function fitting, which are presented in Sec. 3.6.4.

3.4.3 Gaps in the data

The good data in a TOD are usually alternated with corrupted data, which can be affected by RFI, instrumental problems, bad weather, etc. Moreover, the MFI adopts a calibration technique that injects signal from a calibration diode superimposed on top of the sky signal (Sec. 2.4.2.2), for one second every thirty seconds, and these calibration signals cannot be integrated in the map.

To deal with the interruptions, we adopt the strategy of down-weighting the flagged data, as in Planck Collaboration et al. (2016g), by assigning zero weights to the bad data ($w_i = \sigma_i^{-2} = 0$), which is equivalent to setting an infinite variance.

3.4.4 Template functions

As we mentioned in Section 3.3.6, we implemented an algorithm to fit for a template function at the TOD level, during the map-making step. In order to apply this technique, we need to define a TOD of the template. The code has the capability to generate a template from a totally general map that is delivered by the user, by projecting this map into a template with TOD format. In addition, two special templates are internally generated by PICASSO: a template of the atmosphere (see Sec. 3.4.4.1) and of the CMB dipole (see Sec. 3.4.4.2). The results of the fit of these two templates are reported in Sec. 3.6.4.

The template fitting is applied to the TOD before destriping, independently in intensity and polarization.[3] Once the amplitude of the template A_{out} is estimated, we subtract the $A_{\mathrm{out}}\mathbf{f}$ component from the data (see Eq. 3.44), which

---

[3] For example, if the template fitting is applied to the intensity, there is no effect in the polarization maps, and the other way around.

then passes through the destriping step, and is finally binned into the I, Q and U maps.

We now describe the two templates that are internally implemented into the code: a stable, plane-parallel atmosphere, and the CMB solar plus orbital dipole. However, PICASSO can be extended with other templates of typical contaminants of ground-based observations, like ground pickup of RFI contamination.

3.4.4.1 Atmosphere

An imperfect alignment of the azimuth axis of the telescope mount with the zenith direction can introduce a modulated component of atmospheric emission into the data. Indeed, when the telescope performs azimuth scans at a fixed elevation (as it is the case for QUIJOTE - see Sec. 3.5.1), if the azimuth axis is not perfectly aligned to the zenith, the effective (true) elevation of the scan is not perfectly constant, and the line of sight crosses varying air masses. This leads to a measurement of modulated atmospheric emission given by:

$$\mathbf{f}_{\rm atm} = \frac{T_{\rm atm}}{\sin(\mathbf{el})} \tag{3.50}$$

where **el** is a TOD of the real elevation of the observation, and $T_{\rm atm}$, which is the amplitude of the modulation, is the antenna temperature of the atmosphere at the Zenith[4], at a determined frequency. Here we assume a static, plane-parallel atmosphere, which is a sufficiently good approximation for our purposes[5].

In QUIJOTE the degree of misalignment of the azimuth axis is less than 0.05°, which for a typical precipitable water vapour (PWV; see Sec. 2.5) at the Teide Observatory of 3 mm, corresponding to a temperature amplitude of $T_{\rm atm} = 1.8\,$K at 11 GHz (Pardo et al., 2001), produces temperature fluctuations of about 2 mK, at an elevation of 60°.

In the PICASSO code, we generate the template of the atmosphere with the function:

$$\mathbf{f} = \frac{1}{\sin(\mathbf{el})} \tag{3.51}$$

using the true value of the elevation **el** as derived from the QUIJOTE pointing model, and we recover the amplitude $A = T_{\rm atm}$, which is the average temper-

---

[4] $T_{\rm atm} = T_{\rm atm,0} \cdot (1 - e^{-\tau}) \sim T_{\rm atm,0}\tau$, where $T_{\rm atm,0}$ is the temperature of the atmosphere, and τ is the atmospheric opacity.

[5] Taking as a reference the exact equation of atmospheric emission given in Kasten & Young (1989), it can be noticed that the correction to the approximated Eq. 3.50, at $el = 30°$, is just 0.3%, and is smaller at higher elevations.

ature of the atmosphere at the zenith during the observations (normalized by units of Kelvin).

3.4.4.2 CMB dipole

The Sun's motion with respect to the CMB reference frame produces, via Doppler effect, a solar dipole anisotropy of the CMB radiation, with an amplitude of $\sim 3\,\mathrm{mK}$. In addition, the Earth's motion around the Sun introduces an extra dipole anisotropy, the so-called orbital dipole, with a smaller amplitude than the solar dipole, of $\sim 271\,\mu\mathrm{K}$. In addition, the dipole due to the rotation of the Earth, at the latitude of Tenerife, is very small ($\sim 3\ \mu$K), therefore it is ignored in this analysis.

We call $\mathbf{v} = \mathbf{v}_\mathrm{s} + \mathbf{v}_\mathrm{e}$ the combination of the velocity vector of the Sun $\mathbf{v}_\mathrm{s}$ with respect to the CMB reference frame, and the velocity of the Earth $\mathbf{v}_\mathrm{e}$ with respect to the Sun, in order to model jointly the solar and orbital CMB dipole. For the solar dipole velocity we used the HFI 2018 dipole determination from Planck Collaboration et al. (2020d) $\mathbf{v}_\mathrm{s} = (369.8160 \pm 0.0010)\,\mathrm{kms}^{-1}$, combined with the CMB temperature $T_\mathrm{CMB} = 2.72548\,\mathrm{K}$ from Fixsen (2009) to convert temperature to velocity (back and forth), while the Earth's velocity $\mathbf{v}_\mathrm{e}$ is predicted from the JPL Horizons ephemeris[6]. In this framework, the CMB solar plus orbital dipole can be precisely predicted in time, for any direction of observation, and we can build a time ordered template of the predicted total CMB dipole (Eq. 3.52).

To first order, where the ratio between the module of the velocity $v = |\mathbf{v}_\mathrm{s} + \mathbf{v}_\mathrm{e}|$ and the speed of light c is small ($\beta = v/c \approx 10^{-3} \ll 1$), the CMB dipole is given by (Peebles & Wilkinson 1968):

$$\mathbf{f}_\mathrm{dip} \approx T_\mathrm{CMB}\boldsymbol{\beta}\cos(\boldsymbol{\theta}') \tag{3.52}$$

where $T_\mathrm{CMB}\boldsymbol{\beta}$ is the instantaneous amplitude of the CMB solar plus orbital dipole, and $\boldsymbol{\theta}'$ is the angle between the velocity of the observer and the direction of observation, as a function of time. Eq. 3.52 can be used as a template function of the CMB dipole in the time ordered domain. A fit of $\mathbf{f} = \mathbf{f}_\mathrm{dip}$ can be done during the map-making procedure, by applying the technique that we described in Section 3.3.6. The resulting amplitude is expected to be $A_\mathrm{out} = 1$.

3.4.5 Destriping

Destriping consists in solving Eq. 3.12, whose solution, the baseline vector $\mathbf{a}_\mathrm{out}$, provides a model of the $1/f$ noise to be subtracted from the TOD (see Sec. 3.2

---

[6] https://ssd.jpl.nasa.gov/horizons.cgi

and 3.3.4). In PICASSO, we implemented this step with three options, where we allow the user to select which type of priors on the baselines he/she wants to apply. The options are:

1. No prior on the baselines (i.e., $\mathbf{C}_{\mathrm{a}} = 0$).

2. Approximation with diagonal baselines covariance matrix, $(C_{\mathrm{a}})_{ij} = \delta_{ij} \left\langle \sigma_i \sigma_j \right\rangle / n_{\mathrm{b}}$ where σ_i^2 is the rms of the noise within the baseline i.

3. Full prior of the baselines, where $\mathbf{C}_{\mathrm{a}}$ is given by Eq. 3.19, and is applied with Fourier techniques, as described in Section 3.3.4.

Option (i) was used to construct the maps presented in Génova-Santos et al. (2017) and Poidevin et al. (2019), option (ii) has only been used during the testing and validation phase of the code, while (iii) is the default option to construct the wide-survey maps (Rubiño-Martín et al. in prep). In option (iii), we assume stationary $1/f$ noise properties across the full data-set, with a $1/f$ power spectral density given by Eq. 3.18. The sampling frequency f_{s} and the white noise level σ are estimated from the data, while the knee frequency f_{k} and γ are selected as input values by the user, and are assumed to be stationary.

However, in the real QUIJOTE data, as in any other ground-based experiment, we do not have perfectly stable $1/f$ across all the observations, especially in intensity (Rubiño-Martín et al. in prep). In order to test the effect of a prior that is slightly different from the actual noise in the data, we produced intensity maps with a knee frequency prior of $f_{\mathrm{k}} = 40\,\mathrm{Hz}$ (see Tab. 3.1 for a summary of the noise parameters), which is different from the actual value that was adopted to generate the simulations ($f_{\mathrm{k}} = 20\,\mathrm{Hz}$). The realistic noise simulations that are presented here (Sec. 3.5), as well as the real wide-survey maps, are constructed using option (iii), with the prior parameters in Tab. 3.1.

A detailed study for the selection of the baseline length was performed by Pelaez Santos (2019), with a work based on QUIJOTE-MFI raster scans observations. They showed that $t_{\mathrm{b}} = 2.5\,\mathrm{s}$ provide optimal noise performance, therefore we select this baseline length also for the construction of wide-survey maps. Below, we test that this choice also produces (nearly) optimal results for the wide-survey observing mode. However, in general, t_{b} is an arbitrary parameter that can be selected by the user when running PICASSO. The calculation of the baselines is performed using the full data-set, in order to gain as much information as possible from different crossing of the same pixel.

3.4.6 Projecting into the I, Q, and U maps

The projection of the baselines subtracted TOD ($\mathbf{y} - \mathbf{F} \cdot \mathbf{a}_{\rm out}$) into a map is made by solving Eq. 3.11, as described in Section 3.3.3. The pixel size can be selected by the user, who is asked for the desired resolution in terms of the $N_{\rm side}$ HEALPix parameter (Górski et al., 2005). We used $N_{\rm side} = 512$ to construct the QUIJOTE-MFI maps, which corresponds to an angular resolution of ~ 6.9 arcmin.

In PICASSO, the map binning step is done separately for intensity and polarization: we construct the maps by applying the analytical solution formulated, for the intensity, in Eq. 3.31, and for the Q and U Stokes parameters, in Eq. 3.34 and 3.35. The variance maps of I, Q, and U are constructed, respectively, with Eq. 3.32 and 3.42. Finally, in the process of constructing the maps, we sum the number of data samples that are contained in ("hit") each pixel, and we produce the so-called $n_{\rm hit}$ map. In the case of polarization, the Q and U maps are stored only in pixels where the number of hits is greater or equal 3 ($n_{\rm hit} \geq 3$), in order to ensure the minimal number of crossings of the pixel necessary to determine the Q and U parameters. In the case of polarization, we also build the $r_{\rm cond}$ map formulated in Eq. 3.43, which quantifies the goodness of the Q and U reconstruction, given the variety of orientations of the angle $\boldsymbol{\phi}$ in each pixel. Pixels with $r_{\rm cond} > 3$ are excluded from the Q and U maps.

Since the MFI provides two TODs for each horn and frequency of the instrument (from the pairs of channels ($\mathbf{V}_1 \pm \mathbf{V}_2$) and ($\mathbf{V}_3 \pm \mathbf{V}_4$), where the sum is for the intensity and the difference for polarization, as explained in Sec. 3.3.1), a set of 16 I, Q and U maps is produced, with separate runs of the map-making code for intensity and polarization. The two maps from the same horn and frequency (e.g., Horn 3, 11 GHz, from ($\mathbf{V}_1 \pm \mathbf{V}_2$) and ($\mathbf{V}_3 \pm \mathbf{V}_4$)) are combined a posteriori with a weighted average (as in Eq. 3.53 and 3.54), giving as a final result a set of 8 I, Q and U maps, one for each of the two frequencies of the four horns.

3.5 Simulations

The PICASSO map-making code is tested and validated with simulations. Although the code is general and can be used to map any kind of observation (wide-survey or raster scans), in this work we used a realistic simulation of the QUIJOTE-MFI wide-survey (Rubiño-Martín et al. in prep). The simulated TODs contain the sky signal following the equations of the instrumental response of the MFI (Eq. 3.22 and 3.23), and three configurations of noise: no-noise, white only noise, and realistic white plus correlated $1/f$ noise (hereafter, no-noise, white and white plus $1/f$, respectively, see details in Sec. 3.5.3). Analogous to what is done to the real data, every 30 s we subtracted a median value from the TOD, with the goal of filtering to first order the $1/f$ noise in one azimuth scan of 360 deg.

In the next sub-sections we describe the scanning strategy (Sec. 3.5.1), the sky signal (Sec. 3.5.2), and the noise (Sec. 3.5.3) that are used for the simulations.

3.5.1 Wide survey scanning strategy

The scanning strategy of the QUIJOTE-MFI wide-survey observations consists of continuous spins of the telescope at a constant elevation, with long term elevation re-pointing, at $el = [30, 35, 40, 50, 60, 65, 70, 75, 80]$ deg. The scanning speed is 12 deg/s, and one azimuth scan of 360 deg is completed every 30 s. After 24 h of observation we cover the full sky observable from the Teide Observatory (Tenerife, Spain, 2400 m a.s.l.), with a coverage in declination that depends on the elevation of the observation.

The effective time of observation is $\sim 11,042$ h, across four different instrumental setups (or periods). Elevation $el = 30°$ gives the widest declination coverage, which is $\delta \in [-35, 90]$ deg, corresponding to a sky coverage of 78%. A complete description of the data-set can be found in Rubiño-Martín et al. (in prep.).

3.5.2 Simulated sky signal

We simulated the sky signal by projecting the intensity and polarization maps of a simulated sky into the TODs, according to the MFI instrumental response equations described in Sec. 3.3.1. The sky signal simulated maps that we use in this work were developed in the context of the RADIOFOREGROUNDS project[7].

The sky simulations at the four MFI frequencies contain foregrounds from the Planck FFP10 sky model (Planck Collaboration et al. 2020f,d), a CMB realization from the Planck 2015 best-fit cosmology (Planck Collaboration et al. 2016e) with tensor-to-scalar ratio $r = 0$, and a realistic CMB solar plus orbital dipole (from Eq. 3.52). The simulated sky input maps are shown in Fig. 3.3 (without the CMB dipole component). Finally, we added a template of the atmosphere (from Eq. 3.50, with $T_{\rm atm} = 1\,$K), only when we wanted to test the fitting of this component. The simulations are convolved to the native angular resolution of the experiment, approximated with a Gaussian beam with full

---

[7] http://www.radioforegrounds.eu/

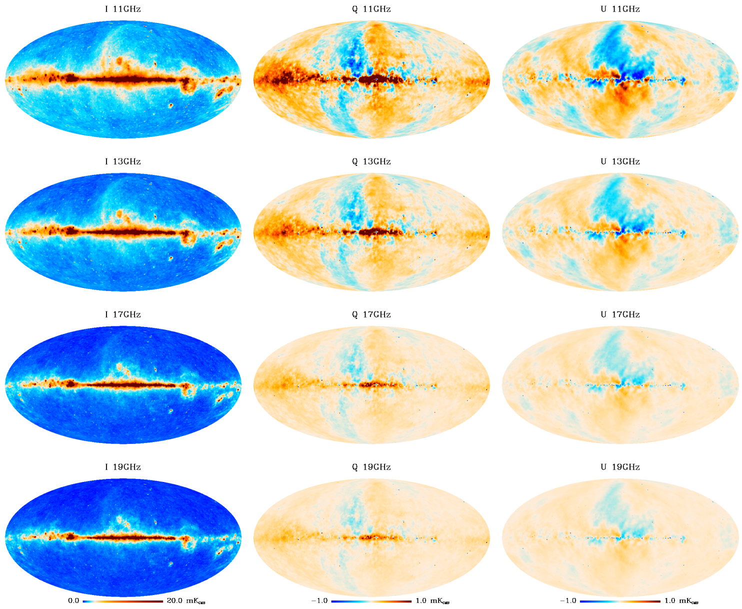

FIGURE 3.3— Simulated sky signal I-Q-U full sky maps, in Galactic coordinates. The rows show, from top to bottom, the maps at 11, 13, 17 and 19 GHz. The columns show, from left to right, the maps of Stokes I, Q, and U parameters.

width half maximum (FWHM) of 0.85 deg at 11 and 13 GHz, and 0.63 deg at 17 and 19 GHz.

These maps are used as a reference sky to produce synthetic TOD vectors. In this step, the pointing coordinates, the weights and the flags are extracted from the TODs of the corresponding real wide-survey observations.

3.5.3 Noise

The noise is added to the simulated input sky at the TOD level. In the white only case, the noise is produced as a random Gaussian realization with a variance given by the inverse weight of the data samples (Eq. 3.24). In this way, the noise mimics the actual noise variance structure in the real data. In the case of realistic white plus $1/f$ noise, we use inverse Fourier techniques based on a power spectral density given by Eq. 2.7, computed with the realistic noise parameters of the MFI reported in Table 3.1. The $1/f$ parameters are assumed to be stable in time, and they are the same for all the MFI channels.

3.6 Results

The main result of this work is the validation and characterization of the PICASSO map-making code, at the map and angular power spectrum level, by using realistic simulations of the QUIJOTE-MFI wide-survey described in Sec. 3.6.1. Fig. 3.4 shows the reconstructed I, Q and U maps obtained with PICASSO at the four MFI frequencies, for the case of realistic noise levels (including both white noise and $1/f$ noise).

For the sake of definiteness, we focus our discussion on the two extreme frequencies of the MFI: at 11 GHz, where the sky signal is brighter, and at 19 GHz, where the sky signal is fainter. A detailed study of two of these maps, including a comparison with the input data and the residual levels of the reconstruction, is shown in Fig. 3.5 and 3.6. Sec. 3.6.1 contains a characterization of these residual maps, including real space statistics. The angular power spectra of these maps, together with an analysis of the signal error within the mask in Fig. 3.8, are shown in Sec. 3.6.2 (Fig. 3.9 and 3.10), while a detailed characterization of the transfer function is shown in Sec. 3.6.3 (Fig. 3.11). Afterwards, in Sec. 3.6.4 we present the validation of the fitting of a template function implemented in PICASSO (as described Sec. 3.3.6 and 3.4.4).

3.6.1 Reconstructed maps and real space statistics

We have tested our code using the realistic simulations of the QUIJOTE-MFI wide-survey described in Sec. 3.5, which include sky signal, CMB dipole, CMB anisotropies and noise. As described in Sec. 3.4.6, from the four channels ($\mathbf{V}_1$, $\mathbf{V}_2$, $\mathbf{V}_3$, $\mathbf{V}_4$) of a determined horn and frequency of the MFI, PICASSO produces two maps: m_1 for the pair of channels ($\mathbf{V}_1$, $\mathbf{V}_2$), and m_2 for ($\mathbf{V}_3$, $\mathbf{V}_4$). We call w_1 and w_2 the corresponding weight maps, which are obtained as the inverse of the variance maps defined in Sec. 3.3.3 (Eq. 3.32 and 3.42). The two maps and weights are constructed with two independent runs of the code, and are combined a posteriori with a weighted average:

$$m = \frac{m_1 w_1 + m_2 w_2}{w_1 + w_2} \tag{3.53}$$

The weight map of the combination is given by:

$$w = \frac{(w_1 + w_2)^2}{w_1 + w_2 + 2\rho(w_1 w_2)^{1/2}} \tag{3.54}$$

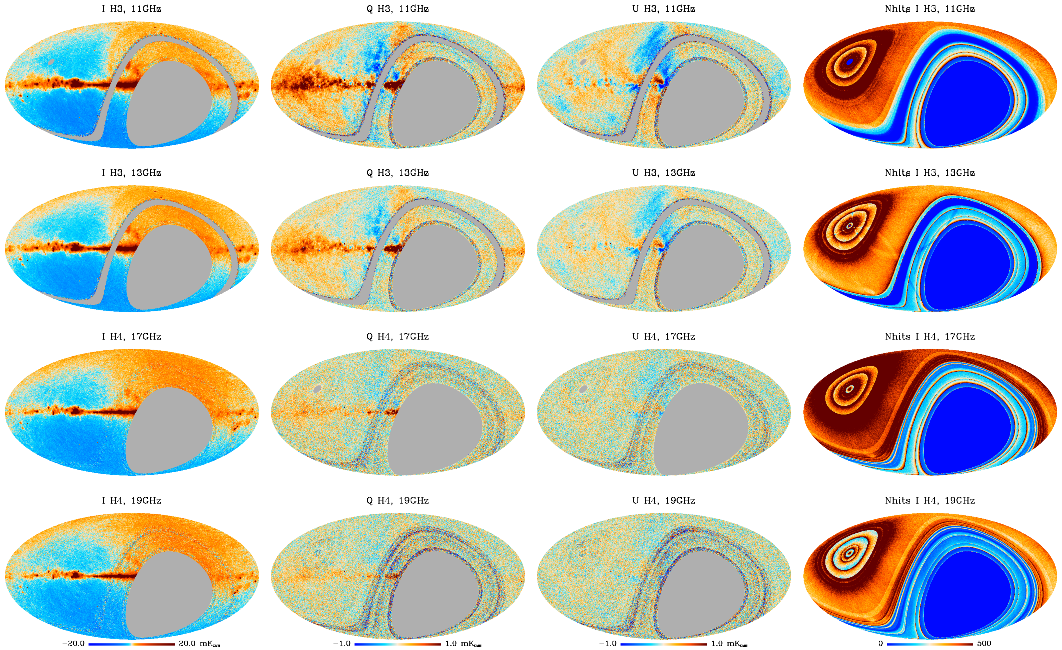

FIGURE 3.4— Reconstructed I-Q-U maps of the simulated microwave sky, in Galactic coordinates, as they would be observed by QUIJOTE-MFI across the full sky area accessible from the Teide observatory, after processing the corresponding TOD with PICASSO. The rows show, from top to bottom, the maps at 11, 13, 17 and 19 GHz, of horn number 3 for the low frequencies, and of horn number 4 for the high frequencies. The columns show, from left to right, the maps of I, Q, U, and the number of hits of the intensity at the correspondent frequency. The $N_{\rm hits}$ maps vary with frequency since the flagging also changes with frequency (see chapter 4, Sec.4.1.6). In intensity, the signal includes the CMB dipole. For display purposes, the maps are degraded to $N_{\rm side} = 256$ (pixel size $\sim$ 13.7 arcmin).

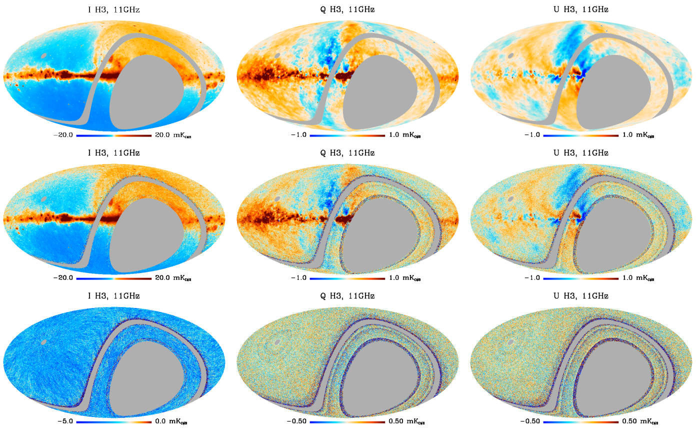

FIGURE 3.5— Stokes I, Q, and U sky maps at 11 GHz, from horn number 3. We show in the top row the input sky with CMB dipole included, in the central row the reconstructed maps obtained with PICASSO from the TODs containing realistic white plus $1/f$ noise, and in the bottom row the residual noise maps, obtained as the difference between the two maps above. For display purposes, the maps are degraded to $N_{\rm side} = 256$.

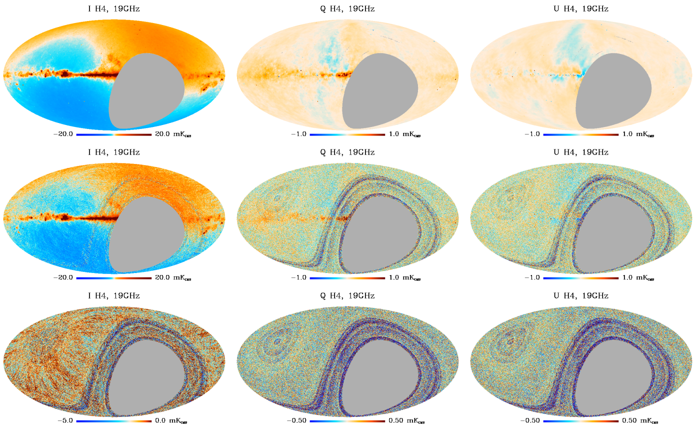

FIGURE 3.6— Same as Figure 3.5, but for the maps at 19 GHz, from horn number 4.

where ρ is the correlation between the two combined channel maps. In this case we use $\rho = 0$, therefore the formula reduces simply to $w = w_1 + w_2$. In summary, from each horn of the MFI and for each Stokes parameter, we obtain two combined frequency maps, one for each of the two frequencies of a selected horn. For example, from horn number 3 we construct one combined map at 11 GHz and one at 13 GHz, and from horn number 4 we obtain one combined map at 17 GHz and one at 19 GHz.

We construct the maps with PICASSO using $N_{\rm side} = 512$, in order to have an appropriate sampling of the MFI beams, and a baseline length of 2.5 s (Pelaez Santos, 2019). The maps of I, Q, and U, and the number of hits ($n_{\rm hit}$) of 40 ms time samples in pixels of $N_{\rm side} = 512$, are shown in Fig. 3.4, for the case of white plus $1/f$ noise. We show the maps obtained from horn number 3 at 11 and 13 GHz, and from horn number 4 at 17 and 19 GHz. In this figure, we can see how simulated I-Q-U maps of the microwave sky, in Galactic coordinates, would be observed by QUIJOTE-MFI at 11, 13, 17 and 19 GHz, across the full sky area accessible from the Teide observatory, after processing the corresponding TOD with PICASSO.

A quick look at the maps shows the bright emission of the CMB dipole in intensity. As expected, the CMB dipole has the same amplitude at each frequency, contrarily to the synchrotron emission of the galaxy, which decreases with frequency. This reconstruction of the CMB dipole is encouraging, as indicates that PICASSO reconstructs with good precision the sky signal even at large angular scales. We recover 100 % of the injected CMB orbital plus solar dipole, with a precision of the order of 0.1 %, at all frequencies, and independently for all the noise cases (either no-noise, white, or white plus $1/f$ noise).

The grey regions in the maps correspond to the sky area that is not observed by QUIJOTE, including a small circle[8] around the North Celestial Pole (NCP), the southern sky at low declination, and an intermediate band close to Dec.= 0 deg, which must be flagged due to interference by geostationary satellites at QUIJOTE frequencies, especially at 11 and 13 GHz (see details in Rubiño-Martin et al. in prep, in Sec. 2.4.5, and in Sec. 4.1.5).

Some of the maps show evident ring structures, located around the NCP, and at low declination, in the band that crosses the Galactic center. The rings correspond to discontinuities in the sky coverage and integration time (see $n_{\rm hit}$ map in the last column of Fig. 3.4), and, consequently, to variations of the

---

[8] The size of the NCP blank circle changes with frequencies because the position of each horn in the focal is different, therefore they observe at slightly different effective elevations, corresponding to a slightly different declination coverage. In addition, a different flagging is applied at different frequencies, providing a declination coverage that is proper to each of them.

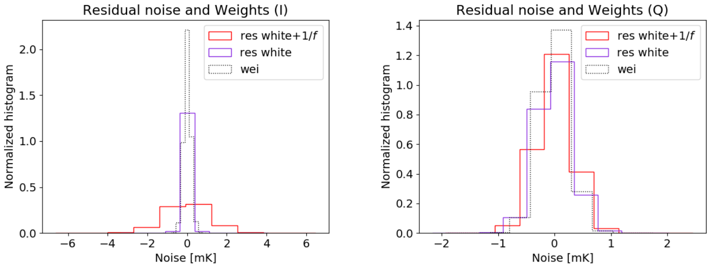

FIGURE 3.7— Histogram of the noise distribution in intensity (I, left) and polarization (Q, right), obtained from the residual maps, and compared with the white noise expectation obtained from the weight maps (black dotted line). We show in purple the results obtained with simulation at 11 GHz containing white noise only, and in red the case where $1/f$ noise is also present (corresponding to the maps shown in Fig. 3.5).

noise properties across the map. This is a direct consequence of the scanning strategy. Indeed, the rings delimit the declination bands that are observed at different elevations. The very low declination regions can only be accessed with low elevation scans, and therefore the amount of data there is much smaller than in the center of the map, and the noise is larger. The highest declinations are also only accessible by low elevation scans, however in this case there is a projection effect that compensates for that, producing more hits approaching the North Celestial Pole.

We present here a more detailed analysis of the maps at 11 GHz (in Fig. 3.5) and 19 GHz (in Fig. 3.6). Figs. 3.5 and 3.6 allow a visual comparison to be made between the input sky signal of the simulations and the maps constructed with PICASSO (shown in Fig. 3.4). In the upper row of the figures, we show the I, Q and U input sky maps with the CMB dipole included, in the central row the maps reconstructed with PICASSO from simulations with white plus $1/f$ noise, and in the bottom row the difference between the recovered map and the input sky, being them residual noise maps. We can notice from the difference maps that there are no obvious sky signal residuals, either at small or large angular scales. This demonstrates that PICASSO correctly reconstructs the injected sky signal at both frequencies. A more quantitative analysis at the angular power spectrum level is presented in Sec. 3.6.2 and 3.6.3.

However, we note that the residual noise maps of the intensity present $1/f$ correlated noise structures that PICASSO was not able to remove perfectly. On the other hand, the residual noise in polarization is apparently consistent with white noise. This can be quantified using the histograms shown in Fig. 3.7, where we compare the actual distribution of the noise obtained from the residual maps with the expected white noise level. The latter can be computed directly from the weight maps (or estimated from a Gaussian realization with variance given by the inverse of the weight map), and for this reason it is labelled as "wei" in the figure. In the histograms we can see that the distribution of the noise in intensity when $1/f$ is included (upper panel, red thick line) is wider than the expected white noise levels given by the weights (upper panel, black dotted line), while the noise in polarization (lower panel, red thick line) is statistically consistent with the expected white noise reference (lower panel, black dotted line). In other words, in polarization, PICASSO is performing optimally, in the sense that it recovers the expected white noise level. However, in intensity, there is a measurable correlated noise residual in the map-making solution, as expected for the QUIJOTE-MFI data.

This result can be easily explained in terms of the actual correlated noise injected in the TODs as compared with the baseline length that we used. We estimated the baselines for both the intensity and polarization data using a length $t_\mathrm{b} = 2.5\,\mathrm{s}$, which corresponds to a frequency of the baselines $f_\mathrm{b} = 1/2.5\,\mathrm{Hz} = 0.4\,\mathrm{Hz}$. The knee frequency of the injected noise in intensity is $f_\mathrm{k} = 20\,\mathrm{Hz}$, which is much higher than the frequency of the baselines. In the polarization data, instead, we have a $1/f$ noise component with a knee frequency $f_\mathrm{k} = 0.3\,\mathrm{Hz}$, which is comparable but lower than f_b. A shorter baseline length could be an option to improve the noise cleaning of the intensity maps, but short baselines also imply a poorer reconstruction of the large angular scales, in particular if the prior does not perfectly match the actual noise (see Kurki-Suonio et al., 2009 for a study with $\mathbf{C}_\mathrm{a}^{-1} = 0$). We tested, for example, a baseline length $t_\mathrm{b} = 1\,\mathrm{s}$, and we obtained a more noisy reconstruction of the large angular scales signal, as compared with $t_\mathrm{b} = 2.5\,\mathrm{s}$. This is in agreement with Pelaez Santos (2019), where they estimate the optimal baseline length to be $t_\mathrm{b} = 2.5\,\mathrm{s}$ for raster scans. Moreover, the scan speed and the beam size set a lower limit for the baseline length, which is given by some multiple of $t_\mathrm{B} = \mathrm{FWHM}/(v\cos(el))$, the time that the telescope takes to scan one beam FWHM, with azimuthal scan speed v, and at the constant elevation el. Typical values for QUIJOTE are $v = 12\,\mathrm{deg/s}$, $el = 60\,\mathrm{deg}$ and FWHM=1 deg, which gives $t_\mathrm{B} = 0.17\,\mathrm{s}$. This means that, in order to preserve structures with sizes of few beams (e.g., 5–10 FWHMs) and not to confuse them with features associated with noise in the maps, the baseline length should be longer than 5–$10t_\mathrm{B}$, i.e. 0.8–1.7 s. This highlights the importance of scanning the sky as fast as possible, in order to be able to efficiently suppress the $1/f$ noise.

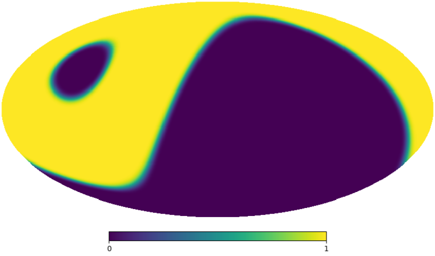

FIGURE 3.8— Mask adopted for angular power spectra estimations.

3.6.2 Validation with angular power spectra

We analyze here the angular power spectra of the simulated QUIJOTE-MFI wide-survey. The C_ℓ's are computed with the publicly available XPOL[9] code, which is based on a pseudo-C_ℓ estimator, and accounts for incomplete sky coverage (Tristram et al. 2005).

Pseudo-C_ℓ is a very useful tool for computing the angular power spectra of maps with incomplete sky coverage, and with a large number of pixels. However, it is potentially affected by residual mode coupling at low multipoles, particularly if the map contains a dipole. Therefore, we need to carefully remove the CMB dipole from our simulations before computing the power spectrum. For the analysis in intensity, we fit and remove a dipole component from the simulated map subtracted from the foregrounds and the CMB anisotropies, and we use the dipole subtracted residual to characterize the noise.

For this work, we use a mask of the high signal-to-noise QUIJOTE sky area, which encompasses the declination range $\delta \in [6°, 70°]$, as shown in Fig. 3.8. We applied to the mask a five degrees apodization with a cosine function, with the apodization routine of the NAMASTER[10] publicly available code (Alonso et al. 2019). Apodization is needed here in order to avoid border effects for the computation of angular power spectra with a incomplete sky coverage.

The angular power spectra of the two selected frequency maps (11 GHz of horn 3 and 19 GHz of horn 4) are shown in Fig. 3.9. The plots show, for the two frequencies (11 GHz on the left and 19 GHz on the right), the TT, EE and BB auto power spectra of the maps (respectively in the top, central and bottom position), where EE and BB represent the auto-spectra of the commonly called polarization E and B-modes. The different lines in these plots represent the C_ℓ of the map recovered with PICASSO (thick lines), of the input sky map

---

[9] https://gitlab.in2p3.fr/tristram/Xpol

[10] https://github.com/LSSTDESC/NaMaster

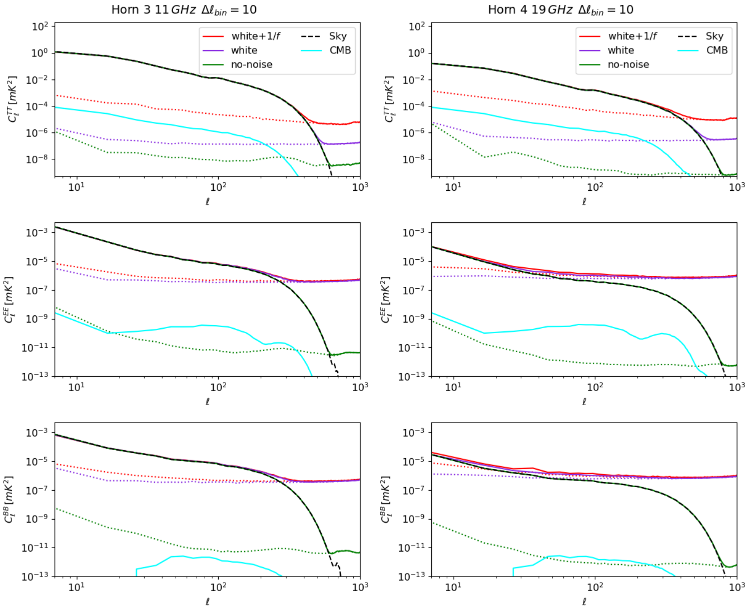

FIGURE 3.9— Angular power spectra of the two selected frequency maps, 11 GHz (left) and 19 GHz (right), from horns 3 and 4 respectively. Different colors correspond to the maps simulated with different noise properties: in red the case with white plus $1/f$ noise, in purple the simulation with white noise only, and in green the simulation without noise. The light blue line shows the power spectrum of the CMB anisotropies, convolved with the beam window function of the MFI at the correspondent frequency. We show, for the two frequencies, the TT, EE and BB auto power spectra of the maps, respectively in the top, central and bottom position. The different lines represent the C_ℓ of the recovered simulated map (thick lines), of the input sky map (dashed black line) and of the residual noise map (map minus sky; dotted lines). The C_ℓ's are not corrected for the beam window function, while the pixel window function correction is applied.

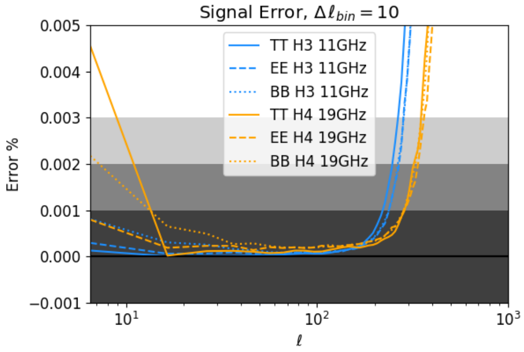

FIGURE 3.10— Percentage signal error of TT (thick line), EE (dashed line), and BB (dotted line), at 11 GHz (blue) and 19 GHz (orange). It is computed as the percentage ratio between the angular power spectrum of the signal error map and of the recovered map, in the case with no-noise. The shaded areas mark the deviation of the signal error from zero by (0.001, 0.002, 0.003)% .

(dashed black line) and of the residual noise map (dotted lines). Finally, the colors represent the noise properties of different simulations: in red we represent the simulation with white plus $1/f$ noise, in purple with only white noise, and in green the result from a simulation without noise. For comparison purposes, the light blue line depicts the power spectrum of the simulated CMB map, convolved with the beam window of the MFI at 11 and 19 GHz, and computed within the same sky mask (Fig. 3.8). In this particular simulation, the CMB BB signal is entirely due to lensing (no tensor modes). The C_ℓ's are not corrected for the beam window function, while the correction for the pixel window function is applied.

Let us now describe the results represented in the power spectra of Fig. 3.9. First, we analyze the angular power spectrum of the signal error, which is the map of the residual (map minus input sky) when no noise is added into the simulated data-set (Ashdown et al. 2007). The signal error is represented by the green dotted lines in Fig. 3.9, and it quantifies the error introduced by the map-making when reconstructing the sky signal, despite the absence of noise. We can notice that the TT, EE and BB signal error of PICASSO lies several orders of magnitude below the angular power spectrum of the map (green thick lines) at the relevant multipoles for QUIJOTE ($10 < \ell < 400$), meaning that the error made by PICASSO when reconstructing the sky signal into the map is low with respect to the level of the signal itself. We show in Fig. 3.10 the TT, EE and BB percentage signal error angular power spectra. We can see here that the signal error is very small, being lower than 0.005% at multipoles $\ell < 400$, for TT, EE and BB, while in the range $20 < \ell < 200$ the signal error is lower than 0.001%. It then increases in the two extreme regimes: at very low multipoles, showing that the reconstruction of the large angular scales is well under control down to $\ell = 10$, and at high multipoles $\ell > 400$, where the signal drops due to the effect of the beam window function. The signal error in polarization (EE and BB) keeps low values (<0.01%) also at lower multipoles ($2 < \ell < 10$), which is particularly important for reionization and CMB B-modes science. However, the finite sky coverage impose limitations in the reconstruction of large angular scale modes, as we will better characterize in Sec. 3.6.3.

We can now compare the simulations with no noise (green lines in Fig. 3.9) with the simulations containing white noise (purple lines in Fig. 3.9). The angular power spectrum of the residual in the white noise only case is approximately flat at multipoles $\ell > 20$, as expected for white noise. In the low multipole range, instead, it shows a mild growth, which is probably related to the increase of the signal error at $\ell < 20$, particularly in the intensity case, although some residual mode-coupling due to the finite sky coverage could be present.

Finally, we compare with realistic simulations containing white plus $1/f$ noise, which are represented by the red color lines in Fig. 3.9. In intensity (TT), we can notice the effect of the $1/f$ contamination in two different multipoles regimes. First, at low multipoles, we can clearly see the typical $1/\ell$-like rise of the power spectrum, which is due to the residual $1/f$ correlated noise structures in the intensity maps. Second, at high multipoles, we can observe that the noise level of the $1/f$ simulation is about two orders of magnitude higher than that of the white noise only simulation, while we could expect them to be comparable. This effect is due to the high $1/f$ knee frequency of the intensity data, as compared with the sampling frequency of the TOD. Indeed, since we simulate $1/f$ noise with a knee frequency of $f_{\rm k} = 20\,{\rm Hz}$, and we bin the TOD in 40 ms time intervals, we have significant $1/f$ noise drifts even within one single time bin. This artificially enhances the r.m.s. of the data samples (σ_i of Eq. 3.24) and therefore also the white noise level of the intensity maps.

In polarization (EE and BB), where the simulated $1/f$ noise is small, we can see that the white plus $1/f$ noise power spectrum is close to the white noise only case, indeed overlapping at high multipoles. This means that the selection of the baseline length is producing (nearly) optimal results, in the sense that the code recovers the white noise levels at high multipoles. However, also in this case, we observe a rise of the noise angular power spectrum at low multipoles,

Horn	Frequency [GHz]	$\sigma_{1\text{-deg}}\ [\mu K]$	α	$\ell_{\rm k}$
		TT		
3	11.0	98.5	1.31	370.3
3	13.0	87.7	1.22	390.2
4	17.0	128.5	1.19	428.7
4	19.0	142.4	1.41	323.5
		EE		
3	11.0	33.0	1.45	37.1
3	13.0	29.3	1.26	39.2
4	17.0	44.6	1.17	38.4
4	19.0	45.0	1.31	38.1

Table 3.2— Fitting of the TT and EE noise angular power spectra of the simulation with white plus $1/f$ noise, according to Eq. 3.55.

which is due to a combination of residual large-scales correlated noise and signal error.

To conclude, we can notice that the power spectrum of the sky signal is well reconstructed, if the signal to noise is sufficiently good. In the realistic case with $1/f$ noise, at 11 GHz (red line in the left panels of Fig. 3.9), the TT angular power spectrum of the map is above the noise contribution up to $\ell \sim 300$, while the EE and BB C_ℓ's are well reconstructed up to $\ell \sim 100$. At 19 GHz, where the sky signal is weaker, the quality of the reconstruction is worse. At this frequency we have a good reconstruction of TT up to $\ell \sim 100$, while the EE and BB power spectra are noise dominated at all multipoles.

3.6.2.1 Fit of the noise angular power spectrum

We fit the noise angular power spectra with the following empirical model:

$$C_\ell = C_{\rm w}\left(1+\left(\frac{\ell_{\rm k}}{\ell}\right)^{\alpha}\right), \tag{3.55}$$

analogous to the $1/f$ noise in the frequency space given by Eq. 2.7. The parameter $C_{\rm w}$ represents the white noise level of the maps. In practice, it can be obtained as the average of the angular power spectrum at high multipoles ($\ell \in [700, 800]$ for TT and $\ell \in [400, 500]$ for EE and BB). Note that $C_{\rm w}$ can be translated into the commonly used quantity $\sigma_{1\text{-deg}}$, which is the r.m.s. of the map in a 1-degree beam, with the relation $\sigma_{1\text{-deg}} = \sqrt{C_{\rm w}/\Omega_{1\text{-deg}}}$, where $\Omega_{1\text{-deg}}$ is the solid angle of a Gaussian beam with a FWHM of 1-degree. The parameter

ℓ_k is the knee-multipole that pinpoints the transition between a $1/\ell$ and a flat (white) regime. The knee-multipole ℓ_k is obtained analytically after fitting a linear slope in $\log_{10}(C_\ell - C_\mathrm{w})$ as function of $\log_{10}(\ell)$, in a range of intermediate multipoles $\ell \in [10, 100]$ for TT, and $\ell \in [10, 80]$ for EE and BB. Here α is the angular coefficient of the linear slope, and q is the fitted intercept,[11] the ℓ_k is given by:

$$\ell_\mathrm{k} = 10^{\left(\frac{q-\log_{10}(C_\mathrm{w})}{\alpha}\right)}. \tag{3.56}$$

Table 3.2 lists the C_w, ℓ_k and α parameters extracted from the simulations with white plus $1/f$ noise for TT and EE. As expected, the $1/f$ noise in intensity is reflected by a large ℓ_k, while in polarization, where the $1/f$ noise is low, the ℓ_k is also much lower. It is interesting to notice that the noise parameters $\gamma = 1.5$ and $f_\mathrm{k} = 20\,\mathrm{Hz}$ injected in the intensity simulation (see Tab. 3.1) are translated into a $\alpha \approx 1.2$ and $\ell_\mathrm{k} \approx 400$ in the angular power spectrum domain. Analogously, the parameters $\gamma = 1.8$ and $f_\mathrm{k} = 0.3\,\mathrm{Hz}$ used for the simulated noise in polarization correspond, at the angular power spectrum level, to $\alpha \approx 1.3$ and $\ell_\mathrm{k} \approx 40$.

3.6.3 Transfer function

We quantified the large angular scale suppression introduced by PICASSO and by the wide-survey scanning strategy, by performing a study of the transfer function of the simulated wide-survey maps (Fig. 3.11). We used the simulations in the ideal case with no-noise and no CMB dipole, for horn number 3 at 11 GHz, as presented in Sec. 3.6.2.

The transfer function is computed as the ratio between the C_ℓ of the reconstructed map and the C_ℓ of the input sky, both computed within the mask in Fig. 3.8. In order to control the possible residual mode coupling at large angular scales that could affect the pseudo-C_ℓ estimator, we computed the (binned) low multipoles points of the angular power spectra ($\ell < 60$) with ECLIPSE, a fast and robust implementation of a quadratic maximum likelihood C_ℓ estimator (Bilbao-Ahedo et al., 2021), after degrading the maps to $N_\mathrm{side} = 32$ (pixel size $\sim$1.8 deg). The power spectra at multipoles higher than $\ell = 60$ are computed with the pseudo-C_ℓ code XPOL.

The results are shown in Figure 3.11, for TT, EE and BB. We can observe that in TT PICASSO recovers $\sim$ 100% of the Galactic signal at multipoles $\ell > 10$, while there is a loss of power of $\sim$ 3% at multipoles $2 < \ell < 10$, and of $\sim$ 20% at $\ell = 2$. However, as it can be clearly seen in the intensity residuals shown in Fig. 3.5 and 3.6, when we include the CMB dipole ($\ell = 1$)

---

[11] Analytically, the intercept is given by $q = \log_{10}(C_\ell(1) - C_\mathrm{w}) = \log_{10}(C_\mathrm{w}) + \alpha \log_{10}(\ell_\mathrm{k})$.

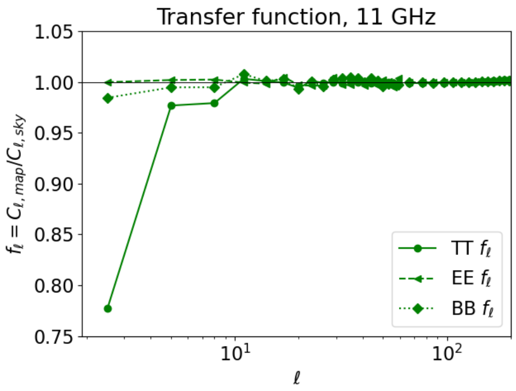

FIGURE 3.11— Transfer function of the PICASSO map-making code, obtained from a simulation of the QUIJOTE-MFI wide survey, at 11 GHz, in absence of noise and CMB dipole. The thick line represents the intensity (TT), and the dashed and dotted lines, represent the polarization (respectively EE and BB).

is perfectly recovered at the map level. We understand that PICASSO is able to reconstruct the CMB dipole because its signal is sufficiently high, while the Galactic signal at angular scales with $2 < \ell < 10$ has less power, and is therefore more complex to reconstruct.[12] In polarization, the transfer function of EE and BB shows that with PICASSO we can recover $\sim 100\%$ of the signal at $\ell > 8$, while the loss of power at lower multipoles is not larger than 2%. This behaviour of PICASSO in polarization is particularly promising in prospective for future works aimed to detect the primordial B-modes. Similar results are found for the other simulated MFI frequencies.

3.6.4 Fit of a template function

We report here on the results of the template function fitting performed by our implementation of the code (Sec. 3.3.6). We tested this technique with two templates: a TOD projection of the CMB dipole, and a stable plane-parallel atmosphere of the type $1/\sin(\mathbf{el})$ (see Sec. 3.4.4 for a more detailed description of the templates).

With this aim, we used a set of realistic simulations of intensity at 11 GHz,

---

[12] Note that for the computation of the transfer function we use a map that does not include the CMB dipole, in order to avoid any possible mixing or the large angular scale modes.

Template	$< A >$	$\sigma_{<A>}$	σ_A^{MC}	$\sigma_A^{\mathrm{analytic}}$
Atmosphere	1.009	0.006	0.018	0.001
CMB dipole	1.09	0.08	0.26	0.01

TABLE 3.3— Result of the fitting technique during map-making for a stable plane-parallel atmosphere and for the CMB dipole. Realistic simulations have been used to estimate the uncertainty for the fitted amplitudes A, by generating 10 independent TOD noise realizations, added on top of the same simulated TOD containing the sky signal. This table reports the average among the 10 estimated amplitudes ($< A >$), the uncertainty for the average recovered amplitude ($\sigma_{<A>}$), the uncertainty for a single estimate of A obtained as the scatter of the MC realizations (σ_A^{MC}), and the analytic uncertainty for A obtained with Eq. 3.49 ($\sigma_A^{\mathrm{analytic}}$) .

which contain the sky signal, the CMB solar plus orbital dipole, the CMB anisotropies, and 10 independent realizations of white plus $1/f$ noise, simulated using the values in Table 3.1, with the noise generator described in Sec. 3.4.2. These simulations can be directly used for the fitting of the CMB solar plus orbital dipole, while for the fitting of the atmospheric component, we added the term $1\,\mathrm{K}/\sin(\mathbf{el})$, with an amplitude $A_{\mathrm{atmo}} = 1$ representing the temperature of the atmosphere at the zenith in units of Kelvin. By construction, the expected value of the fitted amplitude of the CMB dipole is $A_{\mathrm{d}} = 1$, and for the atmosphere it is $A_{\mathrm{atmo}} = 1$.

We report in Table 3.3 the average of the results obtained for the atmospheric and CMB dipole fitting, using the results from the 10 realizations mentioned above. We also report different estimates of the uncertainty: the uncertainty for the average recovered amplitude ($\sigma_{<A>}$), the uncertainty for a single estimate of A obtained as the scatter[13] of the Monte Carlo (MC) realizations (σ_A^{MC}), and the analytic uncertainty for A obtained with Eq. 3.49 ($\sigma_A^{\mathrm{analytic}}$).

We verify that the method is unbiased by looking at the average of the recovered amplitudes, $< A >$. Under the assumption of independent realizations, the uncertainty for the average $< A >$ is $\sigma_{<A>} = \sigma_A^{\mathrm{MC}}/\sqrt{N}$. However, the realizations are not totally independent: although we inject independent noise realizations in the simulations, we always adopt the same dataset, sky signal, geometry of the observations, and data flagging. Therefore, the simulations are partially correlated, and the final uncertainty $\sigma_{<A>}$ could be slightly underestimated. On the other hand, the fact that the number of simulations is small may induce an overestimated uncertainty as computed from the scatter. Under the assumption that $\sigma_{<A>}$ provides a reliable estimate of the uncertainty of

---

[13] Sample variance: $\sigma = \sqrt{\sum_{i=1}^{N}(A_i - < A_i >)^2/(N-1)}$, being $< \cdot >$ the average of the estimated amplitudes A, and N the number of samples.

the average recovered amplitudes, we can observe that the method is unbiased. The average estimated amplitude $< A >$ is compatible with the expected value $A = 1$ within $1.5\,\sigma$ and $1.1\,\sigma$, in the case of the atmosphere and of the CMB dipole, respectively.

Finally, we assess the uncertainty of one single estimate of the amplitude A, which is the uncertainty to quote when we apply the fitting procedure with the real data (for which only one realization of the data-set is available). We quote the uncertainty on A as the scatter of the results obtained with different MC realizations, $\sigma^{\rm MC}$ (4-th column in Tab. 3.3; where MC indicates that the uncertainty is obtained as the standard deviation of Monte Carlo realizations). This estimate of the uncertainty can be compared with the analytical one obtained with Eq. 3.49, which is reported in the last column in Tab. 3.3. We can clearly notice that $\sigma_A^{\rm analytic}$ underestimates the uncertainty on A. Indeed, the analytical estimator assumes a Gaussian posterior of the fitted amplitude parameter A, and it assumes that the modeling of $1/f$ noise is perfect. The most realistic uncertainty, is given by the standard deviation of the ten Monte Carlo measurements of A, $\sigma_A^{\rm MC}$, which accounts for the injected noise into the data. We tested the estimate of the uncertainty also including only white noise, obtaining that the theoretical formula and the MCMC provide totally consistent estimates.

The result of this analysis is that, an atmospheric component of the type $1/\sin(\mathbf{el})$ can be recovered by our technique with an uncertainty $\sigma^{\rm MC}_{A_{\rm atmo}} = 0.018$, which is a precision of $\sim 2\%$. On the other hand, for the CMB dipole, we can reach a precision of $\sim 26\%$, with $\sigma^{\rm MC}_{A_{\rm d}} = 0.26$. There are various factors that can explain the difference in the precision achieved for $A_{\rm atmo}$ and $A_{\rm d}$, despite the atmosphere and the CMB dipole seams to introduce in the maps the same level of fluctuations of the order of few mK (depending on the elevation in the case of the atmosphere). First, the telescope scans one full period of the atmospheric fluctuation in only one scan. For example, in one single ring-like scan at $el = 60°$, which takes 30 s in the scanning strategy of the wide-survey, the atmospheric pattern is entirely measured, and the amplitude of the fluctuation is of the order of few mK (see Sec. 3.4.4.1). The CMB dipole, instead, given the QUIJOTE latitude on Earth and the scanning strategy, is scanned from its maximum to its minimum (which are approximately ± 3 mK on a map) with several hours of separation, because, in order to measure it, we have to wait it to transit across the sky. As a consequence, the complete measurement of the CMB dipole is spread in time, and the variations introduced in the TOD by the CMB dipole in one single ring scan are much smaller than its peak amplitude of ≈ 3 mK, and are therefore also smaller than the atmospheric fluctuations in one scan. In addition, the large $1/f$ noise drifts over a slowly varying template such as that of the CMB dipole complicate the action of recovering its amplitude at the TOD level with this technique.

3.7 Conclusions

We presented PICASSO, a map-making code implemented for the construction of the maps of the MFI instrument of the QUIJOTE experiment. PICASSO is based on the destriping algorithm with priors on the baselines for the suppression of the $1/f$ noise, and implements a technique to fit for a general template at the map-making level. This feature is particularly useful for the analysis of ground-based CMB experiments.

We performed simulations of the QUIJOTE-MFI wide-survey (Rubiño-Martín et al. in prep) to test the performance of PICASSO. We showed a realistic simulated version of the QUIJOTE-MFI intensity and polarization wide-survey maps (Fig. 3.4), at 11, 13, 17 and 19 GHz. We then conducted a detailed analysis of the simulated maps at the map level and at the power spectrum level, with special emphasis on the stability of the reconstruction of the large angular scales. PICASSO is able to reconstruct the CMB dipole with $\sim 0.1\,\%$ accuracy, at the map level.

We presented the angular power spectra of the simulated maps with no-noise, white noise, and realistic white plus $1/f$ noise (Fig. 3.9). We studied the signal error and the transfer function of the map-making code, in combination with the scanning strategy of the wide-survey. PICASSO performs well at all angular scales: the signal error is lower than 0.001% at multipoles in $20 < \ell < 200$, for TT, EE and BB (Fig. 3.10), at all the QUIJOTE-MFI frequencies. Furthermore, the results obtained for the transfer function (Fig. 3.11) show that PICASSO performs a perfect reconstruction of the sky signal at multipoles $\ell > 10$ in TT and $\ell > 8$ in EE and BB, for the partial sky coverage of the MFI wide survey. Moreover, in polarization, the larger angular scales $2 < \ell < 8$ are precisely recovered, within $2\,\%$ error, which is below the cosmic variance limit at these multipoles.

Finally, we tested the template fitting procedure that is implemented in PICASSO, using a template of the atmosphere and of the solar plus orbital CMB dipole (Sec. 3.6.4). For the noise levels in the QUIJOTE-MFI wide survey, we expect to recover the amplitude of the atmospheric fluctuations with a precision of $2\,\%$, and of $26\,\%$ for the CMB dipole.

4

The QUIJOTE-MFI wide survey

> *"The Galaxy kept turning sleepless in its bed of soft emptiness, as if moved by the pricking of all the worlds and atoms that lit up and radiated."*
> Italo Calvino, Le Cosmicomiche

The production of the QUIJOTE-MFI maps of the intensity (I) and linear polarization (Q, U) of the full northern sky, the so-called wide-survey maps, constitute one of the main goals of this project. They cover $\sim 78\%$ of the sky, corresponding to the declination band $\delta = -32^\circ$ to $\delta = 88^\circ$, at central frequencies $\nu \sim$ 11, 13, 17, 19 GHz. The typical sensitivity of the maps is $\sigma_{\rm I,1deg} \sim 60-200\,\mu$K and $\sigma_{\rm QU,1deg} \sim 35-70\,\mu$K, when smoothed to 1 degree beam. Here we present the wide-survey maps, and their characterization and validation at the map and angular power spectrum level. In particular, this thesis presents the characterization of the noise properties, the flagging of interference, the study of the angular power spectra of the maps and of the noise, and the validation of the internal calibration of the maps based on cross-correlations. The maps and the aforementioned analyses will be published in Rubiño-Martín et al. (in prep). The wide-survey maps and the associated data products will be publicly delivered.

4.1 Data

4.1.1 Scanning strategy

The QUIJOTE-MFI wide survey maps have been obtained from observations in *nominal* mode (see Sec. 2.2.2 and Sec. 3.5.1), which consists of continuous 360° azimuth scans of the telescope, at (nominal) constant elevation. The scan speed in nominal mode was $v_{\rm AZ} = 6\,{\rm deg}\cdot{\rm s}^{-1}$ until January 9 2014, and this was

Per	From – To (dd/mm/yy)	Description	Elevation [deg]	T_I [h]	T_P [h]
1	12/11/12 10/04/14	Config. 1 for all horns. No extended shielding.	30, 60, 65, 70	1652	0.0
2	11/04/14 30/11/15	Horn1 in config. 2. Extended shielding installed.	30, 40, 50, 60, 65	2084	2084
5	01/05/16 14/10/16	All horns in config. 2. Horn 1 not operative.	30, 40, 50, 60	972	0.0
6	15/10/16 01/11/18	Same as in period 5.	35, 50, 60, 65, 70	3710	3710

Table 4.1— Dates, description, pointed elevations, and integration time in intensity and polarization, for the four periods of the wide-survey observations campaign. See Sec. 2.3.1 and Fig. 2.4 for a description of configuration 1 and 2. Table adapted from Rubiño-Martín et al., (in prep).

later changed to $v_\mathrm{AZ} = 12\,\mathrm{deg}\cdot\mathrm{s}^{-1}$, in order to reduce the contamination from $1/f$ noise.

After 24 h of observation in this mode, we cover a full band in right ascension, and a declination range that depends on the elevation of the observation. Low elevations provide the coverage of a wider declination range, at the expense of a larger contamination from the atmosphere. In order to achieve a wide and uniform sky coverage, and a good signal-to-noise in the data, we periodically re-point the telescope at a different elevation selected from the list $el = [30, 35, 40, 50, 60, 65, 70, 75, 80]\,\mathrm{deg}$. However, not all the observed elevations are used in the final maps, and not all the elevations are observed in every period. We summarize the final effective data-set in Tab. 4.1.

4.1.2 Periods

The MFI data are catalogued in six *periods*, which are defined by changes in the instrumental configuration or the start of a new cooling cycle (see Sec. 2.3.1 and Tab. 4.1). The MFI wide survey observations started in May 2013 and finished in June 2018. Wide-survey data were taken during four periods: period 1, 2, 5, and 6. The dates that define the periods, and the elevations pointed during each period are reported in Tab. 4.1.

The configuration of the instrument changed from period to period, as well as its noise properties. In period 1 all the horns were in the first configuration, in which the X and Y channels were uncorrelated, and the (X+Y) and (X-Y) channels were correlated (see Sec. 2.3.1). Therefore, during period 1, the

$1/f$ noise of the uncorrelated channels difference was larger than that of the correlated channels, and the latter can not be used in polarization. In addition, in period 1 the extended shielding in QT-1 was not installed yet, resulting in an excess of RFI contamination from satellites emission picked up by the far-sidelobes of the beam that significantly affected the polarization data. For these reasons, the data from period 1 are used (with some caution) to construct the intensity maps only, and not the polarization ones.

During period 2, the second configuration was adopted in horn number 1, while the other horns remained in the first one. In addition, an extended shielding was installed in QT-1 in order to reduce the RFI far side-lobes contamination. Therefore, in period 2, all the data can be used to construct the intensity maps, but only the correlated channels are used to construct the polarization maps. However, due to a problem with the modulator of horn number 1, its data are not used to construct polarization maps.

In the periods 5 and 6 all the horns moved to the second configuration, and both the correlated and uncorrelated pairs of channels became effectively correlated. Consequently, in period 5 and 6 we can use all the data to construct the intensity and polarization maps, except horn one for the same reasons mentioned above.

At a later stage, we identified problems in the polarization data of period 2 from horn 4, and of period 5 from horn 2. These data are therefore excluded for the construction of the final maps.

4.1.3 Noise statistics

In order to keep track of the noise properties of wide-survey data across periods, we statistically studied the noise parameters of the observations taken at $el = 60^\circ$, in the four periods. The sums and differences of channels were analyzed, since these combinations are the effective data from which we extract the I, Q and U maps. The noise streams are obtained by subtracting a time ordered domain projection of the wide-survey maps from the CTODs. The power spectrum densities are computed as the Fourier transform of the auto-correlation function of the noise streams. This methodology avoids possible bias introduced by gaps in the data (flagged or corrupted by the activation of the calibration diode).

We fit the noise power spectral density $P(f)$ with the function given in Eq. 2.7, at frequencies $f > f_{\rm cut} = 1/30\,{\rm s} = 0.033\,{\rm Hz}$. Given that we remove a median value from the CTODs in each azimuth scan of the telescope (every 30 s), we have an approximately constant $P(f) \approx P(f_{\rm cut})$ at $f < f_{\rm cut}$ (see Fig. 3.2). First of all, we determine the white noise level from the median values of the weights (w_i) in the CTOD as:

$$\frac{\sigma^2}{f_{\rm s}} = \frac{\tau_{\rm s}}{{\rm median}(w_i)}, \tag{4.1}$$

where $\tau_{\rm s} = 40\,{\rm ms}$ is the bin size. As already mentioned in Sec. 3.3.1, the weights are the inverse variance of the data samples within one bin, scaled by the number of sample in one bin ($n_{\rm s} = 40$). The white noise level can then be subtracted by the power spectral density to construct the function $\log(P(f) - \sigma^2/f_{\rm s})$, which is a linear function of $\log(f)$ given by:

$$\log\left(P(f) - \frac{\sigma^2}{f_{\rm s}}\right) = \log\left(\frac{\sigma^2}{f_{\rm s}}\right) + \gamma\log(f_{\rm k}) - \gamma\log(f) = q - \gamma\log(f) \tag{4.2}$$

We use this linear relation to fit for the parameters γ and $f_{\rm k}$: the angular coefficient of the linear fit provides the γ parameter, while from the intercept q we can analytically derive the value for $f_{\rm k}$ as:

$$\log(f_{\rm k}) = \frac{q - \log\left(\frac{\sigma^2}{f_{\rm s}}\right)}{\gamma} \tag{4.3}$$

This fitting procedure is applied for every CTOD file (see Sec. 2.4.1), to the sums (X+Y and (X+Y)+(X-Y), for intensity) and differences (X-Y and (X+Y)-(X-Y), for polarization) of channels. The measurement of the parameters γ and $f_{\rm k}$ is performed in the ranges $f \in [0.6, 1.6]\,{\rm Hz}$ and $f \in [0.03, 0.09]\,{\rm Hz}$, respectively for the sum and difference of channels. These ranges were calibrated with simulations, in order to adjust the $1/f$ slope in the range between the low frequency cut-off and the expected knee frequency, which is different in intensity and polarizarion.

We report in Tab. 4.2–4.5 the typical values for γ and $f_{\rm k}$ of the data at elevation 60°, from period 1, 2, 5, and 6 and horns number 2, 3 and 4. We can use these results to have a rough understanding and characterization of the noise properties of the wide-survey data across time. We can observe that the $1/f$ noise of horn 3 in intensity (sum of channels) is approximately stable in time, with $f_{\rm k} \sim 40\,{\rm Hz}$ and $\gamma \sim 1$ in period 1, with some enlargement of the knee frequency at 13 GHz during period 5 and 6, which is however compensated by a decrease of the power of the $1/f$ slope given by the γ parameter.[1] Horn 3 is the one with lower $1/f$ noise in intensity. Indeed, horns 2 and 4 have a knee frequency in the range $40 - 150\,{\rm Hz}$ (depending on the period) and $\gamma \sim 1$.

---

[1] These differences could be related with the uncertainty of the fit, and to degeneracy between the fitted parameters.

		σ^2/f_s [mK^{2}s]	f_k [Hz]	γ	σ^2/f_s [mK^{2}s]	f_k [Hz]	γ
Horn	Channel	High frequency			Low frequency		
2	X+Y	0.95	110	0.9	0.56	110	0.8
	X-Y	0.96	86	0.9	0.57	69	0.9
	(X+Y)+(X-Y)	0.52	110	0.9	0.43	110	0.9
	(X+Y)-(X-Y)	0.53	0.4	1.7	0.43	0.2	1.8
3	X+Y	0.32	29	1.0	0.47	43	0.9
	X-Y	0.32	9	1.1	0.48	13	1.1
	(X+Y)+(X-Y)	0.29	35	1.0	0.42	50	1.0
	(X+Y)-(X-Y)	0.29	0.2	1.6	0.42	0.2	1.4
4	X+Y	2.01	67	0.9	3.52	91	0.9
	X-Y	2.01	63	0.9	3.56	86	0.9
	(X+Y)+(X-Y)	1.77	72	1.0	2.20	130	0.9
	(X+Y)-(X-Y)	1.77	0.5	1.5	2.22	0.2	2.2

TABLE 4.2— Noise parameters for the wide-survey data in period 1, at elevation 60 deg. X+Y and (X+Y)+(X-Y) are for intensity, while X-Y and (X+Y)-(X-Y) are for polarization.

		σ^2/f_s [mK^{2}s]	f_k [Hz]	γ	σ^2/f_s [mK^{2}s]	f_k [Hz]	γ
Horn	Channel	High frequency			Low frequency		
2	X+Y	0.88	150	0.9	0.55	220	0.8
	X-Y	0.87	170	0.8	0.54	79	0.9
	(X+Y)+(X-Y)	0.47	110	1.0	0.40	200	0.8
	(X+Y)-(X-Y)	0.47	0.3	2.1	0.39	0.2	1.6
3	X+Y	0.28	37	0.9	0.45	57	0.9
	X-Y	0.28	98	0.8	0.45	430	0.6
	(X+Y)+(X-Y)	0.26	36	0.9	0.80	43	0.9
	(X+Y)-(X-Y)	0.26	0.3	1.2	0.80	0.1	1.7
4	X+Y	0.81	39	1.1	0.68	60	1.0
	X-Y	0.89	94	0.8	0.69	280	0.7
	(X+Y)+(X-Y)	0.62	60	1.0	0.53	100	0.9
	(X+Y)-(X-Y)	0.72	0.2	1.7	0.53	0.2	1.6

TABLE 4.3— Same as in Fig. 4.2 for period 2, except for horn 3, high frequency, which is for observations at $el = 65\,$deg, because of the RFI that contaminate this channel, at $el = 60\,$deg, in period 2.

		σ^2/f_s [mK^{2}s]	f_k [Hz]	γ	σ^2/f_s [mK^{2}s]	f_k [Hz]	γ
Horn	Channel	High frequency			Low frequency		
2	X+Y	1.06	49	1.1	0.97	79	-1.0
	X-Y	1.06	0.1	2.0	0.97	0.5	-1.4
	(X+Y)+(X-Y)	0.99	60	1.1	0.95	75	-1.0
	(X+Y)-(X-Y)	1.00	22	1.0	0.95	8	-1.0
3	X+Y	0.35	20	1.0	0.47	60	0.9
	X-Y	0.35	0.4	1.0	0.47	0.2	1.2
	(X+Y)+(X-Y)	0.36	23	1.0	0.48	55	0.9
	(X+Y)-(X-Y)	0.36	6	0.9	0.50	28	0.7
4	X+Y	1.03	0.69	1.1	0.97	120	1.0
	X-Y	1.03	0.3	1.6	0.97	0.8	1.0
	(X+Y)+(X-Y)	1.03	71	1.1	0.95	110	1.0
	(X+Y)-(X-Y)	1.00	0.3	1.4	0.98	0.1	2.1

TABLE 4.4— Same as in Fig. 4.2 for period 5.

		σ^2/f_s [mK^{2}s]	f_k [Hz]	γ	σ^2/f_s [mK^{2}s]	f_k [Hz]	γ
Horn	Channel	High frequency			Low frequency		
2	X+Y	1.06	100	0.9	0.67	160	0.8
	X-Y	1.06	0.1	1.9	0.67	0.4	1.4
	(X+Y)+(X-Y)	0.77	150	0.9	0.77	150	0.8
	(X+Y)-(X-Y)	0.77	11	0.9	0.77	12	0.9
3	X+Y	0.32	32	0.9	0.39	88	0.8
	X-Y	0.32	0.3	0.9	0.39	0.2	1.0
	(X+Y)+(X-Y)	0.31	32	0.9	0.41	80	0.9
	(X+Y)-(X-Y)	0.31	49	0.6	0.41	83	0.5
4	X+Y	0.71	120	0.9	0.79	140	0.9
	X-Y	0.72	0.2	1.4	0.79	0.5	1.1
	(X+Y)+(X-Y)	0.63	120	0.9	0.69	140	0.9
	(X+Y)-(X-Y)	0.63	0.3	1.4	0.69	0.1	2.0

TABLE 4.5— Same as in Fig. 4.2 for period 6.

The larger knee frequency of the intensity data from horn 2 and 4 can also be associated with atmospheric fluctuations, due to the increasing brightness of

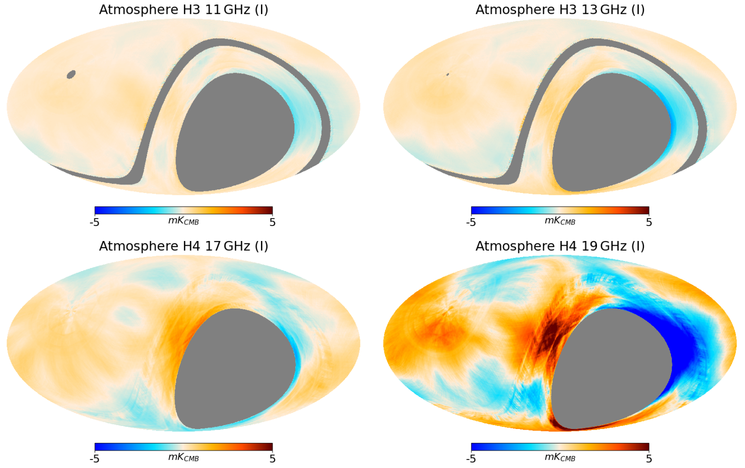

FIGURE 4.1— Atmospheric pattern removed by the intensity maps of the QUIJOTE-MFI wide-survey. We show one example map at the four MFI frequencies in order to illustrate the increasing impact of the atmosphere at higher frequencies: horn 3 at 11 GHz and 13 GHz, and horn 4 at 17 GHz and 19 GHz. For visualization purposes, the maps are smoothed to 1 degree angular resolution.

the atmosphere when approaching the 22 GHz water vapour emission line (see Fig. 2.9).

In the polarization data we can observe the clear transition between configuration 1 (periods 1 and 2) and configuration 2 (periods 5 and 6), which results in a smaller knee frequencies of the difference of the X and Y channels. However, we can notice that, after this transition in the instrument configuration, the polarization channel of horn 2 and 3 that had low $1/f$ noise in configuration 1 got worse in configuration 2. Finally, we can notice that horn 4 is the only one that effectively has lower $1/f$ noise in both the correlated and uncorrelated channels in the second configuration.

4.1.4 Atmosphere

As described in Sec. 2.5, the atmosphere is a source of $1/f$ noise at the MFI frequencies, especially at 17 and 19 GHz since these channels are closer to the water vapour emission line at $\nu \sim$22 GHz. In order to minimize the effect of

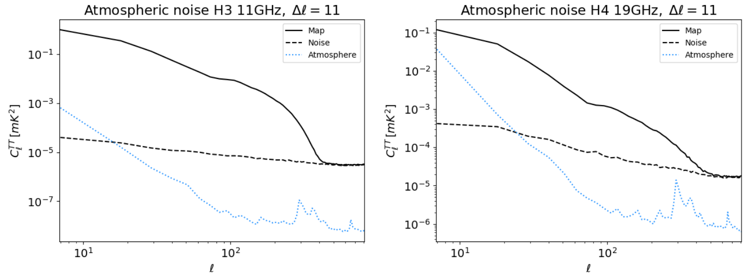

FIGURE 4.2— Angular power spectrum of the atmospheric pattern removed from the intensity maps of the QUIJOTE-MFI wide-survey, for horn 3 at 11 GHz and horn 4 at 19 GHz. Black shows the angular power spectrum of the wide-survey map and its noise (dashed line - from the *half*-difference null-lest, see Sec. 4.5.3). The blue dotted line shows the power spectrum of the atmospheric pattern shown in Fig. 4.1

.

the atmosphere, the time ordered data are corrected by an atmospheric component that is reconstructed by extracting from the large angular scales of all the MFI channels a signal with the expected atmospheric spectrum, based on the expected frequency ratios of the atmospheric model between MFI frequencies, for typical PWV values at the Teide Observatory (see chapter 2, Sec. 2.5, and in Rubiño-Martín et al., in prep). The correction is done only in intensity, and it was implemented by Robert Watson (University of Manchester).

We show in Fig. 4.1 the atmospheric pattern in the QUIJOTE-MFI maps, which are obtained as the difference between maps constructed from uncleaned data and maps constructed from data corrected by the atmosphere. We can notice that, as expected, the amplitude of the atmospheric pattern increases with frequency, while the spatial distribution of the atmospheric emission is similar between different frequencies. The regions that are more affected by the atmospheric contamination are the low and high declination regions, which are accessible only with low elevation observations, which cross a large air-mass.

We computed the angular power spectra of the atmospheric residuals that are shown in Fig. 4.1, and we compared them with the angular power spectrum of the map and the respective noise level. This is shown in Fig. 4.2, where it can be seen that the power of the atmospheric pattern is subdominant at small angular scales ($\ell \gtrsim 20$), but it gains detectable power at large angular scales ($\ell \lesssim 20$). In this figure, only the two extreme frequency cases are shown (11 and 19 GHz) but the same behaviour is valid at all frequencies.

4.1.5 Interference

The problem of RFI at MFI frequencies is relevant, as already discussed in Sec. 2.4.5, where we mentioned that regions (in local coordinates) where geostationary satellites are observed need to be flagged from the scientific data-set. As a general information, the most affected declination range is $\delta \in [-10^\circ, -1^\circ]$, which is totally flagged at 11 and 13 GHz, and only partially flagged at 17 and 19 GHz.

In the wide-survey data, additional spurious localized RFI have been identified, appearing as short bright stripes in the maps. This kind of interference could come, for example, from radio-communication signals emitted by moving satellites or airplanes. We performed a careful analysis to ensure that these sources of emission did not have an astrophysical origin, by checking their presence in the *halfring* null-test maps. This null-test, as described in detail in see Sec. 4.5, consists in producing two maps: one from the data taken in the azimuth range $0^\circ < az < 180^\circ$ (local East), and another in the complementary part of the ring, in $180^\circ < az < 360^\circ$ (local West). The sky signal is equally projected in both maps, while an RFI, which does not follow the sky transit motion, is observed only in one of the two *halfring* splits. Therefore, the difference between the two *halfring* maps can be used to identify non-astrophysical features in the data. We flag localized RFI by excluding the data enclosed in a ellipse that surrounds the interference in the Galactic coordinates frame, but only in the elevation and azimuth range where the interference is observed.

In addition to that, several geostationary satellites that were not previously identified (see Sec. 2.4.5), as well as far side-lobes of the brightest satellites, appeared as residual constant-declination stripes in the maps. We identified the geostationary satellites by inspecting templates of the function of the azimuth, $f(az)$, which are obtained from the CTODs of common elevation observations, stacked in bins of the azimuth. The contribution from sky signal and noise in the $f(az)$ functions averages to zero, while the RFI signal emerges (if its local coordinates are stable in time), therefore $f(az)$ can be used as a template of the RFI at each observed elevation, as a function of the azimuth. We used the $f(az)$ templates to identify the location of particularly bright geostationary satellites, by assigning the azimuth intervals and the elevations where they were observed. The location of these RFI, together with the size and coordinates of localized features described in the previous paragraph, are included in 3481 lines of IDL code, which is used to flag from the CTOD the newly identified RFI.

We decided not to flag the fainter residual satellites, but to mitigate their effect with a two-stage correction: at the CTOD level and at the map level. For the correction at the CTOD level, we subtract from the CTOD the $f(az)$

template of the interference. Subsequently, we apply an additional correction at the map level, which consists in filtering a function of the declination $f(dec)$ from the map. More details can be found in Rubiño-Martín et al., (in prep).

Although these filters constitute a method to correct for the RFI without the necessity of flagging a large amount of data, it could alter and suppress the large angular scales of the sky signal. In order to control this effect, we performed an analysis of the transfer function of the filters, by using simulations of the wide-survey data. The results of this analysis will be presented in in Rubiño-Martín et al., (in prep).

4.1.6 Flagging

In addition to the removal of RFI contaminated data, and to the basic flagging described in Sec. 2.4.1, some extra flagging is applied to the wide-survey data, at the CTOD level, in order to discard excessively noisy or corrupted data. In order to flag noisy data, an automatic procedure is applied that identifies and flags the azimuth scans with outlier r.m.s. values, with respect to the median r.m.s. of the scans performed during each period. The statistics of the r.m.s. is computed for the sum and difference of channels (for intensity and polarization, respectively), separately for each period.

Additional flags are also applied to the time ordered data samples that cross the brightest solar system planets (Venus, Jupiter and Mars), by flagging the data falling within a circle of 2° radius from the central coordinates of the objects.

4.2 Pipeline

The main steps of the QUIJOTE-MFI data processing pipeline are reported in Sec. 2.4, while a detailed description will be presented in Génova-Santos et al. (in prep.). In this section we briefly mention the steps that are specific for the QUIJOTE-MFI wide-survey data.

4.2.1 Map-making

The PICASSO map-making code has been used to construct the wide-survey maps, as extensively described in chapter 3. Before constructing the polarization maps, we re-calibrated the gain unbalance (r-factor, see Sec. 2.4.2) using the fitting function technique implemented in PICASSO (see Sec. 3.3.6). We fitted a projection of the intensity map (of each horn, frequency and channels pair) to the polarization CTODs, and we used the estimated amplitude to correct the polarization data for a leakage term, as given in Eq. 2.14.

Finally, we produced one map for each pair of MFI channels, with $N_{\rm side} = 512$ (pixel resolution $\sim 0.1°$), and a baseline length of $t_{\rm b} = 2.5\,$s, using priors on the baselines given by the parameters in Tab. 3.1. The correlated and uncorrelated channels from a given horn and frequency are combined a posteriori with a weighted average, obtaining finally the combined map m and the corresponding weight map w, as presented in Sec. 3.6.1 (Eq. 3.53 and 3.54), using the noise correlation values shown in Sec. 4.5.5.

We obtained eight intensity maps and six polarization maps: horn 1 11 GHz (I only), horn 1 13 GHz (I only), horn 2 17 GHz (I, Q, U), horn 2 19 GHz (I, Q, U), horn 3 11 GHz (I, Q, U), horn 3 13 GHz (I, Q, U), horn 4 17 GHz (I, Q, U), and horn 4 19 GHz (I, Q, U). These maps are shown in Fig. 4.3 and 4.4. The maps at the same frequencies, from horns 1, 3, and 2, 4, can be subsequently combined, leading finally to four I, Q, and U frequency maps, at 11, 13 17 and 19 GHz. However, the maps from horn 1 are affected by residual artifacts coming from RFI contamination of data taken before installing the shielding, so they are not released nor used for any of the scientific analysis.

4.2.2 Re-calibration and post-processing

The maps are re-calibrated, using the Crab nebula (Tau A) as a primary calibrator, by using the models presented in Sec. 2.4.2.2. We re-calibrate, independently in each period, the intensity and polarization amplitudes, as well as the polarization angle, in order to improve the precision of the final calibration of the data.

Finally, a post-processing is applied to the maps as they come out from PICASSO. It consists in: subtracting a monopole, subtracting a dipole, and filtering the residual RFI structures with a function of the declination, as described in Sec. 4.1.5. We refer to Rubiño-Martín et al., (in prep) for more details on these steps.

4.3 Maps

The QUIJOTE-MFI wide-survey maps are shown in Fig. 4.3–4.8. Fig. 4.3 and 4.4 show all the horn and frequency maps, in intensity an polarization (Stokes parameters I, Q, and U), smoothed to a 1 degree angular resolution for visualization purposes. We also show the corresponding weight maps in Fig. 4.5 and 4.6, and the $n_{\rm hit}$ maps in Fig. 4.7 and 4.8. The maps are displayed in Galactic coordinates, and the grey regions correspond to the sky area that is not observed, including the southern sky, a few degrees around the North Celestial Pole, and the flagged satellites band, as indeed it was already seen from the simulations presented in Sec. 3.6.1. A detailed characterization and validation of the maps follows in the next sections.

4.3.1 Sky maps

Looking at the maps that are shown in Fig. 4.3 and 4.4, it can be observed that there is a bright horizontal structure that corresponds to the Galactic plane emission, which is a combination of synchrotron radiation, anomalous microwave emission, and free-free. The structures that extend outside the Galactic plane, which are particularly evident in polarization, correspond instead to magnetized Galactic filaments, loops, and spurs, emitting mainly synchrotron radiation. The intensity maps of horns 2 and 4 show large angular-scale patterns in intensity. These are due to a combination of residual instrument and atmospheric $1/f$ noise that was not completely removed from the data.

As we will see next, the map with the best signal-to-noise is that from horn 3, at 11 GHz. We therefore show in Fig. 4.9 a closer picture of the I-Q-U horn 3 map at 11 GHz, at the original angular resolution (FWHM $\sim 0.9°$), degraded to $N_{\rm side} = 256$ for display purposes.

4.3.2 $n_{\rm hit}$ maps

From the maps of the number of pixel crossings, the $n_{\rm hit}$ maps (Fig. 4.7 and 4.8), we can observe the distribution of the sky coverage obtained with the wide-survey observations. We can see evident ring structures, corresponding to the declination limits of observations performed at different elevations. They delimit a central band (rotated "s" shape in Galactic coordinates), that corresponds to the intermediate declination range, which is uniformly covered by wide-survey observations. At its borders, a low and a high declination area can be identified, where the number of pixel crossings (and therefore of the integration time) is low, because they are accessible only with low elevation scans (see Sec. 4.1.1). However, as commented in Sec. 3.6.1, the number of hits at high declination is larger than that at low declination due to projection effects. In addition, in the low declination band (circle surrounding the southern sky blank area) the number of crossing is even lower, because of the heavy flagging imposed by RFI contamination from geostationary satellites located in this area (see Sec. 2.4.5 and 4.1.5). Finally, note that the number of hits in intensity is larger than that in polarization. This is mainly because data from period 1 are not used to construct polarization maps, data from period 2 are not used in polarization for horn 4, and data from period 5 are not used in polarization for horn 2 (see Sec. 4.1.2).

4.3.3 Weights maps

The structures that are observed in the $n_{\rm hit}$ maps (Fig. 4.7 and 4.8) are also reflected in the *weight* maps (Fig. 4.5 and 4.6), which are a representation of the white noise level across the sky observed with the wide-survey, as propagated through the map-making code (Eq. 3.32 and 3.42). Large $n_{\rm hit}$ regions correspond to areas with large integration time, and where therefore the white noise level is lower, and the weights are larger. On the other hand, low $n_{\rm hit}$ regions correspond to areas with short integration time, and where therefore the white noise level is higher, and the weights are smaller.

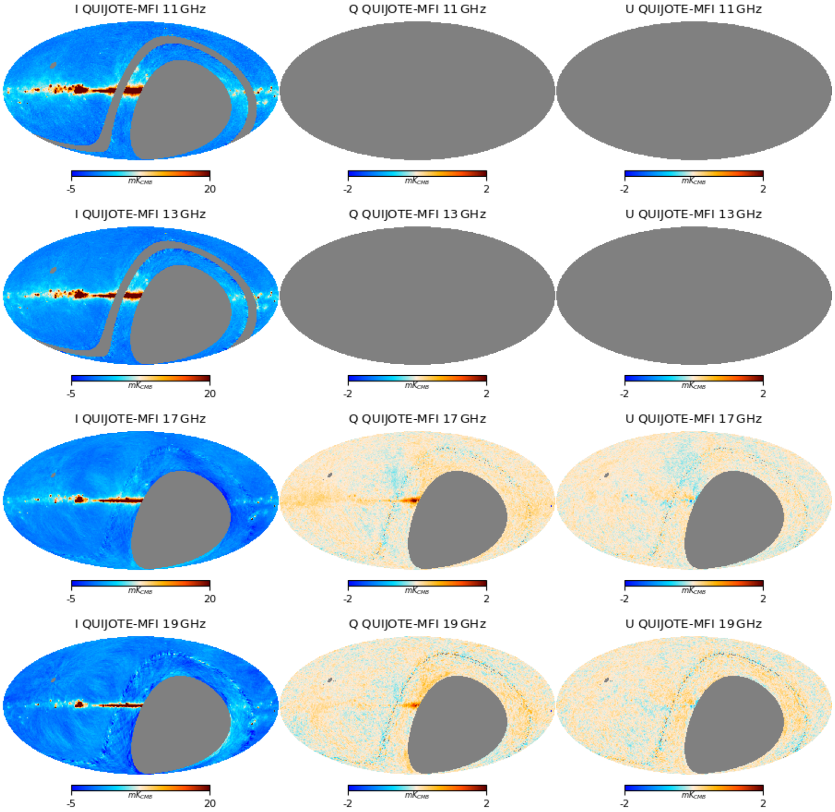

FIGURE 4.3— QUIJOTE-MFI wide-survey maps from horn 1 and horn 2. The maps are ordered from top to bottom with decreasing frequency to appreciate the scaling of the foregrounds signal: 11 GHz (first row), 13 GHz (second row), 17 GHz (third row), 19 GHz (last row). The columns are, from left to right, the I, Q and U recovered Stokes parameters. For visualization purposes, the maps are smoothed to 1 degree angular resolution. Units are $\mathrm{mK_{CMB}}$.

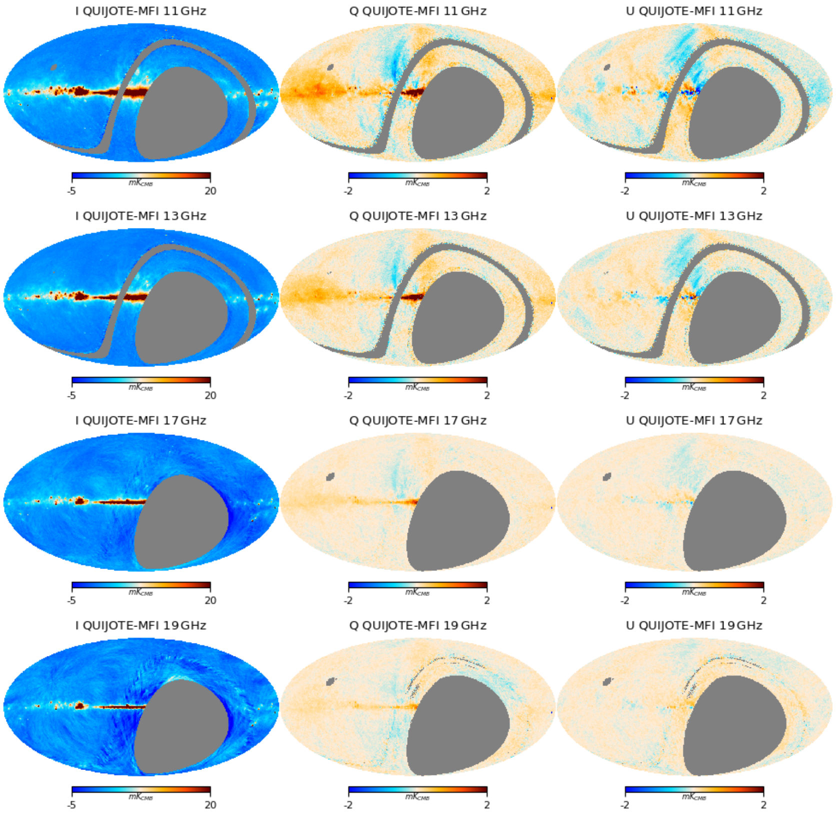

FIGURE 4.4— Same as in Fig. 4.3 but for horn 3 and horn 4.

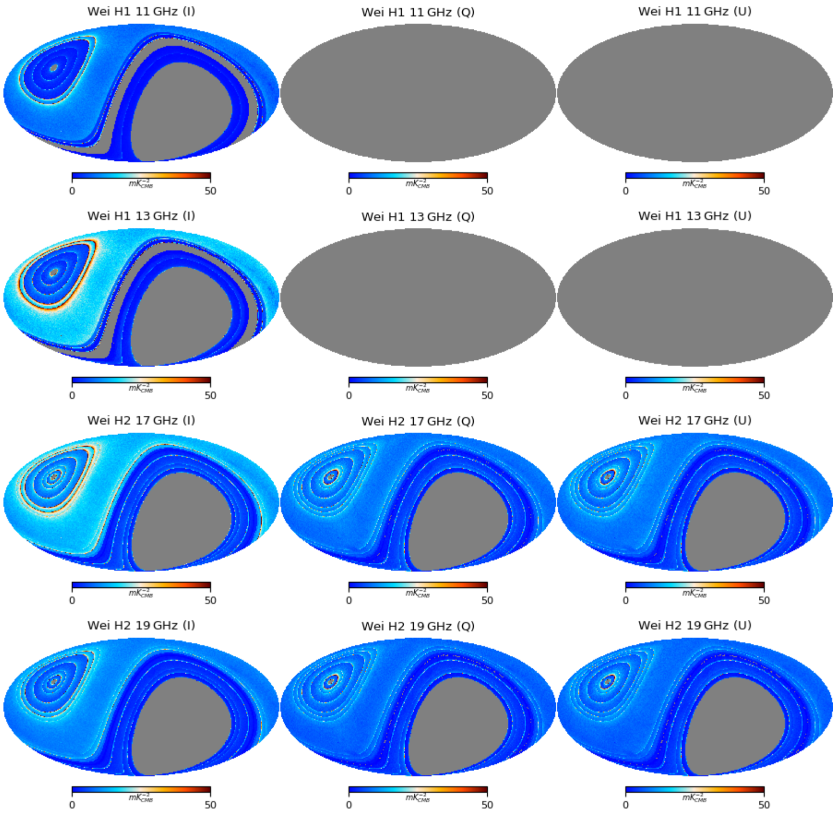

FIGURE 4.5— Weight maps of the QUIJOTE-MFI wide-survey from horn 1 and horn 2. The maps are ordered from top to bottom with decreasing frequency: 11 GHz (first row), 13 GHz (second row), 17 GHz (third row), 19 GHz (last row). The columns are, from left to right, the weights of the I, Q and U recovered Stokes parameters. Units are $\mathrm{mK}_{\mathrm{CMB}}^{-2}$.

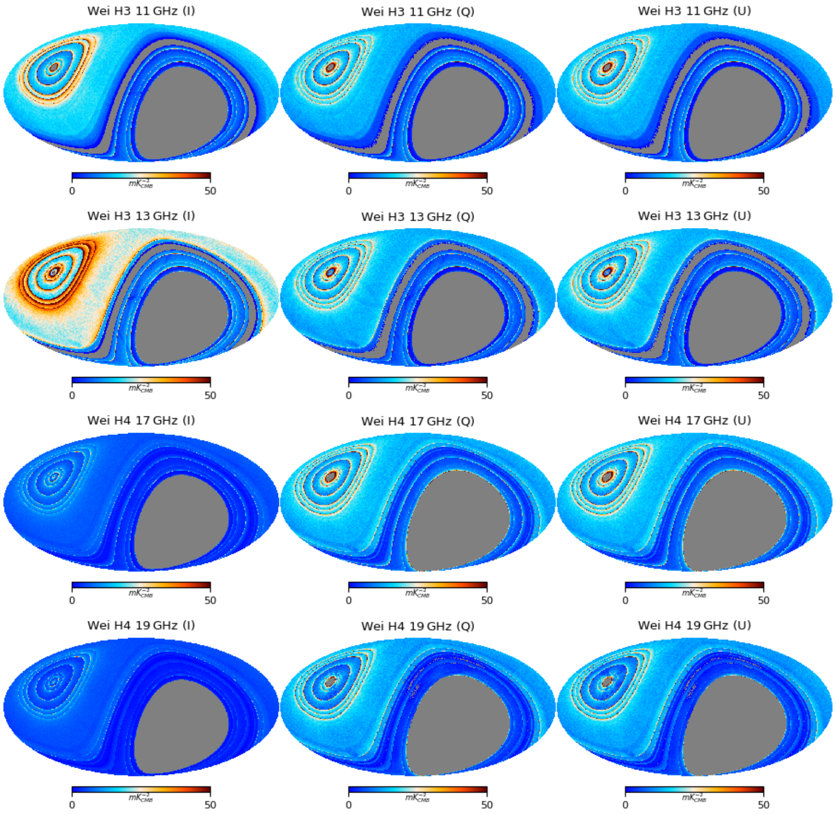

FIGURE 4.6— Same as in Fig. 4.5 but for horn 3 and horn 4.

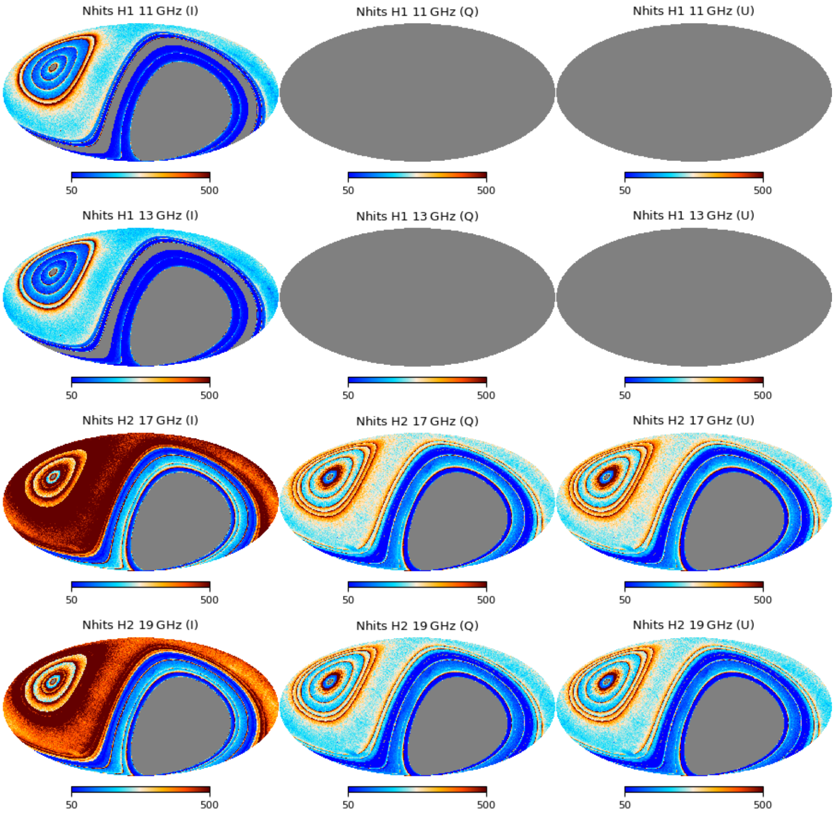

FIGURE 4.7— $n_{\rm hit}$ of the QUIJOTE-MFI wide-survey maps from horn 1 and horn 2. The maps are ordered from top to bottom with decreasing frequency: 11 GHz (first row), 13 GHz (second row), 17 GHz (third row), 19 GHz (last row). The columns are, from left to right, the $n_{\rm hit}$ of the I, Q and U recovered Stokes parameters. Units are number of hits of 40 ms samples in $n_{\rm side} = 512$ pixels.

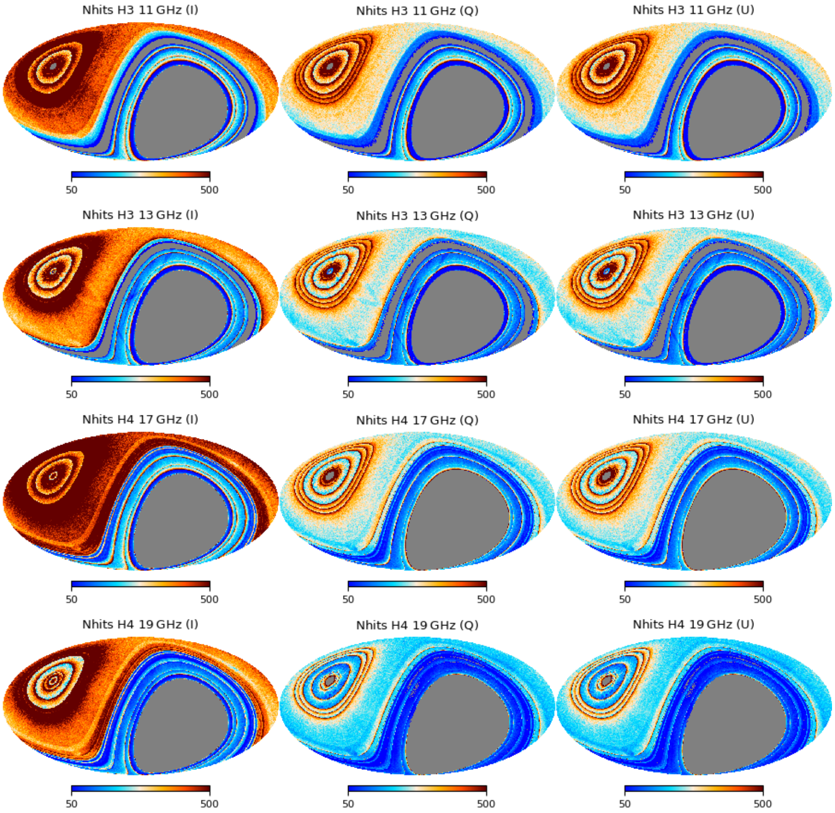

FIGURE 4.8— Same as in Fig. 4.7 but for horn 3 and horn 4.

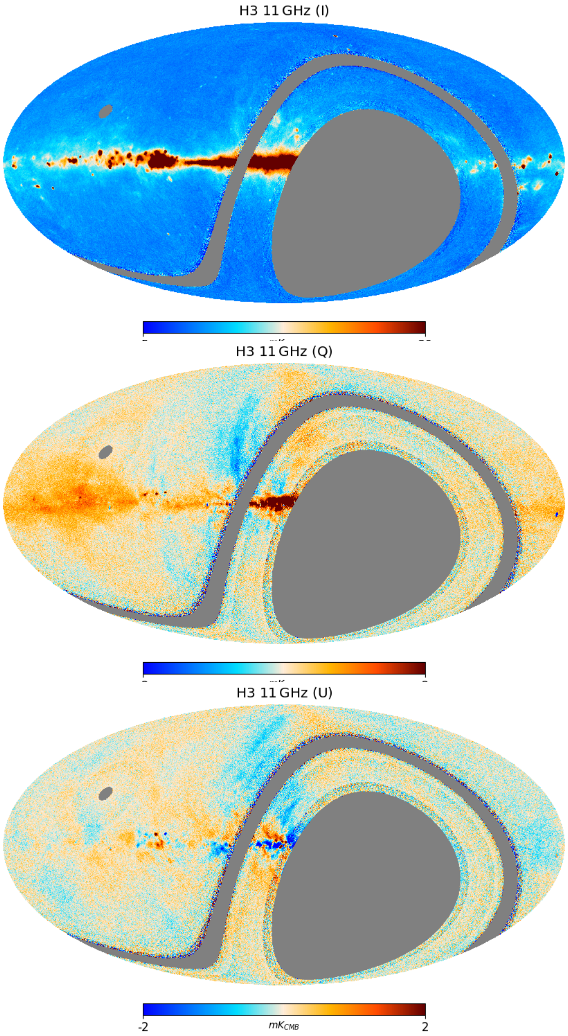

FIGURE 4.9— I, Q and U QUIJOTE-MFI wide-survey maps from horn 3 at 11 GHz, at the native angular resolution. For visualization purposes, the maps are degraded to $N_{\rm side} = 256$ ($\sim 0.2^\circ$). Units are $\mathrm{mK_{CMB}}$.

4.4 Angular power spectra

In order to characterize the synchrotron emission in harmonic space, we computed the angular power spectra (TT, EE, BB, TE, TB, and EB) of the maps within masks with different Galactic latitude cuts ($|b| > 5°$, $10°$, $20°$, $30°$, $40°$), and in the declination range $6° < \delta < 70°$. We applied to the masks a five degrees apodization with a cosine function, with the apodization routine of the NaMaster code (Alonso et al., 2019).

The spectra have been computed, within the aforementioned masks, with the NaMaster code enabling the option of "purification" of the E and B modes, which allows a better corrections of the E and B mixing matrix for cut-sky spectra.[2] The spectra are corrected (as in Eq. 1.43) by the MFI beam window functions that are shown in Fig. 2.6, and by the pixel window function.

The noise level is estimated from the *half*-difference null-test, which is presented in Sec. 4.5.3. The angular power spectrum of the *half*-difference map provides an estimate of the noise spectrum (N_ℓ), which is used here to subtract the noise contribution from the angular power spectra of the maps, in order to obtain the spectrum of the observed sky signal, as:

$$C_\ell^{\rm sky} = C_\ell^{\rm map} - N_\ell. \tag{4.4}$$

The uncertainty of the angular power spectra of the maps is assumed to be due to the noise in the data,[3] and to residual error of the power spectrum estimator, therefore it is estimated as the scatter of the spectra of synthetic maps obtained by adding to a fixed sky model (s) 100 noise simulations (n_i, $i = 1, ..., 100$) that have been generated specifically for the analysis of the wide-survey maps, based on the *half*-difference null-test (see Rubiño-Martín et al., in prep). We used as a sky model the simulations presented in chapter 3 (Sec. 3.5.2). The uncertainties of the map spectrum is therefore:

$$\sigma(C_\ell^{\rm map}) = std_i(C_\ell^{s+n_i}) \tag{4.5}$$

while the uncertainties of the noise only spectrum are estimated as:

$$\sigma(N_\ell) = std_i(C_\ell^{n_i}) \tag{4.6}$$

---

[2] A comparison of the performance of the codes NaMaster (with and without purification option of the E and B modes) and Xpol, with the QML code ECLIPSE (which provides more stable results at low ($\ell < 60$) multipoles, Bilbao-Ahedo et al., 2021), has shown that both NaMaster and Xpol produce consistent results at multipoles $\ell > 30$, except for the EB spectra computed with Xpol, which presents unexpected large oscillations, probably due to uncorrected mode coupling. In general, the NaMaster code with purification produces results more similar to those from the QML.

[3] No cosmic variance term is included in the uncertainties, given that the dominant signal is from the foregrounds and not from the CMB.

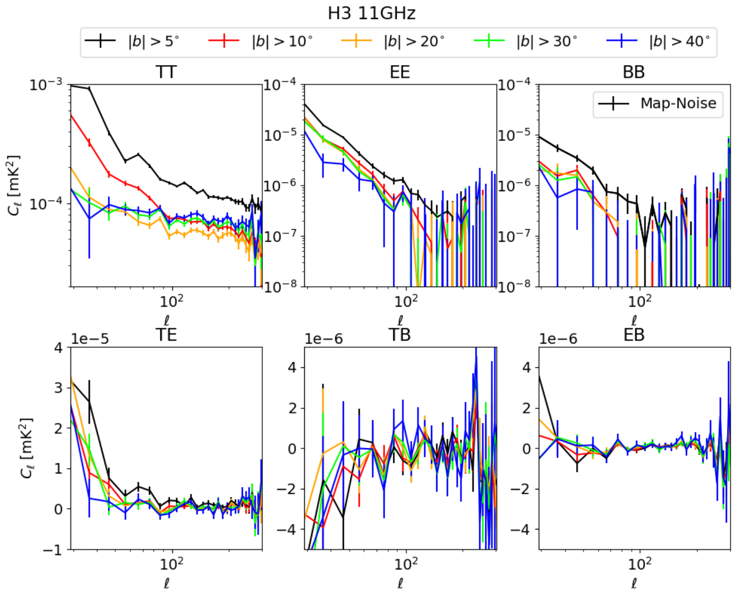

FIGURE 4.10— Angular power spectra of the sky signal (obtained as the C_ℓ of the map minus the C_ℓ of the noise, thick lines) and of the noise (*half*-difference null-test, see Sec. 4.5.3) of the 11 GHz map from horn number 3. We show the spectra of TT, EE, and BB, in logarithmic scale, in the top row, and the TE, TB, and EB cross-spectra, in linear scale, in the bottom one.

where N_ℓ^i are the spectra of the noise simulations. Finally, the uncertainty on spectrum of the observed sky ($C_\ell^{\rm sky}$) is obtained as the simple error propagation of Eq. 4.4:

$$\sigma(C_\ell^{\rm sky}) = \sqrt{\sigma(C_\ell^{\rm map}) + \sigma(N_\ell)} \tag{4.7}$$

with $\sigma(C_\ell^{\rm map})$ and $\sigma(N_\ell)$ given by Eqs. 4.5 and 4.6.

The results for the 11 GHz maps, from horn number 3, are shown in Fig. 4.10, where we show the sky signal spectra of TT, EE, and BB in the top row, and the TE, TB, and EB cross-spectra in the bottom one, in the multipole range $30 < \ell < 300$. Note that the signal observed here mainly comes from the emission of Galactic foregrounds, therefore, in polarization, the main component

$\lvert b \rvert$	$f_{\rm sky}$	A	α	c
		$[\mu{\rm K}^2]$		$[\mu{\rm K}^2]$
		EE		
5°	0.38	1.52 ± 0.15	-3.00 ± 0.16	0.07 ± 0.09
10°	0.34	1.05 ± 0.17	-2.72 ± 0.25	-0.13 ± 0.11
20°	0.27	0.81 ± 0.19	-2.96 ± 0.35	-0.09 ± 0.12
		BB		
5°	0.38	0.52 ± 0.14	-3.09 ± 0.41	0.12 ± 0.09
10°	0.34	0.20 ± 0.12	-3.13 ± 0.89	-0.06 ± 0.09
20°	0.27	0.18 ± 0.14	-3.05 ± 1.19	-0.09 ± 0.10

TABLE 4.6— Fitted power law parameters (Eq. 4.8) for the EE and BB spectra of the QUIJOTE 11 GHz polarization maps, for masks with different Galactic latitude cuts ($|b| >$ 5°, 10°, 20°), in the declination range $6° < \delta < 70°$, covering the corresponding sky fraction $f_{\rm sky}$ reported in the table.

$\lvert b \rvert$	$f_{\rm sky}$	$A_{\rm BB}/A_{\rm EE}$
5°	0.38	0.34 ± 0.10
10°	0.34	0.19 ± 0.12
20°	0.27	0.22 ± 0.18

TABLE 4.7— Ratio of the BB over EE fitted amplitudes at $\ell = 80$, for the QUIJOTE 11 GHz polarization maps, for masks with $|b| > 5°$, 10°, 20° and $6° < \delta < 70°$.

is synchrotron. We can observe that, in intensity (TT), we have a significant detection of the sky signal, for all the masks, in the whole range of multipoles. In polarization, the sky signal is significantly detected up to $\ell \sim 100$ for EE, in all the masks. The BB signal is detected up to $\ell \sim 100$ for the mask with $|b| > 5°$, up to $\ell \sim 80$ for the masks with $|b| > 10°$ and $|b| > 20°$.

4.4.1 Fit of EE and BB auto-power spectra

In order to characterize the relative power of the E and B-modes in the QUIJOTE maps, we carried out the fitting of the EE and BB spectra, in the range of multipoles $30 < \ell < 300$, with a power law of the type (as in Krachmalnicoff et al., 2018):

$$C_\ell = A \left(\frac{\ell}{80} \right)^\alpha + c \tag{4.8}$$

where A is the amplitude at $\ell = 80$, α is the slope, and c is a global constant which represents the contribution on unresolved Poisson distributed sources. We report the fitted parameters in Tab. 4.6, obtained for the masks with $|b| >$

5°, 10°, and 20°, where BB is detected, at least, up to $\ell \sim 80$. We computed then the ratio between the amplitude of the EE and BB spectra at $\ell = 80$ for these three masks, obtaining the results shown in Tab. 4.7, which point to a $A_{\rm BB}/A_{\rm EE}$ ∼0.2–0.3. This agrees with the results that will be presented in Vansyngel et al. (in prep.), which contains a detailed study of the polarization QUIJOTE-MFI maps from an harmonic space perspective, in combination with the WMAP and Planck maps.

A similar work by Krachmalnicoff et al. (2018), presented an analysis based on the S-PASS maps of the southern sky at 2.3 GHz (Carretti et al., 2019), obtaining (at $b > |20|°$) the power law indices $\alpha_{EE} = -2.59 \pm 0.01$ and $\alpha_{BB} = -2.59 \pm 0.02$, and values of the BB/EE amplitudes ratio $A_{\rm BB}/A_{\rm EE} = 0.41 \pm 0.08$, which is somewhat higher but statistically consistent with our results. Similar studies were also done using Planck data (Planck Collaboration et al., 2018c), where they obtained, for the synchrotron component, power law indices[4] $\alpha_{EE} = -2.84 \pm 0.05$ and $\alpha_{BB} \sim -2.76 \pm 0.09$, and the ratio $A_{\rm BB}/A_{\rm EE} = 0.34$ (with $f_{\rm sky} = 0.78$, ℓ=4—140, using the `Commander` component-separation technique). Our results are consistent with those from Planck for the synchrotron component. The same study was also presented in Planck Collaboration et al. (2018c) for the dust component, where they quoted a ratio $A_{\rm BB}/A_{\rm EE} = 0.50$, and power law indices (in C_ℓ) $\alpha_{EE} = -2.28 \pm 0.04$ and $\alpha_{BB} = -2.48 \pm 0.06$ (with $f_{\rm sky} = 0.42$, ℓ=40—600, using frequency map cross-correlation). The results obtained in this work support the evidence that the ratio of B and E-modes for synchrotron is lower than that measured for the dust.

4.4.2 TE, TB and EB cross-power spectra at 11 GHz

We observe a positive correlation between intensity and E-modes ($C_\ell^{TE} > 0$), obtaining a marginal detection of the TE spectrum at low multipoles. We also observe, as expected, a null correlation[5] in TB and EB. We discuss, in particular, the EB cross-spectrum that, under the assumption of parity-invariant radiation processes, and accurate calibration of the polarization angle, is expected to be zero. We computed the uncertainty of the EB spectrum combining

---

[4] The analysis in Planck Collaboration et al. (2018c) was done fitting the D_ℓ instead of the C_ℓ, therefore we relate power law index measured in Planck with our result as $\alpha_{Planck} \sim \alpha{+}2$.

[5] Recent works by Weiland et al. (2011); Clark et al. (2021) observed a positive TB cross-spectrum for thermal dust emission, using Planck 353 GHz data, and predicted a not-null EB spectrum ($\langle D_\ell^{EB} \rangle \lesssim 2.5\,\mu{\rm K}^2_{\rm CMB}$) for thermal dust. The origin of these correlations is attributed to misalignment between the dust density and the local magnetic field. However at our frequencies we observe synchrotron radiation, which is generated by the direct presence of the magnetic field, and the previously mentioned misalignment should not be present, corresponding to an expected $C_\ell^{TB} = C_\ell^{EB} = 0$.

in quadrature the uncertainty given by Eq. 4.7 with a component that depends on the uncertainty on the polarization angle (Minami et al., 2019), as:

$$\sigma'^2(C_\ell^{\mathrm{sky,EB}}) = \sigma^2(C_\ell^{\mathrm{sky,EB}}) + \left(\frac{1}{2}\left(C_\ell^{\mathrm{sky,EE}} - C_\ell^{\mathrm{sky,BB}}\right)\tan(4\alpha)\right)^2 \tag{4.9}$$

where $C_\ell^{\mathrm{sky,EE}}$ and $C_\ell^{\mathrm{sky,BB}}$ are the observed EE and BB spectra, and $\alpha = 1°$ is a conservative estimate of uncertainty on the polarization angle. In the range of relevant multipoles for the QUIJOTE experiment $30 < \ell < 300$, the EB spectrum is compatible with zero.

4.5 Noise characterization

A very common and useful tool for the characterization and validation of maps relies on the study of null-tests maps, which are maps obtained from the split of the full data-set into two complementary sub-sets (e.g., m_1 is obtained from the first half of the data and m_2 from the second half). The normalized difference between two null-test maps provides a map of the noise of the data, which is usually studied at the map and angular power spectrum levels, in order to characterize the noise properties of the map containing all the data. The study of the null-tests also allows us to identify and characterize possible systematics in the data. We present in the following section (Sec. 4.5.1) the formalism of the null-tests analysis, and in Sec. 4.5.2 the definition and the study of the null-tests of the wide-survey maps. Then, in Sec. 4.5.4 and 4.5.5, we use the null-tests to measure the level of noise correlation between the two frequencies of the same horn (inter-frequency) and between the correlated and uncorrelated channels of the same horn and frequency (inter-channel).

4.5.1 Null-tests formalism

The data that are used to construct the map m are splitted in two subsets that contain the same sky signal and independent noise properties: m_1 and w_1 are, respectively, the map and the weights of the first data split, and m_2 and w_2 are the map and weights of second one. The weighted sum of the two maps is computed as:

$$s = \frac{w_1 \cdot m_1 + w_2 \cdot m_2}{w_1 + w_2} \ , \tag{4.10}$$

which approximately resembles the total map m. The difference of the two maps is defined as:

$$d = \frac{m_1 - m_2}{w} \ , \tag{4.11}$$

which is normalized by the factor:

$$w = \sqrt{(w_1 + w_2)\left(\frac{1}{w_1} + \frac{1}{w_2}\right)} \tag{4.12}$$

If there are not systematic problems in the data, m_1 and m_2 contain the same sky signal, which cancels out in the subtraction. It results that the difference map d is a combination of the noise in m_1 and m_2. In particular, it can be shown that, by applying simple error propagation under the assumption that the noise in m_1 and m_2 is uncorrelated, the variance of the difference map d (Eq. 4.11) corresponds to the variance of the weighted sum map s (Eq. 4.10), which in turn represents the variance of the final map m:

$$\sigma_d^2 = \sigma_s^2 \sim \sigma_m^2 \tag{4.13}$$

Consequently, the difference maps can be used as a representation of the noise of the final map, and the angular power spectrum of the difference map corresponds to the angular power spectrum of the noise of the final map.

4.5.2 Null-tests of the wide-survey maps

A number of data split options have been implemented for the QUIJOTE-MFI wide-survey maps, in order to perform null-tests as described above. They are:

- **Half**. The selection of the data from the full mission is performed according to the calendar date of the observations, by splitting, in each period, the first half of the observations from the second one. In other words, we select the first half of the observations taken in each of the four periods (p=1,2,5,6) to construct m_1, and the second half is used for m_2. The difference between the two half maps is representative of the global noise properties of the final QUIJOTE-MFI wide-survey maps.

- **Rings**. The scanning strategy of the QUIJOTE-MFI wide-survey consists of consecutive scans of 30 s, at fixed elevation, scanning 360 deg in azimuth, the so called *rings* (more details in Section 4.1.1). Two consecutive rings are expected to have a correlated contribution from the atmosphere and from large scales ($f < f_{\rm cut} = 1/30\,{\rm s}^{-1}$) instrumental $1/f$ noise, while the $1/f$ at scales smaller than one ring ($f > f_{\rm cut}$) is not correlated from ring to ring. In this null-test the data are selected in even and odd rings: if the data belong to a ring that is labelled with an even number they go to split number 1, and if the data belong to a ring labelled with an odd number they go to split number 2. In the difference map of this null-test, the atmospheric $1/f$ noise is expected to cancel out, while the instrumental noise that varies in time scales shorter than 30 s will be preserved. In this way we can characterize at the map and power spectrum level the effect of the $1/f$ noise with frequency higher than 1/30 s.

- **Daynight**. A data split between the data taken during the day or during the night is also implemented. The day is defined as the 12 hours starting at 8:00 and ending at 20:00 (UTC), and the night are the complementary 12 hours. A null-test with day and night maps would highlight the differences between the data taken during the day and during the night. The data taken during the day are expected to be more noisy due to the higher atmospheric temperature, higher PWV values, higher temperature of the cryostat and possible far-sidelobes contamination from the Sun.

- **Halfrings**. The data are selected if they are taken in the rising direction (East), at azimuth $az < 180$ deg, or in the setting direction (West), at $az > 180$ deg. This null-test is useful to identify the sources of RFI, as describes in Sec. 4.1.5. Indeed, while the telescope is observing by scanning with fixed rings in local coordinates (see Sec. 4.1.1), an astrophysical source transits across the sky, and it is observed twice a day: when it rises ($az < 180$ deg) and when it is sets ($az > 180$ deg). A source of RFI, however, does not follow the rise and set path. For example, a geostationary satellite is stable in local coordinates, and it is observed in only one azimuth position, with $az < 180$ deg or $az > 180$ deg, not in both intervals. The subtraction of the maps obtained from the two azimuth ranges cancels out the sky signal, while the RFI remains, because it not observed in both maps, but only in one of them. For this reason this null-test is used as a check of residual interference.

- **PWV**. We divide the data according to the average level of PWV during the observations, in each period. We construct one map with data take with low PWV, and the other with data with high PWV. PWV information is extracted by GPS-based measurements from an antenna located at the Observatorio Amosférico de Izaña, about 1 km away from the Teide Observatory.[6] This data split allows us to characterize the effect of the atmospheric $1/f$ contamination according to the water vapour concentration during the observations.

---

[6] These data were kindly provided to us by Emilio Cuevas, the director of the Centro de Investigaciøn Atmosféricas de Izaña.

- **Tbem**. The data are selected according to the average temperature of the BEM during the observation. We construct maps of observations with high and low BEM temperatures, in order to characterize possible systematics and gain fluctuation effects deriving from temperature variations of the BEM.

4.5.2.1 Construction of the null-test maps

For the construction of the various null-test maps, the PICASSO code (chapter 3 and Guidi et al., submitted) takes as an input the type of null test, and identifies the data splits while importing the TOD. We implemented the selection of the data directly in the PICASSO map-making code, for the null-tests[7] of *rings*, *daynight*, and *halfrings*. For the *half*, PWV and *tbem* null-test maps, the PICASSO code instead requires a list of the selected observations for the corresponding data split, or a master file indicating which observations, among those give in input, belong to a certain split. The data samples that do not belong to the selection are down-weighted ($w_i = \sigma_i^{-2} = 0$) during the construction of the map.

The baselines of the null-test maps can be either calculated using the full data set, or only with the data of the selected split. The computation of the baselines with the full data set has the advantage that the reconstruction of the $1/f$ noise is more accurate, thanks to the large number of data samples crossing the pixel (see Chapter 3 fore more details). However, if we use the full data-set instead of the two totally independent splits alone for the determination of the baselines, we unavoidably generate a correlation between the two null-test maps, and such a correlation is not always desired. Usually, for the analysis of the null-tests, we look for two uncorrelated samples of the full data set. Consequently, in most of the cases (depending on the final goal of the analysis) it is convenient to make maps of the null-tests using two independent determinations of the baselines, which are obtained separately with the data of each single data split.

4.5.2.2 Angular power spectra of the null-tests

We computed the angular power spectra of the null-test maps with the same mask and methodology as in Sec. 4.4, with no correction of the beam and pixel

---

[7] Four additional data-splits are implemented in PICASSO, what we call the *samples*, *altsamples*, *2samples*, *5samples* null-tests. They assign consecutive samples (or groups of 2 and 5 samples) to the two data splits, in order to attempt a perfect cancellation of the $1/f$ noise in the difference maps, and reach the white noise level at all angular scales. However, these null-tests are affected by not-fully understood effects at pixel and beam scales.

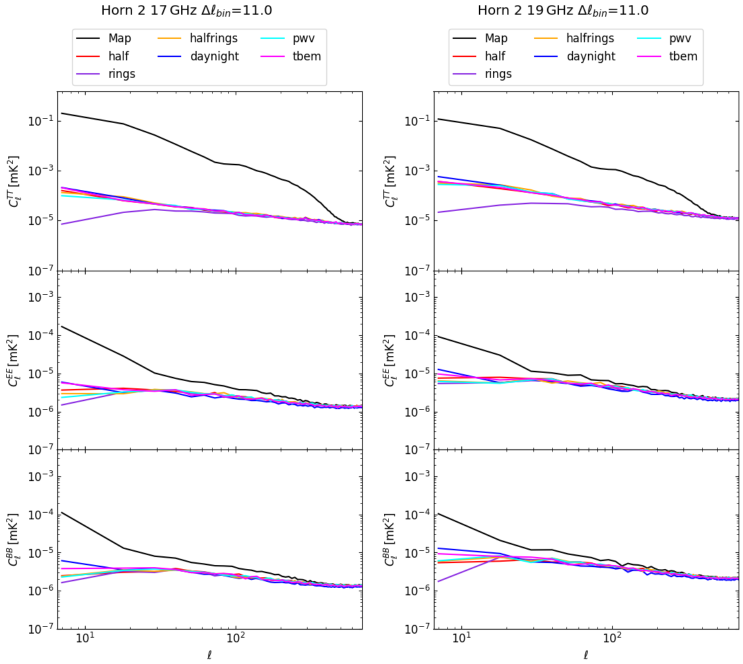

FIGURE 4.11— Angular power spectra of the map and null-tests of the wide-survey data from horn 2, 17 GHz (left) and 19 GHz (right). TT, EE and BB are represented, respectively, in the upper, central and bottom panels. The power spectrum of the map is shown in black. The power spectra of the null-tests are shown in different colors as represented in the legend.

window function. The angular power spectra of the null-tests of horns 2, 3 and 4 are shown in Fig. 4.11–4.13.

The *half*-difference null-test traces the global noise of the maps, being it asymptotically flat at high multipoles, towards the white noise level of the maps, and increasing at low multipoles (large angular scale) due to residual $1/f$ noise. Other null-tests such as *PWV*, *daynight* and *tbem*, are useful to characterize the $1/f$ noise due to the level of PWV during the observation, to day/night environmental and instrumental drifts, and to variations of the BEM temperature. We can notice that they all approximately trace the global $1/f$ power given by the *half*-difference null-test, showing good internal agreement.

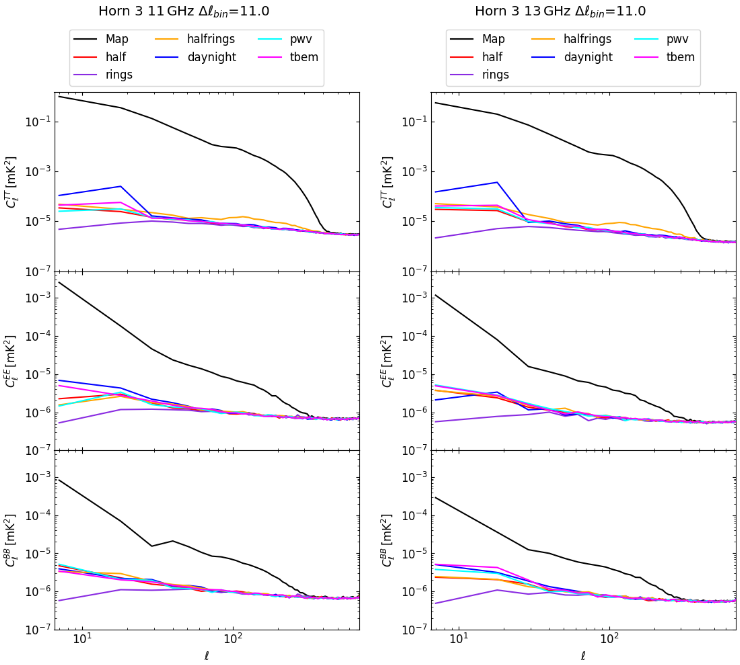

FIGURE 4.12— Same as in Fig. 4.11 for horn 3, 11 GHz (left) and 13 GHz (right).

In the *rings* null-test, instead, the $1/f$ noise contribution that affects time scales smaller than that of one azimuth scan (30 s), is canceled. It follows that the power spectrum of the *rings* null-test is comparable to the others at intermediate and high multipoles, while it decreases at low multipoles. This effect is particularly evident in intensity, where the $1/f$ noise is higher, telling us that there are $1/f$ variations in the data at scales longer than 30 s.

The *half*-difference null-test is taken as a reference for the global noise level of the QUIJOTE-MFI wide survey maps, and it is analyzed in detail in Sec. 4.5.3.

4.5.3 Noise angular power spectra from the *half*-difference

The *half*-difference null-test provides, in the harmonic space, the (total) noise angular power spectra ($N(\ell)$) of the wide-survey maps. They are shown in

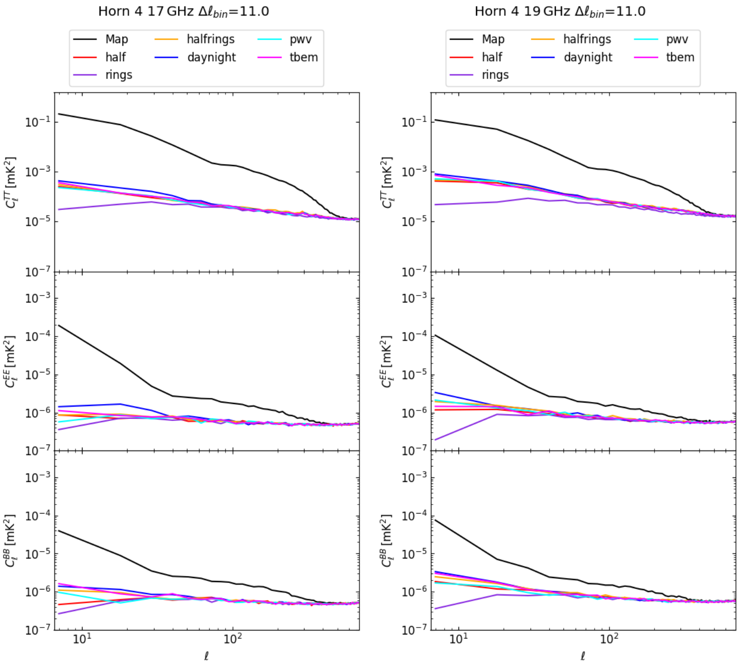

FIGURE 4.13— Same as in Fig. 4.11 for horn 4, 17 GHz (left) and 19 GHz (right).

Fig. 4.14, which is a clear picture of quality of the maps as a function of multipoles, depending on the horn and frequency channel. The error bars are obtained as the scatter of the noise simulations, as in Sec. 4.4.

We can notice that, in intensity (TT), horn number 3 is the one with best quality in terms of noise, while horn number 4 is the most noisy one. In polarization, instead, horn number 4 performs better than the others, while horn 2 is the most noisy one. The noise of the polarization data from horn number 3 is slightly larger than that from horn number 4, but given that the signal at low frequencies is brighter, the polarization maps of horn number 3 are those with better signal-to-noise. All these considerations are in good agreement with the discussion presented in Sec. 4.1.3, where we presented the noise parameters of the wide-survey data in the time ordered domain.

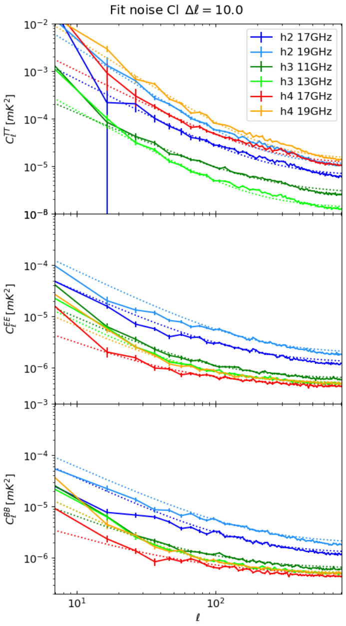

Horn	Freq [GHz]	$\sigma_{1\text{-deg}}$ [μK]	α	ℓ_k
		TT		
2	17	134	1.5	229
2	19	175	1.8	229
3	11	86	1.3	221
3	13	61	1.6	192
4	17	176	1.5	230
4	19	201	1.8	244
		EE		
2	17	59	1.2	144
2	19	74	1.3	174
3	11	42	1.2	86
3	13	38	1.4	75
4	17	36	1.1	54
4	19	38	1.2	73
		BB		
2	17	59	1.3	148
2	19	74	1.2	173
3	11	42	1.1	85
3	13	38	1.3	76
4	17	36	0.9	62
4	19	38	1.3	77

FIGURE 4.14— Left: angular power spectra of the *half*-difference of the wide-survey data. TT, EE and BB are represented, respectively, in the upper, central and bottom panels. The power spectra of the different MFI channels are shown with different colours (see legend), and the dotted lines represent the fitted model. Right: fitted parameters from the angular power spectra, with the procedure presented in Sec. 3.6.2.1.

We fitted the noise power spectra represented in Fig. 4.14 to an $1/\ell^{\alpha}$ slope (as in Eq. 3.55), with the technique described in Sec. 3.6.2.1. The fitted model is represented by the dotted lines plotted on top of the measured noise spectra, while the fitted parameters are reported in the right panel of the same figure. We can notice that the noise in intensity is dominated by a $1/\ell$ component, which is due to the large $1/f$ noise in the intensity data. In polarization instead, we can notice that the correlated noise is less important since the knee-multipole $\ell_{\rm k}$ is significantly lower than that of the intensity.

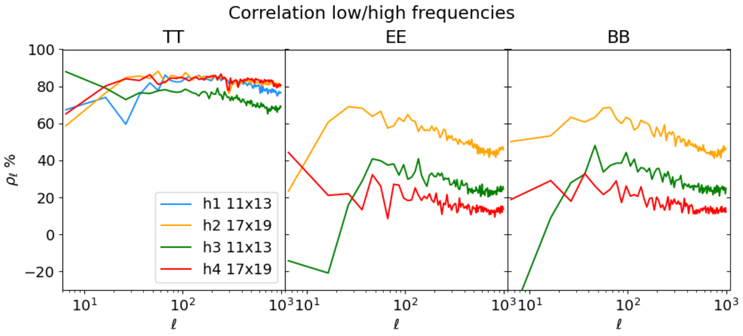

FIGURE 4.15— Inter-frequencies correlation of the noise in the low and high frequency maps, observed by the same horn, for TT (left), EE (center), BB (right).

4.5.4 Inter-frequency correlation

The data coming from two different frequency splits of the same MFI horn (e.g., Horn 3 11 GHz and 13 GHz) are contaminated by approximately the same $1/f$ noise. This is due to the fact that all the channels from the same horn share the same amplifier, which is the main source of $1/f$ noise (see Fig. 2.4). In order to quantify the degree of correlation of the noise of the two maps that are obtained from the low and high frequencies of the same horn, we computed the correlation between the *half*-difference noise maps (d) using cross-correlations as:

$$\rho \equiv \left\langle \frac{C_\ell^{\mathrm{d}(h,f_1),\mathrm{d}(h,f_2)}}{\sqrt{C_\ell^{\mathrm{d}(h,f_1)} C_\ell^{\mathrm{d}(h,f_2)}}} \right\rangle_{\ell \in [20,200]} \tag{4.14}$$

In this notation, $h = (1, 2, 3, 4)$ indicates the MFI horn, and f_1 and f_2 are its low and high frequencies. $C_\ell^{\mathrm{d}(h,f_1),\mathrm{d}(h,f_2)}$ is the cross-correlation of the half difference maps at two different frequencies, from the same horn h, and $C_\ell^{\mathrm{d}(h,f_1)}$ and $C_\ell^{\mathrm{d}(h,f_2)}$ are the auto power spectra of the two half difference maps. The ratio between the cross-correlation and the square-root of the two auto power spectra (the argument inside $< \cdot >$ in Eq. 4.14) corresponds to the correlation between the noise of the two frequency maps as a function of the multipoles, which we can call ρ_ℓ. After checking that ρ_ℓ is approximately constant in ℓ, we can average it in the range $\ell \in [20, 200]$, to obtain a global estimate of the correlation ρ. We also provide a simplistic uncertainty for the estimated

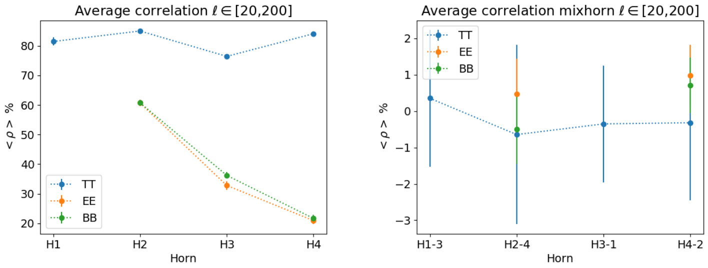

FIGURE 4.16— Average inter-frequency correlation of the noise in the low and high frequency maps, observed by the same horn (left panel; error bars are lower than the points size), and observed by two different horns (right panel). The values are reported in Tab. 4.8.

Horn	TT corr (%)	EE corr (%)	BB corr (%)
1	81.5±1.4	-	-
2	85.0±0.3	60.7±1.0	60.8±0.9
3	76.5±0.4	32.8±1.4	36.2±1.1
4	84.1±0.3	20.9±1.2	21.7±1.2

TABLE 4.8— Inter-frequency correlation of the noise in the low and high frequency maps, observed by the same horn, corresponding to the values shown in the left panel of Fig. 4.16.

correlation ρ, by computing the standard deviation of ρ_ℓ in the aforementioned multipole range, scaled by the square-root of the number of averaged values.

We show the results from this correlation analysis in Fig. 4.15, where we draw the TT, EE and BB ρ_ℓ, and in the left panel of Fig. 4.16, where we collect the average correlations of each horn. We can notice that the inter-frequency correlation, in intensity, is at the level of ∼ 80%, while in polarization it is 60 − 20%, depending on the horn. The estimated values are reported in Tab. 4.8. We verified that the source of correlation in polarization is consistent with the residual $1/f$ noise in the data, which is higher than expected in the correlated channels in period 5 and 6, as commented in Sec. 4.1.3.

In order to check that the observed inter-frequency correlation is due to the instrumental $1/f$ noise and not to the correlated signal produced by the atmosphere, we performed the same correlation analysis, but we compared the two frequencies coming from two different horns among those observing the same frequency bands, as:

$$\rho = \left\langle \frac{C_\ell^{\mathrm{d}(h,f_1),\mathrm{d}(h',f_2)}}{\sqrt{C_\ell^{\mathrm{d}(h,f_1)} C_\ell^{\mathrm{d}(h',f_2)}}} \right\rangle_{[20,200]} \tag{4.15}$$

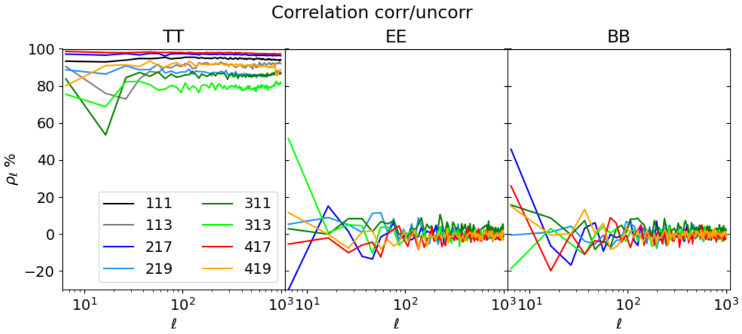

FIGURE 4.17— Correlation of the noise maps between the correlated and uncorrelated channels, from the same horn and frequency, for TT (left), EE (center), BB (right).

with $(h, h') = (1, 3)$, $(3, 1)$, $(2, 4)$, $(4, 2)$. The result of this analysis is shown in the right panel of Fig. 4.16. We can observe that in this case the correlation between low and high frequencies coming from two different horns is negligible. It follows that the noise correlation introduced by the atmosphere is lower than that induced by the instrumental $1/f$ noise.

4.5.5 Inter-channel correlation

Given the MFI instrument model (Sec. 2.3.1), for any given horn, in intensity, we expect a high level of correlation between the noise affecting the correlated and uncorrelated channels. This is because the X and X+Y channels share the same LNA (as shown in Fig. 2.4), which injects the same $1/f$ in the two channels. The same consideration is valid for the Y and X-Y channels.

Similarly to the inter-frequency analysis presented in the previous section, we measure the correlation of the noise between the correlated and uncorrelated channels maps, of each single MFI horn and frequency, before combining them as in Eq. 4.10. The procedure is totally equivalent to that presented in Sec. 4.5.4, where the *half*-difference maps of two different frequencies are replaced by the *half*-difference maps of the correlated (d_c) and uncorrelated (d_u) channels, from the same horn an frequency, as:

$$\rho = \left\langle \frac{C_\ell^{\mathrm{d_c},\mathrm{d_u}}}{\sqrt{C_\ell^{\mathrm{d_c}} C_\ell^{\mathrm{d_u}}}} \right\rangle_{\ell\in[20,200]} \tag{4.16}$$

The results are presented in Fig. 4.17, where we show the correlation as a function of multipoles, and in Fig. 4.18, where we show the average correlation

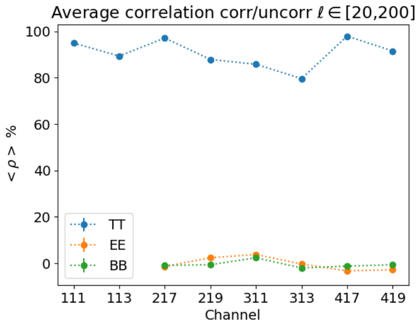

FIGURE 4.18— Average correlation of the noise maps between the correlated and uncorrelated channels, from the same horn and frequency. Error bars are lower than the points size.

Horn,freq	TT corr (%)	EE corr (%)	BB corr (%)
1,11	94.99±0.09	-	-
1,13	89.37±1.07	-	-
2,17	97.14±0.08	−1.36±1.10	−0.91±1.37
2,19	87.91±0.34	2.40±1.19	−0.60±1.04
3,11	85.82±0.26	3.81±0.75	2.38±1.18
3,13	79.65±0.42	−0.32±0.89	−2.01±0.91
4,17	97.95±0.01	−3.26±1.07	−1.22±1.12
4,19	91.56±0.22	−2.81±0.80	−0.61±1.15

TABLE 4.9— Inter-channel correlation of the noise between the correlated and uncorrelated channels, from each MFI horn and frequency, corresponding to the values shown in Fig. 4.18.

for each horn and frequency. It can be observed that the correlation in intensity is very high, around $\sim 90\,\%$, as expected due to the large amount of $1/f$ noise in the data. On the other hand, in polarization, there is approximately no correlation, as expected from the low level of $1/f$ in polarization data. The estimated average correlation values can be found in Tab. 4.9.

4.6 Internal calibration tests with cross-correlations

We performed several cross-correlation analyses to test the internal calibration of the wide-survey maps. We tested the:

- *Inter-horn* calibration (see Sec. 4.6.1), which provides the relative amplitude between the signal measured by different horns that measure the same frequency (e.g., H1/H3 at 11 GHz). We did this test in intensity and polarization.
- *Inter-period* calibration (see Sec. 4.6.2), which provides, for each MFI horn/frequency channel, the relative amplitude between the signal measured in different periods and in the final map, in which all the periods are combined together. We did this test in intensity and polarization.
- *Intra-nulltest* calibration (see Sec. 4.6.3), which provides the relative amplitude of the signal between the two halves of each null-tests, among those defined in Sec. 4.5. We did this test in intensity and polarization.
- *CMB cross-calibration* (or detection of the CMB) (see Sec. 4.6.4), which provides the relative amplitude between the CMB anisotropies intensity map and the QUIJOTE-MFI maps. We did this test in intensity only since there is not sufficient signal-to-noise to obtain sensitive results in polarization.

The calibration uncertainty quoted for the QUIJOTE maps is 5% (Rubiño-Martín et al., in prep), which is due to a combination of the $1/f$ noise in the maps and the intrinsic uncertainty of the models that are used for the flux density calibration (Génova-Santos et al., in prep.). We used the aforementioned tests as a cross-check of the calibration of the QUIJOTE-MFI maps. The details and the results of these analyses are presented in the following sections, as well as in Rubiño-Martín et al. (in prep.).

4.6.1 Inter-horn

If we assume that two different MFI horns h and h', that are sensitive to the same frequency f, differ by a relative calibration factor A, we can simply relate[8] the two maps m as:

$$m(h, f) = A \cdot m(h', f) \tag{4.17}$$

---

[8] There is not perfect equality in Eq. 4.17 due to the different noise in the maps. However, the next step is a cross-correlation with a map whose noise is uncorrelated with that in $m(h, f)$ and $m(h', f)$, therefore the cross-correlation of the noise turns to zero. This note is also valid for the development of the equations in Sec. 4.6.2 and 4.6.3.

where (h,h')=(1,3) for $f = 11$, 13 GHz, and (h,h')=(2,4) for $f = 17$, 19 GHz. We can do a cross-correlation of the right and left terms of the equation above with a reference map X, whose noise is uncorrelated with that of $m(h,f)$ and $m(h',f)$, and obtain:

$$C_\ell^{(h,f),X} = A^X \cdot C_\ell^{(h',f),X} \tag{4.18}$$

In general, the ratio of cross-correlations $A^X(\ell) = C_\ell^{(h,f),\,X}/C_\ell^{(h',f),\,X}$ is a function of the multipoles, and, under the assumption that this ratio is constant, we can compute an average in a selected range of multipoles, and determine one single value for A^X. This can also be repeated with a number n_X of different reference maps X, to obtain a final estimate for A averaged among all available A^X. The cross-calibration factor A and its uncertainty σ_A can therefore be analytically written as:

$$A = \left\langle \left\langle \frac{C_\ell^{(h,f),\,X}}{C_\ell^{(h',f),\,X}} \right\rangle_{\ell\in[30,200]} \right\rangle_X \tag{4.19}$$

$$\sigma = std_X \left(\left\langle \frac{C_\ell^{(h,f),\,X}}{C_\ell^{(h',f),\,X}} \right\rangle_{\ell\in[30,200]} \right) / \sqrt{n_X} \tag{4.20}$$

where $\langle\rangle_{\ell\in[30,200]}$ indicates an average operation in the range $\ell \in [30, 200]$, and $\langle\rangle_X$ is the average over the results obtained with different external maps. The value $\ell = 30$ is used as the reference lowest multipole for two reasons: at $\ell \gtrsim 30$ the pseudo-C_ℓ estimator is not affected by mode coupling due to the incomplete sky coverage (see Sec. 2.4.7), and the filtering operations that are applied to the maps do not suppress or mix the power of the sky signal (see Sec. 4.1.5). These two effect are instead noticeable at $\ell \lesssim 30$. The uncertainty on A can be estimated with Eq. 4.20, as the standard deviation of the values of A^X obtained with each single external map, scaled by the square-root of the number n_X of external maps involved in the analysis.

The WMAP and Planck-LFI maps are good external reference candidates for this analysis, because they are dominated by the emission of low frequency foregrounds, like QUIJOTE is, and their noise is not correlated with that of the QUIJOTE maps. We used therefore the 9-year WMAP maps (frequency bands: K, Ka, Q, and V) and the Planck-LFI maps of release 2 (2015, bandpass corrected, at frequencies: 30, 44, and 70 GHz), which has good control over the intensity-to-polarization leakage.

The cross-correlations needed for this analysis are computed with XPOL, within the area selected by the mask shown in Fig. 4.19, which covers the declination range $\delta \in [8, 77]$ deg. The mask is apodized with a 5 degrees cosine

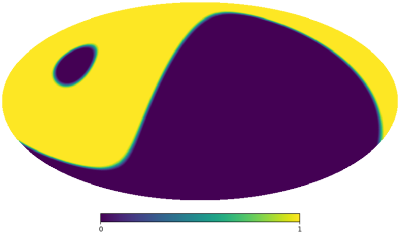

FIGURE 4.19— Mask used for the inter-horns analysis, covering $\delta \in [8, 77]\, deg$.

function with the apodization routine of the NaMaster publicly available code Alonso et al. (2019). The maps to be used in this analysis must be smoothed to a common angular resolution, since we compare horns with slightly different beams. We convolve all the maps to 1° angular resolution.

We applied this methodology to the realistic wide-survey simulated maps presented in chapter 3, using as external references WMAP and Planck-LFI maps simulated with the same sky model presented in Sec. 3.5.2. We ran the analysis with one simulated map, for two noise cases: white noise only and white+$1/f$ noise. Testing this methodology with simulations allows us to quantify the level of precision that can be achieved in the determination of the cross-calibration factors A, given the signal-to-noise of the simulated data. As the calibration of the simulations is perfect by construction, we therefore expect values of $A \sim 1$. Any deviation from unity is attributable to the level of precision of the methodology, and to the error introduced by the noise in the maps.

The results with simulations are shown in Fig. 4.20 (white noise only) and 4.21 (with realistic white plus $1/f$ noise). We can notice that with the simulations we can control the cross-calibration in intensity (TT) at better than the 0.04% level, with white noise only, at all frequencies. When we include realistic $1/f$ noise the precision is at the level of ~0.1% at 11, 13, and 17 GHz, and ~0.4% at 19 GHz. In polarization (EE and BB), instead, where the signal is fainter and the white noise dominates over the $1/f$ component (see discussion in chapter 3, Sec. 3.6.2), we can control the calibration at $2-4\%$ level, both with white noise only or also with $1/f$. In polarization, the 11 and 13 GHz points are not available, since, as explained in Sec. 4.1, we do not have polarization maps from horn 1.

The results obtained with the real wide-survey maps are shown in Fig. 4.22.

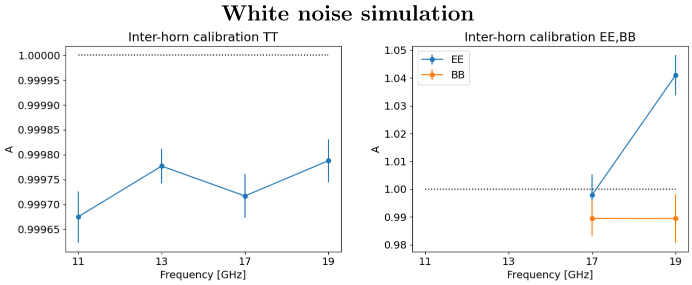

FIGURE 4.20— Inter-horns calibration for the four frequencies, obtained with a simulation including white noise only.

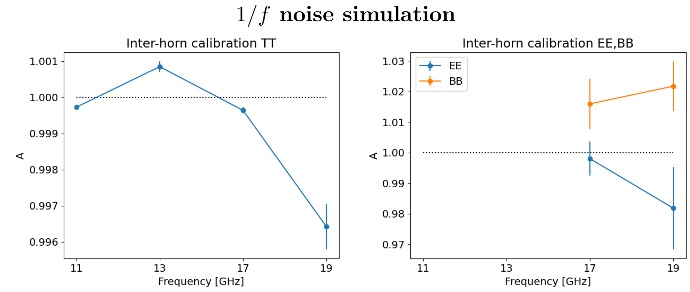

FIGURE 4.21— Same as in Fig. 4.20, obtained with a realistic simulation including white and $1/f$ noise.

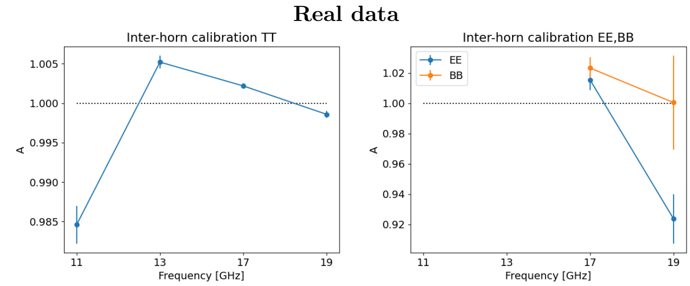

FIGURE 4.22— Same as in Fig. 4.20, obtained with the real QUIJOTE-MFI wide-survey data.

Here we can notice that the relative calibration between horns in intensity is accurate at the 0.5% level at 13, 17, and 19 GHz, and at 2% level at 11 GHz. In polarization it deviates by 2% from unity at 17 GHz, and is ∼ 4% at 19 GHz if we average EE and BB. In conclusion, this suggests that the quoted 5% calibration uncertainty is reasonable for these QUIJOTE-MFI maps.

4.6.2 Inter-period

A very similar analysis to that described in the previous section can be done with the maps of data taken at a given period (see Sec. 4.1.2 for the MFI periods definition), with the aim to characterize the relative calibration amplitude between the period maps and the final maps containing all the data. The inter-periods cross-calibration factor A_p (of horn h at frequency f) and its uncertainty σ_{A_p} can be analytically written as:

$$A_p = \left\langle \left\langle \frac{C_\ell^{(h,f,p),\,X}}{C_\ell^{(h,f),\,X}} \right\rangle_{\ell\in[30,200]} \right\rangle_X \tag{4.21}$$

$$\sigma_{A_p} = std_X \left(\left\langle \frac{C_\ell^{(h,f,p),\,X}}{C_\ell^{(h,f),\,X}} \right\rangle_{\ell\in[30,200]} \right) / \sqrt{n_X} \tag{4.22}$$

where (h, f, p) indicates the QUIJOTE map of horn h, frequency f and period p, and (h, f) is the final QUIJOTE map of the same MFI channels containing all the data. The external maps X and multipole range are the same as in Sec. 4.6.1.

This analysis provides a relative (period/total) calibration factor for each period p, horn h, and frequency f, as plotted in Fig. 4.24 – 4.26. By construction, for a given (h, f), we expect the average of the A_p from the four periods to be close to unity, given that the total map is approximately an average of the period maps (neglecting the weights). Mathematically, it is:

$$\frac{(p_1 + p_2 + p_5 + p_6)/4 \times X}{m \times X} = \sum_{p=1,2,5,6} A_p/4 \sim 1 \tag{4.23}$$

where p_1, p_2, p_5, p_6 are the period maps, m is the total map, and × denotes the cross-correlation operation.

As described in Sec. 4.1.2, horn 1 has data only in period 1 and 2. This is taken into account when computing the various cross-correlation options, excluding horn 1 in period 5 and 6. In addition, period 1 has observations only at high elevations, and part of the sky is not covered. For this reason,

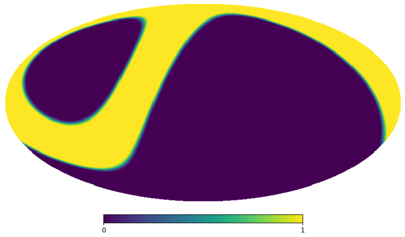

FIGURE 4.23— Mask used for the inter-periods analysis, covering $\delta \in [8, 50]\,deg$.

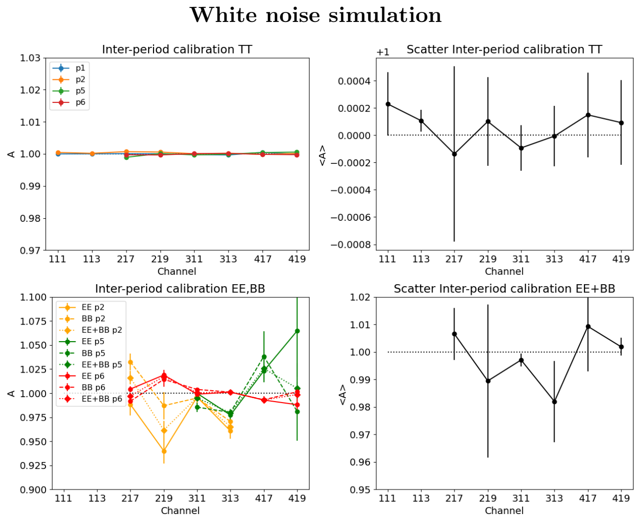

FIGURE 4.24— Inter-periods calibration with a simulation including white noise only. The intensity (TT) is shown on the top row, and the polarization (EE-thick line, BB-dashed line, and the average of EE and BB labelled as "EE+BB"-dotted line) is shown on the bottom row. The figures in the left panels show the relative calibration amplitudes estimated with Eq. 4.21, and on the right we show the average and scatter of the results among the different periods, for each single channel. Periods 1, 2, 5, and 6 are shown, respectively, in blue, orange, green, and red colors.

in this case we have to use a mask that covers a smaller sky fraction, in the declination range $\delta \in [8, 50]$ deg, as shown in Fig. 4.23. The mask is apodized

$1/f$ noise simulation

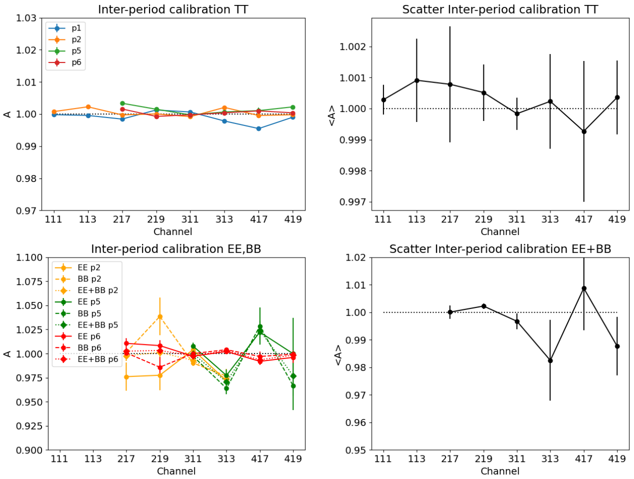

FIGURE 4.25— Same as in Fig. 4.24, for the simulation with white plus $1/f$.

Real data

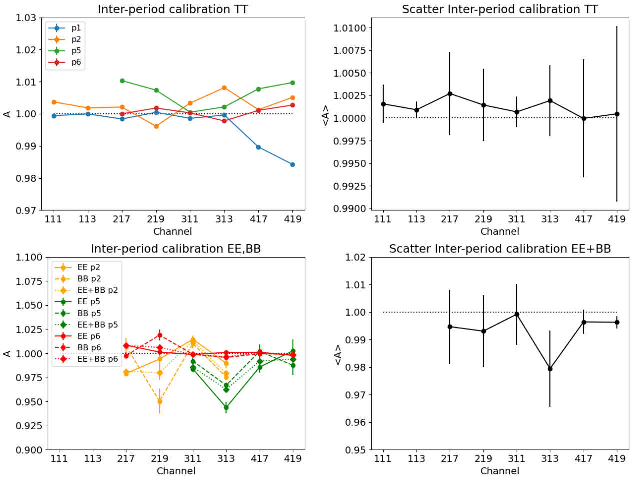

FIGURE 4.26— Same as in Fig. 4.24, for the real QUIJOTE-MFI wide-survey data.

with a 5 deg cosine function, with the apodization routine of the NaMaster. The cross-correlations are computed with Xpol within this mask.

The results of this analysis obtained with simulations are shown in Fig. 4.24 and 4.25, for white noise only and realistic white plus $1/f$ noise, respectively, for intensity (TT) and polarization (EE, BB, and the average of EE and BB labelled as "EE+BB"). We also show the average among different periods and the scatter (standard deviation divided by the square-root of the number of averaged points) of the estimated A_p for each horn and frequency channel, in order to quantify the global stability of the cross-calibration of different periods, which is expected to be ~ 1. We can notice from Fig. 4.24 and 4.25 that, in intensity, we are sensitive to cross-calibration mismatches at a level better than ∼0.1% and ∼0.3% at all frequencies if we consider, respectively, white noise only or also realistic $1/f$. In polarization, instead, we can control the cross-calibration within periods at the level of $2-5$%, in the case of the simulation with white and white+$1/f$ noise.

The results obtained with real data are shown in Fig. 4.26 with the same scheme as for the simulations. Here we can notice that in intensity the different periods show a larger scatter than that obtained with the $1/f$ noise simulations (4.25). However, the scatter is within ∼ 1%, which is small with respect to the quoted calibration uncertainty of the maps, which is at the level of 5%. In conclusion, the cross-calibration within periods is well under control, at the 1% level. We obtained a similar result also in polarization (bottom panels in Fig. 4.26), which shows a scatter of the periods cross-calibration factors that is not larger than 5%, consistent with the quoted 5% global calibration uncertainty.

4.6.3 Intra-nulltest

With this analysis, we tested the relative calibration between the two split maps of the null-tests. For each null-test n (*half*, *rings*, *daynight*, *halfrings*, PWV, *tbem*, see Sec. 4.5), we can compute the relative amplitude A_n between the split number 1 of horn h and frequency f ($s1(h,f)$) and the split number 2 of the same horn and frequency ($s2(h,f)$). A_n can be estimated, together with its uncertainty σ_{A_n}, as:

$$A_n = \left\langle \left\langle \frac{C_\ell^{s1(h,f),\,X}}{C_\ell^{s2(h,f),\,X}} \right\rangle_{\ell\in[30,200]} \right\rangle_X \tag{4.24}$$

$$\sigma_{A_n} = std_X \left(\left\langle \frac{C_\ell^{s1(h,f),\,X}}{C_\ell^{s2(h,f),\,X}} \right\rangle_{\ell\in[30,200]} \right) / \sqrt{n_X} \tag{4.25}$$

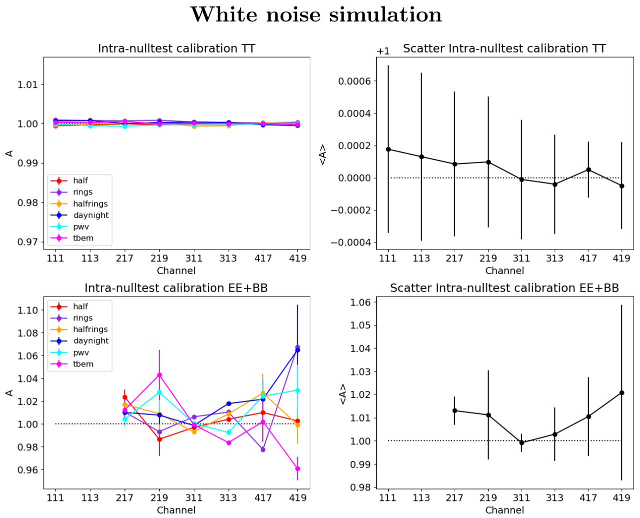

FIGURE 4.27— Intra-nulltests calibration test for the simulation of the QUIJOTE-MFI wide-survey data, with only white noise. The intensity (TT) is shown on the top row, and the polarization (average of EE and BB labelled as "EE+BB") is shown on the bottom one. The figures in the left panels show the relative calibration amplitudes estimated with Eq. 4.24 and 4.25, and on the right we show the average and scatter of the results among the different data splits, for each single channel. Each null-test is shown with a different color, as specified in the legends.

The external maps X and multipole range used in this analysis are the same as in Sec. 4.6.1. The cross-correlations are computed within the area selected by the standard mask that is used for the scientific analysis of the QUIJOTE-MFI maps, which is shown in Fig. 3.8.

We show the results obtained with simulations of the wide-survey containing white noise only in Fig. 4.27, and with realistic white plus $1/f$ noise in Fig. 4.28, for intensity (TT) and polarization (average of EE and BB labelled as "EE+BB"). We also show the average and the scatter (standard deviation divided by the square-root of the number of averaged points $n_X = 6$) among the estimated relative amplitudes for different null-tests, for each horn and frequency channel, in order to quantify the global stability of the null-tests relative calibration, which is expected to be ~ 1.

We can notice from Fig. 4.27 that, if we have only white noise, we are able

$1/f$ noise simulation

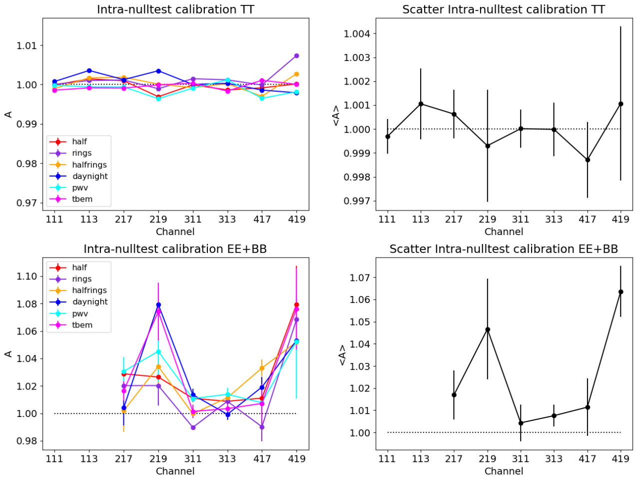

FIGURE 4.28— Same as in Fig. 4.27, for the case of white plus $1/f$ noise.

Real data

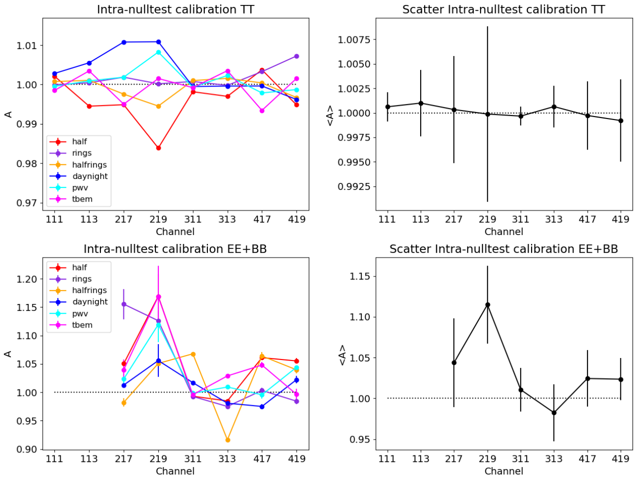

FIGURE 4.29— Same as in Fig. 4.27, for the QUIJOTE-MFI wide-survey data.

to control the stability of the calibration of the various null-tests to within the 0.1% level, in intensity. In polarization, instead, the scatter is larger, and reaches in some cases the value of $\sim 2-3\%$. If we include realistic $1/f$ noise in the simulations, we can observe, from Fig. 4.28, that the scatter in intensity increases, but that we can control the relative calibration of the null-tests within the 0.3% level. The polarization case is very similar to that of white noise only (as expected given the low $1/f$ in the polarization MFI data), confirming the possibility to control the relative amplitude of the null-test data splits within the $2-3\%$ level, depending on the frequency channel.

The results obtained with real data are shown in Fig. 4.29. We can observe that, in intensity, we have good control over the relative amplitudes of the data splits, which are always consistent with unity within 2%, with a scatter of $\sim 0.1\%-0.8\%$, depending on the frequency. In polarization, instead, we observe a significantly larger scatter, especially in horn number 2 which is known to be extremely noisy in polarization. However, given the 5% global calibration uncertainty of QUIJOTE-MFI and the uncertainty associated with this particular methodology (see Fig. 4.28) the measured A_p are consistent with unity, within the expected level of uncertainty.

4.6.4 Detection of the CMB anisotropies

In the QUIJOTE-MFI wide-survey intensity maps, the CMB can be detected with cross-correlations. The method is based on the computation of the level of correlation of the QUIJOTE maps with the CMB anisotropies, accounting simultaneously for the chance alignment between the CMB and the Galactic foregrounds. We assume that the QUIJOTE map $\mathbf{m}_{\rm QJT}$ of a given horn and frequency is a linear combination of the CMB map $\mathbf{m}_{\rm CMB}$, of a template of Galactic foregrounds $\mathbf{f}$, and of the noise $\mathbf{n}$, as:

$$\mathbf{m}_{\rm QJT} = A \cdot \mathbf{m}_{\rm CMB} + B \cdot \mathbf{f} + \mathbf{n} \tag{4.26}$$

where A and B are the parameters of the linear combination with, respectively, the CMB map $\mathbf{m}_{\rm CMB}$ and the foreground map f. If we perform cross-correlations of the QUIJOTE map with the CMB and with the foregrounds map, we get:

$$\begin{cases} C_\ell^{\rm QJT,CMB} = A \cdot C_\ell^{\rm CMB,CMB} + B \cdot C_\ell^{\rm f,CMB} \\ C_\ell^{\rm QJT,f} = A \cdot C_\ell^{\rm CMB,f} + B \cdot C_\ell^{\rm f,f} \end{cases} \tag{4.27}$$

where $C_\ell^{X,Y}$ is the cross-correlation of map X with map Y, as a function of multipoles. In Eq. 4.27, we assumed that the noise map of QUIJOTE does not

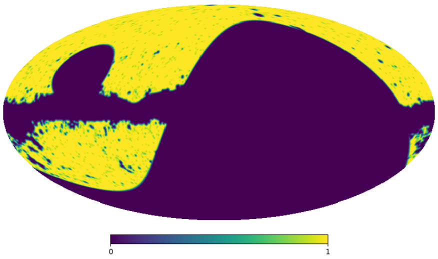

FIGURE 4.30— Mask for the cross-correlation with the CMB. The mask excludes the low confidence regions of the CMB map, and is apodized with a simple 2-degrees smoothing.

play any role in the cross-correlations, and that the parameters A and B do not change with the angular scale. By solving this system of equations with respect to A we get:

$$A = \left\langle \frac{C_\ell^{\mathrm{QJT,CMB}}}{C_\ell^{\mathrm{CMB,CMB}}} - \frac{C_\ell^{\mathrm{QJT,f}}}{C_\ell^{\mathrm{f,f}}} \cdot \frac{C_\ell^{\mathrm{CMB,f}}}{C_\ell^{\mathrm{CMB\times CMB}}} \right\rangle_{\ell\in[100,200]} \tag{4.28}$$

where $< \cdot >$ is an average of the argument within all multipoles in the range $\ell \in [100, 200]$, i.e., in proximity of the first peak of the CMB angular power spectrum. This range of multipoles is a specific selection in which, first, the CMB power spectrum is in the signal dominated regime with respect to the signal error of the QUIJOTE maps (as shown in Fig. 3.9), and second, any residual from the dipole mode coupling that is left by the power spectrum estimator is negligible (see discussion in Sec.3.6.2). If the CMB anisotropies are correctly recovered, and the QUIJOTE maps are properly calibrated, we expect to measure with Eq. 4.28 a value of $A = 1$, which can be read as the amplitude of the CMB anisotropies map measured by QUIJOTE-MFI, relative to a reference CMB map.

We performed this analysis with the simulated intensity maps of the QUIJOTE-MFI wide-survey constructed as presented in chapter 3, smoothed to 1-degree, and for the cases with no-noise, white noise and $1/f$ noise. It can be noticed from Fig. 3.9 that, while in the cases of no-noise and white noise the CMB can be detected with high signal to noise, the power of the residual $1/f$ noise is above the level of the CMB at all multipoles. Consequently, the detection of the CMB with $1/f$ is more affected by the noise.

For the simulations, we use as a foregrounds template the simulated foregrounds map at 11 GHz (see Sec. 3.5.2), scaled to 22.8 GHz with a temperature

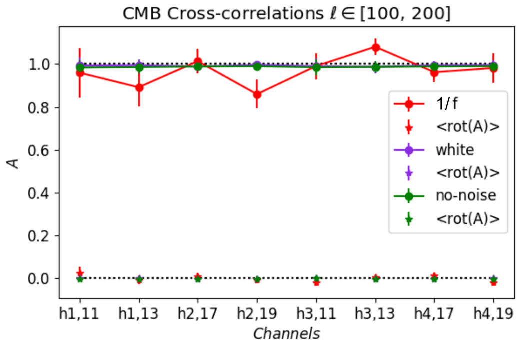

FIGURE 4.31— Amplitude A of the CMB in the simulated QUIJOTE-MFI maps, obtained with cross-correlations. The analysis is performed with simulations containing white plus $1/f$ noise (red), white noise (purple) and no-noise (green). The circles represent the result of the correlation, and the star-marked points represent the average of the cross-correlations with rotations of the CMB map. The error bars for the measurement of A are obtained from the scatter of the measured amplitude A in the rotations.

Channel	A-no noise	A-white noise	A-$1/f$ noise
h1,11	0.98 ± 0.04	0.99 ± 0.04	0.96 ± 0.12
h1,13	0.99 ± 0.03	0.99 ± 0.03	0.89 ± 0.09
h2,17	0.99 ± 0.02	0.99 ± 0.02	1.01 ± 0.06
h2,19	0.99 ± 0.02	1.00 ± 0.02	0.86 ± 0.07
h3,11	0.99 ± 0.04	0.99 ± 0.04	0.99 ± 0.06
h3,13	0.99 ± 0.03	0.99 ± 0.03	1.08 ± 0.04
h4,17	0.99 ± 0.02	0.99 ± 0.02	0.96 ± 0.04
h4,19	0.99 ± 0.02	1.00 ± 0.02	0.98 ± 0.07

TABLE 4.10— Amplitude A of the CMB in the simulated QUIJOTE-MFI maps, obtained with cross-correlations. The analysis is performed with simulations without noise (first column), with white (second column) noise and with white plus $1/f$ noise (third column). The error bars are obtained with rotations of CMB map.

spectral index $\beta = -3$, and the CMB map is a CMB realization from the Planck 2015 best-fit cosmology.

The cross-correlations are computed with XPOL, using the Planck confidence mask for temperature (Planck Collaboration et al., 2020g), which excludes the low confidence regions of the CMB map from the sky observed by QUIJOTE. The mask is apodized with a simple 2 degrees smoothing, and it is shown in Fig. 4.30.

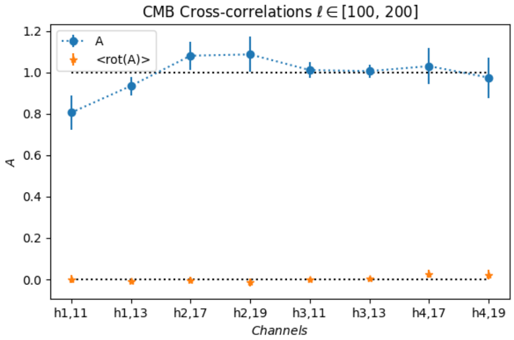

FIGURE 4.32— Amplitude A of the CMB in the QUIJOTE-MFI wide-survey maps, obtained with cross-correlations. The blue circles represent the result of the correlation, and the star-marked orange points represent the average of the cross-correlations with rotations of the CMB map. The error bars for the measurement of A are obtained with rotations of the CMB map.

Channel	A	$< \mathrm{rot}(A) >$	σ_A
h1,11	0.805	0.002	0.082
h1,11	0.934	−0.009	0.045
h2,17	1.080	−0.002	0.068
h2,19	1.086	−0.013	0.086
h3,11	1.010	−0.000	0.037
h3,13	1.005	0.005	0.033
h4,17	1.030	0.027	0.086
h4,19	0.974	0.023	0.097

TABLE 4.11— Amplitude A of the CMB in the QUIJOTE-MFI wide-survey maps, obtained with cross-correlations. The error bars are obtained with rotations of the CMB map.

We estimate the uncertainty of the parameter A with rotations of the CMB maps. We perform 19 rotations of the CMB in Galactic longitude, with $\Delta l = 18\,\mathrm{deg}$, and we estimate with Eq. 4.28, for each rotation angle, the rotated amplitude $\mathrm{rot}(A)$. The expected correlation of the QUIJOTE map with a rotated CMB map is zero, so $< \mathrm{rot}(A) >= 0$, and the standard deviation of the distribution can be used as an estimate of the uncertainty on A.

The results are shown in Fig. 4.31 and are reported in Tab. 4.10, where we show the amplitude A of the correlation between all channels of the simulated QUIJOTE-MFI maps and the CMB (rounded points), and, as a null-test, the average of the results obtained with the rotated CMB maps (star-marked points). The analysis is performed with no-noise (green), white noise (purple) and $1/f$ noise simulations (red). We can notice that, in the cases of no-noise and white noise only, we detect the CMB with a precision of $\approx 2-4\%$, with the error bar fully dominated by foregrounds. When we include the $1/f$ noise, we recover the CMB with a precision of $\approx 4-12\%$, meaning that, despite the noise, we obtain $\approx 10-20\,\sigma$ detection of the CMB, depending on the QUIJOTE channel.

We applied this methodology also to the real QUIJOTE-MFI wide-survey data. For the CMB anisotropies we used the SMICA (Planck Collaboration et al., 2018c) CMB intensity map. For the foregrounds we used the K band map of WMAP (Bennett et al., 2013), subtracted by the aforementioned CMB. We show the results in Fig. 4.32 and Tab. 4.11. We can notice that, in all the channels (except for horn 1 which has well known problems of interference and $1/f$ noise) we detect the CMB with an amplitude that is compatible with that of the SMICA CMB map, at more that 10σ, depending on the channel. This result is important for two reasons: first, it is the first detection of the cosmological signal from the QUIJOTE-MFI maps, and second, it can be seen as one more successful test of the calibration of the QUIJOTE-MFI wide-survey intensity maps.

4.7 Conclusions

We presented the wide-survey maps from QUIJOTE-MFI (Rubiño-Martín et al., in prep), and we performed a characterization at the angular power spectrum level and with cross-correlations. In particular, we show the maps in Fig. 4.3–4.9, which provide new images of northern sky at 11, 13, 17, and 19 GHz, where the dominant components are Galactic AME (in I) and synchrotron (in I,Q,U).

The analysis of the angular power spectra of the maps at 11 GHz (from horn number 3) is presented in Sec. 4.4. We measured the ratio between the E and B-modes in the maps, at $\ell = 80$, and find it to be $A_{\rm BB}/A_{\rm EE} = 0.34 \pm 0.10$ at $|b| > 5^\circ$. The spectra can be modeled with a power law ($C_\ell \sim \ell^\alpha$) with index $\alpha = -3.00 \pm 0.16$ for EE and $\alpha = -3.09 \pm 0.41$ for BB, at $|b| > 5^\circ$. We also measured the TB and EB cross-spectra, which are compatible with zero, as expected, and we obtained a marginal detection of the TE spectrum at low multipoles.

A detailed characterization of the noise in the maps is then presented in Sec. 4.5.2 and Sec. 4.5.3, and the noise correlation properties of different frequency maps and channels are presented, respectively, in Sec. 4.5.4 and Sec. 4.5.5, where we measured $\sim 80\,\%$ (TT) and $\sim$20–60 % (EE, BB) noise correlation in the data from different frequencies of the same horn, and $\sim 90\,\%$ (TT) and ~ 0

(EE, BB) noise correlation between the correlated and uncorrelated channels. Following, several internal consistency checks of the calibration of the maps, based on cross-correlations, are shown in Sec. 4.6, supporting the quoted calibration uncertainty of the maps of 5 %. Finally, in Sec. 4.6.4 we present the detection of the CMB anisotropies in the QUIJOTE maps, with a technique that is based on cross-correlations. The CMB is detected at 10–20 σ, depending on the frequency.

5

Study of the microwave Haze as observed by QUIJOTE

> *"I was almost happy of the amount of I SAW YOU that appeared around, because it was a sign that the attention on me was awake and therefore my brighter day would not have escaped them."*
> Italo Calvino, Le Cosmicomiche

The Haze is a region presenting an excess of emission observed at microwave wavelengths near the Galactic center. It extends towards high Galactic latitudes ($|b| \approx 35^\circ$) with an elliptic shape, with its major axis perpendicular to the Galactic plane (Dobler & Finkbeiner, 2008; Planck Collaboration et al., 2013). The microwave Haze has a counterpart in γ-rays, the so-called Fermi bubbles (Dobler et al., 2010), showing a spatial correlation with two polarized radio plumes (Carretti et al., 2013). Different models have been proposed to explain the origin of the Haze, including the exotic scenario of dark matter decay in the Galactic halo. The most plausible scenario to-date states that the Haze is generated by syncrotron emission from cosmic-ray electrons accelerated by energetic events occurring in the Galactic center: from activity of the black hole in the center of the Milky Way, or from stellar activity in its surroundings. In this chapter we present an analysis based on new observations of the Haze performed with QUIJOTE-MFI (at 11 and 13 GHz), in combination with ancillary data from WMAP (23–44 GHZ), Planck-LFI (30–70 GHz) and the S-PASS radio survey of the southern sky (at 2.3 GHz). We analyze the Haze emission in intensity an polarization, characterizing it spectral properties. This work will be published in Guidi et al., (in prep.).

5.1 Introduction

5.1.1 Discovery of the microwave Haze

During the last decades the scientific community has made great efforts to provide an accurate characterization of the Galactic foregrounds at radio and microwave wavelengths, with the final goal of doing cosmology with the CMB, as we stressed in the previous chapters. Indeed, the target of the two satellite missions Wilkinson Microwave Anisotropy Probe (WMAP) and Planck was the CMB, but, first of all, they obtained full sky images of the Galactic emission at multiple frequencies between 23 and 857 GHz. These data provided a picture of the emission of our own Galaxy that we did not have before, and opened the door to many new discoveries, among them that of the microwave Haze.

The Haze was discovered in the process of disentangling the Galactic emission from the cosmological CMB signal using WMAP data between 23 and 60 GHz by Finkbeiner (2004), and it was confirmed by further studies (Dobler & Finkbeiner, 2008; Dobler, 2012; Pietrobon et al., 2012; Planck Collaboration et al., 2013). During this process, a diffuse and extended signal became evident in the residuals after removing all the already known emission mechanisms from the WMAP frequency maps. The microwave or WMAP Haze is indeed an excess of diffuse emission with an elliptically symmetric shape centered in the Galactic center, extending toward the north and the south of the Galactic plane and reaching high Galactic latitudes $|b| \approx 35°$. The Haze has a flat spectrum at the lowest WMAP frequencies. The temperature spectral index of the Haze is $\beta \approx -2.5$, which is significantly flatter than that of typical Galactic synchrotron emission with $\beta \approx -3.1$.

The Planck collaboration also detected the Haze excess (Planck Collaboration et al., 2013) with an independent dataset between 30 and 70 GHz. They measured the spectrum of the South Haze bubble using Planck and WMAP data, showing a synchrotron-like power law with a flat spectral index $\beta = -2.56$. This spectrum is in agreement with what had been previously observed with WMAP data alone.

5.1.2 γ-ray and X-ray counterparts

The microwave Haze has a γ-ray counterpart, the so-called Fermi bubbles, which were discovered in the Fermi-LAT data at energies $2 - 50$ GeV (Dobler et al., 2010; Su et al., 2010). The Fermi bubbles are two extended γ-ray lobes located in a position coincident to that of the WMAP Haze, but with a larger extension in Galactic latitude, reaching $|b| \approx 50°$, and with a flat spectrum. This multi-wavelength correspondence confirmed the interpretation of the microwave

Haze as a real sky component, and it was attributed to synchrotron emission of a young population of cosmic-ray electrons. In fact, cosmic-ray electrons with energies $10 - 100\,\mathrm{GeV}$ produce microwave synchrotron during their interaction with a magnetic field, but also γ-ray photons through Inverse Compton scattering (IC) with the Interstellar Radiation Field (ISRF).

In addition, recent observations of the eRosita X-ray space telescope (Merloni et al., 2012) detected a distinct but possibly related structure: two circular and symmetric soft-X-ray (0.3–2.3 keV) bubbles, which extended up to high Galactic latitude $|b| \approx 85°$ (Predehl et al., 2020). The eRosita bubbles enclose the Fermi bubbles, and the northern one partially overlaps with the North Polar Spur (NPS), a large and polarized filament that emerges from the Galactic center and goes toward the north, pointing to a possible connection between the NPS and the Haze.

The Haze, moreover, is not peculiar to our own Galaxy. Li et al. (2019) reported the first detection of a Haze-like structure in an external galaxy (NGC 3079), using radio (C-band) and X-ray data. The spectral index of this extra-galactic Haze is $\beta \approx -3.1$ at radio wavelengths, which is typical for synchrotron emission, and takes the slightly flatter value $\beta \approx -2.8$ in the joint fit of radio and X-ray data.

5.1.3 Polarization at radio and microwave frequencies

It is well known that the synchrotron emission is polarized, and to confirm that the Haze has a synchrotron origin it should be possible to observe an associated polarized component. Such a component was identified for the first time by the S-PASS southern sky survey at 2.3 GHz, which detected two giant radio polarized plumes extending from the center of our Galaxy (Carretti et al., 2013). The plumes spatially correlate with the Fermi bubbles, with the microwave Haze, and with X-ray structures observed by ROSAT (Almy et al., 2000; Carretti et al., 2013) that connect the plumes with the center of the Galaxy. Interestingly, the radio plumes appear to be more extended than the Fermi bubbles, reaching $|b| \approx 60°$.

The radio polarized plumes can also be roughly identified in the low frequency maps of Planck and WMAP, although the signal-to-noise is not as good as in S-PASS. The combination of S-PASS and WMAP data allowed measuring the spectral index of the polarized emission between 2.3 GHz and 23 GHz, which is $\beta = -3.2$ (Carretti et al., 2013). It should be noted that the spectral index is significantly flatter in intensity than in polarization. This result makes the interpretation of the Haze/bubbles very puzzling, since this difference in the spectral index suggests that the cosmic-ray electrons that generate the intensity of the Haze and the polarization of the plumes belong to two different electron populations.

5.1.4 Haze models

A variety of scenarios have been proposed in order to explain the possible origin of the Haze signal. One of the most popular and intriguing proposals is that the WMAP Haze is generated by secondary emission of dark matter particles (Hooper et al., 2007; Cholis et al., 2009; Dobler et al., 2010; Delahaye et al., 2012; Gaskins, 2016; Egorov et al., 2016). Indeed, the annihilation or decay of dark matter particles (e.g., into an electron position pair) injects cosmic rays into the Galactic halo, which can propagate and emit synchrotron radiation, even far from where they were generated, and produce a smooth and diffuse emission in the region surrounding the Galactic center. However, the γ-ray counterpart and the polarized radio signal attributed to the Haze reveal a more complex structure than the diffuse emission that could be generated by dark matter annihilation. We observe γ-ray bubbles with sharp edges (Su et al., 2010) and radio polarized sharp filaments and plumes (Biermann et al., 2010; Jones et al., 2012; Crocker & Aharonian, 2011; Carretti et al., 2013; Planck Collaboration et al., 2016c), which contradicts the dark matter hypothesis as a complete explanation of this phenomena. But even though the microwave Haze cannot be fully explained by dark matter secondary emission, it is not excluded that a fraction of the Haze emission has a dark matter origin (Egorov et al., 2016).

Other proposed progenitors for the Haze emission demand energetic events in the Galactic center. AGN activity of the super-massive black hole in the center of the Milky Way (SgrA*) (Zubovas & Nayakshin, 2012; Guo et al., 2012; Guo & Mathews, 2012; Ackermann et al., 2014; Fox et al., 2015; Zhang & Guo, 2020, 2021), or nuclear activity in the central Galactic region such as star-formation, star-bursts, or supernovae explosions, could power outflows of hot and magnetized plasma and accelerate cosmic rays (Crocker & Aharonian, 2011; Crocker, 2012; Lacki, 2014; Carretti et al., 2013; Zhang et al., 2021).

A study from Crocker et al. (2015) proposed a unified model for the microwave Haze, radio plumes, and Fermi bubbles, as generated by outflows powered by nuclear activity. For the first time, this model provided an explanation for the change of the spectral index in the outer and inner part of the bubbles, which is what is observed in the data. According to Crocker et al. (2015) the observed emission is produced by: i) shock re-accelerated young cosmic-rays electrons that are responsible for the flat (or hard) synchrotron emission of the microwave Haze; ii) an old population of cosmic-rays electrons that escape the

Survey	Freq. [GHz]	FWHM [deg]	Cal. unc. [%]	Reference
S-PASS	2.3	0.15	5	Carretti et al. (2019)
QUIJOTE (11)	11.1	0.93	5	Rubiño-Martín et al. (in prep.)
QUIJOTE (13)	12.9	0.92	5	Rubiño-Martín et al. (in prep.)
WMAP (K)	22.8	0.88	0.2	Bennett et al. (2013)
Planck-LFI (30)	28.4	0.54	0.35	Planck Collaboration et al. (2020e)
WMAP (KA)	33.0	0.66	0.2	Bennett et al. (2013)
WMAP (Q)	40.7	0.51	0.2	Bennett et al. (2013)
Planck-LFI (44)	44.1	0.45	0.26	Planck Collaboration et al. (2020e)
WMAP (V)	60.7	0.35	0.2	Bennett et al. (2013)
Planck-LFI (70)	70.4	0.22	0.20	Planck Collaboration et al. (2020e)

Table 5.1— Summary of the data that are used in this work. We show central frequencies, beam FWHMs and quoted calibration uncertainties of each survey.

contact discontinuity of the shock, and emit the steeper synchrotron radiation observed in the S-PASS plume; iii) colliding hadrons enclosed in the contact-discontinuity surface that radiate the γ-rays, which is what we observe in the Fermi bubbles. A γ-ray component of IC emision, from the same electrons that radiate the microwave Haze, is also present, but it is subdominant.

However, even if the scenarios proposed in the literature partially explain some of the Haze characteristics, none of them provide a complete description. New observations are crucial for the understanding of the origin of the Haze, and independent determinations of the spectral index of the emission across the Haze area can yield a clearer picture of this complex region.

5.2 Data

In this section we provide new observational constraints on the Haze microwave emission using data from the QUIJOTE experiment. We perform a full reanalysis of the Haze bubbles and filaments, by combining the intensity and polarization microwave data from QUIJOTE-MFI (at 11 and 13 GHz, 17 and 19 GHz data are not used because of their low signal-to-noise at large angular scales) with other available data from S-PASS, WMAP and Planck-LFI. In particular, the QUIJOTE data provide a natural spectral complement to the already existing sky surveys, placing new observations between the low frequency data of S-PASS (2.3 GHz) and the WMAP and Planck low frequency channels (23 and 30 GHz, respectively).

We present the data-set that has been used in this work, which is composed by the QUIJOTE-MFI data at 11 and 13 GHz (see Sec. 5.2.1), in combination

	HAZE	HAZE 2	HAZE 3	ρ-Ophiuchi
(l,b)	$(16°,2°)$	$(352°,22°)$	$(37°,13°)$	$(352°,16°)$
Δaz	47°	33°	86°	18°
Period	Time [h]			
1	248.9	-	-	-
2	454.8	70.3	-	-
3	-	-	-	23.1
4	-	-	-	11.6
5	37.8	-	-	211.9
6	1.0	28.5	494.4	12.2
Tot	742.5	98.8	494.4	258.7

Table 5.2— General characteristics of the raster scan observations, for the four fields used in this work. We report the central coordinates of the fields (in Galactic coordinates), the typical length of the azimuth rasters, and the number of hours of the observations, during different periods, and in total.

	11 GHz [$\mu K_{\rm CMB}/1°$]			13 GHz [$\mu K_{\rm CMB}/1°$]		
	I	Q	U	I	Q	U
a	47.0	19.6	19.7	37.2	18.4	18.7
b	82.3	28.5	28.4	57.1	24.8	24.8
c	102.5	39.4	39.3	78.6	38.8	38.6

Table 5.3— Noise level of the QUIJOTE maps in a 1°-FWHM beam. This is obtained as the median of the uncertainty maps (Fig. 5.2) computed within a 5° radius circle centered in three different positions: close to the Galactic center (a) at $(l,b) = (5°,0°)$, in the proximity of the NPS (b) at $(l,b) = (40°,20°)$, and in a region where only wide-survey (c) data are available at $(l,b) = (100°,-30°)$.

with ancillary data (see Sec. 5.2.2) from S-PASS at 2.3 GHz (Carretti et al., 2019), WMAP at ∼23, 33, 41, 61 GHz (Bennett et al., 2013), and Planck-LFI at ∼30, 44, 70 GHz (Planck Collaboration et al., 2020e). A summary table of the data-set can be found in Tab. 5.1.

5.2.1 QUIJOTE-MFI data

This work is based on the data from the QUIJOTE-MFI wide-survey (see Chapter 4 and Rubiño-Martín et al., in prep) combined with additional raster scan observations (see Sec. 2.2.2) dedicated to the Haze area, in order to improve the signal-to-noise in the region of interest. The raster scan observations were performed with a scanning speed of 1 deg/s on the sky, across four sky fields, called

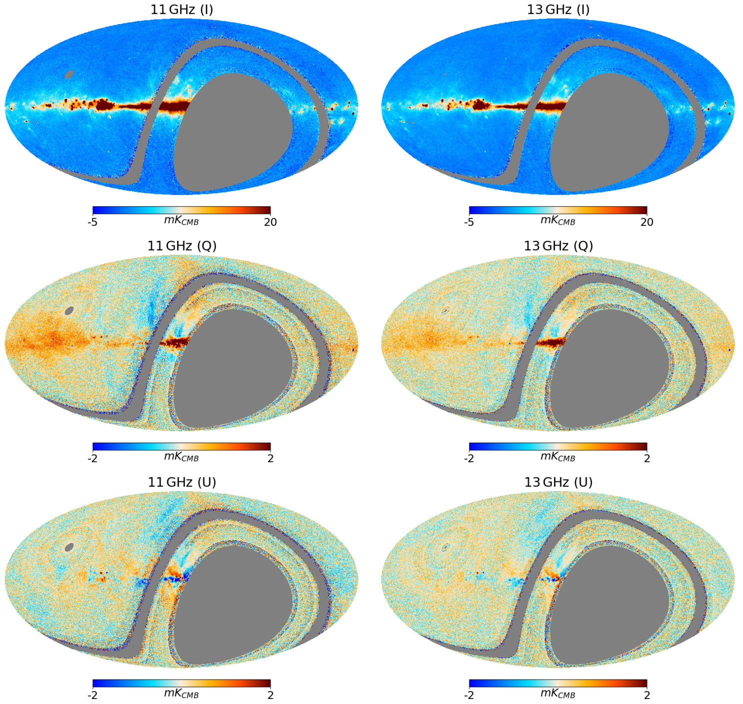

FIGURE 5.1— I, Q, and U maps from QUIJOTE at 11 GHz (left) and 13 GHz (right), at the original angular resolution and pixel size ($N_{\rm side} = 512$). These maps are obtained as the combination of data from the wide-survey (see chapter 4) and raster scans in the HAZE, HAZE2, HAZE3, and ρ-Ophiuchi regions.

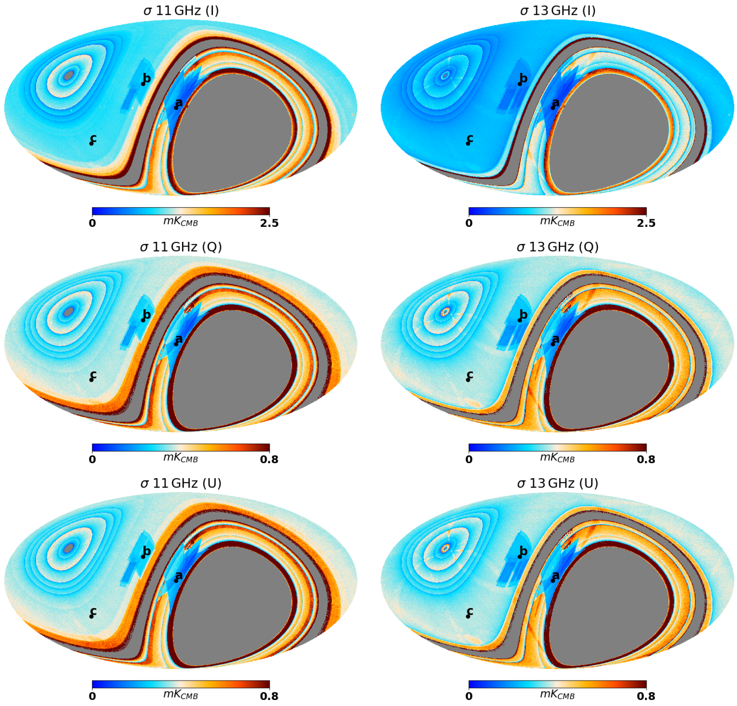

FIGURE 5.2— Uncertainty (σ) per pixel with $N_{\rm side} = 512$, of the I, Q, and U maps from QUIJOTE at 11 GHz (left) and 13 GHz (right), at the original angular resolution and pixel size ($N_{\rm side} = 512$). We indicate here the location of "a", "b" and "c" mentioned in Sec. 5.2.1 and Tab. 5.3, whose Galactic coordinates are, respectively: $(l, b) = (5^\circ, 0^\circ)$, $(40^\circ, 20^\circ)$, and $(100^\circ, -30^\circ)$.

Map	11 GHz	13 GHz
I	5.214	4.682
Q	1.333	1.320
U	1.335	1.321

TABLE 5.4— Multiplicative scaling factor that is applied to the statistical uncertainty obtained from the QUIJOTE weight maps ($\sigma = 1/\sqrt{w}$) to account for the $1/f$ noise contribution (Rubiño-Martín et al., in prep).

"HAZE", "HAZE2" and "HAZE3", and across the ρ-Ophiuchi cloud complex[1], covering a sky fraction $f_{\rm sky} \sim 5\%$. The approximate central coordinates of each field are indicated in Tab. 5.2, together with the total observing time during different periods (as defined in Sec. 4.1.2).

We use the 11 and 13 GHz frequency maps (central frequencies 11.1 and 12.9 GHz) that are shown in Fig. 5.1, where we present the I, Q, and U maps at the original angular resolution and pixel size ($N_{\rm side} = 512$ in the HEALPix[2] pixelization scheme; Górski et al., 2005). The maps are constructed with the `PICASSO` map-making code that has been implemented for QUIJOTE-MFI (see Chapter 3 and Guidi et al., submitted). The maps are obtained with a single run of the map-maker, in order to combine the wide-survey data and the additional raster observations with an efficient subtraction of the correlated $1/f$ noise.

The location of the additional raster observations can be observed in Fig. 5.2, where we show the statistical uncertainty (σ) of the data in each pixel, with $N_{\rm side} = 512$. The σ-maps are obtained from the weight maps ($\sigma = 1/\sqrt{w}$ where w is given by Eq. 3.54), and are scaled by a factor that accounts for the $1/f$ noise contribution, which is characterized from the *half*-difference null-test of the wide-survey (Sec. 4.5.2), as presented in Rubiño-Martín et al., (in prep). The scaling factors used in this work are reported[3] in Tab. 5.4.

The location of raster observations can be seen as the bluish regions in these maps, corresponding to a decrease of the uncertainty. The raster scan data improve the noise level with respect to the wide-survey data alone in two specific areas: in the Galactic center region (around the location identified by "a" in

---

[1] These observations had a different scientific goal, the study of the ρ-Ophiuchi cloud complex, but they lie in the same part of the sky where the Haze is located, and therefore they are also used here.

[2] https://sourceforge.net/projects/healpix/

[3] The weight maps that are used for this analysis were constructed neglecting the contribution from the correlation between channels (Eq. 3.54 with $\rho = 0$). However, the scaling factors reported in Tab. 5.4 account for this effect, bringing the final weights to the correct level.

Fig. 5.2), and in the proximity of the NPS (around "b" in Fig. 5.2). We report in Tab. 5.3 the typical noise level of the new QUIJOTE maps in a 1°-FWHM beam, including wide-survey and raster data, and we compare this with the noise level achieved with wide-survey data alone. These numbers have been obtained by computing the median value of the uncertainty maps, within circles with a radius of 5°, centered in three different positions: close to the Galactic center at $(l, b) = (5°, 0°)$ (a), in the proximity of the NPS at $(l, b) = (40°, 20°)$ (b), and in a region where only wide-survey data are available, at $(l, b) = (100°, -30°)$ (c). We observe that the raster scan data improve the noise level, both in intensity and polarization, by a factor ~ 2 in the Galactic center, and by ~ 1.2–1.5 in the NPS region. Finally, given the integration time in the same area, we found that these numbers correspond to an instantaneous sensitivity of ~ 0.42–$0.44\,\mathrm{mK}\sqrt{\mathrm{s}}$ in intensity, and ~ 0.13–$0.14\,\mathrm{mK}\sqrt{\mathrm{s}}$ in polarization.

In the analysis presented in this chapter, we use the QUIJOTE-MFI maps convolved at 1° angular resolution with the window function of QUIJOTE-MFI presented in Sec. 2.4.3 and in Génova-Santos et al. (in prep.), and degraded to $N_{\mathrm{side}} = 64$ (pixel resolution $\sim 0.9°$). In order to obtain uncertainty maps at this resolution, we performed 100 white noise realizations, whose amplitude is given by the uncertainty maps presented above. We applied the same smoothing and degradation of the data to the noise simulations, and we computed the standard deviation of the noise realizations to obtain a smoothed and degraded variance map. Finally, as presented in Sec. 4.5.4, the noise of the 11 GHz and 13 GHz maps of QUIJOTE is partially correlated. The correlation of the noise in intensity is $\rho = 0.76$ and in polarization it is $\rho = 0.35$. We account for this correlation in this work, and for a calibration uncertainty of 5%.

5.2.2 Ancillary data

The ancillary data that are used in this work are the WMAP 9-year maps (Bennett et al., 2013) in the K, Ka, Q and V bands (central frequencies 22.8, 33.0, 40.7 and 60.7 GHz), and the `NPIPE` Planck-LFI maps (Planck Collaboration et al., 2020e), at 30, 44 and 70 GHz (central frequencies 28.4, 44.1, and 70.4 GHz). In addition, for the analysis in polarization, we include the S-PASS data (Carretti et al., 2019) at 2.3 GHz. We account for a calibration uncertainty of 0.2% in WMAP, of 0.35%, 0.26% and 0.2% in Planck, respectively at 30, 44 and 70 GHz, and of 5% in S-PASS. We summarize the main data parameters in Tab. 5.1.

All the maps are smoothed to the common angular resolution of 1°, and degraded to $N_{\mathrm{side}} = 64$ which corresponds to a pixel size of $\sim 0.9°$ and prevents noise pixel-to-pixel correlation. For the computation of spectral indices we ap-

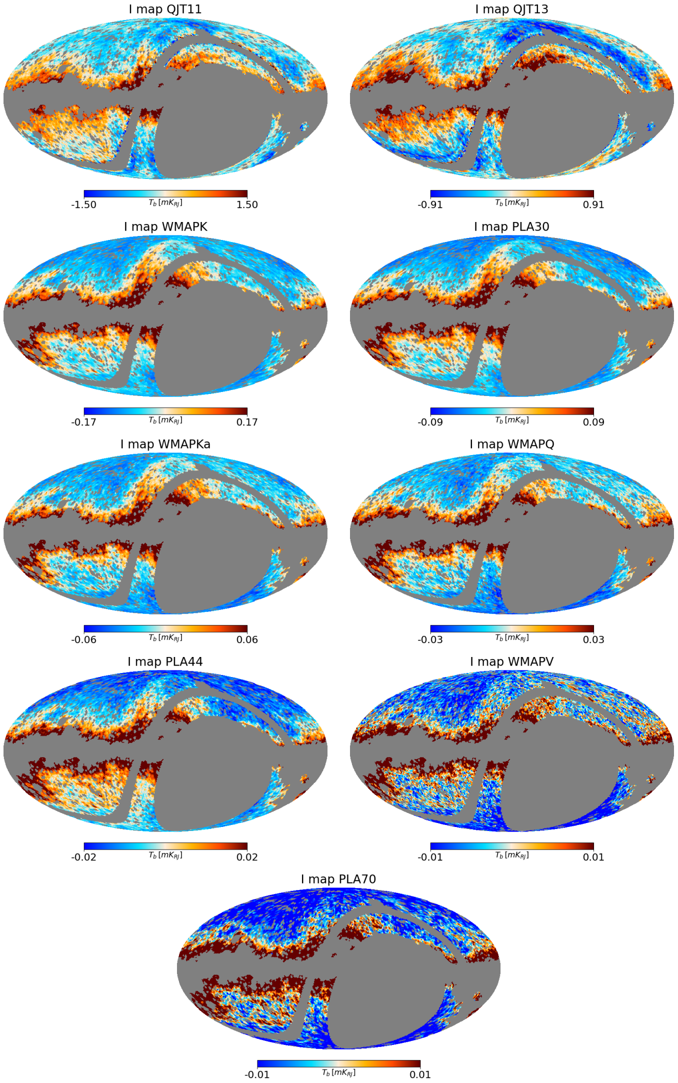

FIGURE 5.3— Intensity maps ordered in frequency: QUIJOTE 11 GHz, QUIJOTE 13 GHz, WMAP K, Planck 30 GHz, WMAP Ka, WMAP Q, Planck 44 GHz, WMAP V, Planck 70 GHz. The maps are in units of mK Rayleigh-Jeans, and the colour bar range values are scaled with a synchrotron-like power law: $1.5 \cdot (\nu/11\,\mathrm{GHz})^{\beta}$, with $\beta = -3$.

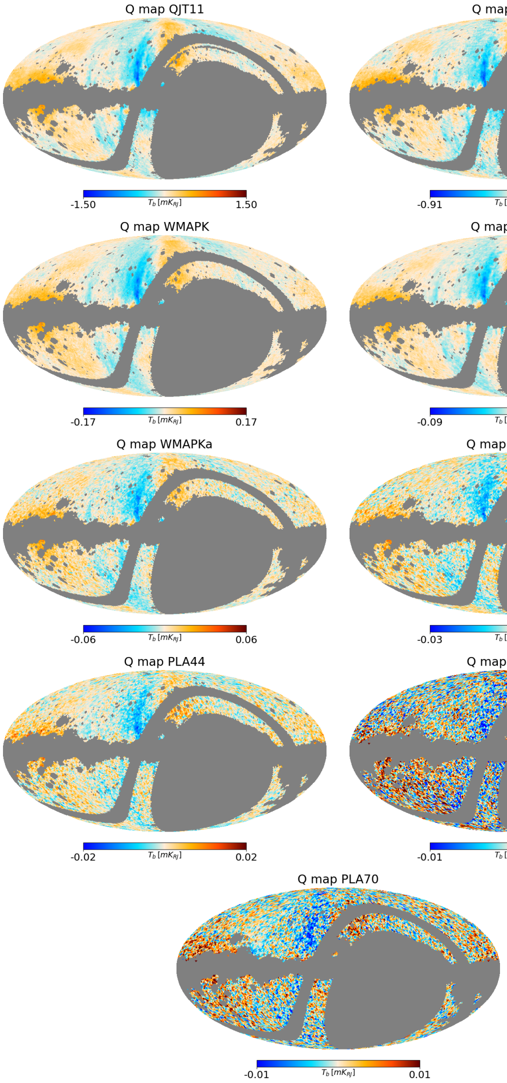

FIGURE 5.4— Same as in Fig. 5.3 for Stokes Q maps.

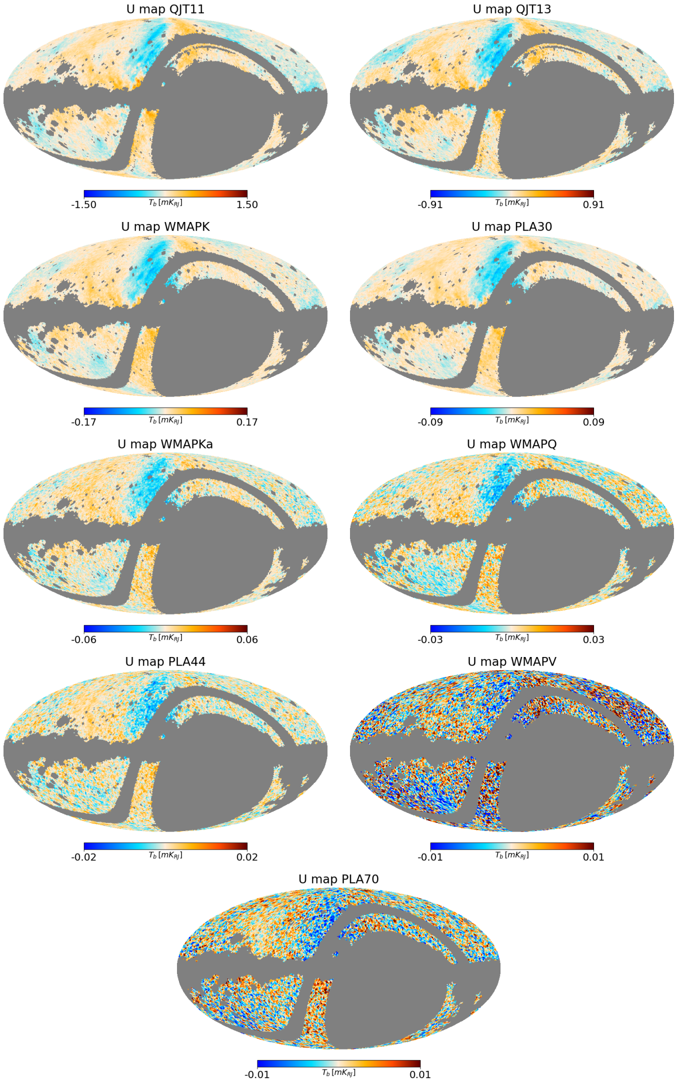

FIGURE 5.5— Same as in Fig. 5.3 for Stokes U maps.

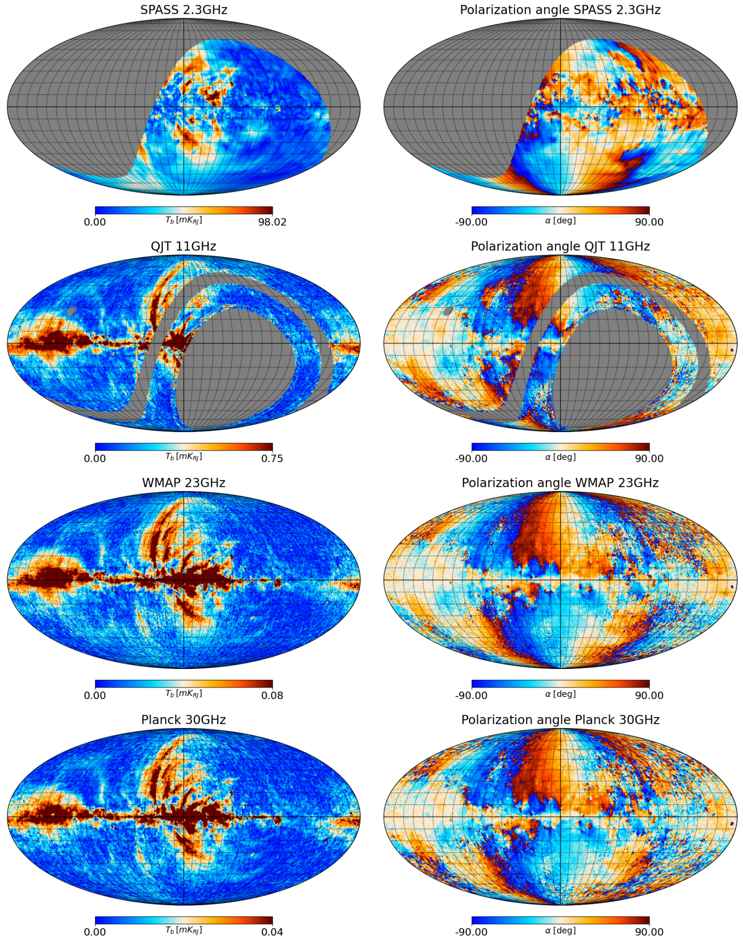

FIGURE 5.6— Debiased P maps (left) and polarization angle (right) of S-PASS at 2.3 GHz (not corrected for Faraday rotation, see Sec. 5.2.3), QUIJOTE at 11 GHz, WMAP at 23 GHz, and Planck at 30 GHz.

ply colour corrections as it is explained in chapter 2, Sec. 2.4.4. The colour corrections of QUIJOTE, Planck and WMAP are applied by using the python code `fastcc` developed by Peel et al. (research note in prep.), which includes colour correction models as described in Sec. 2.4.4, for different data-sets including QUIJOTE-MFI, Planck, and WMAP. No colour correction for S-PASS data is applied.

Fig. 5.3, 5.4 and 5.5 show the I, Q and U maps that have been used for the first part of this study, which applies a template fitting technique (see Sec. 5.3.1) to the QUIJOTE, WMAP and Planck-LFI maps (results in Sec. 5.4.1 and 5.4.2). Fig. 5.6, instead, shows the debiased polarization amplitude $P_{\rm MAS}$ maps (computed as described in Sec. 5.3.2) and the polarization angle maps at the frequencies that we selected to perform a study of the polarization spectral index analysis, which are: S-PASS at 2.3 GHz, QUIJOTE 11 GHz, WMAP K and Planck 30 GHz (results in Sec. 5.4.3).

From a quick visual inspection of the polarization amplitude and polarization angle maps in Fig. 5.6, we see that, while the QUIJOTE, WMAP and Planck maps show very high similarity in the synchrotron polarized structures and angles, at the S-PASS frequency there is evident depolarization in the Galactic plane, up to $|b| \approx 15$ deg. We can also see a rotation of the polarization angle up to high Galactic latitudes as differences in the polarization angle maps (see e.g., region 10 defined in Fig. 5.2.4), which are produced by Faraday rotation along the line of sight (Carretti et al., 2019; Iacobelli et al., 2014). In some of the regions that are studied in this work Faraday rotation is important at 2.3 GHz. We therefore correct the S-PASS maps for Faraday rotation as described in Sec. 5.2.3. QUIJOTE, WMAP and Planck data are not corrected for Faraday rotation, since the effect is expected to be negligible at these frequencies, i.e., within the uncertainty of the calibration angle.

For the subsequent analysis, in order to assign uncertainties to the data, we use uncertainty maps at the same angular and pixel resolution as for the maps ($N_{\rm side} = 64$ and 1° resolution). In order to propagate the smoothing and the degradation through the uncertainty maps, we generated 1000 noise simulations based on the original error maps of each data-set, we convolved and degraded them to the final resolution, and finally we constructed the degraded error maps as the standard deviation within the noise realizations, pixel by pixel.

5.2.3 Faraday rotation correction to S-PASS

Low frequency photons suffer the effect of Faraday rotation and depolarization along their path across a magnetized interstellar medium, before they reach the observer. Carretti et al. (2019), Iacobelli et al. (2014) and Fuskeland et al.

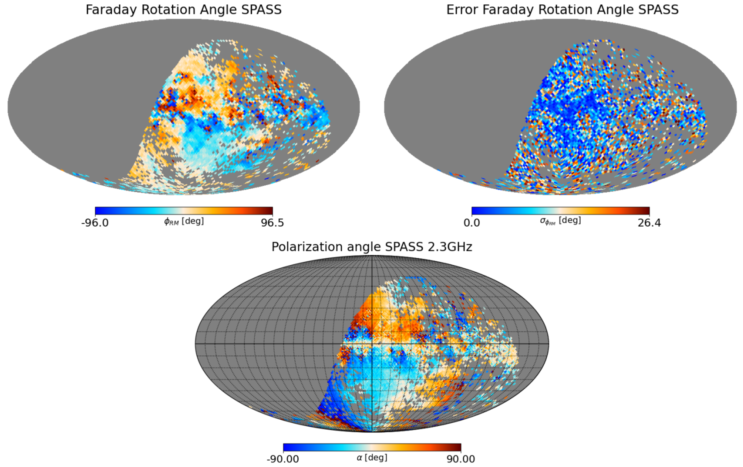

FIGURE 5.7— S-PASS Faraday rotation angle (upper left) and uncertainty (upper right), in units of degrees, and following the CMB convention on polarization angles. In the bottom, the S-PASS polarization angle map after correcting the Faraday rotation.

(2019) discussed in detail these effects in the S-PASS data, which clearly shows depolarization in the Galactic plane, and rotation also at high Galactic latitudes. As we anticipated in Sec. 5.2.2, in this work we account for these effects by correcting the Faraday rotation and masking regions with evident depolarization.

In order to correct for the Faraday rotation at 2.3 GHz, we applied a backwards rotation of the Q and U maps of S-PASS, by the Faraday rotation angle $\phi_{FR} = RM\lambda^2$, where RM is the rotation measure map delivered by the S-PASS collaboration[4] (Carretti et al., 2019) and λ is the S-PASS observed wavelength.[5] The rotation is applied as follows:

$$\begin{pmatrix} Q' \\ U' \end{pmatrix} = \begin{pmatrix} \cos(2\phi_{RM}) & \sin(2\phi_{RM}) \\ -\sin(2\phi_{RM}) & \cos(2\phi_{RM}) \end{pmatrix} \begin{pmatrix} Q \\ U \end{pmatrix} \tag{5.1}$$

where Q and U are the original S-PASS maps, and Q' and U' are the corrected

---

[4] `https://sites.google.com/inaf.it/spass/healpix-maps`

[5] We produced an independent RM measurement using S-PASS, QUIJOTE, WMAP and Planck data. We obtained results that are consistent with the S-PASS RM map across the North and South Haze bubbles.

ones[6].

The final uncertainty of the *Q'* and *U'* maps is the propagation of the uncertainty of Q, U and ϕ_{RM}, through Eq. 5.1:

$$\begin{aligned}\sigma^2_{Q'} =& \sigma^2_Q \cos^2(2\phi_{RM}) + \sigma^2_U \sin^2(2\phi_{RM}) \\ &+ 4\sigma^2_{\phi_{RM}}(U\cos(2\phi_{RM}) - Q\sin(2\phi_{RM}))^2\end{aligned} \tag{5.2}$$

$$\begin{aligned}\sigma^2_{U'} =& \sigma^2_Q \sin^2(2\phi_{RM}) + \sigma^2_U \cos^2(2\phi_{RM}) \\ &+ 4\sigma^2_{\phi_{RM}}(U\sin(2\phi_{RM}) + Q\cos(2\phi_{RM}))^2.\end{aligned} \tag{5.3}$$

Fig. 5.7 shows the Faraday rotation angle map at 2.3 GHz (upper left), and the corresponding uncertainty (upper right), obtained from the rotation measure map of S-PASS as $\phi_{FR} = RM \cdot \lambda^2$. The pixels where no RM is provided are excluded from the analysis. The same figure also shows, in the bottom panel, the S-PASS polarization angle map after correcting the Faraday rotation. This map can be compared with the polarization angle maps represented in Fig. 5.6, showing that, after applying the correction, the spatial distribution of the S-PASS polarization angles is much more similar to that at other frequencies.

5.2.4 Selection of the regions

We identified ten regions of particular interest for the study of the Haze, of which six have been observed by QUIJOTE. They are shown in Fig. 5.8 and are listed as follows:

1. The North Polar Spur (NPS);
2. A bright polarized feature in between of the NPS and the Haze filament, at $(l, b) \sim (30^\circ, 35^\circ)$;
3. The Haze filament identified in Vidal et al. (2015) and Planck Collaboration et al. (2016c) as region *IX*, which surrounds the North Fermi bubble in γ-rays, at $(l, b) \sim (7^\circ, 47^\circ)$;
4. A polarized region located below the Haze filament, at $(l, b) \sim (20^\circ, 27^\circ)$;
5. The North Haze bubble identified by the S-PASS map, at $(l, b) \sim (-4^\circ, 31^\circ)$;

---

[6] Note that we apply the CMB convention for the polarization angle, while the S-PASS maps are delivered with the IAU convention. This inverts the sign of the U map, and therefore also the sign of the polarization angle.

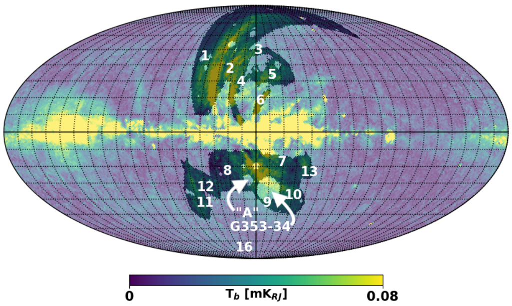

FIGURE 5.8— Selected regions for the analysis (see Sec. 5.4.3) overlaid to the WMAP K polarization amplitude map.

6. The Galactic Center Spur (GCS), at $(l, b) \sim (5°, 16°)$;
7. A rectangle enclosing the South Haze bubble, with $|l| < 35°$ and $-35° < b < -10°$ (as selected by Planck Collaboration et al., 2013), in combination with the mask that is used for the template fitting analysis (see Sec. 5.3.1.1);
8. The same rectangle as in region 7 but restricted to the overlap with the QUIJOTE sky coverage;
9. The South Haze bubble identified by the S-PASS map, at $(l, b) \sim (-1°, -30°)$;
10. The South Haze bubble as in region 9, excluding two structures that produce localized Faraday depolarization (region "A" and G353.34 from Iacobelli et al. (2014), whose location is indicated in Fig. 5.8).
11. The western side of the eRosita bubble (Predehl et al., 2020), at $(l, b) \sim (58°, -45°)$.
12. A faint polarized loop structure with unknown origin, at $(l, b) \sim (53°, -35°)$.
13. The eastern side of the eRosita bubble (Predehl et al., 2020), at $(l, b) \sim (-29°, -26°)$.

We use this numbering to identify these specific regions in this work.

5.3 Methodology

In this section, we describe the two methodologies that are applied in this work: the template fitting procedure, both in intensity and in polarization, and the correlation TT-plots analysis in polarization.

5.3.1 Template fitting

In order to isolate the diffuse emission of the Haze from the other Galactic foregrounds, we apply a template fitting technique, following the same formalism as in Finkbeiner (2004); Dobler & Finkbeiner (2008); Planck Collaboration et al. (2013). We assume that each frequency map is a linear combination of several templates, which spatially trace the Galactic emission of different mechanisms, such as the synchrotron, free-free, thermal dust and AME. We can analytically show this as:

$$d_\nu = a_\nu \cdot \mathbf{P}_\nu \tag{5.4}$$

where d_ν is the map at frequency ν, $\mathbf{P}_\nu$ is a the template matrix that contains one template map per column, estimated at frequency ν, and a_ν is a vector of coefficients indicating the amplitude of the templates. The template fitting problem consists in determining the amplitudes a_ν that provide the best description of the data with the templates in $\mathbf{P}_\nu$. We solve the problem with a maximum likelihood approach, by applying an extended formalism to include the correlation between different templates.[7] The logarithm of the posterior of this problem, including priors for the fitted amplitudes a_ν is given by:

$$\ln \mathcal{P} \propto (d - a \cdot \mathbf{P})^T C_\mathrm{w}^{-1} (d - a \cdot \mathbf{P}) + (a - a_0)^T C_\mathrm{a}^{-1} (a - a_0) + c \tag{5.5}$$

where we neglect the frequency subscript ν for brevity. Here, C_w is the noise covariance matrix of the data, a_0 is the central value of the amplitude priors, C_a is the covariance matrix of the template amplitudes, and c is a global constant. The solution of equation 5.5 is:

$$a = (\mathbf{P}^T C_\mathrm{w}^{-1} \mathbf{P} + C_\mathrm{a}^{-1})^{-1} \cdot (P^T C_\mathrm{w}^{-1} d + C_\mathrm{a}^{-1} a_0) \tag{5.6}$$

By means of the term $C_\mathrm{a}^{-1} a_0$, we can apply priors on the fitting of the foreground templates. In particular, the off-diagonal elements of C_a allow us to introduce in the fitting the degree of correlation between the templates, which is measured for synchrotron and dust to be at the order of 20-40%, with some evident spatial variation (Peel et al., 2012; Choi & Page, 2015; Krachmalnicoff et al., 2018).

---

[7] This formalism was developed and applied for the radio/microwaves map-making problem. See for example Keihänen et al. (2010), Guidi et al. (submitted) or Chapter 3 of this thesis.

5.3.1.1 Templates

The fitting is performed in intensity and polarization, using independently the I, Q and U Stokes parameters maps. All the templates are convolved to 1° angular resolution and degraded to $N_{\rm side} = 64$, as we did for the data (see Sec. 5.2). The intensity and polarization templates are shown, respectively, in Fig. 5.9 and 5.10. A detailed description follows in this section.

Synchrotron. The full-sky intensity map by Haslam et al. (1982), at 408 MHz, is dominated by synchrotron emission, and it is only marginally contaminated by free-free along the Galactic plane and in bright free-free sources (e.g., M42). This makes the 408 MHz map a good tracer of diffuse synchrotron emission in intensity. We use the reprocessed version of this map by Remazeilles et al. (2015) as a template, and we scale it in frequency using a power law spectrum assuming a spatially-constant spectral index $\beta_{\rm s} = -3.1$ across the full sky. In addition, as indicated by Dobler (2012), the cosmic ray propagation length is energy dependent, and this results in a synchrotron radiation that is more extended around the Galactic disk at 408 MHz compared with the higher frequencies (like QUIJOTE, Planck and WMAP). In order to trace this excess at low frequency, and following Dobler (2012) and Planck Collaboration et al. (2013), we adopt an elliptic Gaussian template centered in the Galactic center, with extension $(l, b) = (\pm 20^\circ, \pm 5^\circ)$.

In polarization, we use the 2018 Stokes Q and U `Commander`[8] synchrotron solution (Planck Collaboration et al., 2018c), scaled to each central frequency with a power law with a spectral index $\beta = -3.1$, which is assumed to be constant across the sky.

Thermal dust and AME Thermal and spinning dust are two distinct foreground components produced by dust grains. The thermal dust follows a modified black body spectrum that shows up mainly at high frequencies (ν>100 GHz), while the spinning dust is significant at intermediate frequencies (10 GHz $\lesssim \nu \lesssim$ 60 GHz). The carriers of the AME have not been unequivocally identified yet, but the most accredited hypothesis to date is that AME is produced by the rotation of small dust grains (for a review see Dickinson et al., 2018b and chapter 1, Sec. 1.5 of this thesis).

---

[8] `Commander` is software developed for the component separation of Planck data. It consists of a pixel based Bayesian parametric method (MCMC Gibbs sampling algorithm), aimed to fit the parameters describing different Galactic foreground components. See Eriksen et al. (2004, 2008) for more details.

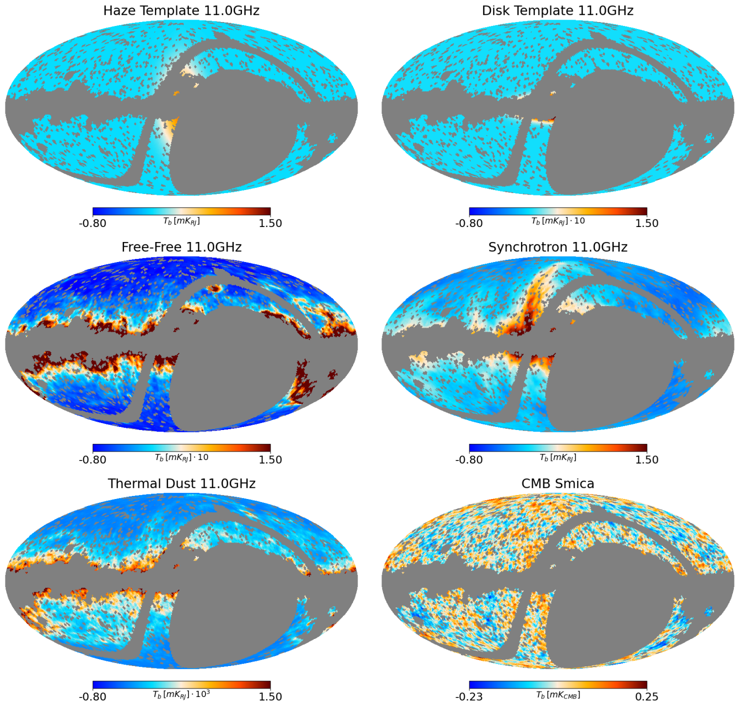

FIGURE 5.9— Intensity template maps at 11 GHz. They are: a simple model of the Haze as described in Sec. 5.3.1.1 (top left), a disk template for the Galactic plane diffuse synchrotron emission (multiplied by 10 for display purposes; top right), free-free (multiplied by 10 for display purposes; middle left), synchrotron (middle right), dust (multiplied by 10^3 for display purposes; bottom left) which is used to adjust both thermal dust and AME, and the CMB anisotropies (bottom right). The maps are in units of mK Rayleigh-Jeans, and have had the mean subtracted. The grey area represents the mask that is used for the analysis, which is a combination of the QUIJOTE sky coverage with the free-free and CMB mask, as described in Sec. 5.3.1.1.

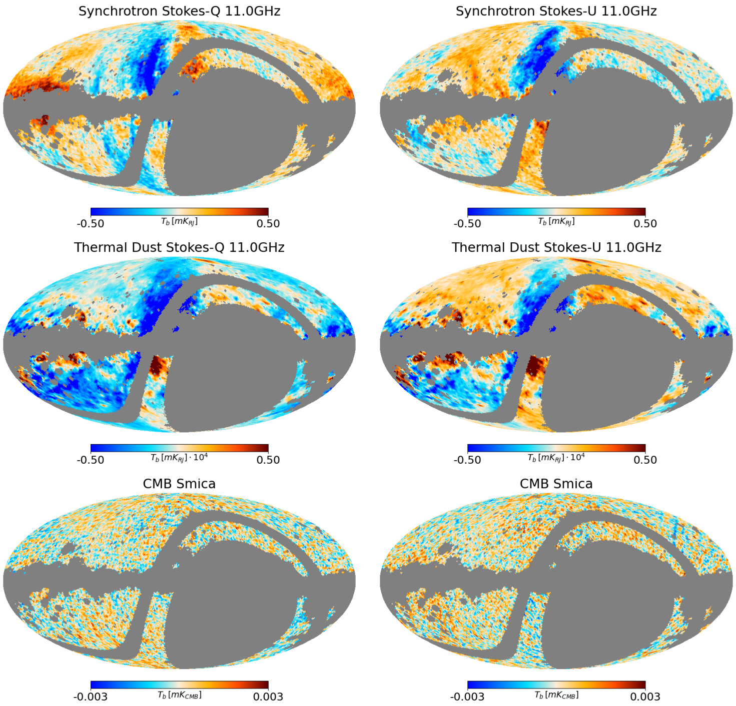

FIGURE 5.10— Polarization template maps at 11 GHz, of Stokes Q (left) and U (right). They are, from top to bottom: synchrotron, thermal dust (multiplied by 10^4 for display purposes) and the CMB. The maps are in units of mK Rayleigh-Jeans, and are mean corrected. The grey area represents the mask that is used for the analysis, which is a combination of the QUIJOTE sky coverage with the free-free and CMB mask, as described in Sec. 5.3.1.1.

We could use two independent templates to fit thermal dust and AME, using the `Commander` solution (Planck Collaboration et al., 2016a) for the two components. However, AME and thermal dust are very highly correlated, and a simultaneous fit of the two components could be affected by strong degeneracy. In addition, we noticed that the `Commander` AME map presents an excess of emission with a shape similar to that of the Haze. There is the possibility that a fraction of the Haze emission leaked into this map. Moreover, Planck Collaboration et al. (2016c) reported that the degeneracy between the AME and free-free components could affect the stability of the `Commander` AME solution, due to the lack of low-frequency information. Therefore, in order to perform a blind and unbiased fit of the foregrounds we decided not to use the `Commander` AME map, fitting the combination of thermal dust and AME with single template. We adopt the 2015 `Commander` solution for thermal dust, scaled at each central frequency with the modified black body spectrum of thermal dust reported in Planck Collaboration et al. (2016a). Due to the dust and AME correlation, this template will capture, other than the thermal dust component, the AME emission at intermediate frequencies.

In this work we assume no polarized AME (which is well justified given the observational constraints, as reported in chapter 1, Sec. 1.5.4), and, for the dust, we only fit the thermal component in polarization. For the polarized dust emission, we use the Q and U 2018 `Commander` template of thermal dust (Planck Collaboration et al., 2018c), scaled to each central frequency as indicated in Planck Collaboration et al. (2016a).

Free-free. We construct the free-free intensity template using the Hα map by Finkbeiner (2003). We correct the Hα map for dust absorption by applying the methodology of Dickinson et al. (2003), and using the reddening $E(B-V)$ map[9] of Planck (Planck Collaboration et al., 2014a). We assume uniform mixing between gas and dust by setting an effective dust fraction along the line of sight[10] $f_d = 0.5$, an average electron temperature $T_e = 7000\,\mathrm{K}$ across the full sky, and we scale the corrected Hα map from Rayleigh (R) to μK, at each central frequency, by computing the conversion factor with Eq. (11) in Dickinson et al. (2003). Despite these approximations, what is important here is to construct a good enough tracer of the spatial distribution of free-free emission, independently from the absolute scale. With this aim, applying a

---

[9] `https://irsa.ipac.caltech.edu/data/Planck/release_1/all-sky-maps/previews/HFI_CompMap_DustOpacity_2048_R1.10/`

[10] We also tested $f_d = 0.33$, but this change did not affect the resulting Haze morphology and spectrum.

good correction of dust absorption is important.

This template provides a sufficiently good approximation of the free-free in the sky, except for the regions with high dust absorption. Furthermore, we expect large fluctuation of the gas temperature in the brightest Hα regions, which can produce some inaccuracy in the template (Dickinson et al., 2003; Planck Collaboration et al., 2013). In order to avoid such problematic regions, we mask the pixels with absorption larger than one magnitude ($2.51 \cdot E(B-V) > 1\,\mathrm{mag}$), or with H$\alpha$ intensity greater than $10\,\mathrm{R}$.

CMB. The 2018 `SMICA`[11] CMB map (Planck Collaboration et al., 2018c) is subtracted from each frequency map, both in intensity and in polarization, at 1° angular resolution. As discussed in Dobler (2012), the foreground contamination of the CMB map could produce a bias in the determination of the Haze spectrum. However, the new Planck data provide a more precise CMB map today. We assume therefore that the CMB bias mentioned above is negligible as compared with other sources on uncertainty. In order to confirm that, we repeated the analysis using the `Commander` CMB map, obtaining compatible results on the Haze separation.

The Haze. Similarly to Dobler & Finkbeiner (2008) and Planck Collaboration et al. (2013), in the fitting of the intensity, we include a template that approximately traces the emission of the Haze. Even if we do not have a precise characterization of the spatial distribution of the Haze, an approximated template is needed in order to avoid a bias in the fit of other foreground templates. We use a Gaussian ellipse in Galactic coordinates, centered in the Galactic center, with minor and major axes, respectively, $\sigma_l = 15°$, $\sigma_b = 25°$.

Monopole and dipole. In order to overcome any possible issue related with zero levels, we subtract the average value of the unmasked pixels from the maps and from the templates. In addition, we fit a monopole component at each frequency in order to adjust any residual zero level mismatch. Finally, from the residual maps at frequencies $\nu > 40\,\mathrm{GHz}$, we noticed a residual dipole aligned with the CMB dipole. For this reason, and since we are not fitting a CMB dipole component from the maps, before the template fitting we remove a dipole with the HEALPix routine `remove_dipole`, extracted from high galactic latitude pixels ($|b| > 20°$).

---

[11] Spectral Matching Independent Component Analysis (SMICA) is one of the methods that was implemented for the component-separation of Planck data. It is based on a linear combination between the Planck frequency channels, using weights that depend on the multipole. See Cardoso et al. (2008) for more details.

Mask. Following Dobler & Finkbeiner (2008) and Planck Collaboration et al. (2013), we mask all the regions where the templates can deviate from the real foreground emission. The mask includes, as described above for the free-free, the regions where the Hα emission exceeds 10 R, or where the dust extinction is larger than 1 magnitude. In addition, we mask the point sources from the Planck LFI catalog (Planck Collaboration et al., 2016d). We used the mask excluding the LFI compact sources that is available in the Planck Legacy Archive[12] (PLA). Finally, in order to avoid any possible bias from foreground residuals in the CMB map, we mask the pixels that are outside the confidence region[13] of the CMB map that we are using.

5.3.1.2 Priors

Our implementation of the template fitting procedure, which is described in Sec. 5.3.1, allows us to apply priors on the amplitude of the foreground templates. The priors are introduced by the vector a_0, which contains the central values of the prior at frequency[14] ν, and by the covariance matrix $C_{\rm a}$. The elements of the covariance matrix are defined as:

$$C_{{\rm a},ij} = cov(a_i, a_j) = E\left[(a_i - a_{0i})(a_j - a_{0j})\right] \tag{5.7}$$

where $E[\cdot]$ denotes the expected value operator, a_0 the expected amplitude, and the indices i and j indicate the foreground maps at the frequency ν (e.g., i=thermal dust, j=synchrotron, at 11 GHz). The diagonal elements of $C_{\rm a}$ are:

$$C_{{\rm a},ii} = cov(a_i, a_i) = \sigma_i^2 \tag{5.8}$$

where σ_i is our choice for the width of the Gaussian prior for the amplitude of the template i. We assign to the width of the priors the analytic uncertainty on a_i that is obtained by the second derivative of the logarithm of the posterior in Eq. 5.5, neglecting the priors term ($C_{\rm a}^{-1} = 0$). It is:

$$\sigma_i^2 = (\mathbf{P}_i^T C_{\rm w}^{-1} \mathbf{P}_i)^{-1} \tag{5.9}$$

where $\mathbf{P}_i$ is the i^{th} column of the templates matrix $\mathbf{P}$, so it is simply the map of the i^{th} template (e.g., i=thermal dust). The off diagonal elements of $C_{\rm a}$ are:

$$C_{{\rm a},ij} = cov(a_i, a_j) = \rho_{ij} \cdot \sigma_i \sigma_j \tag{5.10}$$

---

[12] The mask used in this work can be found in the PLA: `http://pla.esac.esa.int/pla/aio/product-action?MAP.MAP_ID=LFI_Mask_PointSrc_2048_R2.00.fits`

[13] The CMB mask used in this work is taken from the fits file containing the CMB map (SMICA, PR3-2018), downloaded from the PLA (`http://pla.esac.esa.int/pla`).

[14] For brevity in the notation, the subscript ν is not explicit, keeping in mind that the fitting is always performed at a determined frequency.

where ρ_{ij} is the correlation between the templates i and j. It is known that different foreground mechanisms are spatially correlated (e.g., Choi & Page, 2015), therefore $\rho_{ij} \neq 0$ and C_{a} is not diagonal. In this work, we assign average values of correlation between the intensity templates of the foregrounds, by computing ρ_{ij} as:

$$\rho_{ij} = \left\langle \frac{C_\ell^{\mathbf{P}_i \times \mathbf{P}_j}}{\sqrt{C_\ell^{\mathbf{P}_i} \cdot C_\ell^{\mathbf{P}_j})}} \right\rangle_{2<\ell<200} \tag{5.11}$$

where $C_\ell^{\mathbf{P}_i \times \mathbf{P}_j}$ is the cross power spectrum between the template maps i and j (e.g., i=thermal dust, j=synchrotron, at 11 GHz), while $C_\ell^{\mathbf{P}_i}$ and $C_\ell^{\mathbf{P}_j}$ are their auto power spectra. The level of correlation between templates is not the same at large and small angular scales. As ρ_{ij} is a function of the multipole ℓ, in order to provide an average level of correlation, we compute the mean value of $\rho_{ij}(\ell)$ in the multipole range $\ell \in [2, 100]$.

We computed the power spectra of Eq. 5.11 with the publicly available code Xpol (which has already been used in this thesis, see reference in Sec. 3.6.2), and we used a mask of the full sky, excluding a band in Galactic latitude $|b| < 5°$ to mask the brightest Galactic plane emission. The averages in the multipole range $2 < \ell < 200$, are $\rho_{s,d} = 0.30$ for synchrotron and thermal dust, $\rho_{s,f} = 0.14$ for synchrotron and free-free, and $\rho_{d,f} = 0.26$ for thermal dust and free-free. In polarization we have $\rho_{s,d} = 0.20$ for synchrotron and thermal dust, in agreement with Choi & Page (2015), who measured a correlation $\rho = 0.2$ between Planck 353 GHz and WMAP 23 GHz in the multipole range $30 < \ell < 200$.

Finally we define the central values of the priors. For synchrotron and free-free we use $a_{0,s} = a_{0,f} = 1$, since the template maps are specifically computed at each central frequency, and the expected emission by synchrotron and free-free are the template map themselves. For the fitting of the thermal dust and the AME we use an unique template, which is the thermal dust of `Commander`, scaled at the corresponding central frequency, as described in Sec. 5.3.1.1. Here we assume that AME and the thermal dust are totally correlated, and that we can capture these two components with the same template, with an expected amplitude $a_{0,d} = 1 + r$, where r is an average AME to thermal dust ratio. We define r as a representative value of the ratio between the `Commander` AME and the thermal dust maps, computed (following Planck Collaboration et al., 2016a) at the same central frequency ν:

$$r(\nu) = \left\langle \frac{\mathrm{AME}(\nu)}{\text{th-dust}(\nu)} \right\rangle \tag{5.12}$$

where <> indicates the median over the pixels enclosed in the mask described in Sec. 5.3.1.1. We impose a prior on the total dust amplitude which is centered in $a_{0,d} = 1 + r$, with r being computed[15] with Eq. 5.12.

For the rest of the templates, which are the Galactic ellipse of diffuse synchrotron, the monopole and the Haze, we do not want to impose any stringent prior. Therefore we assign to them $a_0 = 0$ and $\sigma \approx \infty$.

In polarization, we fit a synchrotron and a thermal dust template, separately in Q and U. Similarly to the case of the intensity, the templates are computed to match the emission of the foreground at the corresponding central frequency, therefore we assign the expected central value with the prior $a^{Q,U}_{0,s} = a^{Q,U}_{0,d} = 1$. The width of the priors are computed with Eq. 5.9. The off-diagonal elements of the covariance matrix are computed as in Eq. 5.10 and 5.11, giving $\rho^{Q,U}_{s,d} = 0.2$.

5.3.2 Polarization T-T plots

5.3.2.1 T-T plots of $P_{\rm MAS}$

The low frequency polarized foregrounds are dominated by synchrotron radiation, which is described, as we saw in Sec. 1.5.1, by a power law spectrum:

$$d_\nu = \left(\frac{\nu}{\nu_0}\right)^\beta \cdot d_{\nu_0} \tag{5.13}$$

where d_ν are the polarization data at frequency ν, d_{ν_0} are the polarization data at a reference frequency ν_0, and β is the synchrotron spectral index.

It is possible, therefore, to derive the synchrotron spectral index across a coherent region with a simple correlation analysis between the polarized emission of two frequency maps. We can fit a linear dependence of d_ν as a function of d_{ν_0}:

$$d_\nu = m \cdot d_{\nu_0} + q \tag{5.14}$$

where q is a relative offset, and the slope m is related to the spectral index β (with Eq. 5.13 and 5.14) as:

$$\beta = \frac{\ln(m)}{\ln(\nu/\nu_0)} \tag{5.15}$$

The uncertainty on β can be derived as the propagation of the uncertainty on m, σ_m, as:

$$\sigma_\beta = \frac{\sigma_m}{m}\frac{1}{\ln(\nu/\nu_0)} \tag{5.16}$$

---

[15] The r factors are $r = 247.9$, 197.0, 42.9, 16.9, 8.4, 2.9, 1.8, 0.2, 0.04 at respectively ν(GHz) = 11.1, 12.9, 22.8, 28.4, 30.0, 40.6, 44.1, 60.8, 70.4.

This technique is commonly used to compute the spectral index of the polarization amplitude $P = \sqrt{Q^2 + U^2}$, in Rayleigh-Jeans temperature units. However, with P being a positive definite quantity, it is affected by noise bias. Several techniques have been proposed to estimate an unbiased polarization amplitude (Plaszczynski et al., 2014; Vidal et al., 2016). In this paper, we use the unbiased polarization amplitude P_{MAS} by applying the Modified Asymptotic estimator (MAS) presented in Plaszczynski et al. (2014), as:

$$P_{\mathrm{MAS}} = P - b^2 \frac{1 - e^{-P^2/b^2}}{2P}, \tag{5.17}$$

with

$$b = \sqrt{(Q\sigma_U)^2 + (U\sigma_Q)^2}/P \tag{5.18}$$

where P is the noise biased polarization amplitude (as defined above), and σ_Q and σ_U represent the uncertainties on the measured Q and U parameters. The uncertainty on P_{MAS} is given by:

$$\sigma_{P_{\mathrm{MAS}}} = \sqrt{(Q\sigma_Q)^2 + (U\sigma_U)^2}/P \tag{5.19}$$

5.3.2.2 T-T plots of Q and U combined projection

In order to overcome problems related with polarization noise bias in the data, due to zero-level mismatch, and also to variation of the spectral index with the polarization angle of the emission, we apply the technique that was proposed in Fuskeland et al. (2014). This methodology does not compute the polarization amplitude P, which is affected by noise bias, and allows to marginalize the result over the polarization angle. We make direct use of the Q and U Stokes maps that, after a projection into a rotated reference, are mixed to construct the data vector $d(\alpha)$:

$$d(\alpha) = Q\cos(2\alpha) + U\sin(2\alpha) \tag{5.20}$$

where α is the rotation angle. We can use the data $d(\alpha)$ and Eq. 5.15 and 5.16 to compute the spectral index as a function of α, for a set of 18 angles distributed in the range $\alpha \in [0°, 85°]$, in steps of 5°. The resulting (strongly correlated) spectral indices $\beta_i = \beta(\alpha_i)$ are finally averaged with weights:

$$\beta = \frac{\sum_{i=1}^{18}(\beta_i/\sigma^2_{\beta_i})}{\sum_{i=1}^{18}(1/\sigma^2_{\beta_i})} \tag{5.21}$$

Due to correlation of the estimated $\beta(\alpha_i)$ as a function of the angle, the statistical uncertainty on the final spectral index β is taken to be the minimum uncertainty among the 18 measurements:

$$\sigma_\beta^{\mathrm{stat}} = \min_{i\in[1,18]} \left(\sigma_{\beta_i}\right) \tag{5.22}$$

However, variations of the spectral index as a function of the polarization angle can induce an additional uncertainty on the determination of β across a wide region. We can define an intrinsic uncertainty due to this effect as the standard deviation of the β_i estimated at different rotation angles, as:

$$\sigma_\beta^{\mathrm{int}} = \mathrm{std}_i \left(\beta_i\right) \tag{5.23}$$

In order to account for the effect that dominates the uncertainty of the spectral index in each particular region (statistical or intrinsic uncertainty), we adopt as a final uncertainty the maximum between the two estimates of the error:

$$\sigma_\beta = \max\left(\sigma_\beta^{\mathrm{stat}}, \sigma_\beta^{\mathrm{int}}\right) \tag{5.24}$$

In the process of estimating the spectral index with correlation plots of $d(\alpha)$, we perform the linear fit considering the uncertainties of $d(\alpha)$ in both axes, and, for each angle α, we apply colour corrections. The main results of this work, in polarization, (Sec. 5.4.3) are obtained by applying the methodology described in this section. However, in a few special cases, we compare the resulting spectral indices with those obtained with the more common methodology described Sec. 5.3.2.1, the T-T plots of the polarization amplitude P_{MAS}.

5.3.2.3 T-T plots posterior distribution

In order to check the goodness of the linear regression of the T-T plots for each angle α_i, we compute the posterior distribution of the spectral index parameter $P(\beta)$. We noticed, indeed, that in low signal-to-noise areas, the wings of the posterior distribution of the spectral index are not reaching zero, and therefore the determination of the spectral index is not appropriate, showing bias towards steep values. In order to be sure that the estimated β is unbiased, we have to verify that the posterior of the T-T plots is well defined, otherwise we should exclude those regions.

We define the posterior of the slope between the data at frequency ν (y-axis data, with error σ_y) and ν_0 (x-axis data, with error σ_x). It is:

$$P(m(\beta)) = N \cdot \exp^{-\frac{1}{2}\chi^2} \tag{5.25}$$

with N being a normalization factor and χ^2 the chi-square of the linear regression:

$$\chi^2 = \sum_j \frac{(y_j - m(\beta)\cdot x_j - q)^2}{(\sigma_{y_j}^2 + m^2(\beta)\cdot\sigma_{x_j}^2)} \tag{5.26}$$

where j runs over the pixels enclosed in the area selected for the T-T plots, and q is the best-fit intercept for the given m ($q =< y - mx >$). The slope m is related with the spectral index β, so we can find the posterior of the spectral index by converting m into β with Eq. 5.15. Given that we solve a linear regression for a set of 18 angles α, we can compute a posterior distribution $P(\beta) = P(\beta_i)$ for each of them. The final posterior is then the product $P_{\rm tot} = \prod_i P(\beta_i)$, whose maximum should coincide with the β in Eq. 5.21.

5.4 Results

We report in Sec. 5.4.1 and 5.4.2 the results obtained for the Haze with the methodology of template fitting (Sec. 5.3.1), respectively in intensity and in polarization. In this part of the analysis, after fitting the foreground templates across the full sky, we perform a detailed study of the residuals in regions of particular interest among those listed in Sec. 5.2.4.

Subsequently, in Sec.5.4.3 we show the results obtained with the correlation T-T plots in polarization, following the methodology described in Sec. 5.3.2.2. Also in this case, we concentrate the analysis on the regions that are presented in Sec. 5.2.4.

5.4.1 Intensity template fitting

We performed a template-fitting component separation using the intensity frequency maps of QUIJOTE, WMAP and Planck (see Tab. 5.1 and Sec. 5.2 for a more detailed description of the data). Fig. 5.3 shows the CMB subtracted sky maps within the sky area used in this analysis, which is limited by the QUIJOTE sky coverage and by the mask of reliable foregrounds description (see Sec. 5.3.1.1 for further details on the mask).

The templates that are used for the component separation in intensity are shown Fig. 5.9. They are: synchrotron, free-free, dust (thermal dust and AME are adjusted with the same template of thermal dust), a disk template[16] for the Galactic plane diffuse synchrotron emission, and the Haze, as described in Sec. 5.3.1.1. The CMB is fixed and subtracted from the maps before the fitting. The fitted amplitudes for these templates are reported in Tab. 5.5.

As a result of this simple component separation, we construct the residual map R_ν, by subtracting the foreground templates $\mathbf{P}_\nu$ scaled by the fitted amplitudes a_ν from the corresponding frequency map d_ν. It is:

$$R_\nu = d_\nu - a_\nu \cdot \mathbf{P}_\nu \tag{5.27}$$

---

[16] The reconstruction of the Haze signal does not change significantly if we exclude the Galactic diffuse disk and Haze templates from the fit.

	I					
Map	Sync	Free-free	Dust	Disk [mK$_{\rm RJ}$]	Mono [mK$_{\rm RJ}$]	Haze [mK$_{\rm RJ}$]
QJT 11	0.939 ± 0.001	1.296 ± 0.005	358 ± 1	8.92 ± 0.09	$(9.4 \pm 0.6)\times10^{-3}$	0.724 ± 0.008
QJT 13	0.881 ± 0.001	1.247 ± 0.005	231.7 ± 0.6	5.35 ± 0.07	$(6.2 \pm 0.5) \times 10^{-3}$	0.525 ± 0.006
WMAP K	1.06762 ± 0.00002	0.85154 ± 0.00004	44.3654 ± 0.0007	0.3856 ± 0.0002	$(0.0 \pm 1.0)\times10^{-6}$	0.18617 ± 0.00002
PLA 30	1.07105 ± 0.00002	0.87480 ± 0.00002	18.0176 ± 0.0002	0.0335 ± 0.0001	$(0.0 \pm 4.2)\times10^{-7}$	0.10063 ± 0.00001
WMAP Ka	0.98191± 0.00006	0.85116 ± 0.00007	9.0479 ± 0.0003	0.0745 ± 0.0002	$(0.0 \pm 8.6)\times10^{-7}$	0.06574 ± 0.00001
WMAP Q	0.89188 ± 0.00008	0.88052 ± 0.00009	3.7382 ± 0.0002	0.0735 ± 0.0001	$(0.0 \pm 6.9)\times10^{-7}$	0.01767 ± 0.00001
PLA 44	0.90230 ± 0.00009	0.89698 ± 0.00008	2.6876 ± 0.0001	0.0472 ± 0.0001	$(0.0 \pm 5.5)\times10^{-7}$	0.01764 ± 0.00001
WMAP V	0.8617 ± 0.0004	0.8308 ± 0.0003	1.1598 ± 0.0001	0.0384 ± 0.0002	$(0.0 \pm 9.3)\times10^{-7}$	0.00601 ± 0.00001
PLA 70	0.8503 ± 0.0002	0.8229 ± 0.0001	1.02460 ± 0.00004	0.0107 ± 0.0001	$(0.0 \pm 3.4)\times10^{-7}$	0.00599 ± 0.00001

	Q			U		
Map	Sync	Dust	Mono [mK$_{\rm RJ}$]	Sync	Dust	Mono [mK$_{\rm RJ}$]
QJT 11	0.941 ± 0.001	-105 ± 7	$(3.2 \pm 0.2)\times10^{-3}$	0.745 ± 0.002	193 ± 8	$(2.1 \pm 0.2)\times10^{-3}$
QJT 13	0.940 ± 0.002	-20 ± 5	$(1.8 \pm 0.2)\times10^{-3}$	0.868 ± 0.003	30 ± 6	$(1.2 \pm 0.2)\times10^{-3}$
WMAP K	0.989 ± 0.002	-2.0 ± 0.4	$(-7.8 \pm 3.9)\times10^{-5}$	0.947 ± 0.003	11.6 ± 0.4	$(0.0 \pm 3.8)\times10^{-5}$
PLA 30	1.036 ± 0.002	-0.9 ± 0.1	$(-5.0 \pm 1.6)\times10^{-5}$	1.034 ± 0.002	1.8 ± 0.1	$(0.0 \pm 1.5)\times10^{-5}$
WMAP Ka	0.975 ± 0.005	0.6 ± 0.2	$(4.1 \pm 3.2)\times10^{-5}$	0.898 ± 0.007	3.4 ± 0.2	$(0.0 \pm 3.1)\times10^{-5}$
WMAP Q	1.021 ± 0.009	0.3 ± 0.1	$(3.2 \pm 2.8)\times10^{-5}$	0.968 ± 0.012	1.9 ± 0.1	$(0.0 \pm 2.7)\times10^{-5}$
PLA 44	1.072 ± 0.008	0.51 ± 0.06	$(5.6 \pm 1.8)\times10^{-5}$	0.973 ± 0.009	1.36 ± 0.07	$(0.0 \pm 1.7)\times10^{-5}$
WMAP V	1.059 ± 0.034	0.39 ± 0.06	$(7.0 \pm 3.1)\times10^{-5}$	0.865 ± 0.045	1.19 ± 0.07	$(0.0 \pm 3.0)\times10^{-5}$
PLA 70	1.467 ± 0.024	0.56 ± 0.02	$(1.2 \pm 0.1)\times10^{-4}$	1.003 ± 0.031	1.05 ± 0.03	$(0.0 \pm 1.3)\times10^{-5}$

TABLE 5.5— Intensity (I, top) and polarization (Q bottom left, U bottom right) template coefficients, fitted as described in Sec. 5.3.1.

Ideally, the residual R_ν is a map of the noise at frequency ν. However, the foreground templates may not perfectly model the emission that they are supposed to trace, and some residual sky structure could leak in the residual map. In particular, we are interested in the Haze component, which we fit with an approximate Gaussian elliptic template centered in the Galaxy. This template is not expected to trace perfectly the spatial distribution of the Haze, then part of it could remain as a residual. For this reason, following Dobler & Finkbeiner (2008) and Planck Collaboration et al. (2013), we construct a residual plus Haze map as:

$$R^H_\nu = R_\nu + a^H_\nu \cdot \mathbf{P}^H_\nu \tag{5.28}$$

where $\mathbf{P}^H_\nu$ is the Haze template and a^H_ν is the fitted Haze amplitude.

The residual maps can then be used to compute the physical properties of the isolated emission of the Haze as compared with the global synchrotron emission. With this aim we define the total synchrotron map as the residual map, plus the fitted Haze and synchrotron as:

$$R^S_\nu = R^H_\nu + a^s_\nu \cdot \mathbf{P}^s_\nu \tag{5.29}$$

where $\mathbf{P}^s_\nu$ is the synchrotron template, a^s_ν its amplitude at frequency ν, and R^H_ν the residual plus Haze map (Eq. 5.28).

We show the residual (R_ν) and residual plus Haze (R^H_ν) maps (Fig. 5.11), and a zoom-in of the latter maps around region 8 (southern Haze area, Fig. 5.12), and we study the Haze spectrum as compared with the total synchrotron spectrum by integrating the signal of R^H_ν and R^S_ν in selected regions among those listed in Sec. 5.2.4 (results are shown in Fig. 5.14 and 5.15).

5.4.1.1 Intensity Haze maps

We notice from Fig. 5.11, representing R_ν (left) and R^H_ν (right) for several selected frequencies (QUIJOTE 11 and 13 GHz, WMAP K and Planck 30 GHz), that the residual maps of Planck and WMAP are approximately flat and consistent with noise, except for some faint large scale residual, and some positive and negative fluctuations close to the Galactic plane, where the reconstruction of a complex component like the free-free could fail. When adding the Haze to the residual, we could clearly see that this extra component is detected above the noise of the maps. The residual maps for QUIJOTE, instead, show large angular scales residuals. These structures are not observed in the maps of the null-test shown in Fig. 5.13, which are obtained as the *half*-difference described in Sec. 4.5.2, and which are expected to be maps of residual noise artifacts in the data. Therefore, the structures in the residual maps (Fig. 5.11) are most-likely

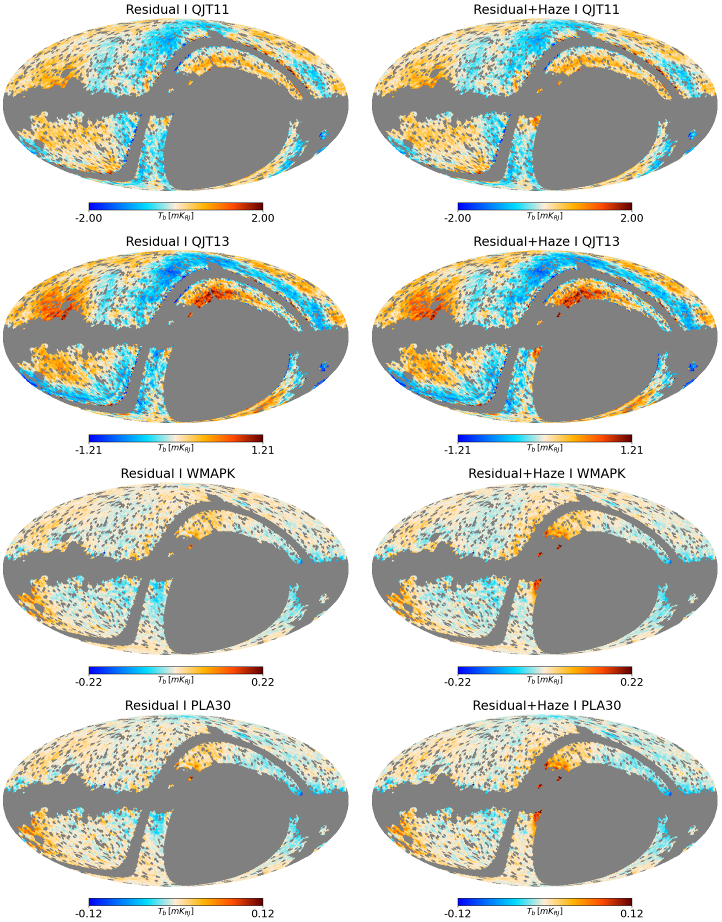

FIGURE 5.11— Residual (left) and residual plus Haze (right) intensity maps of, in order, QUIJOTE 11 GHz, QUIJOTE 13 GHz, WMAP K, Planck 30 GHz. The maps are in mK Rayleigh-Jeans temperature units, and the colour bar is scaled with a synchrotron-like power law: $2\,mK \cdot (\nu/11\,\mathrm{GHz})^{\beta}$, with $\beta = -3.0$. The grey area represents the mask of regions that are excluded for the analysis, which is a combination of the QUIJOTE sky coverage with the free-free and CMB masks, as described in Sec. 5.3.1.1.

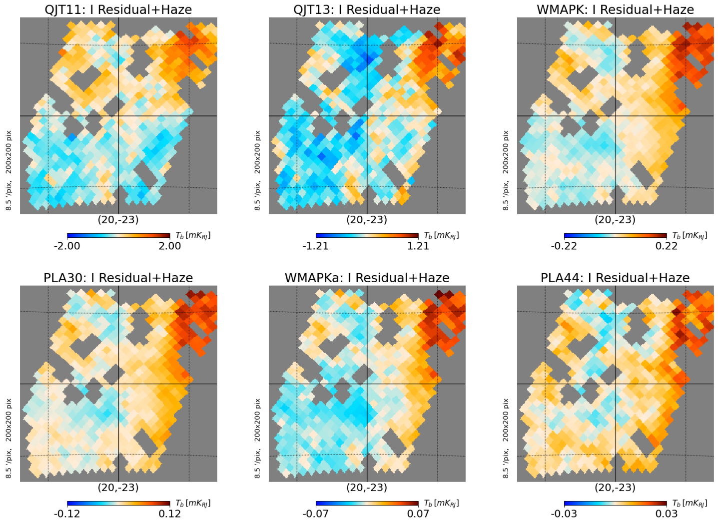

FIGURE 5.12— Residual plus Haze intensity maps in the selected southern Haze region (region 8, see Sec. 5.2.4).The grid is centered in the coordinates $(l, b) = (20^\circ, -23^\circ)$ and it is spaced by 10° in Galactic latitude and longitude. The maps shown here are QUIJOTE at 11 and 13 GHz, WMAP K and Ka, and Planck 30 and 44 GHz, ordered with increasing frequency. The mask, units, and colour bar are the same as in Fig. 5.11.

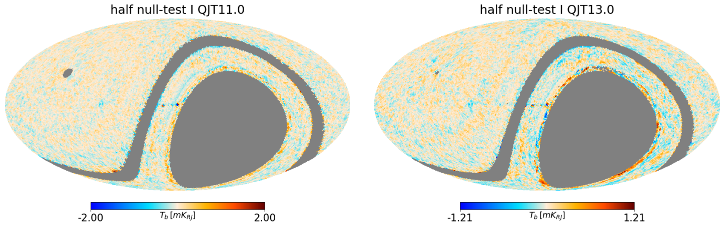

FIGURE 5.13— Null-test intensity maps obtained from the *half*-difference (see Sec. 4.5.2) of the 11 GHz (left) and 13 GHz (right) QUIJOTE-MFI nominal plus Haze and ρ-Ophiuchi raster maps. For comparison purposes, the colour scale is the same as in Fig. 5.11.

associated with residual sky signal (synchrotron or AME) that is not properly traced by the templates applied to model the different components. In particular, an excess of emission is visible in the region below the Galactic center, corresponding to the southern Haze area (region 8 defined in Sec. 5.2.4). This excess of emission is visible in the residual map, and is enhanced in the residual plus Haze map.

A closer look of the residual plus Haze maps in the southern Haze area enclosed in region 8 is shown in Fig. 5.12, where we observe, in all the maps, including QUIJOTE, a diffuse excess of emission attributed to the Haze component.

Beyond the Haze, we can notice another sky structure in the residual map of QUIJOTE, which corresponds to the lower part of the NPS (region 1), close to the Galactic center. This indicates that our templates do not perfectly match the base of the NPS region, and that it could be associated with a synchrotron component with a spectrum that is different with respect to the sky average. A detailed study of the NPS with QUIJOTE data is beyond the scope if this work and will be presented by Watson et al. (in prep).

5.4.1.2 Intensity Haze spectrum

Under the hypothesis that the Haze is synchrotron emission, both the Haze and the total synchrotron are characterized by a power law spectrum (as in Eq. 5.13), which is defined by two parameters: the amplitude and the spectral index β. We applied two different methodologies for the determination of the Haze and total synchrotron spectral indices with intensity data. First, we performed a correlation T-T plot analysis of the residual plus Haze (and plus synchrotron) maps, by correlating R_ν^H (or R_ν^S) of WMAP K (22.8 GHz) with the same maps at other frequencies. With this aim, at each frequency ν, we fitted a linear slope to the pixel-to-pixel correlation plot of R_ν^H against $R_{22.8}^H$ (or R_ν^S against $R_{22.8}^S$), given by:

$$R_\nu^{H/S} = m_\nu \cdot R_{22.8}^{H/S} + q_\nu \tag{5.30}$$

obtaining the slope m_ν and the relative offset to WMAP K, q_ν. We performed the linear fit accounting for errors in both axes,[17] where the uncertainty is given as the standard deviation of the residual map in the selected area, added in quadrature with the uncertainty on the fitted template multiplied by the template itself (either Haze or synchrotron, as a simple error propagation). We measured the spectral index from the slope of the linear fit m_ν as in Eq. 5.15,

---

[17] For this fit we used the Orthogonal Distance Regression (ODR) `SciPy` package (`https://docs.scipy.org/doc/scipy/reference/odr.html`).

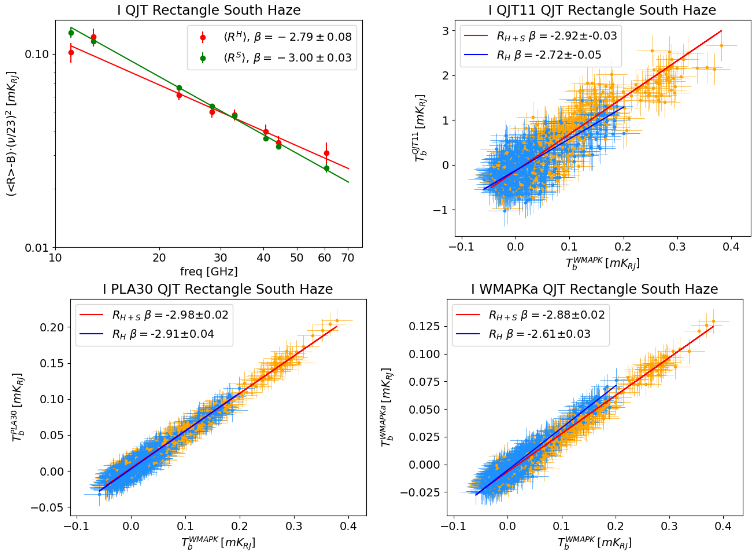

FIGURE 5.14— Intensity integrated spectrum of the Haze enclosed in region 8 (see Sec. 5.2.4 and maps in Fig. 5.12; upper left panel). In the top left panel is in red the data and the fit of the residual plus Haze spectrum multiplied by a factor three (for display purposes), and in green is the same for the total synchrotron. The other panels show the T-T plots of the residual plus Haze (light-blue/blue) and total synchrotron (orange/red) intensity maps for, respectively, QUIJOTE 11 GHz-WMAP K, Planck 30 GHz-WMAP K, and WMAP Ka-WMAP K whose estimated spectral indices are reported in Tab. 5.6, and in the legend of each panel.

and the error on β is computed propagating the uncertainty as in Eq. 5.16. With this methodology, we obtained a set of spectral indices, one for each frequency other than WMAP K, within a selected region on the sky.

Here we look at the southern Haze area (region 7) that has been identified by previous works (Dobler & Finkbeiner, 2008; Planck Collaboration et al., 2013). However, the sky observed by QUIJOTE does not cover the full area of region 7, and we restrict our analysis in the overlap with the QUIJOTE sky coverage (region 8), as shown in Fig.5.12.

The T-T plots within region 8, for a subset of frequency pairs, are shown in Fig. 5.14, while the complete set of measured spectral indices are reported in Tab. 5.6. We can notice that, for every frequency pair (except QUIJOTE 13,

Este documento incorpora firma electrónica, y es copia auténtica de un documento electrónico archivado por la ULL según la Ley 39/2015.
Su autenticidad puede ser contrastada en la siguiente dirección https://sede.ull.es/validacion/
Identificador del documento: 3640963 Código de verificación: kFOZNQ7k
Firmado por: FEDERICA GUIDI UNIVERSIDAD DE LA LAGUNA Fecha: 08/07/2021 13:04:39
José Alberto Rubiño Martín UNIVERSIDAD DE LA LAGUNA 08/07/2021 13:55:01
RICARDO TANAUSU GENOVA SANTOS UNIVERSIDAD DE LA LAGUNA 08/07/2021 16:29:55
María de las Maravillas Aguiar Aguilar UNIVERSIDAD DE LA LAGUNA 16/07/2021 12:40:49
214 / 263

Map	$\beta^H \pm \sigma_{\beta^H}$	$\beta^S \pm \sigma_{\beta^S}$
QJT 11	-2.72 ± 0.05	-2.92 ± 0.03
QJT 13	-3.24 ± 0.05	-2.96 ± 0.03
PLA 30	-2.91 ± 0.04	-2.98 ± 0.02
WMAP Ka	-2.61 ± 0.03	-2.88 ± 0.02
WMAP Q	-2.73 ± 0.03	-3.03 ± 0.02
PLA 44	-2.83 ± 0.03	-3.05 ± 0.02
WMAP V	-2.65 ± 0.05	-2.95 ± 0.04
$< \beta >$	-2.78 ± 0.20	-2.97 ± 0.05

TABLE 5.6— Spectral indices of the R^H and R^S maps with respect to WMAP K, in region 8 (see Sec. 5.2.4). In the last row we report the weighted average of the spectral indices listed above with an uncertainty given by the standard deviation of the results (the error derived from the direct propagation of the weights is 0.01).

which is an outlier in this context and must be investigated further) the spectrum of the Haze is flatter than that of the total synchrotron, with a difference in the spectral index of about $\Delta\beta = \beta_H - \beta_{H+S} \approx 0.2$–$0.3$. The weighted average of the spectral indices obtained with correlation plots at different frequencies is $\beta^H = -2.78 \pm 0.20$ for the residual plus Haze maps, and it is $\beta^S = -2.97 \pm 0.05$ for the total synchrotron maps. The spectral indices reported in Tab. 5.6 are not measured independently because, for each of them, we make reference to the same map, WMAP K. For this reason, the uncertainty quoted for the average spectral index is approximated as the standard deviation of the various measurements, instead of the propagation of the weighted average (which would provide us a much smaller error ($\sigma_\beta = 0.01$) for both β^H and β^S, but which is not realistic). Anyway, the standard deviation is an overestimation of the error bar, as it assumes that all the measurements are not partially but fully correlated. Therefore, this error bar estimate is not realistic either, but the measured difference in the spectral index is significant, as we will see later.

We repeated the measurement of the spectral index of the Haze and of the total synchrotron with a different approach, which is based on the fit of the SED of the selected area (region 8) in intensity. We computed the average of the emission in the unmasked R^H and R^S pixels within the selected region, after adjusting the zero level of the maps with respect to WMAP K, using the offsets q_ν obtained with the T-T plots described above (Eq. 5.30). The uncertainty on the SED points is given as the standard deviation of the residual map, scaled by the square-root of the number of averaged pixels, and summed in quadrature with the calibration uncertainty of each frequency map. We assume a power

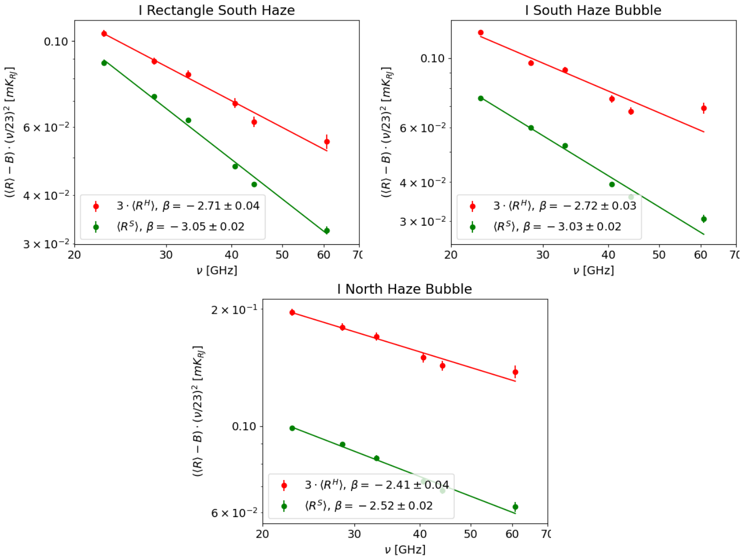

FIGURE 5.15— Intensity integrated spectrum in the rectangle enclosing the southern Haze region (region 7), in the South Haze bubble (region 9) and in the North Haze bubble (region 5). In red is the spectrum of the residual plus Haze, and in green is the total synchrotron.

law behaviour for the spectrum of the Haze ($\langle R^H_\nu\rangle - q^H_\nu$) and of the total synchrotron ($\langle R^S_\nu\rangle - q^S_\nu$) at our frequencies, therefore we can write the linear relation of $\ln\left(\left\langle R^{H/S}_\nu\right\rangle - q^{H/S}_\nu\right)$ against $\ln(\nu)$, as:

$$\ln\left(\left\langle R^{H/S}_\nu\right\rangle - q^{H/S}_\nu\right) = \beta^{H/S}\cdot\ln(\nu) + const \tag{5.31}$$

whose slope provides the the spectral index β.

The integrated spectrum in region 8 is shown in the first sub-panel of Fig. 5.14. With a linear fit to these data,[18] we measure $\beta^H = -2.79 \pm 0.08$ and $\beta^S = -3.00 \pm 0.03$, which is in agreement with the average spectral index of the correlation plots analysis presented above (see Tab. 5.6).

---

[18] The fit is performed with a MCMC sampling of the full posterior of the data, implemented with the `Python` `emcee` package (`https://emcee.readthedocs.io/en/stable/`).

We can compare these numbers with those obtained in Planck Collaboration et al. (2013) in region 7, which are $\beta^H = -2.56 \pm 0.05$ and $\beta^S = -3.1$. Our results show, in agreement with Planck Collaboration et al. (2013), that the southern Haze emits with a flatter index than the total synchrotron, but there is a discrepancy in the recovered Haze spectral index. In order to test the origin of this discrepancy, we reproduced the results of Planck Collaboration et al. (2013), by applying their same methodology, with no priors, excluding QUIJOTE data, and integrating the same southern Haze area (region 7). In this case, we obtained $\beta^H = -2.48 \pm 0.04$ and $\beta^S = -3.16 \pm 0.02$, which is consistent with the Planck's results. As an additional cross-check, we repeated the analysis by applying the priors (Sec. 5.3.1.2), but excluding QUIJOTE data, and integrating in region 7. We measured in this case $\beta^H = -2.71 \pm 0.04$ and $\beta^S = -3.05 \pm 0.02$ (see Fig. 5.15), showing that the effect of the priors is a shift of the Haze spectral index towards steeper values. The application of the priors has been tested with simulations, where we noticed a clear improvement in the fitting of the foregrounds, when compared with the case with no-priors. For this reason we finally applied priors in our analysis, despite it produces slightly different results on the Haze as compared with previous works. In conclusion, the discrepancy is due to the fact that this work studies a smaller area (region 8) than that of Planck Collaboration et al. (2013) (region 7). Region 8 has a steeper spectral index than that in region 7. Another difference, other than the use of new QUIJOTE data, is the use of priors in this work. This allows us to have a better control over the foregrounds fitting, and the result is a steepening of the spectral index of the Haze component.

There are more regions that are interesting for the study of the Haze, but which are unfortunately not accessible by QUIJOTE. These are: the full rectangle enclosing the southern Haze (region 7) and the South Haze bubble (region 9), which are located in the southern sky and that are not totally accessible by QUIJOTE. One more interesting region is the North Haze bubble (region 5), which is observed by QUIJOTE but that coincides with a region of the map with large atmospheric contamination. We studied these three regions by applying our template fitting methodology with priors, using only WMAP and Planck data.

We show the integrated spectra of these three regions in Fig. 5.15. In the rectangle enclosing the southern Haze (region 7) we obtain a spectral index for the Haze of $\beta^H = -2.71 \pm 0.04$ and for the total synchrotron of $\beta^S = -3.05 \pm 0.02$ (as already mentioned), which are compatible with the results obtained in the South Haze bubble (region 9), with $\beta^S = -2.72 \pm 0.03$ and $\beta^S = -3.03 \pm 0.02$. In the North Haze bubble, instead, we obtain a flatter Haze spectrum with

$\beta^H = -2.41 \pm 0.04$, and also a flatter total synchrotron spectrum, being $\beta^S = -2.52 \pm 0.02$. We detect a significant difference between the spectral index of the North and South Haze bubbles in intensity, being the spectrum of the northern bubble flatter than that in the South. As in other regions, the Haze component is flatter than the total synchrotron, but in the northern bubble also the total synchrotron spectrum is significantly flatter than that in other regions. Interestingly, as we report later (Sec. 5.4.3), the polarization between 23 GHz and 30 GHz shows the same behaviour, with the northern bubble having a fatter spectrum that the southern one, and with the polarization spectral indices being compatible with that in intensity.

5.4.2 Polarization template fitting

We applied the template fitting procedure in polarization, by fitting a synchrotron and thermal dust component to the Q and U frequency maps independently, across the full unmasked sky (see Sec. 5.3.1 for a detailed description of the methodology). The CMB is fixed and subtracted from the maps before the fitting. The resulting fitted amplitudes are reported in Tab. 5.5.

We computed the residual polarization amplitude maps as

$$P^{\rm res} = \sqrt{(Q^{\rm res})^2 + (U^{\rm res})^2} \qquad (5.32)$$

where $Q^{\rm res}$ and $U^{\rm res}$ are the residual Q and U maps, obtained after the subtracting the fitted foregrounds from the original Q and U frequency maps. At this stage we do not attempt to debias the polarization amplitude map, so $P^{\rm res}$ could be marginally affected by noise bias. The residual polarization maps $P^{\rm res}$ are shown in Fig. 5.16, while in Fig. 5.17 and 5.18 we present a study of the spectrum of the North and South Haze bubbles, corresponding to regions number 5, 7 and 8, as defined in Sec. 5.2.4.

5.4.2.1 Polarization residual maps

Fig. 5.16 shows the residual polarization amplitude map $P^{\rm res}$ of QUIJOTE 11 and 13 GHz, of WMAP K and of Planck 30 GHz. We can observe that the WMAP K and Planck 30 GHz residual maps are consistent with noise. In particular, the residual polarization map of Planck 30 GHz has very low values as compared with the other residual maps. This is due to the fact that for the template fitting procedure we use the `Commander` synchrotron solution (see Sec. 5.3.1.1), which strongly relies, by construction, on the 30 GHz Planck polarization data.

The QUIJOTE polarization residual maps, instead, show structures that can be associated with residual sky signal. Noise maps of QUIJOTE obtained

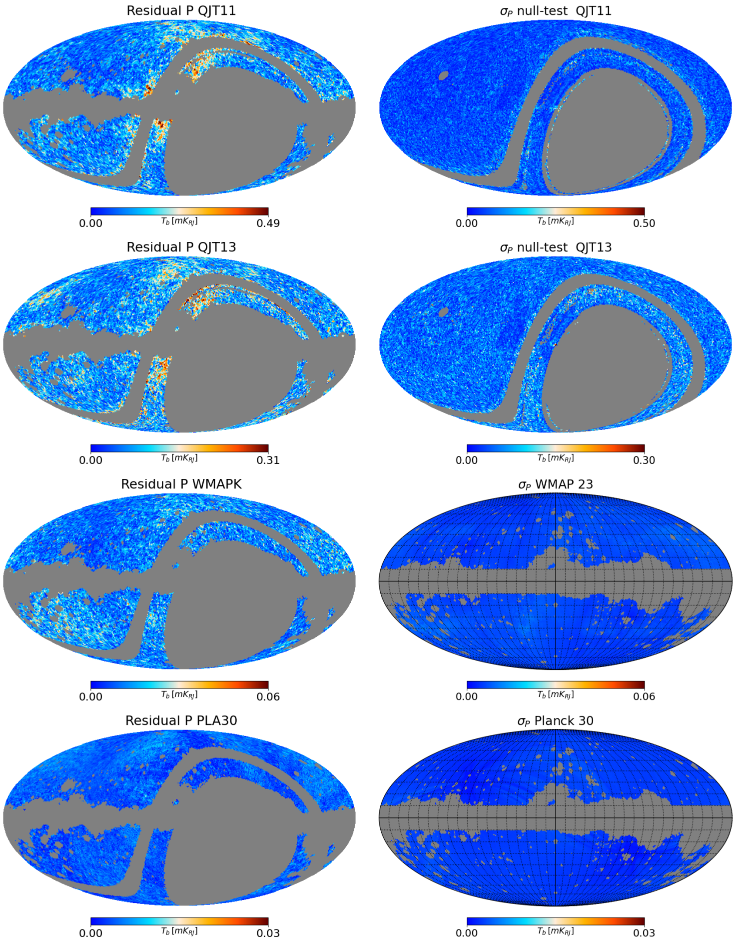

FIGURE 5.16— Residual P maps (left) and uncertainties (right) of: QUIJOTE 11 GHz, QUIJOTE 13 GHz, WMAP K, Planck 30 GHz. The uncertainty maps for QUIJOTE that are shown in this figure are obtained from the *half*-difference null-test (see Sec. 4.5.2, which is expected to highlight possible residual noise structures and systematics in the data.)

with the *half*-difference null-test (Sec. 4.5.2) are displayed in the right column of Fig. 5.16, showing that the noise level can not explain the excess of signal that is instead observed in the maps of the residuals (left column of Fig. 5.16). We can observe, at 11 GHz and 13 GHz, evident residual structures across the full Haze area, but with larger extension, reaching towards the north $b \sim 85°$. In addition, in the lower part of the NPS (bottom of region 1), close to the Galactic plane, we observe residual sky signal. This structure is also present in the intensity residual maps in Fig. 5.11. We refer to Watson et al. (in prep) for a detailed study of the NPS.

5.4.2.2 Polarization residual spectrum

With the same procedure that is applied in intensity, we computed the spectrum of the emission, integrated in several selected regions. In this case, as stated in Sec. 5.3.1.1, we do not perform the fit of an independent Haze template, because the projection of the Haze in the Stokes Q and U maps is unknown. Therefore, if the data contain a Haze component, which is not identified as synchrotron with the sky average spectral index, or thermal dust (even if it is a very minor component at these frequencies), it can be observed in the residual map P^{res} defined in Eq. 5.32. For this reason, we look for a polarized Haze component in the residual plus synchrotron spectrum (Eq. 5.34), by comparing it with the spectrum of the synchrotron alone (Eq. 5.33).

In a selected region, we fit (as in Eq. 5.31) the spectral index of the average polarized synchrotron alone, which is defined as:

$$S_\nu = P^s_\nu = \sqrt{\left(a^{Q,s}_\nu \cdot Q^s_\nu\right)^2 + \left(a^{U,s}_\nu \cdot U^s_\nu\right)^2} \tag{5.33}$$

where P^s_ν is the polarization amplitude map of the fitted synchrotron template, Q^s_ν and U^s_ν are the Stokes Q and U synchrotron template maps, and $a^{Q,s}$ and $a^{U,s}$ are the corresponding synchrotron fitted amplitudes. The synchrotron plus the residual map is then given by:

$$R^S_\nu = P^{\mathrm{res}}_\nu + P^s_\nu \tag{5.34}$$

which could contain the Haze component, if detected. In this analysis, the relative zero level is adjusted with T-T plots of the Q and U residual maps at each frequency ν, with respect to WMAP K at 22.8 GHz.

We show the spectra of the polarized synchrotron (S, in black) and of the residual plus synchrotron (R^S, in green) maps, averaged in two selected regions: the rectangle enclosing the South Haze bubble (region 7 and 8, in Fig. 5.17)

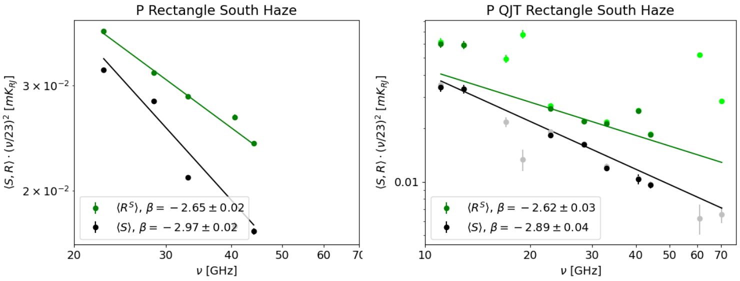

FIGURE 5.17— Polarization integrated spectrum after template fitting in the rectangle enclosing the South Haze (region 7, left) and in the overlap with the QUIJOTE sky coverage (region 8, right). The (dark) green points represent the colour-corrected integrated residual plus synchrotron and the green line is the fit of a linear slope to these points. The black points represent the colour-corrected integrated synchrotron and the black line is the fit of a linear slope to these points. The light-green and grey points, corresponding to QUIJOTE data at 17 and 19 GHz, to WMAP V, and to Planck 70 GHz, are not included in the fit because they are affected by noise.

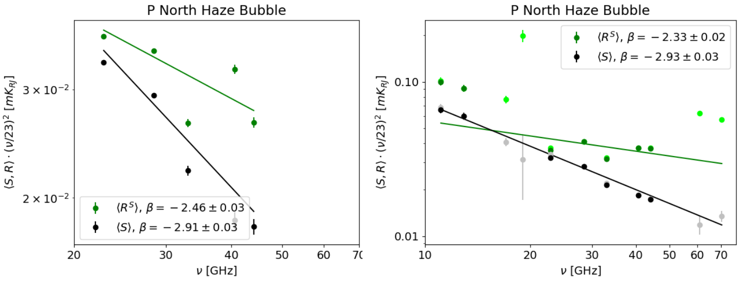

FIGURE 5.18— Same as in Fig. 5.17, but for the North Haze bubble (region 5, left) and in the overlap with the QUIJOTE sky coverage (right).

and the North Haze bubble (region 5, in Fig. 5.18). The error bars are the scatter (standard deviation) of the residual polarization map normalized by the square-root of the number of unmasked pixels, summed in quadrature with the calibration uncertainty of the frequency maps. The left panels of Fig. 5.17 and 5.18 are obtained with WMAP and Planck data only, excluding QUIJOTE, and considering region 7 and 5 in their entirety. The right panels, instead, include QUIJOTE data at 11 and 13 GHz, and therefore the selected regions are 8 and 5, corresponding to the available QUIJOTE sky coverage.

We can notice that in the South Haze region, when we use only WMAP and Planck data (region 7, left panel of Fig. 5.17), we measure a spectrum of the residual plus synchrotron with $\beta = -2.65 \pm 0.02$, which is compatible at 1σ with the spectral index of the intensity residual plus Haze reported in the previous section (see left panel of Fig. 5.15). We measure for the polarized synchrotron alone $\beta = -2.97 \pm 0.02$, which is compatible with the total synchrotron spectrum of the intensity in the same area. Similarly to the intensity, we observe, in polarization, a difference in the spectral indices of the residual plus synchrotron and the synchrotron alone, with the residual plus synchrotron (which could contain a Haze component) being flatter than the average synchrotron.

The right panel of the same figure (Fig. 5.17) shows the spectra of the southern Haze region in the QUIJOTE sky area (region 8), including also QUIJOTE data. We can notice here that the polarized residual plus synchrotron spectrum shows hints of deviation from a simple power law across the frequency range $11 - 44$ GHz. While the fitted synchrotron alone follows a clear power law relation with spectral index $\beta = -2.89 \pm 0.04$, the 11 and 13 GHz points of the residual plus synchrotron are significantly higher than the extrapolation of a power law obtained with the WMAP and Planck data. This enhancement of the signal at 11 and 13 GHz is a direct consequence of the excess of emission that we observe, in region 8, in the polarization residual maps shown in Fig. 5.16.

The same analysis is repeated in the North Haze bubble (region 5), the results of which are shown in Fig. 5.18. In the North Haze bubble, using only WMAP and Planck data, we obtain a residual plus synchrotron spectrum with $\beta = -2.46 \pm 0.03$, which is compatible with the residual plus Haze spectrum in intensity (see bottom panel of Fig. 5.15). The synchrotron spectrum across this region is a power law with spectral index $\beta = -2.91 \pm 0.03$, being steeper than the residual plus synchrotron spectrum. However, we notice that the WMAP and Planck spectral points have a large scatter, therefore we do not recover a precise power law relation.

Also in this region, when we include the QUIJOTE data points (right panel in Fig. 5.18), we can notice an excess of signal with respect to the extrapolation of a power law obtained from the WMAP and Planck data alone. We conclude that in the QUIJOTE maps we detect an excess of signal in the North Haze bubble that deviates from the average sky synchrotron, and that could be ascribed to a polarized Haze component.

Note that, as already mentioned, the residual polarization map used in this analysis can be affected by noise bias. In order to verify the robustness of these results, we computed the SED of the unbiased polarization amplitude $\langle P_{\mathrm{MAS}} \rangle$ (see Sec. 5.3.2.1), averaging in the region of the North and South Haze bubbles

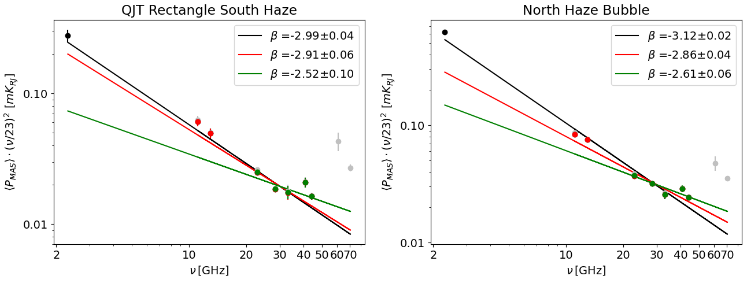

FIGURE 5.19— Spectrum of the unbiased polarization amplitude $P_{\rm MAS}$, integrated in the southern Haze rectangle overlapping with the QUIJOTE sky (region 8), and in the North Haze bubble. We show in green the fit performed over the WMAP and Planck points, in red the fit adding QUIJOTE 11 and 13 GHz data, and in black the fit when we add also S-PASS. The grey points, corresponding to WMAP V and Planck 70 GHz, are not included in the fit as they show large deviations from the power law spectrum driven by lower frequencies, possibly due to their noise levels and to the contribution of sky components other than synchrotron.

(region 5 and 8). The relative zero level is adjusted before computing $P_{\rm MAS}$ with T-T plots of the Q and U frequency maps, with WMAP K as a reference. The uncertainties are obtained as the standard deviation of the average signal within 11 apertures of 7° radius, which are drawn in the common sky area between QUIJOTE and S-PASS with negligible sky emission. The spectra of $\langle P_{\rm MAS}\rangle$ in the two regions are shown in Fig. 5.19, where we included also S-PASS polarization data. We can clearly see in these figures that the spectrum that is fitted across frequencies in the range $23-44$ GHz (Planck and WMAP data) is flat (green line), and not well determined in some cases. When we include low frequency data as QUIJOTE (11 and 13 GHz) and S-PASS (2.3 GHz) we can see a change of the slope towards steeper values. This is an interesting behaviour, which can be interpreted with a double electron population generating the Haze emission, with a flat synchotron spectrum at frequencies $\nu > 23$ GHz, which hardens up at low frequencies. An independent picture of this result is shown in the next section, where we performed a detailed analysis with T-T plots in polarization.

5.4.3 T-T plots of Haze polarized plumes and spurs

With the aim of studying the Haze region in polarization with a different approach to that presented in Sec.5.4.2, we performed a correlation T-T plots analysis as described in Sec. 5.3.2.2, in the regions presented in Sec. 5.2.4. In

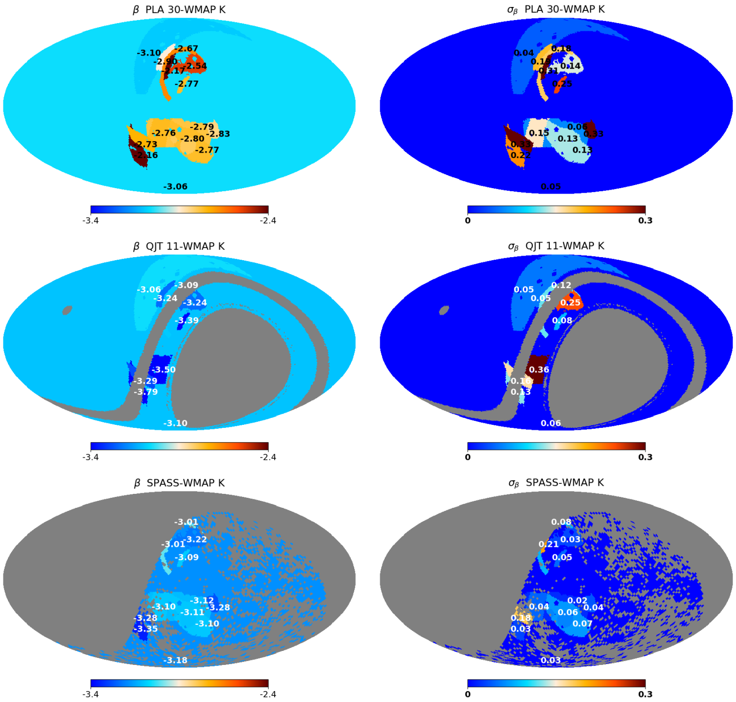

FIGURE 5.20— Polarization spectral indices in the selected regions (left) and uncertainties (right), obtained with a T-T plots analysis based on data from Planck 30 GHz, QUIJOTE 11 GHz S-PASS 2.3 GHz, and WMAP K as pivot.

Label	Region	$\beta_{(23-30)}$	$\beta_{(11-23)}$	$\beta_{(2.3-23)}$
-	Full-sky	-3.06 ± 0.05	-3.10 ± 0.06	-3.18 ± 0.03
1	NPS	-3.10 ± 0.04	-3.06 ± 0.05	-
2	Ext Haze Filament	-2.90 ± 0.19	-3.24 ± 0.05	-
3	Haze Filament	-2.67 ± 0.18	-3.09 ± 0.12	-3.01 ± 0.08
4	Int Haze Filament	-2.17 ± 0.31	-	-3.01 ± 0.21
5	North Haze bubble	-2.54 ± 0.14	-3.24 ± 0.25	-3.22 ± 0.03
6	GCS	-2.77 ± 0.25	-3.39 ± 0.08	-3.09 ± 0.05
7	Rectangle South Haze	-2.79 ± 0.06	-	-3.12 ± 0.02
8	QJT Rectangle South Haze	-2.76 ± 0.15	-3.50 ± 0.36	-3.10 ± 0.04
9	South Haze bubble	-2.80 ± 0.13	-	-3.11 ± 0.06
10	South Haze bubble clean	-2.77 ± 0.13	-	-3.10 ± 0.07
11	eRosita West	-2.16 ± 0.22	-3.79 ± 0.13	-3.35 ± 0.03
12	Region 12	-2.73 ± 0.33	-3.29 ± 0.16	-3.28 ± 0.18
13	eRosita East	-2.83 ± 0.33	-	-3.28 ± 0.04

Table 5.7— Polarization spectral indices in the selected regions obtained with a T-T plots analysis based on data from Planck 30 GHz, QUIJOTE 11 GHz S-PASS 2.3 GHz, and WMAP K as pivot. For the determination of the spectral indices we use the methodology described in Sec. 5.3.2.2.

this analysis, we also include the S-PASS data at 2.3 GHz, corrected for Faraday rotation as described in Sec. 5.2.3. We computed the spectral indices between the frequency pairs:

- 23–30 GHz (Planck 30 GHz - WMAP K)
- 11–23 GHz (QUIJOTE 11 GHz - WMAP K)
- 2.3–23 GHz (S-PASS 2.3 GHz - WMAP K)

A summary of the results is reported in Tab. 5.7 and a graphical representation of the estimated spectral indices and uncertainties is shown in Fig. 5.20, for the three frequency cases. In order to validate our results, we present a detailed analysis of the posterior distribution of the T-T plots in the appendix (Sec. A.2).

By looking at Fig. 5.20, we can notice that the Haze in polarization appears as two extended and slightly asymmetric bubbles (region 5,7–10), surrounded and connected to the Galactic plane with filaments and spurs (region 2, 3, 4, 6). Our interpretation is that the regions 2–10 are related to the Haze. Indeed, our measurements show that the spectral index of these regions is flat at high frequencies (23–30 GHz) and uniformly moves towards steeper values at lower frequencies (11–23 GHz and 2.3–23 GHz). The typical spectral indices of the

Haze regions at 30–23 GHz are $-2.8 \lesssim \beta \lesssim -2.6$, while at lower frequencies they became steeper, being $-3.2 \lesssim \beta \lesssim -3.0$ at 11–23 GHz and at 2.3–23 GHz.

We use for comparison the average spectral indices of the full-sky and of the NPS (region 1), which is a widely studied region, currently modeled as synchrotron emission originated from the expanding shell of a nearby supernova explosion (e.g., Planck Collaboration et al., 2016c and Watson et al., in prep). We can notice that the spectral indices of the full-sky and of the NPS at 30–23 GHz are steeper than the spectra indices of the Haze associated regions. Instead, at 11–23 GHz we observe the opposite behaviour: the full sky and NPS spectral indices are flatter than those of the Haze associated regions.

We will extend the discussion of these results in Sec 5.5, where we provide an overview and an interpretation of the measurements obtained with different methodologies.

5.5 Discussion

We discuss here the results presented in the previous section, and summarize what we obtained in some specific regions, particularly in the southern Haze area (region 7-10), in the North Haze bubble (region 5), and in North Haze filament (region 3), in intensity and polarization, and with different methodologies.

5.5.1 South Haze area

Previous studies of the Haze emission in intensity have been concentrating in the area below the Galactic center (region 7 in this work) because of the apparently little complexity and low foregrounds contamination of the intensity signal at WMAP and Planck-LFI frequencies. However, the S-PASS polarization data (see Fig. 5.6) provided a more detailed picture of the area, showing an extended polarized plume in the south (region 9), but also localized contaminated areas that appear to be depolarized, and whose location is indicated in Fig. 5.8. These depolarized areas are, in particular, region "A" identified by Iacobelli et al. (2014) and G353.34, a nearby supernova remnant. Moreover, S-PASS data in polarization show that almost the full southern bubble is affected by Faraday rotation at low frequencies. Indeed, from the polarization angle maps shown in Fig. 5.6, we can observe that the polarization angle across the South Haze bubble (region 9) has a transition from positive to negative values when comparing the high (23 GHz and 30 GHz) and low (2.3 GHz) frequencies. In this work, according to these considerations, we identified several regions in the area below the Galactic center (region 7, 8, 9, 10 - see Sec. 5.2.4) and we studied them with different methodologies, including also the new QUIJOTE data, both in intensity and polarization.

First of all, we reproduced the analysis of the Haze in intensity by using Planck and WMAP data in region 7, and applying a similar technique to that in Planck Collaboration et al. (2013). We obtained a spectrum of the Haze in region 7, using only Planck and WMAP data (Fig. 5.15), with $\beta^H = -2.71 \pm 0.04$, and of the total synchrotron with $\beta^S = -3.05 \pm 0.02$. We repeated the same analysis in region 9, which encloses the brightest part of the South Haze bubble, obtaining $\beta^H = -2.72 \pm 0.03$ and $\beta^S = -3.03 \pm 0.02$. From these results we can notice that the intensity Haze spectrum in region 9 (the South Haze bubble) is consistent with the spectrum in region 7, although the latter region is more extended.

The main aim of this work is the characterization of the Haze with the QUIJOTE data at low frequency. Being QUIJOTE a ground based experiment located in the northern hemisphere, provides a survey of the northern sky, but it does not cover the southern sky area enclosing the South Haze bubble (region 9). However, with QUIJOTE data, we have access to a fraction of region 7, that we call region 8 in this work. In Sec. 5.4.1 we presented the intensity analysis in this restricted area, including the low frequency QUIJOTE data, at 11 and 13 GHz. A Haze component is detected in region 8 as shown in Fig. 5.12. We computed the spectrum of the emission in this region, as shown Fig. 5.14, obtaining a spectral index of the Haze $\beta^H = -2.79 \pm 0.08$ and of the total synchrotron $\beta^S = -3.00 \pm 0.03$. The spectrum of the Haze in region 8 is flatter than the total synchrotron by $\Delta\beta = 0.21$, and the central value is slightly steeper than that obtained with WMAP and Planck-LFI data alone in region 7, although there is consistency within 1σ.

A similar analysis is also performed in polarization. A map of the polarization residuals is shown in Fig. 5.16, where we can observe significant residuals across the southern Haze area. It is interesting to compare the results of the template fitting in polarization with the spectra obtained in intensity. In particular, in the South Haze area (region 7), we measured with the template fitting technique and with WMAP and Planck data alone (left panel of Fig. 5.17) a residual plus synchrotron spectrum (which should contain the Haze component, if detected) with $\beta = -2.65 \pm 0.02$ (see Fig. 5.17), while in intensity we have, as already mentioned, $\beta = -2.71 \pm 0.04$ for the residual plus synchrotron. We observe that the spectrum of the emission where we expect to see a Haze component has a spectral index in polarization that is compatible with that obtained in intensity. In addition, the spectrum of the polarized residual plus synchrotron is significantly flatter than the spectrum of the polarized synchrotron alone, which has $\beta^S = -2.97 \pm 0.02$.

If we consider the sky in the overlap with the QUIJOTE coverage, and we look at region 8, we can extend our frequency coverage. In this case, we observe a break of the power law behaviour of the polarized residual plus synchrotron component, with the QUIJOTE data point being above the extrapolated power law from the higher frequencies. A curvature of the South Haze bubble polarization spectrum towards steeper values at low frequencies is confirmed by the results of the T-T plots: it is evident from Fig. 5.20 that the spectral indices in region 7, 8 and 9, so in the whole South Haze complex, are flat ("red") at 23–30 GHz and steep ("blue") at 11–23 GHz and 2.3–23 GHz. This low frequency steepening behaviour, however, is not only valid for the South Haze, but for the full Haze complex, represented by region 2-10. The only region where the low frequency steepening is not observed is the NPS, which indeed is a well known distinct component from the Haze.

We mentioned also about two depolarized spots at 2.3 GHz, corresponding to region "A" and to the nearby supernova remnant G353.34. In order to check that the determination of the spectral index of the South Haze bubble is not affected by the presence of these two extra structures in the area, we repeated the T-T plot by masking region "A" and G353.34 (region 10 in Fig. 5.8). As reported in Tab. 5.7 and in Fig. 5.20, we obtained $\beta = -2.77 \pm 0.13$ at 23–30 GHz and $\beta = -3.10 \pm 0.07$ at 2.3–30 GHz, which are in perfect agreement with the spectral indices computed with the same T-T plots methodology in the whole South Haze bubble, which are $\beta = -2.80 \pm 0.13$ at 23–30 GHz and $\beta = -3.11 \pm 0.06$ at 2.3–30 GHz. We conclude that the depolarized regions across the South Haze do not bias the spectral index determination of the bubble.

5.5.2 North Haze bubble

The North Haze bubble (region 5) is the region, among those studied in this paper, with the flattest spectral index. From the analysis with the intensity data, in the range of frequencies 23-60 GHz[19] (Fig. 5.15, bottom panel) we measured a spectral index of the Haze $\beta^H = -2.41 \pm 0.04$, and of the Haze plus synchrotron $\beta^S = -2.52 \pm 0.02$. Both β^H and β^S are far from the typical sky average synchrotron spectral index $\beta \approx -3$, meaning that, in this area and frequency range, the emission of the Haze is dominant over the Galactic diffuse synchrotron. The flat spectral index in this region could also be due to residual free-free emission, which is bright in this area. However, we can compare this result with the spectral index in polarization between 23 and 30 GHz, where there is no contamination from free-free emission. We obtained, with the T-T plots in the North Haze bubble, a spectral index $\beta = -2.54 \pm 0.14$ between 23

---

[19] We do not include QUIJOTE low frequency intensity data here, due to residual atmospheric 1/f noise in the North Haze bubble region.

and 30 GHz. We notice that the T-T plots result in polarization is compatible with the intensity template fitting result for the total synchrotron, at WMAP and Planck-LFI frequencies, within 1σ. We therefore infer that the observed flat intensity and polarization spectral index in the North Haze bubble is ascribed to the synchrotron emission produced by the Haze component, which dominates over the typical (steeper) synchrotron in this region.

At lower frequencies, we observe a steepening of the polarization spectrum in the North Haze bubble. From the template fitting in polarization and from the SED of the unbiased polarization map $P_{\rm MAS}$ in this region (Fig. 5.18 and 5.19), we can notice that the spectrum is not well determined by WMAP and Planck-LFI data alone. However, the low frequency data of S-PASS (2.3 GHz) and QUIJOTE (11 and 13 GHz) are well aligned in a slope with $\beta \sim -3$, which is compatible with a typical synchrotron spectrum. In addition, with the T-T plot analysis in polarization, we measure steeper values of the spectral index, being it respectively $\beta = -3.24 \pm 0.25$ at 11–23 GHz, and $\beta = -3.22 \pm 0.03$ at 2.3–23 GHz. We interpret this result with a double electron population that generates the polarized synchrotron signal in region 5: one with a flat ($\beta \sim -2.5$) spectral index that dominates in the frequency range 20 GHz – 44 GHz, and one with a steeper spectrum ($\beta \sim -3.2$) that emerges at $\nu < 20$ GHz. QUIJOTE data provide a result that is compatible with that presented by Carretti et al. (2013) based on S-PASS data, fitting well with the interpretation presented in Crocker et al. (2015), and summarized in Sec. 5.1.4.

5.5.3 Comparison between South and North Haze bubbles

An interesting consideration is connected with the recent results presented by Jew & Grumitt (2020), who computed with a novel technique the spectral indices of the North and South Haze bubbles between 30 and 44 GHz, using Planck data. They reported a difference between the polarization spectral index of the two bubbles, being $\beta = -2.36 \pm 0.09$ in the North and $\beta = -3.00 \pm 0.05$ in the South Haze.[20] In this work, we measure an asymmetry of the spectral indices of the northern and southern Haze bubbles in intensity, in the frequency range 23-60 GHz, consistent with what Jew & Grumitt (2020) found in polarization. We obtain a total synchrotron index $\beta = -2.52 \pm 0.02$ in the North Haze bubble, and $\beta = -3.03 \pm 0.02$ in the South Haze bubble, as shown in Fig. 5.15 using only WMAP and Planck data. There is consistency between our total synchrotron

---

[20] Note that the regions studied in Jew & Grumitt (2020) do not perfectly match with ours. They integrated two approximately symmetric bubbles in the north and in the south corresponding to the γ-ray Fermi bubbles, while we restrict our analysis to the brightest region of the plumes as observed at low frequency (2.3 GHz), in polarization.

intensity spectrum and the polarization spectrum at 30-44 GHz measured by Jew & Grumitt (2020). In addition, our results with T-T plots confirm the asymmetry between the North and South Haze bubbles also in polarization, at 23-30 GHz: the spectral index across the North Haze bubble is $\beta \approx -2.54 \pm 0.14$, and in the South Haze bubble it is $\beta = -2.80 \pm 0.13$. The South Haze bubble has a steeper spectrum than the North Haze bubble, both in intensity and polarization. Interestingly, at lower frequencies, this trend is inverted. The T-T plots between 2.3 GHz and 23 GHz show that the spectrum of the North Haze bubble ($\beta = -3.22 \pm 0.03$) is slightly steeper than that in the South Haze bubble ($\beta = -3.11 \pm 0.06$).

5.5.4 North Haze filament

The North Haze filament (region 3) is an interesting case study. It corresponds to the structure identified by Vidal et al. (2015) and Planck Collaboration et al. (2016c) as the filament surrounding the northern Fermi bubble in γ-rays, and the microwave Haze in the north. In Sec. 5.5 of Planck Collaboration et al. (2016c), a measurement of the spectral index of the filament using Planck 30 GHz and WMAP K data is reported. They measured $\beta = -2.54 \pm 0.16$ with T-T plots of the unbiased $P_{\rm MAS}$ maps at 30 and 23 GHz, with a methodology that is very similar to that described in Sec. 5.3.2.1. In this work, we performed the measurement in the same region, but using a different technique as described in Sec. 5.3.2.2, obtaining $\beta = -2.67 \pm 0.18$ (see Tab. 5.7 and Fig. 5.20).

In the attempt of reproducing the result of Planck Collaboration et al. (2016c) with T-T plots of $P_{\rm MAS}$, we identified a possible source of bias that can introduce significant differences in the estimate of the β. Although the polarization amplitude $P_{\rm MAS}$ is not affected by noise bias if computed as in Plaszczynski et al. (2014), it is a positive quantity, and, in regions with low signal to noise the determination of the spectral index with the classical T-T plot methodology (Sec. 5.3.2.1) can be biased. For example, in the northern Haze filament (region 3), we obtained $\beta = -2.86 \pm 0.07$ using a T-T plot of the $P_{\rm MAS}$ maps, where we allowed to fit both the slope and an offset between the maps. However, if the zero level of $P_{\rm MAS}$ is correctly set, as it is in this case where we first adjust the relative offset of the Q and U maps with the reference, we can force the intercept of the T-T plot slope to be zero. In this case, we obtain a value of the spectral index $\beta = -2.68 \pm 0.03$, which is inconsistent with the previous result, where the intercept was free to vary, but which is in full agreement with the result reported in this chapter (Tab. 5.7), obtained with the method described in Sec. 5.3.2.2 based on Fuskeland et al. (2014).

In Fig. 5.21 we show the T-T plot of the unbiased polarization amplitude

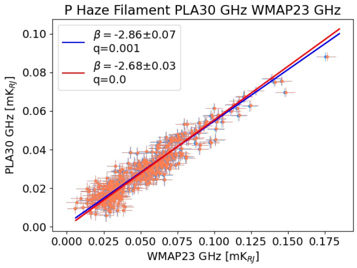

FIGURE 5.21— T-T plot with P_{MAS} in the North Haze filament (region 3), comparing the case where we fix or do not fix the offset of the linear fit, to illustrate the effect of Eddington bias.

in the filament (region 3). The blue line is a fit of the points with freedom on the determination of the slope and of the offset. The red line is the fit over the same data points, but where the intercept is forced to be zero. We can clearly notice that the red and blue lines have a different slopes, and that therefore the recovered spectral indices are also different. The small difference between the red and blue data points is due to the different colour correction that is applied to the same initial data, given that the spectral index resulting from the two fitting methodologies is different. Our final conclusion is that T-T plot of the positive definite unbiased polarization amplitude (P_{MAS}) is affected by noise bias. A possible solution to mitigate the bias consists in fitting the T-T plot with the intercept fixed at zero. The method applied in this work (described in Sec. 5.3.2.2 and based on Fuskeland et al., 2014, 2019), instead, is not significantly biased, since it uses T-T plots of a combination of Q and U data, which can be both positive and negative.

5.6 Conclusions

We derived the spectral properties of the microwave Haze with different methodologies, in intensity and in polarization, using for the first time the new Haze observations from the QUIJOTE experiment, at 11 and 13 GHz, in combination with the publicly available S-PASS (2.3 GHz), WMAP (23–61 GHz) and Planck-LFI (30–70 GHz) data. We applied two different approaches for the study. First, we performed a template fitting analysis in intensity and in polarization, attempting to isolate the emission of Haze as an extra component, out of the classic Galactic foregrounds such as synchrotron, free-free, thermal dust and AME. Afterwards, we performed a correlation T-T plot analysis in polarization, aimed at computing the spectral index in several selected regions possibly related with the Haze.

We performed a detailed characterization, in intensity and polarization, of the microwave emission from the Haze enclosed in regions 5, 7, 8 and 9, which are defined in Sec. 5.2.4 and Fig. 5.8. In addition, we studied several filamentary structures, including: the filament that surrounds the northern Fermi/Haze bubble (Planck Collaboration et al., 2016c, region 3), the bright polarized region in the external side if the Haze filament (region 2), and the GCS (region 6), which is a bright spur extending from the center of the map towards the north, as well as some filamentary structures that might correspond to the recently observed eRosita bubbles (Predehl et al., 2020).

By using the intensity data of QUIJOTE, WMAP and Planck-LFI, as a result of the template fitting, we computed the spectrum of the Haze in the south, in the overlap with the QUIJOTE sky coverage, within region 8. We obtained a synchrotron spectrum with spectral index $\beta = -2.79 \pm 0.08$ (see Fig. 5.14), at frequencies 11–60 GHz. As a general trend, we obtained that the spectrum of the Haze component is flatter than the Galactic synchrotron spectrum. Our results in the whole south Haze area (region 7), however, are in slight tension with those obtained by Dobler & Finkbeiner (2008) and Planck Collaboration et al. (2013) in the same region, indicating a spectral index of the Haze that is steeper than that obtained from previous works (e.g., $\beta \sim -2.71 \pm 0.04$ from this work and $\beta \sim -2.56 \pm 0.05$ from Planck Collaboration et al., 2013).

We also studied the intensity spectrum of the Haze in the North and South bubbles (region 5 and 9), but excluding QUIJOTE data that are not available or affected by noise artifacts. We measured a synchrotron emission from a Haze component with a spectral index $\beta^H = -2.41 \pm 0.04$ in the North Haze bubble and $\beta^H = -2.72 \pm 0.03$ in the South Haze bubble, as shown in Fig. 5.15. We measured for the first time in intensity a difference of the spectral index in the North and South bubbles, in the frequency range 23–60 GHz, with a significance of $\approx 6\sigma$. This behaviour is also observed in polarization between 23 and 44 GHz, in agreement with the results by Jew & Grumitt (2020) between 30 and 44 GHz.

In polarization, we studied the spectra of the Haze-related structures with both a template fitting (see Fig. 5.17 and 5.18) and correlation T-T plot technique, with respect to WMAP K (see Tab. 5.7 and Fig. 5.20). Our results show flat spectrum regions across the Haze area at 23–30 GHz, and an evident steepening at low frequencies, in agreement with Carretti et al. (2013). Interestingly, we noticed that the intensity and polarization spectral indices across region 5

(North Haze bubble) and 7–9 (South Haze bubble) are compatible at frequencies 23–44 GHz.

We observed in Fig. 5.20 that the Haze-related structures (regions 2–10) are significantly flat ($-2.8 \lesssim \beta - 2.6$) if compared with the sky average synchrotron ($\beta \sim -3$) at 23-30 GHz, while at lower frequencies (11-30 GHz and 2.3-30 GHz) the spectrum of the Haze steepens significantly ($-3.2 \lesssim \beta \lesssim -3.0$). On the other hand the NPS (region 1), which is thought to be a nearby supernovae shell not related with the Haze structures, shows the opposite behaviour: its spectral index does not show significant differences across the frequencies presented in this work.

Our results in polarization are compatible with those presented in Carretti et al. (2013), and can be therefore interpreted with the model presented in Crocker et al. (2015). However, in intensity, we do not observe a curvature of the Haze spectral index as we do see in polarization, being the spectrum in region 8 well characterized by a single power law with $\beta^H \sim -2.8$. Further investigation is needed to understand this behaviour, possibly studying the magnetic field in the area, and estimating the expected polarization fraction from different electron cosmic-ray population indicated by the polarization measurements.

6

Conclusions and future prospects

> *"But now it was no longer me*
> *who made the galaxy fly,*
> *it was the galaxy that made me fly,*
> *hanging on its tail."*
> Italo Calvino, Le Cosmicomiche

This thesis is based on the analysis and validation of the data obtained from 2012 to 2018 with the MFI instrument of the QUIJOTE experiment, which observed the northern sky at four frequencies in the range 10–20 GHz. The goal of the experiment is to provide a characterization of the polarized low frequency sky, for the study of the CMB radiation.

In particular, this thesis is focused on the development of the map-making step of the pipeline, which has been validated with simulations, and subsequently applied for the construction of the QUIJOTE-MFI wide-survey maps. It continues with the presentation of the QUIJOTE-MFI wide-survey maps, a detailed validation of the data with null-tests and cross-correlation analyses, and some general scientific results obtained from these data. Finally, a study of the region of the microwave Haze is presented, which is based on new QUIJOTE data from raster scan observations dedicated to the Galactic center region, in combination with the wide-survey data. The main results and conclusions of the thesis are summarized in the following sections.

6.1 Implementation and validation of the PICASSO map-making and code

- The map-making code for the QUIJOTE-MFI experiment (PICASSO) has been developed, starting from the initial implementation presented in Pelaez Santos (2019). The priors on the $1/f$ noise by means of the covariance matrix of the baselines $C_{\rm a}$ have been implemented in PICASSO (see Sec. 3.3.4).

- The possibility of constructing maps from data taken during different periods of the QUIJOTE-MFI campaign has been implemented in PICASSO, allowing the construction of maps with a single run of the code, instead of constructing one map for each period and combine them in a final single map a posteriori (see Sec. 3.3.3). The joint analysis of all the data provides a better determination of the noise baselines, significantly improving the reconstruction of large angular scales in the maps. In addition, the discontinuities due to the different sky coverage in different periods of observation were significantly improved.

- A technique has been implemented to fit a template function at the time order domain level, during the map-making step (see Sec. 3.3.6). This procedure has been validated with simulations of QUIJOTE-MFI wide-survey data, which include as input signal both thermal and $1/f$ noise components, as well as a constant atmospheric emission that is modulated by the change of the airmass, or the CMB dipole. The injected amplitudes of the atmosphere and of the CMB dipole are recovered with precisions of 2% and 26% respectively (see Sec. 3.6.4).

- The definition of different data splits during the map-making step has been implemented in PICASSO. This allows the generation of the total map and a set of null-tests in one single run, using a common baseline solution for the map and the null-tests, obtained from the full input dataset.

- The PICASSO code has been validated, at the map and angular power spectrum levels, with simulations of the QUIJOTE-MFI wide-survey dataset, for three noise cases: no-noise, white noise, and realistic $1/f$ noise (see Sec. 3.6.1 and 3.6.2). It was found that PICASSO is able to reconstruct the input sky signal, both in intensity and polarization, with a signal error lower than 0.001% at multipoles in $20 < \ell < 200$, for TT, EE and BB, at all the QUIJOTE-MFI frequencies. The CMB solar plus orbital dipole is reconstructed in the maps with high ($\sim 0.1\,\%$) accuracy, even in the case of realistic $1/f$ noise in the data. PICASSO performs an accurate subtraction of the $1/f$ noise from polarization data, recovering the expected white noise level, while the residual noise in intensity shows some $1/f$ structure, due to the large correlated noise contamination.

- The transfer function of the code has been estimated, showing that PICASSO performs a perfect reconstruction of the sky signal at multipoles $\ell > 10$ in TT and $\ell > 8$ in EE and BB, for the partial sky coverage of the MFI wide survey. Moreover, in polarization, also the larger angular scales $2 < \ell < 8$ are precisely recovered, within 2 % error (see Fig. 3.11).
- This work is also the content of a paper (Guidi et al.), which is currently submitted for publication.

6.2 Characterization and validation of the QUIJOTE-MFI wide-survey maps

- The PICASSO map-making code has been used to construct the QUIJOTE-MFI maps of the full northern sky survey, the so-called wide-survey maps.
- A detailed search of residual interference in the wide-survey data has been performed, using a joint analysis of the azimuth stacks of the time ordered data and of the *halfring* null-test (see Sec. 4.1.5). All the identified RFI has been flagged from the data before the construction of the final QUIJOTE-MFI maps.
- A detailed characterization of the noise in the wide-survey maps has been performed using a set of null-test maps. The *half*-difference null-test has been selected as representative of the global noise in the maps. A study its angular power spectrum has been performed, by fitting a $1/\ell$ slope to it, in order model the noise properties in the harmonic space (see Fig. 4.14). In addition, it is presented a statistical characterization of the noise in the frequency domain, for all the MFI channels and periods of observation (see Sec. 4.1.3).
- Using the cross-correlations of *half*-difference noise maps, the correlation of the noise between the two frequency splits of each MFI horn has been studied. The derived results are consistent with previous estimates obtained from the data at the time order domain. A noise correlation of $\sim$ 80 % (TT) and $\sim$20–60 % (EE, BB) has been measured in the data from different frequencies of the same horn (see Tab. 4.8). This information is essential for a proper error treatment in all subsequent analyses using a combination of the two frequencies.

- The correlation of the noise between the maps obtained from the "correlated" and "uncorrelated" channels pairs was measured, for each QUIJOTE-MFI horn and frequency split. There is correlation of $\sim 90\,\%$ in TT, while no correlation is detected in polarization (EE and BB; see Tab. 4.9). These values have been used to generate the final weight maps, which are a combination of the weights from the "correlated" and "uncorrelated" channels.

- A set of consistency checks based on cross-correlation techniques has been performed, in order to validate the calibration of the QUIJOTE-MFI wide survey maps, in intensity and in polarization. In particular, the inter-horn, inter-period and intra-nulltest consistency checks are presented. These tests were used to study the relative calibration among different horns observing the same frequencies, among the data taken in different periods, and between the two splits of the null-tests. The results obtained from these analyses show that the internal consistency of the data do not exceed variations of 1% in intensity and 5% in polarization, supporting the quoted calibration uncertainty for the QUIJOTE-MFI wide-survey maps (see Sec. 4.6).

- Cross-correlations of the intensity QUIJOTE-MFI wide-survey maps with a map of the CMB anisotropies were performed, obtaining a detection of the CMB anisotropies at 10–20σ, depending on the QUIJOTE-MFI frequency channel (see Tab. 4.11).

- The analysis of the angular power spectra of the wide-survey maps is presented, in particular for the 11 GHz data from horn number 3, in the range of multipoles $30 < \ell < 300$. The TT, EE, BB, TE, TB, and EB angular power spectra from the sky at different Galactic latitudes have been computed and analyzed. It is observed that the EE spectrum is larger than the BB one. The ratio of the amplitude of the B over E-modes, at $\ell = 80$, is $A_{\rm BB}/A_{\rm EE} = 0.34 \pm 0.10$ within a mask covering the Galactic latitude range $|b| > 5^\circ$, and declinations $6^\circ < \delta < 70^\circ$ (see Tab. 4.7). The spectra can be modeled with a power law ($C_\ell \sim \ell^\alpha$) with index $\alpha = -3.00 \pm 0.16$ for EE and $\alpha = -3.09 \pm 0.41$ for BB, at $|b| > 5^\circ$. The TB and EB spectra are measured to be compatible with zero within the uncertainties, as expected (see Fig. 4.10), while a marginal detection of the TE spectrum is obtained.

- This work will be published in Rubiño-Martín et al. (in prep), and the maps will be made publicly available.

6.3 Analysis of the microwave Haze using new QUIJOTE-MFI data

- New data from raster scan observations of QUIJOTE-MFI in the region surrounding the Galactic center (in the Haze and ρ-Ophiuchi regions) have been analyzed, and combined with the wide-survey data into a map, with a single run of the PICASSO code. The addition of raster scan data leads to an improvement of a factor ~ 2 in the noise, with respect to maps built using wide-survey data only. These new maps provide additional information across the Haze region.

- An analysis of the intensity maps has been performed, based on the fitting of template-maps for the different sky components, including a model of the Haze. The approach of this analysis is similar to that of previous studies carried out with WMAP (Dobler & Finkbeiner, 2008) and Planck-LFI (Planck Collaboration et al., 2013) data. The Haze component is clearly detected in the QUIJOTE-MFI maps, at $\sim 9\sigma$ confidence level, in a region located below the Galactic center ($10^\circ \lesssim l \lesssim 30^\circ$, $-10^\circ \lesssim b \lesssim -35^\circ$, see Fig. 5.12). The spectrum of the Haze emission has been measured at frequencies 11–60 GHz, finding a synchrotron-like power law with spectral index $\beta^H = -2.79 \pm 0.08$ (see Fig. 5.14), which is in slight tension with the results from previous works (e.g., Planck Collaboration et al., 2013) that obtained $\beta^H = -2.56 \pm 0.05$. It is observed, in agreement with previous works, that the spectrum of the Haze component is flatter than the total Galactic synchrotron spectrum, whose measured spectral index is $\beta^s = -3.00 \pm 0.03$.

- The intensity spectrum of the Haze in the North and South bubbles (excluding QUIJOTE data) has been studied, measuring a synchrotron emission from the Haze component with spectral index $\beta^H = -2.41 \pm 0.04$ in the North Haze bubble and $\beta^H = -2.72 \pm 0.03$ in the South Haze bubble (see Fig. 5.15). A difference of the spectral index in the North and South bubbles is measured for the first time in intensity, in the frequency range 23–60 GHz, with a significance of $\approx 6\sigma$.

- The polarization maps have been analyzed by fitting templates of the polarized Galactic foregrounds, following a similar approach to that applied in intensity. An excess of residual sky signal is observed in the QUIJOTE maps at 11 and 13 GHz, which could possibly be associated with a Haze component, or with imperfections of the foreground models adopted for the fitting, as, for example, spatial variations of the synchrotron spectral index.

- Regions that could possibly be associated with a polarized component of the microwave Haze have been identified (see Fig. 5.8), and a correlation T-T plot analysis of the polarization data was performed, obtaining spectral indices of the polarized sky emission at frequencies 30–23 GHz (Planck 30 GHz - WMAP K), 11–23 GHz (QUIJOTE 11 GHz - WMAP K), and 2.3–23 GHz (S-PASS 2.3 GHz - WMAP K). The measured spectral indices are $\beta \sim -2.7$ in most of these regions, at high frequencies (30–23 GHz), while a clear transition towards steeper values of $\beta \sim -3.1$ can be observed at lower frequencies (11–23 GHz and 2.3–23 GHz; see Fig. 5.20), in agreement with previous works (Carretti et al., 2013). In addition, the spectral asymmetry that is measured in intensity between the northern and southern bubbles can also be observed in polarization in the 30–23 GHz range, with the spectrum of the northern bubble ($\beta = -2.54 \pm 0.14$) being flatter that that in the southern one ($\beta = -2.80 \pm 0.13$).

- The results obtained in this work will be published in Guidi et al. (in prep.).

6.4 Publications

An overview of the publication accomplished during the years of this thesis, or currently in preparation, are presented in Tab. 6.1. The main results coming out from this thesis are now submitted or in preparation for publication, and they correspond to the first three items in the table. In addition I will be co-author of a set of papers that will follow the publication of the QUIJOTE-MFI wide survey maps, whose aim is to present specific scientific results obtained from these new data, as described in Sec. 2.2.3. These papers are listed as the items 4–12 in Tab. 6.1. Finally, during the years of the thesis, I have been involved in the publication of four additional papers, two of them related with the QUIJOTE project, and two belonging to a different project based on observation of the Andromeda galaxy (M31) at 6.7 GHz with the Sardinia Radio Telescope[1] (SRT). They are listed in the items 13–16 in the same table.

6.5 Future prospects

The PICASSO code for map-making can be further developed. For example, the fitting of a template function could be easily generalized to determine a set of amplitudes in independent data intervals, instead of in the full dataset, in order to follow possible time variations. This can be applied to fit an

---

[1] `http://www.srt.inaf.it/`

atmospheric component of the type of $1/\sin(el)$ in intervals of one hour, since the amplitude of the template can vary in time depending on the level of PWV during the observation.

In addition, PICASSO is based on totally general principles, and it can be adapted to other experiments. In particular, a version of PICASSO for the map-making of forthcoming data from the TFGI instrument of the QUIJOTE experiment could be implemented.

Concerning the QUIJOTE-MFI wide-survey maps, a set of papers presenting the data, as well as different scientific analyses, are in preparation. Additional consistency checks and validation analyses are under finalization. The maps will be publicly delivered after the acceptance for publication of the paper describing the maps (Rubiño-Martín et al., in prep), which is expected to happen by the end of 2021. These maps will be used for the characterization of the low-frequency foregrounds like AME and synchrotron, in intensity and in polarization, with the final goal of contributing to the detection of primordial B-modes of the CMB.

Moreover, a new instrument, the MFI-2, is under development, and it will be installed on the first QUIJOTE telescope during this year. It will provide improved quality data at the same frequency of the MFI, and a new wide-survey will be carried out in the following years. In addition, a spectrometer (the TMS) in the 10–20 GHz range is under development at the IAC. Data from the TMS will provide an absolute measurement of the sky emission at MFI frequencies, allowing the determination of the zero level of the QUIJOTE-MFI wide survey maps (among other scientific goals that are beyond the scope of this thesis).

The analysis of the microwave Haze in intensity and in polarization will be extended during the next few months. Several improvements to the maps and to template fitting procedure are expected. In particular, a detailed characterization of the large angular scales of the maps will be carried out, in order to confirm that the structures observed in the intensity and polarization residuals are associated with sky signal, and not with remaining noise artifacts. A more accurate determination of the polarization SED uncertainties will be developed. In addition, the fitting of a synchrotron component allowing for spatial variations of the spectral index will be tested. The spectral index map obtained from the analysis of the QUIJOTE-MFI wide-survey data (De la Hoz et al., in prep.) will be used for this purpose.

Item	Reference	Topic	Status
1	Guidi et al.	The PICASSO map-making code.	submitted (chap. 3)
2	Rubiño-Martín et al.	The QUIJOTE-MFI wide-survey.	in prep. (chap. 4)
3	Guidi et al.	The Haze as seen by QUIJOTE.	in prep. (chap. 5)
4	Génova-Santos et al.	QUIJOTE-MFI pipeline.	in prep.
5	De la Hoz et al.	Component separation in polarization*.	in prep.
6	Vansyngel et al.	Polarized diffuse synchrotron with cross-correlations*.	in prep.
7	Poidevin et al.	Study of AME in compact sources*.	in prep.
8	Watson et al.	The North Polar Spur*.	in prep.
9	Peel et al.	Polarized loops and spurs in the Milky Way*.	in prep.
10	Herranz et al.	Catalog of radio-sources*.	in prep.
11	Fernández Torreiro et al.	AME spatial variation in the Galactic plane*.	in prep.
12	López-Caraballo et al.	Study of supernova remnants*.	in prep.
13	Cepeda-Arroita et al. (2021)	AME in Lambda-Orionis using QUIJOTE-MFI and CBASS data.	published
14	Poidevin et al. (2019)	QUIJOTE scientific results – III. Study of the Taurus clouds and L1527.	published
15	Battistelli et al. (2019)	Strong Evidence of AME in M31 as observed with SRT at 6.7 GHz.	published
16	Fatigoni et al. (2021)	Study of M31 as observed with SRT at 6.7 GHz.	accepted

TABLE 6.1— List of first-author or co-author publications accomplished or prepared during this thesis. (*using the QUIJOTE-MFI wide-survey data.)

A

Appendix

A.1 PICASSO input commands

We show below an example of the inputs required to run the PICASSO code. First, PICASSO requires a list of the observations file names to be read (the file names must be in the typical BTOD or CTOD QUIJOTE format, e.g. HAZEA-160608-2356), and for the location of the files. Then, it asks: if the subtraction of the median value of the signal in one ring is required (usually it is not, because it is done at an earlier stage); the name of the observed field (indicative, not mandatory); the horn, frequency, and channel pair to be mapped; the baseline length for destriping; the desired resolution of the maps in term of the HEALPix parameter $N_{\rm side}$; which map the user wants to construct (intensity I or polarization Q, U); a label to be introduced in the name of the output file; and if the data are BTOD or CTOD (See Sec. 2.4.1).

Afterwards, it must be specified if the template fitting procedure is desired (see Sec. 3.4.4), which includes the fit of the function $1/\sin(el)$, of the CMB dipole, and of an arbitrary map given by the user. In this example we include a fit for an arbitrary map, therefore the path and name of the map is the following required input. Then PICASSO asks if simulated noise must be added to the data (useful for simulations, see Sec. 3.5.3). If this is the case, as it is in this example, the following inputs are the knee-frequency and the γ parameter of the $1/f$ noise to be simulated. Following this, it is required to specify which kind of prior should be used for the baseline determination (see Sec. 3.4.5), and if full covariance is selected, the knee-frequency and the γ parameter of the $1/f$ noise prior is also asked. It is then asked if the baseline priors need to be taken into account when fitting for the template function (this is usually not required as it has been demonstrated by tests that the procedure is slower and that it does not improve the precision of the fitted amplitude).

Afterwards, it is asked if the map to be constructed is the full map or a null-test (first or second split of rings, samples, altsamples, five-samples, two-samples, halfrings, daynight; see Sec. 4.5.2). This option is used to construct the independent null-test maps, by constructing the first and second data split with two independent runs of the code. Finally, all null-tests and the maps per period (Sec. 4.1.2) can be ran while producing the full map. In this case, the baselines obtained from the full data-set are subtracted to the data of the null-tests and period maps. The advantage of this option is that with a single run of the code, the map, all the null-test, and the period maps are constructed at once, but the resulting null-test maps are not totally independent because they all use the same baselines. The half, PWV and tbem splits selections are read from a master file that must be located in the same folder of the observations list (`/path/-to/data/`), with the name `list_of_files_master_nulltest.txt`. If this file is not found, the half, PWV and tbem splits are not generated. The data split of the remaining null-tests is performed internally by PICASSO.

Listing A.1— Example of the input interface of PICASSO. A configuration file can be also given to run PICASSO in a non-interactive mode.

```
*** DESTRIPADOR FOR QUIJOTE MFI ***
Version = Feb 17, 2021.
(remember to run: > limit stacksize unlimited )

  > BTOD or CTOD file list with root names:
list_of_files.txt

  > Path to BTOD or CTOD files ...
/path/to/data/

  > Remove medians (0=no, 1=yes) ...
0

  > Source name ...
HAZE

  > Horn (1,2,3,4) ...
3
```

```
  > Frequency: Low (0) / High (1) ...
0

  > Uncorrelated (0) / Correlated (1) channels ...
0

  > Baseline length (in seconds) ...
2.5

  > Nside of output map ...
512

  > Intensity (0) / Polarization (1) ...
1

  > Output file label (or empty) ...
test

  > Output directory ...
/output/path/

  > Write also median-filter map (0=no, 1=yes)
1

  > Use btod (0) or ctod (1)
1

  > (1) to correct for A/sin(el); (2) to correct for
   CMB dipole; (3) to correct for a template coming
   from an input Healpix map in mK, same nside and
   RING scheme, (0) Otherwise
3

  > 'path+name' of the input map to use as template.
    The template must be an Healpix map, with the same
    nside of the map that you are producing now, and
    ordered with a RING scheme.
/path/to/map/name_map.fits
```

```
  > Do you want to add 1/f simulated noise: 0=No, 1=yes.
1

  > Noise simulation Knee frequency fk: [(fk/f)**gamma].
20.0

  > Noise simulation 1/f gamma exponent: [(fk/f)**gamma].
1.5

  > Priors on the baselines: 0=No, 1=Only diagonal,
    2=Full Ca.
2

  > Knee frequency fk: [(fk/f)**gamma].
40.0

  > 1/f gamma exponent: [(fk/f)**gamma].
1.5

  > Do you want to account for the noise covariance matrix
    to fit the template function? 0:No, 1:Yes
0

  > Do you want to do the odd/even rings nulltest? 0=No,
    1=odd rings, 2=even rings
0

  > Do you want to do the odd/even samples nulltest? 0=No,
    1=odd samples, 2=even samples
0

  > Do you want to do the alternative odd/even samples
    nulltest? 0=No, 1=odd samples alt, 2=even samples alt
0

  > Do you want to do the five odd/even samples nulltest?
    0=No, 1=5 odd samples, 2=5 even samples
0
```

```
  > Do you want to do the two odd/even samples nulltest?
    0=No, 1=2 odd samples, 2=2 even samples
0

  > Do you want to do the half-rings (AZ<180 vs AZ>180)
    nulltest? 0=No, 1=(AZ<180), 2=(AZ>180)
0

  > Do you want to do the day/night nulltest?  0=No, 1=day
    data from 8am to 8pm, 2=night data from 8pm to 8am.
0

  > Do you want to make the maps for all the periods and
    all the nulltests? 0=No, 1=Yes
1

  > Master file for the nulltest (half, pwv, tbem):
 list_of_files_master_nulltest.txt
```

A.2 Posterior analysis of the T-T plots

We commented in Sec .5.3.2.2 about the necessity to check that posterior of the T-T plots is closed, in order to ensure that the signal-to-noise in the region is sufficient to provide a correct determination of the spectral index.

We report here the plots of the estimated spectral indices as a function of the projection angle α, and the relative posterior distributions. In Fig. A.1, A.2 and A.3, we show the results for 30–23 GHz, 11–23 GHz, and for 2.3–23 GHz (where S-PASS data are corrected for Faraday rotation as presented in Sec. 5.2.3).

The weighted average of the spectral indices, which is represented as an horizontal black line in the β vs α figures, correspond to the final results of this work, which are represented in Fig. 5.20 and quoted in Tab. 5.7. Colour corrections are applied independently for the determination of the spectral index at each angle α.

In the plots of the posteriors, each coloured line represents the posterior for a determined projection angle α, normalized with its maximum and computed with Eq. 5.25. Here no colour corrections are applied. The red thick line in the plots shows the final posterior normalized with its maximum, obtained as the product of each single posterior distribution. The vertical blue line shows the final spectral index computed with Eq. 5.21, with no colour corrections applied. We can notice that there is a very good match between the final posterior

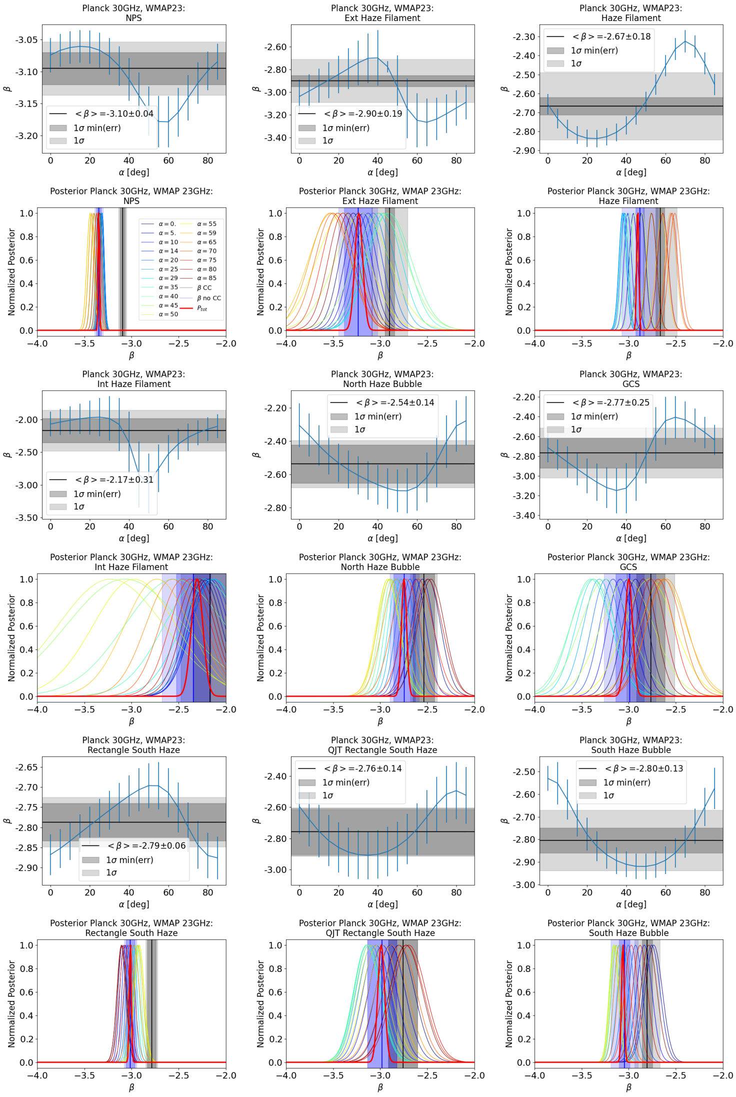

FIGURE A.1— T-T plots Planck 30 GHz-WMAP K: spectral index as a function of the angle and posterior. The legend of the posteriors plots is shown in the first image of the series (second row, left).

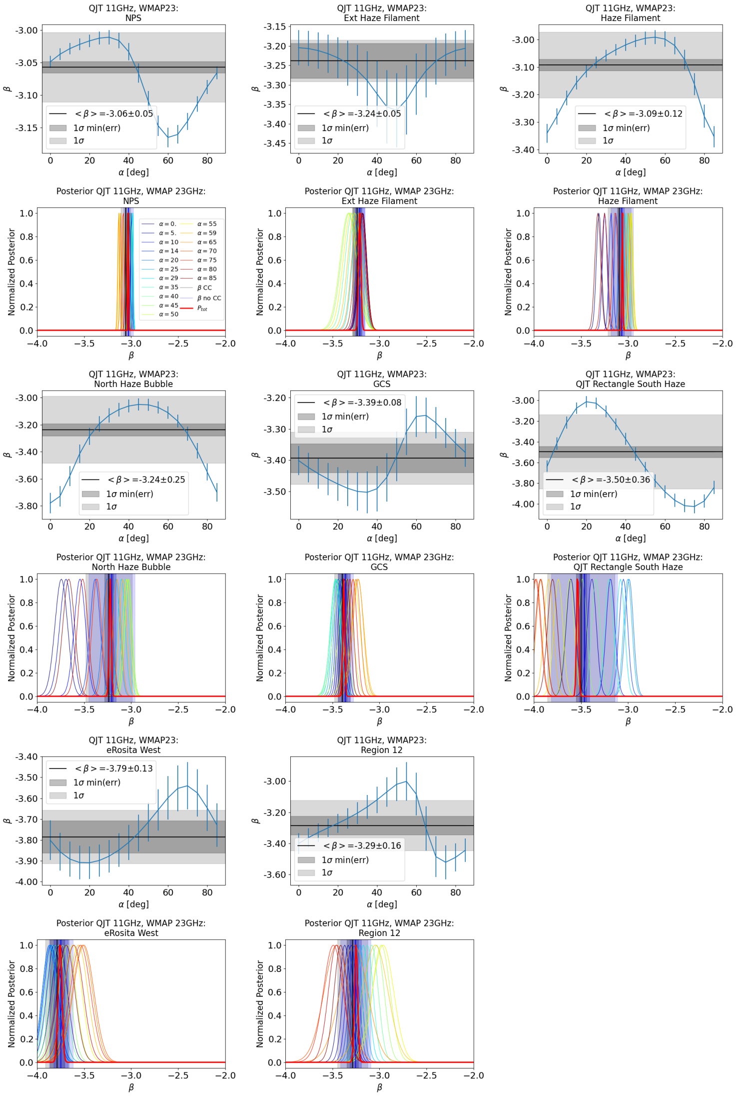

FIGURE A.2— T-T plots QUIJOTE 11 GHz-WMAP K: spectral index as a function of the angle and posterior. The legend of the posteriors plots is shown in the first image of the series (second row, left).

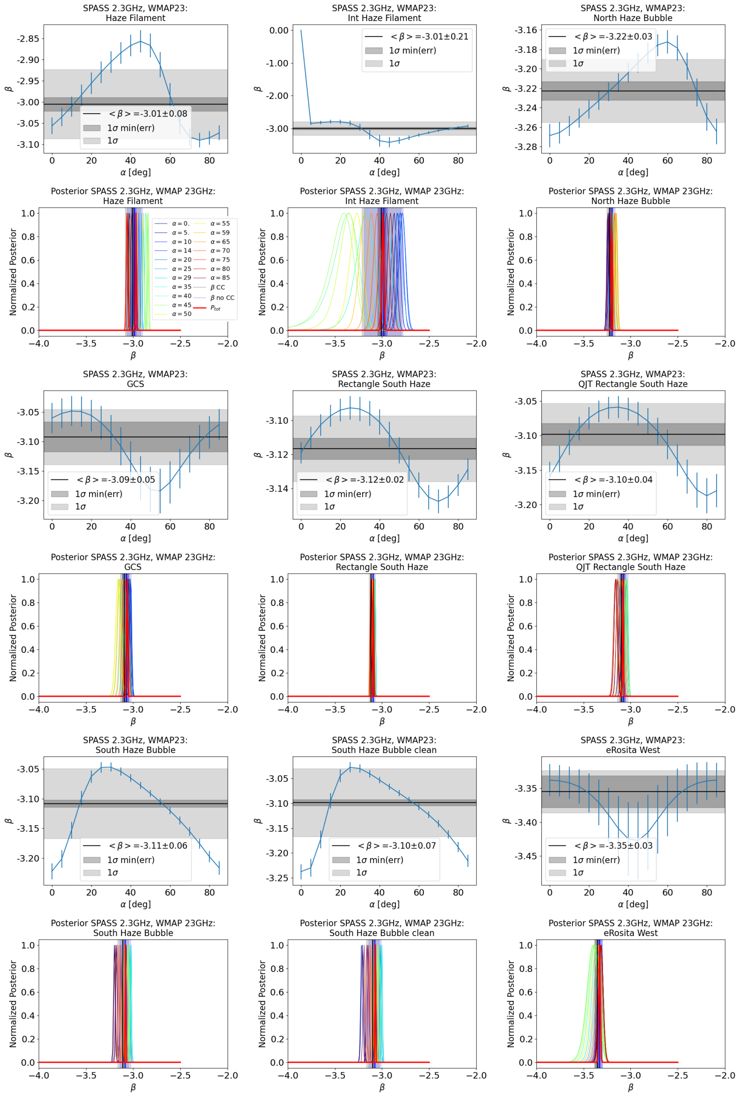

FIGURE A.3— T-T plots S-PASS 2.3 GHz-WMAP K: spectral index as a function of the angle and posterior. The legend of the posteriors plots is shown in the first image of the series (second row, left).

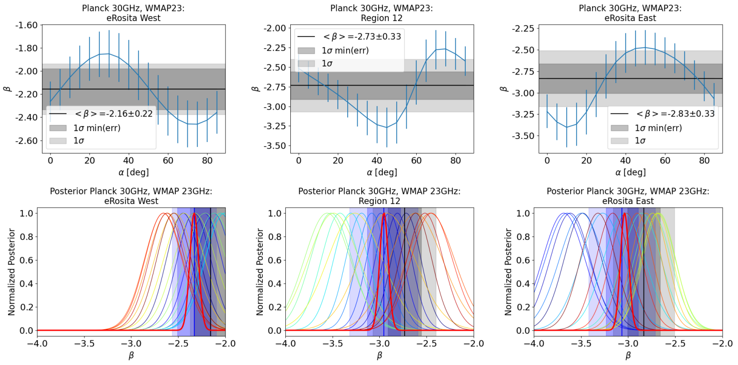

FIGURE A.4— Continuation of Fig. A.1.

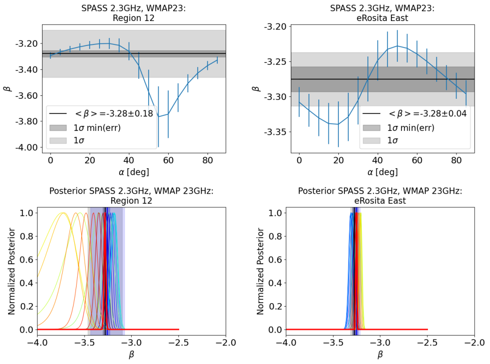

FIGURE A.5— Continuation of Fig. A.3.

distribution and the estimated weighted average spectral index. When we apply colour corrections to the spectral index, we obtain the value represented by the vertical black line in the posterior figures, which corresponds to the horizontal black line of the β vs α figures.

We can notice from Fig. A.1–A.5 that the posterior distributions of the spectral indices, in all the considered regions and frequencies, are closed and approximately Gaussian, and that therefore the spectral indices are well constrained.

In addition, we can observe that, when we use low frequency data as from QUIJOTE at 11 GHz and from S-PASS at 2.3 GHz, the posteriors are narrower than that of Planck 30 GHz, thanks to the wider frequency lever with respect to WMAP K (22.8 GHz), corresponding to a more precise determination of the spectral indices.

Bibliography

Ackermann, M., Albert, A., Atwood, W. B., et al. 2014, ApJ, 793, 64

Almy, R. C., McCammon, D., Digel, S. W., Bronfman, L., & May, J. 2000, ApJ, 545, 290

Alonso, D., Sanchez, J., Slosar, A., & LSST Dark Energy Science Collaboration. 2019, MNRAS, 484, 4127

Alonso-Arias, P., Rubiño-Martín, J. A., Hoyland, R. J., et al. 2020, in Society of Photo-Optical Instrumentation Engineers (SPIE) Conference Series, Vol. 11447, Society of Photo-Optical Instrumentation Engineers (SPIE) Conference Series, 114476N

Alpher, R. A., Bethe, H., & Gamow, G. 1948, Physical Review, 73, 803

Alpher, R. A. & Herman, R. C. 1950, Reviews of Modern Physics, 22, 153

Ashdown, M. A. J., Baccigalupi, C., Balbi, A., et al. 2007, A&A, 471, 361

Battistelli, E. S., Fatigoni, S., Murgia, M., et al. 2019, ApJ, 877, L31

Battye, R. A., Browne, I. W. A., Peel, M. W., Jackson, N. J., & Dickinson, C. 2011, MNRAS, 413, 132

Becker, R. H., Fan, X., White, R. L., et al. 2001, AJ, 122, 2850

Bennett, C. L., Larson, D., Weiland, J. L., et al. 2013, ApJS, 208, 20

Bennett, C. L., Smoot, G. F., Janssen, M., et al. 1992, ApJ, 391, 466

BICEP2 Collaboration, Keck Array Collaboration, Ade, P. A. R., et al. 2018, Phys.Rev.Lett, 121, 221301

Biermann, P. L., Becker, J. K., Caceres, G., et al. 2010, ApJ, 710, L53

Bilbao-Ahedo, J. D., Barreiro, R. B., Vielva, P., Martínez-González, E., & Herranz, D. 2021, arXiv e-prints, arXiv:2104.08528

Blas, D., Lesgourgues, J., & Tram, T. 2011, JCAP, 2011, 034

Bode, P. & Bertschinger, E. 1995, arXiv e-prints, astro

Boesgaard, A. M. & Steigman, G. 1985, ARA&A, 23, 319

Cardoso, J.-F., Martin, M., Delabrouille, J., Betoule, M., & Patanchon, G. 2008, arXiv e-prints, arXiv:0803.1814

Carretti, E., Crocker, R. M., Staveley-Smith, L., et al. 2013, Nature, 493, 66

Carretti, E., Haverkorn, M., Staveley-Smith, L., et al. 2019, MNRAS, 489, 2330

Castro-Almazán, J. A., Muñoz-Tuñón, C., García-Lorenzo, B., et al. 2016, in Society of Photo-Optical Instrumentation Engineers (SPIE) Conference Series, Vol. 9910, Observatory Operations: Strategies, Processes, and Systems VI, ed. A. B. Peck, R. L. Seaman, & C. R. Benn, 99100P

Cepeda-Arroita, R., Harper, S. E., Dickinson, C., et al. 2021, MNRAS, 503, 2927

Challinor, A. 2006, arXiv e-prints, astro

Challinor, A., Fosalba, P., Mortlock, D., et al. 2000, Phys.Rev.D, 62, 123002

Chluba, J. 2018, arXiv e-prints, arXiv:1806.02915

Chluba, J., Kogut, A., Patil, S. P., et al. 2019, Spectral Distortions of the CMB as a Probe of Inflation, Recombination, Structure Formation and Particle Physics

Choi, S. K., Hasselfield, M., Ho, S.-P. P., et al. 2020, arXiv e-prints, arXiv:2007.07289

Choi, S. K. & Page, L. A. 2015, JCAP, 2015, 020

Cholis, I., Goodenough, L., & Weiner, N. 2009, Phys.Rev.D, 79, 123505

Chon, G., Challinor, A., Prunet, S., Hivon, E., & Szapudi, I. 2004, MNRAS, 350, 914

Clark, S. E., Kim, C.-G., Hill, J. C., & Hensley, B. S. 2021, arXiv e-prints, arXiv:2105.00120

Coles, P. & Lucchin, F. 2002, Cosmology: The Origin and Evolution of Cosmic Structure, Second Edition

Conklin, E. K. 1969, Nature, 222, 971

Crocker, R. M. 2012, MNRAS, 423, 3512

Crocker, R. M. & Aharonian, F. 2011, Phys.Rev.Lett, 106, 101102

Crocker, R. M., Bicknell, G. V., Taylor, A. M., & Carretti, E. 2015, ApJ, 808, 107

Delahaye, T., Böhm, C., & Silk, J. 2012, MNRAS, 422, L16

Dickinson, C. 2016, arXiv e-prints, arXiv:1606.03606

Dickinson, C., Ali-Haïmoud, Y., Barr, A., et al. 2018a, New Astronomy Reviews, 80, 1

Dickinson, C., Ali-Haïmoud, Y., Barr, A., et al. 2018b, New Astronomy Reviews, 80, 1

Dickinson, C., Davies, R. D., & Davis, R. J. 2003, MNRAS, 341, 369

Dobler, G. 2012, ApJ, 750, 17

Dobler, G. & Finkbeiner, D. P. 2008, ApJ, 680, 1222

Dobler, G., Finkbeiner, D. P., Cholis, I., Slatyer, T., & Weiner, N. 2010, ApJ, 717, 825

Dodelson, S. 2003, Modern cosmology

Doran, M. 2005, JCAP, 2005, 011

Draine, B. T. 2011, Physics of the Interstellar and Intergalactic Medium

Draine, B. T. & Hensley, B. 2013, ApJ, 765, 159

Draine, B. T. & Lazarian, A. 1999, ApJ, 512, 740

Efstathiou, G. 2006, MNRAS, 370, 343

Egorov, A. E., Gaskins, J. M., Pierpaoli, E., & Pietrobon, D. 2016, JCAP, 2016, 060

Eriksen, H. K., Jewell, J. B., Dickinson, C., et al. 2008, ApJ, 676, 10

Eriksen, H. K., O'Dwyer, I. J., Jewell, J. B., et al. 2004, ApJS, 155, 227

Fan, X., Narayanan, V. K., Strauss, M. A., et al. 2002, AJ, 123, 1247

Finkbeiner, D. P. 2003, ApJS, 146, 407

Finkbeiner, D. P. 2004, ApJ, 614, 186

Fixsen, D. J. 2009, ApJ, 707, 916

Fowles, G. R. 1968, Introduction to Modern Optics

Fox, A. J., Bordoloi, R., Savage, B. D., et al. 2015, ApJ, 799, L7

Fuskeland, U., Andersen, K. J., Aurlien, R., et al. 2019, arXiv e-prints, arXiv:1909.05923

Fuskeland, U., Wehus, I. K., Eriksen, H. K., & Næss, S. K. 2014, ApJ, 790, 104

Gamow, G. 1946, Physical Review, 70, 572

Gaskins, J. M. 2016, Contemporary Physics, 57, 496

Génova-Santos, R., Rubiño-Martín, J. A., Peláez-Santos, A., et al. 2017, MNRAS, 464, 4107

Génova-Santos, R., Rubiño-Martín, J. A., Rebolo, R., et al. 2015, MNRAS, 452, 4169

Górski, K. M., Hivon, E., Banday, A. J., et al. 2005, ApJ, 622, 759

Guo, F. & Mathews, W. G. 2012, ApJ, 756, 181

Guo, F., Mathews, W. G., Dobler, G., & Oh, S. P. 2012, ApJ, 756, 182

Guth, A. H. 1981, Phys.Rev.D, 23, 347

Hafez, Y. A., Davies, R. D., Davis, R. J., et al. 2008, MNRAS, 388, 1775

Hanson, D., Hoover, S., Crites, A., et al. 2013, Phys.Rev.Lett, 111, 141301

Harper, S. 2016, Single dish intensity mapping with the QUIJOTE MFI and GBT

Harrison, E. R. 1970, Phys.Rev.D, 1, 2726

Haslam, C. G. T., Salter, C. J., Stoffel, H., & Wilson, W. E. 1982, A&AS, 47, 1

Hildebrand, R. H., Davidson, J. A., Dotson, J. L., et al. 2000, PASP, 112, 1215

Hivon, E., Górski, K. M., Netterfield, C. B., et al. 2002, ApJ, 567, 2

Hooper, D., Finkbeiner, D. P., & Dobler, G. 2007, Phys.Rev.D, 76, 083012

Hu, W. & Dodelson, S. 2002, ARA&A, 40, 171

Hu, W. & White, M. 1997, New Astronomy, 2, 323

Hubble, E. 1929, Contributions from the Mount Wilson Observatory, 3, 23

Iacobelli, M., Burkhart, B., Haverkorn, M., et al. 2014, A&A, 566, A5

Ichiki, K. 2014, Progress of Theoretical and Experimental Physics, 2014, 06B109

Ichiki, K., Kaji, R., Yamamoto, H., Takeuchi, T. T., & Fukui, Y. 2014, ApJ, 780, 13

Jew, L. & Grumitt, R. D. P. 2020, MNRAS, 495, 578

Jonas, J. L., de Jager, G., & Baart, E. E. 1985, A&AS, 62, 105

Jones, A. P. 2009, A&A, 506, 797

Jones, D. I., Crocker, R. M., Reich, W., Ott, J., & Aharonian, F. A. 2012, ApJ, 747, L12

Jones, M. E., Taylor, A. C., Aich, M., et al. 2018, MNRAS, 480, 3224

Kamionkowski, M., Kosowsky, A., & Stebbins, A. 1997a, Phys.Rev.Lett, 78, 2058

Kamionkowski, M., Kosowsky, A., & Stebbins, A. 1997b, Phys.Rev.D, 55, 7368

Kamionkowski, M. & Kovetz, E. D. 2016, ARA&A, 54, 227

Kasten, F. & Young, A. T. 1989, Appl.Optics, 28, 4735

Keihänen, E., Keskitalo, R., Kurki-Suonio, H., Poutanen, T., & Sirviö, A. S. 2010, A&A, 510, A57

Keihänen, E., Kurki-Suonio, H., & Poutanen, T. 2005, MNRAS, 360, 390

Klypin, A. A., Strukov, I. A., & Skulachev, D. P. 1992, MNRAS, 258, 71

Kogut, A., Banday, A. J., Bennett, C. L., et al. 1996, ApJ, 464, L5

Kovac, J. M., Leitch, E. M., Pryke, C., et al. 2002, Nature, 420, 772

Krachmalnicoff, N., Carretti, E., Baccigalupi, C., et al. 2018, A&A, 618, A166

Kurki-Suonio, H., Keihänen, E., Keskitalo, R., et al. 2009, A&A, 506, 1511

Kusaka, A., Appel, J., Essinger-Hileman, T., et al. 2018, JCAP, 2018, 005

Lacki, B. C. 2014, MNRAS, 444, L39

Lamagna, L., Addamo, G., Ade, P. A. R., et al. 2020, Journal of Low Temperature Physics, 200, 374

Lazarian, A. 2007, JQSRT, 106, 225

Lazarian, A. & Finkbeiner, D. 2003, New Astronomy Reviews, 47, 1107

Lesgourgues, J. 2011, arXiv e-prints, arXiv:1104.2932

Lewis, A. & Challinor, A. 2011, CAMB: Code for Anisotropies in the Microwave Background

Li, J.-T., Hodges-Kluck, E., Stein, Y., et al. 2019, ApJ, 873, 27

Macellari, N., Pierpaoli, E., Dickinson, C., & Vaillancourt, J. E. 2011, MNRAS, 418, 888

Mather, J. C., Cheng, E. S., Eplee, R. E., J., et al. 1990, ApJ, 354, L37

Merloni, A., Predehl, P., Becker, W., et al. 2012, arXiv e-prints, arXiv:1209.3114

Minami, Y., Ochi, H., Ichiki, K., et al. 2019, Progress of Theoretical and Experimental Physics, 2019, 083E02

Miville-Deschênes, M. A., Ysard, N., Lavabre, A., et al. 2008, A&A, 490, 1093

Nagasaki, T., Choi, J., Génova-Santos, R. T., et al. 2018, Journal of Low Temperature Physics, 193, 1066

Nashimoto, M., Hattori, M., Poidevin, F., & Génova-Santos, R. 2020, ApJ, 900, L40

Neugebauer, G., Habing, H. J., van Duinen, R., et al. 1984, ApJ, 278, L1

Omori, Y., Chown, R., Simard, G., et al. 2017, ApJ, 849, 124

Padilla, I. L., Eimer, J. R., Li, Y., et al. 2020, ApJ, 889, 105

Padmanabhan, T. 1993, Structure Formation in the Universe

Pardo, J. R., Cernicharo, J., & Serabyn, E. 2001, IEEE Transactions on Antennas and Propagation, 49, 1683

Peebles, P. J. & Wilkinson, D. T. 1968, Physical Review, 174, 2168

Peebles, P. J. E. 1965, ApJ, 142, 1317

Peel, M. W., Dickinson, C., Davies, R. D., et al. 2012, MNRAS, 424, 2676

Pelaez Santos, A. 2019, Map making and power spectrum estimation for the QUIJOTE experiment: application to MFI data (PhD thesis, Universidad de La Laguna)

Penzias, A. A. & Wilson, R. W. 1965, ApJ, 142, 419

Perrott, Y. C., López-Caniego, M., Génova-Santos, R. T., et al. 2021, MNRAS[fundefined@eprint@ : rXiv]2102.04520]

Petroff, M. A., Eimer, J. R., Harrington, K., et al. 2020, ApJ, 889, 120

Pietranera, L., Buehler, S. A., Calisse, P. G., et al. 2007, MNRAS, 376, 645

Pietrobon, D., Górski, K. M., Bartlett, J., et al. 2012, ApJ, 755, 69

Planck Collaboration, Abergel, A., Ade, P. A. R., et al. 2014a, A&A, 571, A11

Planck Collaboration, Adam, R., Ade, P. A. R., et al. 2016a, A&A, 594, A10

Planck Collaboration, Adam, R., Ade, P. A. R., et al. 2016b, A&A, 586, A133

Planck Collaboration, Ade, P. A. R., Aghanim, N., et al. 2015, A&A, 576, A104

Planck Collaboration, Ade, P. A. R., Aghanim, N., et al. 2016c, A&A, 594, A25

Planck Collaboration, Ade, P. A. R., Aghanim, N., et al. 2014b, A&A, 565, A103

Planck Collaboration, Ade, P. A. R., Aghanim, N., et al. 2016d, A&A, 594, A26

Planck Collaboration, Ade, P. A. R., Aghanim, N., et al. 2013, A&A, 554, A139

Planck Collaboration, Ade, P. A. R., Aghanim, N., et al. 2011, A&A, 536, A20

Planck Collaboration, Ade, P. A. R., Aghanim, N., et al. 2016e, A&A, 594, A13

Planck Collaboration, Ade, P. A. R., Aghanim, N., et al. 2016f, A&A, 586, A141

Planck Collaboration, Ade, P. A. R., Aghanim, N., et al. 2016g, A&A, 594, A6

Planck Collaboration, Aghanim, N., Akrami, Y., et al. 2020a, A&A, 641, A6

Planck Collaboration, Aghanim, N., Akrami, Y., et al. 2020b, A&A, 641, A8

Planck Collaboration, Aghanim, N., Akrami, Y., et al. 2020c, A&A, 641, A3

Planck Collaboration, Aghanim, N., Akrami, Y., et al. 2020d, A&A, 641, A3

Planck Collaboration, Aghanim, N., Armitage-Caplan, C., et al. 2014c, A&A, 571, A5

Planck Collaboration, Akrami, Y., Andersen, K. J., et al. 2020e, A&A, 643, A42

Planck Collaboration, Akrami, Y., Argüeso, F., et al. 2018a, arXiv e-prints, arXiv:1807.06206

Planck Collaboration, Akrami, Y., Argüeso, F., et al. 2020f, A&A, 641, A2

Planck Collaboration, Akrami, Y., Arroja, F., et al. 2018b, arXiv e-prints, arXiv:1807.06211

Planck Collaboration, Akrami, Y., Ashdown, M., et al. 2018c, arXiv e-prints, arXiv:1807.06208

Planck Collaboration, Akrami, Y., Ashdown, M., et al. 2020g, A&A, 641, A4

Planck Collaboration, Akrami, Y., Ashdown, M., et al. 2020h, A&A, 641, A11

Planck HFI Core Team, Ade, P. A. R., Aghanim, N., et al. 2011, A&A, 536, A6

Plaszczynski, S., Montier, L., Levrier, F., & Tristram, M. 2014, MNRAS, 439, 4048

Pogosian, L. & Zucca, A. 2018, Classical and Quantum Gravity, 35, 124004

Poidevin, F., Rubiño-Martín, J. A., Dickinson, C., et al. 2019, MNRAS, 486, 462

Polarbear Collaboration, Adachi, S., Aguilar Faúndez, M. A. O., et al. 2020, ApJ, 897, 55

Polarbear Collaboration, Ade, P. A. R., Akiba, Y., et al. 2014, ApJ, 794, 171

Poletti, D., Fabbian, G., Le Jeune, M., et al. 2017, A&A, 600, A60

Predehl, P., Sunyaev, R. A., Becker, W., et al. 2020, Nature, 588, 227

Rawls, M. L., Thiemann, H. B., Chemin, V., et al. 2020, Research Notes of the American Astronomical Society, 4, 189

Reich, P. & Reich, W. 1986, A&AS, 63, 205

Reich, P., Testori, J. C., & Reich, W. 2001, A&A, 376, 861

Remazeilles, M., Dickinson, C., Banday, A. J., Bigot-Sazy, M. A., & Ghosh, T. 2015, MNRAS, 451, 4311

Renzi, F., Cabass, G., Di Valentino, E., Melchiorri, A., & Pagano, L. 2018, JCAP, 2018, 038

Riess, A. G., Macri, L. M., Hoffmann, S. L., et al. 2016, ApJ, 826, 56

Roll, P. G. & Wilkinson, D. T. 1966, Phys.Rev.Lett, 16, 405

Rubiño Martín, J. A., Alonso Arias, P., Hoyland, R. J., et al. 2020, in Society of Photo-Optical Instrumentation Engineers (SPIE) Conference Series, Vol. 11453, Society of Photo-Optical Instrumentation Engineers (SPIE) Conference Series, 114530T

Rybicki, G. B. & Lightman, A. P. 1986, Radiative Processes in Astrophysics

Sachs, R. K. & Wolfe, A. M. 1967, ApJ, 147, 73

Seljak, U. & Zaldarriaga, M. 1996, ApJ, 469, 437

Silk, J. 1968, ApJ, 151, 459

Smoot, G., Bennett, C., Weber, R., et al. 1990, ApJ, 360, 685

Soliman, A., Ade, P. A. R., Ahmed, Z., et al. 2020, Journal of Low Temperature Physics, 199, 1118

SPIDER Collaboration, Ade, P. A. R., Amiri, M., et al. 2021, arXiv e-prints, arXiv:2103.13334

Steigman, G. 2004, Tracking the baryon density from the Big Bang to the present, 46

Su, M., Slatyer, T. R., & Finkbeiner, D. P. 2010, ApJ, 724, 1044

Sunyaev, R. A. & Zeldovich, I. B. 1980, ARA&A, 18, 537

Sutton, D., Zuntz, J. A., Ferreira, P. G., et al. 2010, MNRAS, 407, 1387

Takakura, S., Aguilar-Faúndez, M. A. O., Akiba, Y., et al. 2019, ApJ, 870, 102

Tegmark, M. 1997, Phys.Rev.D, 56, 4514

Tegmark, M. & de Oliveira-Costa, A. 2001, Phys.Rev.D, 64, 063001

Tramonte, D. 2017, Using CMB, LSS and Galaxy Clusters as Cosmological Probes

Tristram, M., Banday, A. J., Górski, K. M., et al. 2020, arXiv e-prints, arXiv:2010.01139

Tristram, M., Macías-Pérez, J. F., Renault, C., & Santos, D. 2005, MNRAS, 358, 833

Tucci, M., Martínez-González, E., Toffolatti, L., González-Nuevo, J., & De Zotti, G. 2004, MNRAS, 349, 1267

Vidal, M., Dickinson, C., Davies, R. D., & Leahy, J. P. 2015, MNRAS, 452, 656

Vidal, M., Leahy, J. P., & Dickinson, C. 2016, MNRAS, 461, 698

Vignaga, R. 2018, QUIJOTE-MFI: Optics Characterisation and Polarisation Measurements of CMB Foregrounds

Watson, R. A., Rebolo, R., Rubiño-Martín, J. A., et al. 2005, ApJ, 624, L89

Weiland, J. L., Odegard, N., Hill, R. S., et al. 2011, ApJS, 192, 19

Weinberg, S. 2008, Cosmology

White, M., Scott, D., & Silk, J. 1994, ARA&A, 32, 319

White, M. & Srednicki, M. 1995, ApJ, 443, 6

Wolleben, M., Landecker, T. L., Reich, W., & Wielebinski, R. 2006, A&A, 448, 411

Zacchei, A., Maino, D., Baccigalupi, C., et al. 2011, A&A, 536, A5

Zaldarriaga, M. & Seljak, U. 1997, Phys.Rev.D, 55, 1830

Zaldarriaga, M., Seljak, U., & Bertschinger, E. 1998, ApJ, 494, 491

Zeldovich, Y. B. 1972, MNRAS, 160, 1P

Zhang, M., Li, Z., & Morris, M. R. 2021, arXiv e-prints, arXiv:2101.10741

Zhang, R. & Guo, F. 2020, ApJ, 894, 117

Zhang, R. & Guo, F. 2021, arXiv e-prints, arXiv:2102.01710

Zubovas, K. & Nayakshin, S. 2012, MNRAS, 424, 666